



## GULF ELECTRONIC SYSTEMS

Gulf-EL-A10968

SEMIANNUAL TECHNICAL REPORT FOR THE PERIOD  
1 JULY 1971 TO 31 DECEMBER 1971

### CARBON RESEARCH

Sponsored by  
Advanced Research Projects Agency  
Arlington, Virginia

ARPA Order No. 1861

January 31, 1972

R. J. Akins, J. L. Kase, R. J. Price, F. J. Schoen,  
and J. C. Bokros (P.I.) (714-453-1000)

GULF OIL CORPORATION  
GULF ENERGY & ENVIRONMENTAL SYSTEMS COMPANY  
San Diego, California 92112

Program Code Number: 1D10

Contract Date: 26 June 1971

Contract Amount: \$114,980

Expiration Date: 25 August 1972

This research was supported by the Advanced Research Projects Agency of the Department of Defense under Contract No. DAHC15-71-C-0282.

"The views and conclusions contained in this document are those of the authors and should not be interpreted as necessarily representing the official policies, either expressed or implied, of the Advanced Research Projects Agency or the U.S. Government."

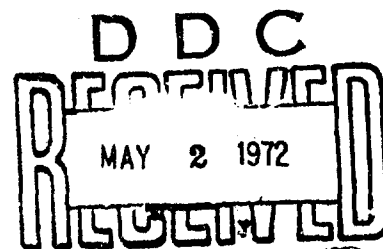
#### DISTRIBUTION STATEMENT A

Approved for public release;  
Distribution Unlimited

Reproduced by  
NATIONAL TECHNICAL  
INFORMATION SERVICE  
Springfield, Va. 22151

GULF ELECTRONIC SYSTEMS  
A DIVISION OF GULF ENERGY & ENVIRONMENTAL SYSTEMS COMPANY  
P.O. BOX 608, SAN DIEGO, CALIFORNIA 92112

AD 740764





## **GULF ELECTRONIC SYSTEMS**

Gulf-EL-A10968

SEMIANNUAL TECHNICAL REPORT FOR THE PERIOD

1 JULY 1971 TO 31 DECEMBER 1971

CARBON RESEARCH

Sponsored by  
Advanced Research Projects Agency  
Arlington, Virginia

ARPA Order No. 1861

January 31, 1972

R. J. Akins, J. L. Kaae, R. J. Price, F. J. Schoen,  
and J. C. Bokros (P.I.) (714-453-1000)

GULF OIL CORPORATION  
GULF ENERGY & ENVIRONMENTAL SYSTEMS COMPANY  
San Diego, California 92112

Program Code Number: 1D10

Contract Date: 26 June 1971

Contract Amount: \$114,980

Expiration Date: 25 August 1972

This research was supported by the Advanced Research Projects Agency of the Department of Defense under Contract No. DAHC15-71-C-0282.

"The views and conclusions contained in this document are those of the authors and should not be interpreted as necessarily representing the official policies, either expressed or implied, of the Advanced Research Projects Agency or the U.S. Government."

GULF ELECTRONIC SYSTEMS  
A DIVISION OF GULF ENERGY & ENVIRONMENTAL SYSTEMS COMPANY  
P O. BOX 608. SAN DIEGO. CALIFORNIA 92112

Unclassified  
Security Classification

| DOCUMENT CONTROL DATA - R & D  |   |   |
|--|---|---|
| (Security classification of title, body of abstract and indexing annotation must be entered when the overall report is classified)   |   |   |
| 1. ORIGINATING ACTIVITY (Corporate author)<br>Gulf Oil Corporation,<br>Gulf Energy & Environmental Systems Company<br>P.O. Box 608, San Diego, California 92112  |   | 2a. REPORT SECURITY CLASSIFICATION<br>Unclassified  |
|  |   | 2b. GROUP   |
| 3. REPORT TITLE<br>Carbon Research   |   |   |
| 4. DESCRIPTIVE NOTES (Type of report and inclusive dates)<br>Semiannual. July 1, 1971 - December 31, 1971  |   |   |
| 5. AUTHOR(S) (First name, middle initial, last name)<br>Jack C. Bokros, Robert J. Akins, James L. Kaae, Robert J. Price, Frederick J. Schoen   |   |   |
| 6. REPORT DATE<br>January 31, 1972   | 7a. TOTAL NO. OF PAGES<br>173   | 7b. NO. OF REFS<br>66   |
| 8a. CONTRACT OR GRANT NO.<br>DAHC15-71-C-0282  | 8b. ORIGINATOR'S REPORT NUMBER(S)<br>Gulf-EL-A10968                         |   |
| b. PROJECT NO.<br>c.<br>d.   | 9b. OTHER REPORT NO(S) (Any other numbers that may be assigned this report) |   |
| 10. DISTRIBUTION STATEMENT<br>Approved for public release; distribution unlimited.   |   |   |
| 11. SUPPLEMENTARY NOTES  |   | 12. SPONSORING MILITARY ACTIVITY<br>Advanced Research Projects Agency<br>Washington, D.C. |
| 13. ABSTRACT<br>The pyrolytic carbons deposited in fluidized beds are a new family of carbonaceous materials with structures and properties that can be controlled over wide ranges. Technologically, these materials are grossly under-utilized. One of the objectives of the present work is to develop a better understanding of the relationships between the structure of pyrolytic carbons and the reactions involved in their formation so that applications may be broadened. For this purpose, a relatively new modification of the fluidized-bed process is being used which allows complete control of the bed surface area during deposition ("steady-state beds").<br>During the first six months, several exploratory "fields" of structures were formed using steady-state beds. It was found that in the pure carbon system, the structure, as measured by density, $L_c$ parameter, and anisotropy, could be easily controlled. For the isotropic deposits formed in the low-temperature region (below about 1400°C), there is a correlation of $L_c$ and density: at a given temperature both increase with increasing propane concentration. This is in spite of a concomitant rise in deposition rate.<br>The hardness of the pure isotropic carbons increases with density and decreases with increasing $L_c$ parameter (other structural parameters being constant). The data indicate that the best deposits are those that are isotropic with high density and small $L_c$ parameters, but the correlation between $L_c$ and density makes the formation of this combination attainable only under special conditions. These conditions are being sought. |   |   |

Unclassified

Security Classification

14

KEY WORDS

LINK A

LINK B

LINK C

ROLE

WT

ROLE

WT

ROLE

WT

Pyrolytic carbons  
Fluidized beds  
Steady-state fluidized beds  
Chemical vapor depositions  
Pyrolytic-carbon wear properties  
Pyrolytic-carbon fatigue properties  
Pyrolytic-carbon strength properties  
Pyrolytic-carbon physical properties

Unclassified

Security Classification

### 13. Abstract (Continued)

Addition of silicon by co-deposition in the presence of chlorine enhances the hardness of the carbon-silicon deposits and modifies the deposition process considerably. Co-deposition with boron in the presence of chlorine, on the other hand, causes the deposits to have large  $L_c$  parameters and to be relatively soft. There is much more to be learned about the deposition, structure, and properties of the carbon-silicon and carbon-boron systems.

The properties of some of the initial series of structures have been measured. The modulus of rupture of the pure carbons increases with increasing density and is believed to be weakened by the flaws associated with soot included in the structure. In spite of the presence of these flaws, the isotropic pyrolytic carbons are all substantially stronger than the vitreous or glassy carbons. A major objective will be to develop an understanding of the origin of these flaws so that they may be eliminated.

Using a test developed for comparative evaluation of wear couples, the wear behavior of a complete series of pure and silicon-alloyed isotropic carbons has been evaluated. In the geometry of this test, volume removed is linear with time; i.e., a constant wear rate is obtained. The wear resistance of pure carbons is very good and correlates with density and hardness. The wear resistance of silicon-alloyed carbons appears to be greater than that of pure carbons and increases with increasing hardness.

One of the most interesting findings, and one that may prove to be of some technological significance, has come from the first series of fatigue tests. Using a cantilevered beam loading arrangement, it has been found that for those unalloyed isotropic carbons tested, the endurance limit is virtually identical to the single-cycle fracture stress.

Measurements are showing a systematic variation of certain physical properties with structure. Thermal expansion measurements made parallel to the deposition plane on a series of isotropic pyrolytic carbons deposited from propane between 1200° and 1400°C show that the thermal expansivity increases with increasing carbon density from  $4 \times 10^{-6} \text{ }^\circ\text{C}^{-1}$  for a density around  $1.4 \text{ g/cm}^3$  to  $6 \times 10^{-6} \text{ }^\circ\text{C}^{-1}$  for a density of  $2.0 \text{ g/cm}^3$ . Combining these values with recently reported values for the c-axis thermal expansivity of low-temperature pyrolytic carbon crystallites yields values for the "accommodation coefficient" (fraction of crystallite expansion which is transmitted to the bulk) ranging from 0.68 for a carbon with a density of  $1.46 \text{ g/cm}^3$  to 0.97 for a carbon with a density of  $1.97 \text{ g/cm}^3$ .

The thermal conductivity perpendicular to the deposition plane was measured on a series of isotropic pyrolytic carbons using the heat-pulse method at temperatures between room temperature and 800°C. The results show that the room temperature thermal conductivity increases with increasing carbon density, from  $0.012 \text{ cal/cm-}^\circ\text{C-sec}$  for a density of  $1.5 \text{ g/cm}^3$  to  $0.018 \text{ cal/cm-}^\circ\text{C-sec}$  for a density of  $2.0 \text{ g/cm}^3$ . The conductivity of all the carbons decreases with increasing measurement temperature.

Using the initial findings as a guide in future work, efforts will be made to modify and improve the structures of the carbons formed in steady-state beds so that properties may be controlled or optimized.

## SUMMARY

The pyrolytic carbons deposited in fluidized beds are a new family of carbonaceous materials with structures and properties that can be controlled over wide ranges. Technologically, these materials are grossly under-utilized. One of the objectives of the present work is to develop a better understanding of the relationships between the structure of pyrolytic carbons and the reactions involved in their formation so that applications may be broadened. For this purpose, a relatively new modification of the fluidized-bed process is being used which allows complete control of the bed surface area during deposition ("steady-state beds").

During the first six months, several exploratory "fields" of structures were formed using steady-state beds. It was found that in the pure carbon system, the structure, as measured by density,  $L_c$  parameter, and anisotropy, could be easily controlled. For the isotropic deposits formed in the low-temperature region (below about 1400°C), there is a correlation of  $L_c$  and density: at a given temperature both increase with increasing propane concentration. This is in spite of a concomitant rise in deposition rate.

The hardness of the pure isotropic carbons increases with density and decreases with increasing  $L_c$  parameter (other structural parameters being constant). The data indicate that the hardest deposits are those that are isotropic with high density and small  $L_c$  parameters, but the correlation between  $L_c$  and density makes the formation of this combination attainable only under special conditions. These conditions are being sought.

Addition of silicon by co-deposition in the presence of chlorine enhances the hardness of the carbon-silicon deposits and modifies the deposition process considerably. Co-deposition with boron in the presence of chlorine, on the other hand, causes the deposits to have large  $L_c$  parameters and to be

relatively soft. There is much more to be learned about the deposition, structure, and properties of the carbon-silicon and carbon-boron systems.

The properties of some of the initial series of structures have been measured. The modulus of rupture of the pure carbons increases with increasing density and is believed to be weakened by the flaws associated with soot included in the structure. In spite of the presence of these flaws, the isotropic pyrolytic carbons are all substantially stronger than the vitreous or glassy carbons. A major objective will be to develop an understanding of the origin of these flaws so that they may be eliminated.

Using a test developed for comparative evaluation of wear couples, the wear behavior of a complete series of pure and silicon-alloyed isotropic carbons has been evaluated. In the geometry of this test, volume removed is linear with time; i.e., a constant wear rate is obtained. The wear resistance of pure carbons is very good and correlates with density and hardness. The wear resistance of silicon-alloyed carbons appears to be greater than that of pure carbons and increases with increasing hardness.

One of the most interesting findings, and one that may prove to be of some technological significance, has come from the first series of fatigue tests. Using a cantilevered beam loading arrangement, it has been found that for those unalloyed isotropic carbons tested, the endurance limit is virtually identical to the single-cycle fracture stress.

Measurements are showing a systematic variation of certain physical properties with structure. Thermal expansion measurements made parallel to the deposition plane on a series of isotropic pyrolytic carbons deposited from propane between 1200° and 1400°C show that the thermal expansivity increases with increasing carbon density from  $4 \times 10^{-6} \text{ }^{\circ}\text{C}^{-1}$  for a density around  $1.4 \text{ g/cm}^3$  to  $6 \times 10^{-6} \text{ }^{\circ}\text{C}^{-1}$  for a density of  $2.0 \text{ g/cm}^3$ . Combining these values with recently reported values for the c-axis thermal expansivity of low-temperature pyrolytic carbon crystallites yields values for the "accommodation coefficient" (fraction of crystallite expansion which is

transmitted to the bulk) ranging from 0.68 for a carbon with a density of  $1.46 \text{ g/cm}^3$  to 0.97 for a carbon with a density of  $1.97 \text{ g/cm}^3$ .

The thermal conductivity perpendicular to the deposition plane was measured on a series of isotropic pyrolytic carbons using the heat-pulse method at temperatures between room temperature and  $800^\circ\text{C}$ . The results show that the room temperature thermal conductivity increases with increasing carbon density, from  $0.012 \text{ cal/cm-}^\circ\text{C-sec}$  for a density of  $1.5 \text{ g/cm}^3$  to  $0.018 \text{ cal/cm-}^\circ\text{C-sec}$  for a density of  $2.0 \text{ g/cm}^3$ . The conductivity of all the carbons decreases with increasing measurement temperature.

Using the initial findings as a guide in future work, efforts will be made to modify and improve the structures of the carbons formed in steady-state beds so that properties may be controlled or optimized.



## CONTENTS

|   |     |
|---|-----|
| SUMMARY . . . . .   | iii |
| 1. INTRODUCTION . . . . .   | 1   |
| 1.1. Background . . . . .   | 1   |
| 1.2. Deposition in Conventional Fluidized Beds . . . . .              | 2   |
| 1.3. Deposition in Steady-State Fluidized Beds . . . . .              | 2   |
| 1.4. Characterization of Pyrolytic Carbon Structures . . . . .        | 4   |
| 2. PROGRAM OBJECTIVES . . . . .                                       | 6   |
| 3. DEPOSITION AND STRUCTURE . . . . .                                 | 7   |
| 3.1. Deposition Equipment . . . . .                                   | 7   |
| 3.2. Materials . . . . .  | 10  |
| 3.3. Deposit Characterization . . . . .                               | 15  |
| 3.4. Deposition Characterization . . . . .                            | 17  |
| 3.5. Results from the Deposition Studies . . . . .                    | 20  |
| 3.5.1. Results for Depositions of Pure Carbons from Propane . . . . . | 23  |
| 3.5.2. Results for Co-Deposited Carbon-Silicon Alloys . . . . .       | 41  |
| 3.5.3. Results for Co-Deposited Boron-Carbon Alloys . . . . .         | 51  |
| 4. MECHANICAL PROPERTIES . . . . .                                    | 55  |
| 4.1. Young's Modulus and Modulus of Rupture . . . . .                 | 55  |
| 4.1.1. Experimental . . . . .   | 55  |
| 4.1.2. Results . . . . .  | 57  |
| 4.2. Fatigue . . . . .  | 62  |
| 4.2.1. Methods . . . . .  | 62  |
| 4.2.2. Results and Discussion . . . . .                               | 65  |
| 4.3. Wear . . . . .   | 68  |
| 4.3.1. Methods . . . . .  | 68  |
| 4.3.2. Results . . . . .  | 70  |
| 5. PHYSICAL PROPERTIES . . . . .                                      | 78  |
| 5.1. Thermal Expansivity . . . . .                                    | 78  |
| 5.2. Thermal Conductivity . . . . .                                   | 83  |

|  |     |
|--|-----|
| REFERENCES . . . . .   | 88  |
| APPENDIX A. WORK STATEMENT . . . . .                                 | A-1 |
| APPENDIX B. PHOTOMICROGRAPHS AND PARTICLE SIZE DISTRIBUTION DATA . . | B-1 |
| APPENDIX C. MECHANICAL PROPERTY DATA . . . . .                       | C-1 |
| APPENDIX D. PHYSICAL PROPERTY DATA . . . . .                         | D-1 |

## FIGURES

|  |    |
|--|----|
| 1. Formation of isotropic pyrolytic carbons through deposition of droplets . . . . .   | 3  |
| 2. Schematic diagram of carbon deposition in a steady-state fluidized bed . . . . .  | 8  |
| 3. Curves relating bed temperature to control temperature for four propane concentrations over the temperature range used in the present study . . . . .   | 9  |
| 4. Plot relating density of coated, 425- $\mu\text{m}$ $\text{ZrO}_2$ particles to their diameter for various coating densities . . . . .  | 11 |
| 5. Plot of specific surface area as a function of sphere diameter for various particle densities . . . . .   | 12 |
| 6. Photomicrograph of $\text{ZrO}_2$ particles used as fluidized bed. Particle density is 98% (of theoretical) . . . . .   | 13 |
| 7. Imprints of a diamond indenter recorded in a thin polymeric film on the surface of an LTI carbon . . . . .  | 16 |
| 8. Plots of coating rate ( $\mu\text{m}/\text{min}$ ) and bed surface area versus time for $D_0 = 200$ and $530 \mu\text{m}$ . . . . .   | 19 |
| 9. Plot of particle size distributions in tube and trap for run 5804-23 . . . . .  | 21 |
| 10. Plot of particle size distributions in tube and trap for run 5408-19 . . . . .   | 22 |
| 11. Plot of coating density as a function of deposition temperature for coatings deposited from propane at 7%, 25%, and 60% concentrations . . . . .   | 26 |
| 12. Apparent crystallite height, $L_c$ , as a function of deposition temperature for carbons deposited from various concentrations of propane . . . . .  | 27 |
| 13. Scanning electron micrographs of carbon surfaces deposited from propane at various temperatures; bed temperature ( $^{\circ}\text{C}$ ), propane concentration (%), and run number are given for each sample . . . . . | 30 |
| 14. Apparent droplet size versus deposition temperature for carbon deposited from various propane concentrations . . . . .   | 31 |

|     |  |    |
|-----|--|----|
| 15. | Apparent droplet size versus coating rate for carbons deposited from propane . . . . .   | 32 |
| 16. | Microhardness as a function of deposition temperature for carbons deposited from propane . . . . .   | 33 |
| 17. | Microhardness as a function of $L_C$ parameter for carbons deposited from propane . . . . .  | 34 |
| 18. | Microhardness versus coating density for carbons deposited from propane . . . . .  | 35 |
| 19. | Correlation of $L_C$ and density for carbons with nearly the same microhardness value . . . . .  | 36 |
| 20. | Coating rate versus deposition temperature for carbons deposited from propane . . . . .  | 38 |
| 21. | Density versus deposition rate for carbons deposited from 7%, 25%, and 60% propane at temperatures in the range 1150° to 1400°C . . . . .  | 39 |
| 22. | $L_C$ parameter versus deposition rate for carbons deposited from 7%, 25%, and 60% propane at temperatures in the range 1200° to 1400°C . . . . .  | 40 |
| 23. | Microhardness versus deposition rate for carbons deposited from 7%, 25%, and 60% propane at temperatures in the range 1200° to 1400°C . . . . .  | 42 |
| 24. | Deposition rates for depositions from propane with a $\text{CH}_3\text{SiCl}_3$ additive for temperatures in the range 1250° to 1400°C and propane concentrations in helium in the range 7% to 60% . . . . .   | 45 |
| 25. | Scanning electron micrograph of as-deposited surfaces of co-deposited silicon-carbon materials . . . . .   | 47 |
| 26. | Apparent droplet size versus weight percent silicon in coating for carbon-silicon materials co-deposited at 1200° to 1400°C from 7%, 25%, and 60% propane in helium with a $\text{CH}_3\text{SiCl}_3$ additive . . . . .   | 48 |
| 27. | Plots of matrix density (a), apparent droplet size (b), and silicon concentration (c) versus deposition temperature for materials co-deposited in the range 1200° to 1400°C from 7%, 25%, and 60% propane in helium with a $\text{CH}_3\text{SiCl}_3$ additive . . . . | 49 |
| 28. | Carbon matrix density versus silicon concentration for carbon-silicon materials deposited at temperatures in the range 1200° to 1400°C from 7%, 25%, and 60% propane with $\text{CH}_3\text{SiCl}_3$ additive . . . . .  | 50 |
| 29. | Microhardness versus silicon concentration for carbons co-deposited with silicon in the range 1200° to 1400°C from propane in helium with added $\text{CH}_3\text{SiCl}_3$ . . . . .   | 52 |

|     |  |    |
|-----|--|----|
| 30. | Four-point bending fixture constructed to test carbon specimens . . . . .  | 56 |
| 31. | Young's modulus of pure carbons as a function of carbon density . . . . .  | 58 |
| 32. | Modulus of rupture of pure carbons as a function of carbon density . . . . .   | 59 |
| 33. | Scanning electron micrographs typical of fracture surfaces of carbons studied . . . . .  | 63 |
| 34. | Fatigue tester with specimen indicating stressed configuration: (a) overall view, (b) close-up of specimen . . . . .   | 64 |
| 35. | Calculated stress-deflection curves for cantilever beam bending of run 5408-5 . . . . .  | 66 |
| 36. | Fatigue behavior of pure LTI carbon (5408-5) in cantilever beam bending . . . . .  | 67 |
| 37. | Close-up view of one cell of wear testing machine . . . . .  | 69 |
| 38. | Typical set of wear marks (specimen 5408-17). . . . .  | 71 |
| 39. | Volume of wear measured on flat as a function of sliding distance for pure LTI carbon discs bearing on pure LTI carbon flats. . . . .  | 72 |
| 40. | Volume of wear measured on flat as a function of sliding distance for silicon-alloyed LTI carbon flats bearing on pure LTI carbon discs . . . . .  | 73 |
| 41. | Volume wear rate as measured from wear on flat versus density of pure LTI carbon disc for various flat materials. . . . .  | 74 |
| 42. | Effect of bearing load on volume wear rate as measured from wear on flat for pure LTI carbon wear couple (flat 5408-7, disc 5408-7). . . . .   | 76 |
| 43. | Typical thermal expansion curve for isotropic pyrolytic carbon (5408-27) measured parallel to deposition plane . . . . .   | 81 |
| 44. | Mean thermal expansivity (22° to 1000°C) parallel to the deposition plane of isotropic pyrolytic carbons deposited from propane at 1200° to 1400°C as a function of carbon density . . . . . | 82 |
| 45. | Typical curve of thermal conductivity versus temperature for isotropic pyrolytic carbon (5408-31) measured perpendicular to deposition plane . . . . .                                       | 86 |
| 46. | Thermal conductivity at 100°C of isotropic pyrolytic carbons as a function of carbon density . . . . .   | 87 |

#### TABLES

|    |   |    |
|----|---|----|
| 1. | Gases and additives used to deposit coatings in steady-state beds . . . . . | 14 |
|----|---|----|

|     |   |    |
|-----|---|----|
| 2.  | Coating conditions and coating results for unalloyed LTI carbons deposited in steady-state fluidized beds from propane . . . . .                            | 24 |
| 3.  | Coating structural data for unalloyed LTI carbons deposited in steady-state fluidized beds from propane . . . . .   | 25 |
| 4.  | Data comparing pore structures of two carbons with sink-float densities near 1.5 g/cm <sup>3</sup> . . . . .  | 28 |
| 5.  | Deposition conditions for co-deposited carbon-silicon alloys deposited in steady-state beds using propane and methyltrichlorosilane . . . . .               | 43 |
| 6.  | Structural data for co-deposited carbon-silicon deposits formed in steady-state fluidized beds using propane and methyltrichlorosilane . . . . .            | 44 |
| 7.  | Deposition conditions for co-deposited boron-carbon alloys deposited in steady-state fluidized beds using propane, methane, and boron trichloride . . . . . | 53 |
| 8.  | Structural data for co-deposited boron-carbon alloys deposited in steady-state fluidized beds using propane, methane, and methyltrichlorosilane . . . . .   | 54 |
| 9.  | Deposition conditions and structure and mechanical properties of carbons deposited with chlorine and hydrogen additives to the atmosphere . . . . .         | 61 |
| 10. | Deposition conditions, structural parameters, and thermal expansivity of pyrolytic carbons . . . . .  | 79 |
| 11. | Deposition conditions, structural parameters, and thermal conductivity of pyrolytic carbons . . . . .   | 85 |

## 1. INTRODUCTION

### 1.1. BACKGROUND

In 1958 the first carbon coatings were deposited in fluidized beds. These coatings were deposited on small uranium-thorium carbide nuclear fuel particles to retain fission products generated during operation in power reactors. For the following five years, efforts were directed primarily toward equipment development; little attention was devoted either to the degree of the structure-sensitivity of the properties of pyrolytic carbon or to the magnitude of the variations in structure that were possible.<sup>(1-10)</sup>

In the early 1960s problems due to variations in structure of carbon coating arose, and in 1963 a concentrated effort was initiated to characterize and control the structure (and hence the properties) of the carbons deposited in fluidized beds.<sup>(11-15)</sup> Shortly thereafter, evidence that completely isotropic, dense carbons could be deposited pyrolytically was reported,<sup>(11)</sup> and the dependence of the mechanical properties on structure was demonstrated.<sup>(12)</sup>

In the late 1960s and early 1970s, great strides were made in the understanding of the carbons deposited in fluidized beds, and many of the relationships between the structure and properties of these materials were established.<sup>(16-31)</sup> The dependences of irradiation-induced dimensional changes on structure are particularly dramatic, and the interested reader may refer to Refs. 31 and 32 for summaries of work performed in this area. The very recent applications of certain structures in bioengineering reported in Ref. 33 provide a further illustration of the technological potential of carbons deposited pyrolytically in fluidized beds.

A major advantage of deposition in fluidized beds is the ability to deposit primarily by the "droplet mechanism"<sup>(15,31)</sup> (see Fig. 1), which can yield strong, isotropic structures when deposition is carried out below about 1500°C. Investigations of the properties of this family of carbons are still relatively new, but preliminary studies indicate that they are likely to have important applications in many fields.<sup>(26,27,30)</sup>

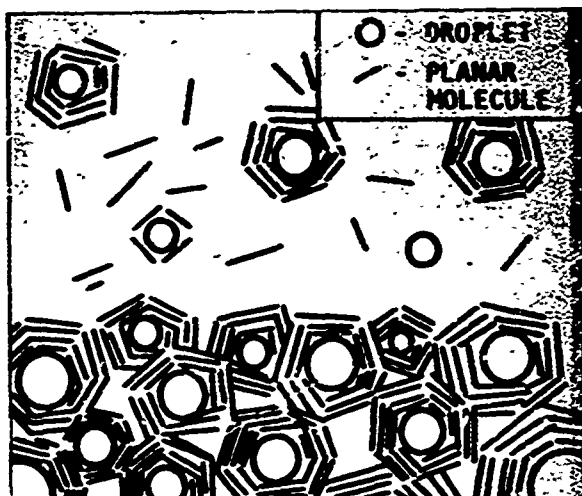
### 1.2. DEPOSITION IN CONVENTIONAL FLUIDIZED BEDS

In the conventional fluidized-bed process, particles with diameters in the range 100 to 1000  $\mu\text{m}$  are fluidized in a vertical tube furnace equipped so that the gas composition, gas flow rate, and temperature can be controlled.<sup>(31)</sup> In practice, a batch of particles is introduced into the furnace, and by controlling the pyrolysis conditions, any one of a variety of carbons can be deposited on the particles. Unfortunately, the structure of the carbon deposited also depends on the bed surface area, which means that when thick carbon coatings are deposited, the bed surface area increases during the course of the deposition, causing the structure of the carbon deposited to change. Variations in the density and microstructure of the deposited carbon with time during conventional deposition runs have been observed and are reported in Ref. 14.

There is a further difficulty when the bed is used as a carrier for larger parts which are to be coated with carbon. In this case, the thickness of the carbon deposited on the part is limited by the volume capacity of the furnace. When the furnace is filled with coated particles, the deposition run must be terminated, thus limiting the ability to deposit thick coatings.

### 1.3. DEPOSITION IN STEADY-STATE FLUIDIZED BEDS

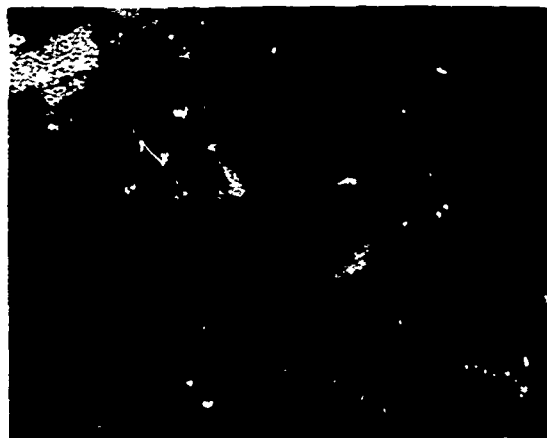
In order to overcome the limitations imposed by the increase in bed volume with time in a conventional apparatus, a process which employs a means for removing particles during coating has been developed, thus



(a) Schematic illustration of formation of isotropic pyrolytic carbon



(b) Scanning electron micrograph of as-deposited surface of isotropic pyrolytic carbon



(c) Transmission electron micrograph of isotropic pyrolytic carbon

K89007

Fig. 1. Formation of isotropic pyrolytic carbons through deposition of droplets



providing the ability to control the volume of the bed. To attain control of the bed surface area, additional means are used to allow the continuous addition of new particles. In principle, it is therefore possible to establish a "steady-state" condition in which particles are withdrawn at a rate which compensates for the addition of both the new particles and the carbon deposited on the bed particles.

In practice, for a given set of conditions, the establishment of truly steady-state conditions would require several iterations, because the efficiency of carbon deposition depends on the conditions of gas flow rate, gas composition, and temperature, as well as the bed area. For the first phase of the present work, it has not been practical to strive for truly steady-state conditions. Accordingly, in the balance of this report the term "steady-state" will be used loosely and will imply only that the bed volume is being controlled during deposition.

#### 1.4. CHARACTERIZATION OF PYROLYTIC CARBON STRUCTURES

The unique characterization of carbon structures has been a continuing problem. Experience has shown that for most purposes, specifying the microstructural type, i.e., laminar, granular, columnar, or featureless,<sup>(31)</sup> together with the degree of preferred orientation,<sup>(20,35)</sup> some measure of the crystalline perfection such as the  $L_c$  parameter,<sup>(31)</sup> and the density is adequate for unique characterization. However, there are some exceptions. The above four parameters have been found to be inadequate to explain the difference between the mechanical properties of isotropic carbons deposited below about 1500°C (low-temperature isotropic, LTI, carbons) and vitreous (or glassy) carbons. Although the two materials both are isotropic and have the same density,  $L_c$  value, and metallographic microstructure, the LTI carbons are significantly stronger than vitreous carbons.<sup>(30)</sup> One difference in structure between the two classes of materials has been revealed by comparing fracture surfaces. Vitreous carbons exhibit a smooth, conchoidal fracture, whereas LTI carbons exhibit tortuous fracture surfaces with morphological features that appear to be generically related to formation by the droplet

mechanism.<sup>(30)</sup> Accordingly, the apparent droplet size as determined using scanning electron microscopy of as-deposited or fracture surfaces may prove to be useful for further characterizing LTI carbons.

## 2. PROGRAM OBJECTIVES

The objective of this program is to investigate the basic deposition process in steady-state fluidized beds in order to obtain a better understanding of how specific carbon structures are formed. The deposition process is being manipulated with additions reported to act as catalysts,<sup>(36)</sup> and the number of structures attainable is being increased through the addition of alloying elements, many of which have been co-deposited with carbon in related processes.<sup>(31,33,37-39)</sup> The structures of the deposited carbon are being related to the deposition conditions, and variations in properties are being interpreted in terms of structure.\*

---

\*The complete Work Statement is given in Appendix A.

### 3. DEPOSITION AND STRUCTURE

(R. J. Akins)

#### 3.1. DEPOSITION EQUIPMENT

The fluidized-bed coating equipment is similar to that used to deposit titanium-alloyed carbon<sup>(38)</sup> except for modifications needed to establish steady-state coating conditions. A schematic of this equipment is shown in Fig. 2. The coater consists of a vertical graphite tube that is fitted with inlet and exhaust lines so that a metered supply of gases containing a hydrocarbon can be passed through a bed of particles, causing fluidization. The hydrocarbon is pyrolyzed in the heated bed of particles, leading to the deposition of carbon on the particles or any other object suspended within the bed. The reaction products are exhausted through a scrubber.

The coater assembly is heated by a 10-kHz induction heating system. The coating temperature is controlled by sighting with an optical pyrometer onto the graphite coater tube and feeding the pyrometer signal into a closed-loop feedback control system which varies the field current in the induction generator, thus modulating the power that is dissipated in the induction heating coil. By proper adjustment of the control system, it is possible to regulate the control temperature to  $\pm 10^{\circ}\text{C}$ . A reference pyrometer, of the disappearing filament type, is used to check the control temperature prior to coating.

The control temperature is generally somewhat higher than the actual temperature in the fluidized bed during coating owing to the additional heat requirements imposed by the endothermic nature of the hydrocarbon gases and if incorrect can lead to misleading results. It is therefore necessary to measure the actual bed temperature during coating by immersing a thermocouple in the bed. Since the presence of a thermocouple in the fluidized bed could result in unknown perturbations during the coating run, separate calibration runs are made using the same coating conditions. With this procedure, calibration curves such as that shown in Fig. 3 can be determined.

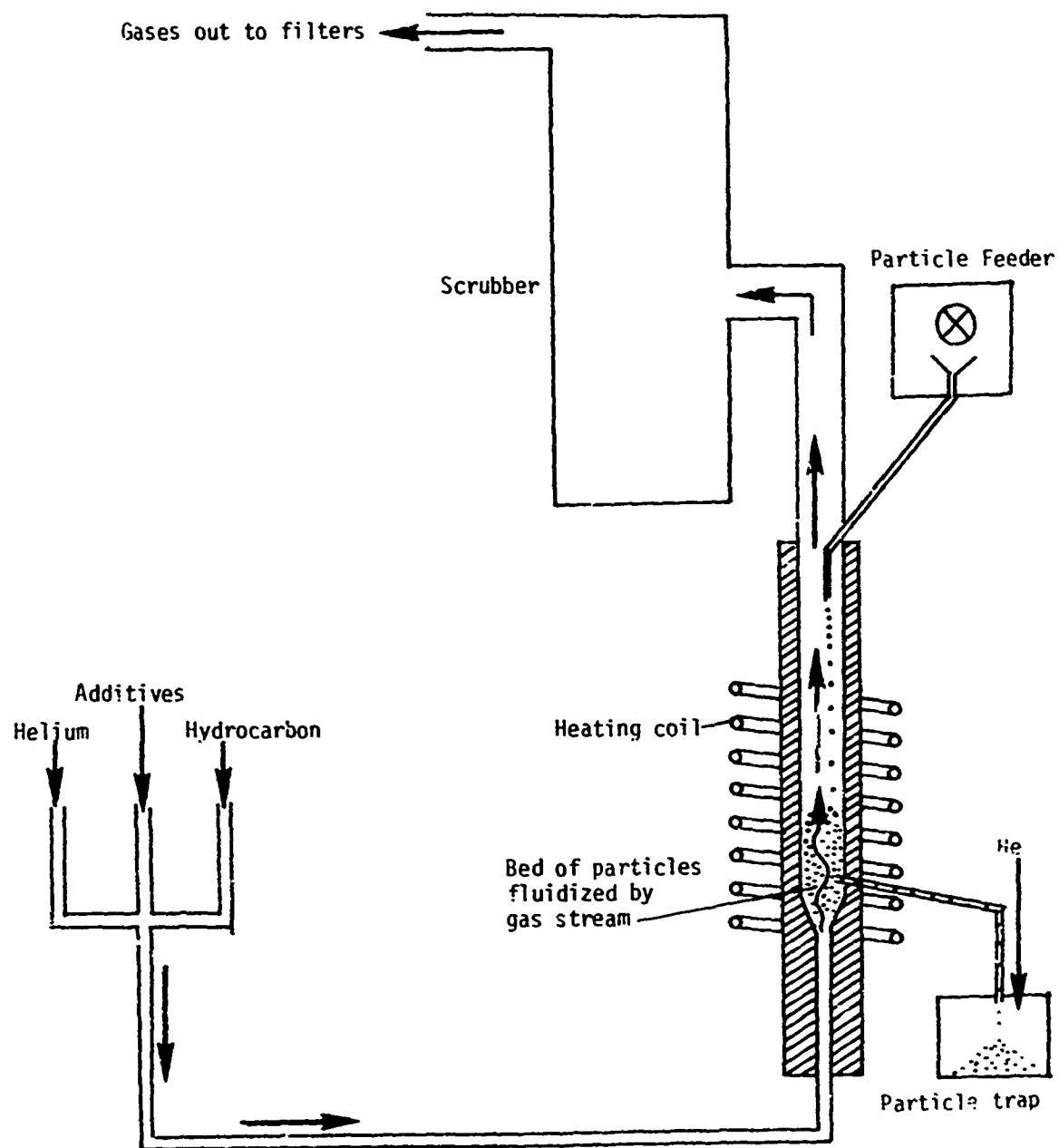


Fig. 2. Schematic diagram of carbon deposition in a steady-state fluidized bed

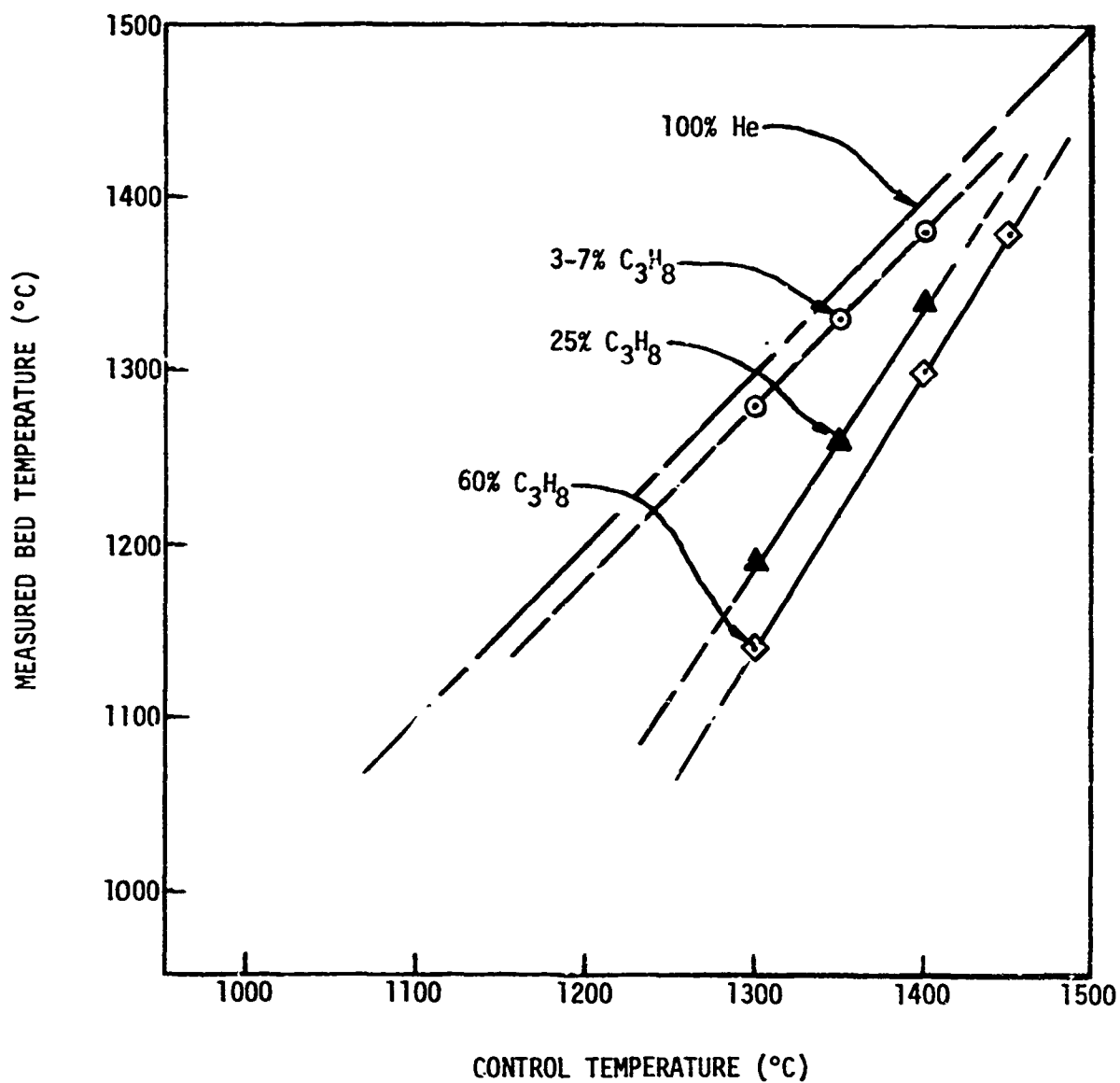


Fig. 3. Curves relating bed temperature to control temperature for four propane concentrations over the temperature range used in the present study

Various additives used either in the co-deposition of other elements with carbon or as a catalyst can be injected into the coater inlet directly if they are gaseous or introduced by passing a portion of the fluidization gas stream through a bubble-contactor if they are liquid. After a given experiment, the additive container (bubbler or gas cylinder) can be reweighed to determine the amount of additive used.

The particle feeding system consists of a constant-volume powder dispenser enclosed in a purged box. Particles are fed at a preset rate into a delivery tube which leads to the unneated space directly above the fluidized bed. The particles are withdrawn from the bed through an overflow tube adjusted to keep a predetermined bed height. During steady-state operation of the bed, a steady stream of particles flows into and out of the fluidized bed. Using these techniques, it is possible to vary either the feed or the withdrawal rates. After each deposition run the particles in the withdrawal trap and those remaining in the coater tube are weighed and a sieve analysis is made of each type. From these data and the density of the carbon deposited, the surface area in the bed at the end of the run may be estimated using the relationships plotted in Figs. 4 and 5.

### 3.2. MATERIALS

The fluidized bed consists of nearly spherical  $ZrO_2$  particles such as those shown in Fig. 6. The use of spherical particles results in smooth fluidization and provides for a calculable surface area.

The gases that are currently being used in the depositions are listed in Table 1.

The carbons are deposited on Poco-type AXZ graphite discs measuring 0.716 in. in diameter by 0.040 in. thick. Prior to coating, the discs are hand polished on No. 600 grit paper to remove machine marks, which simplifies stripping of the deposit from the substrate after coating. The pyrolytic carbon discs, stripped from the substrates, are used for structural characterizations and property measurements.

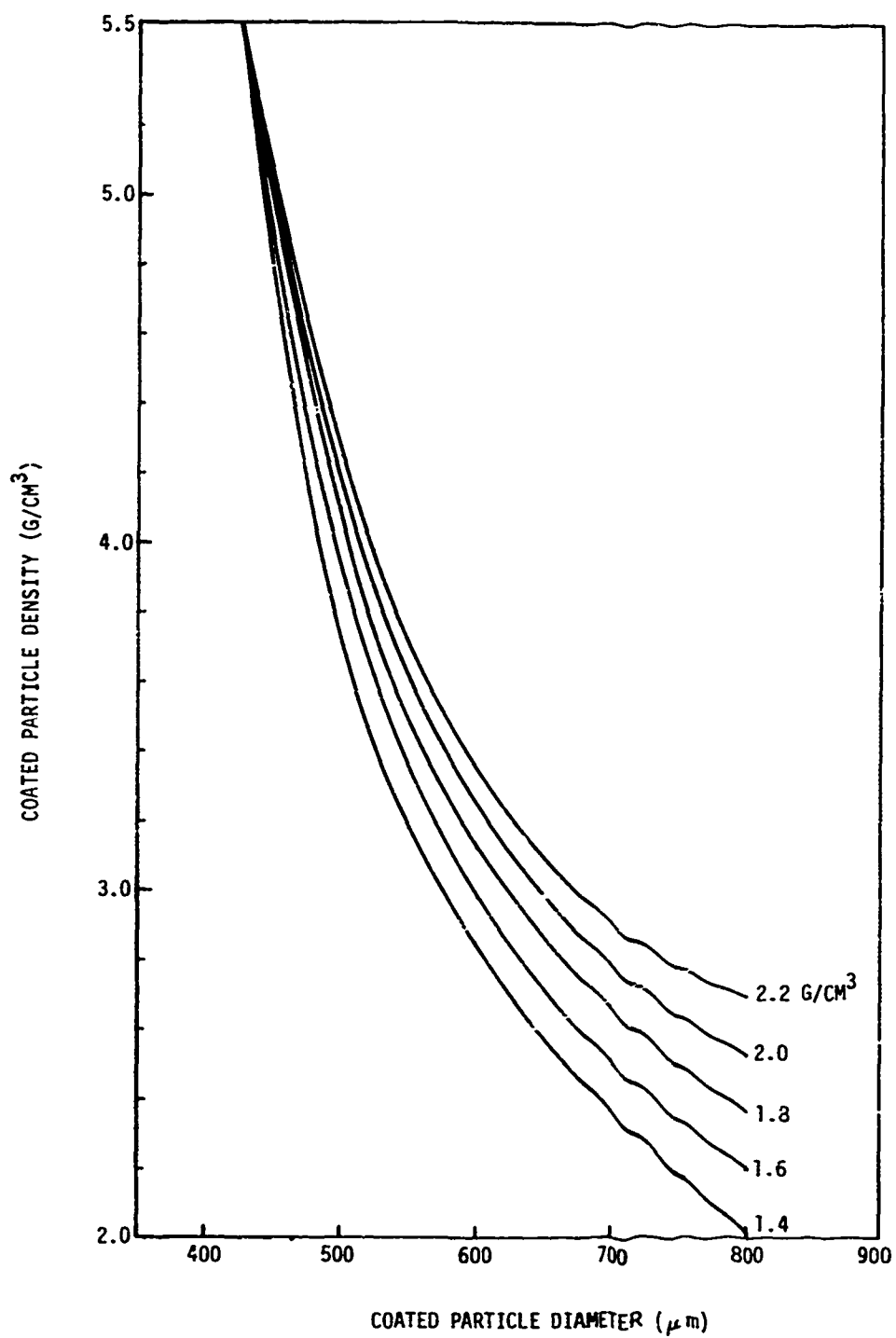


Fig. 4. Plot relating density of coated, 425-μm ZrO<sub>2</sub> particles to their diameter for various coating densities



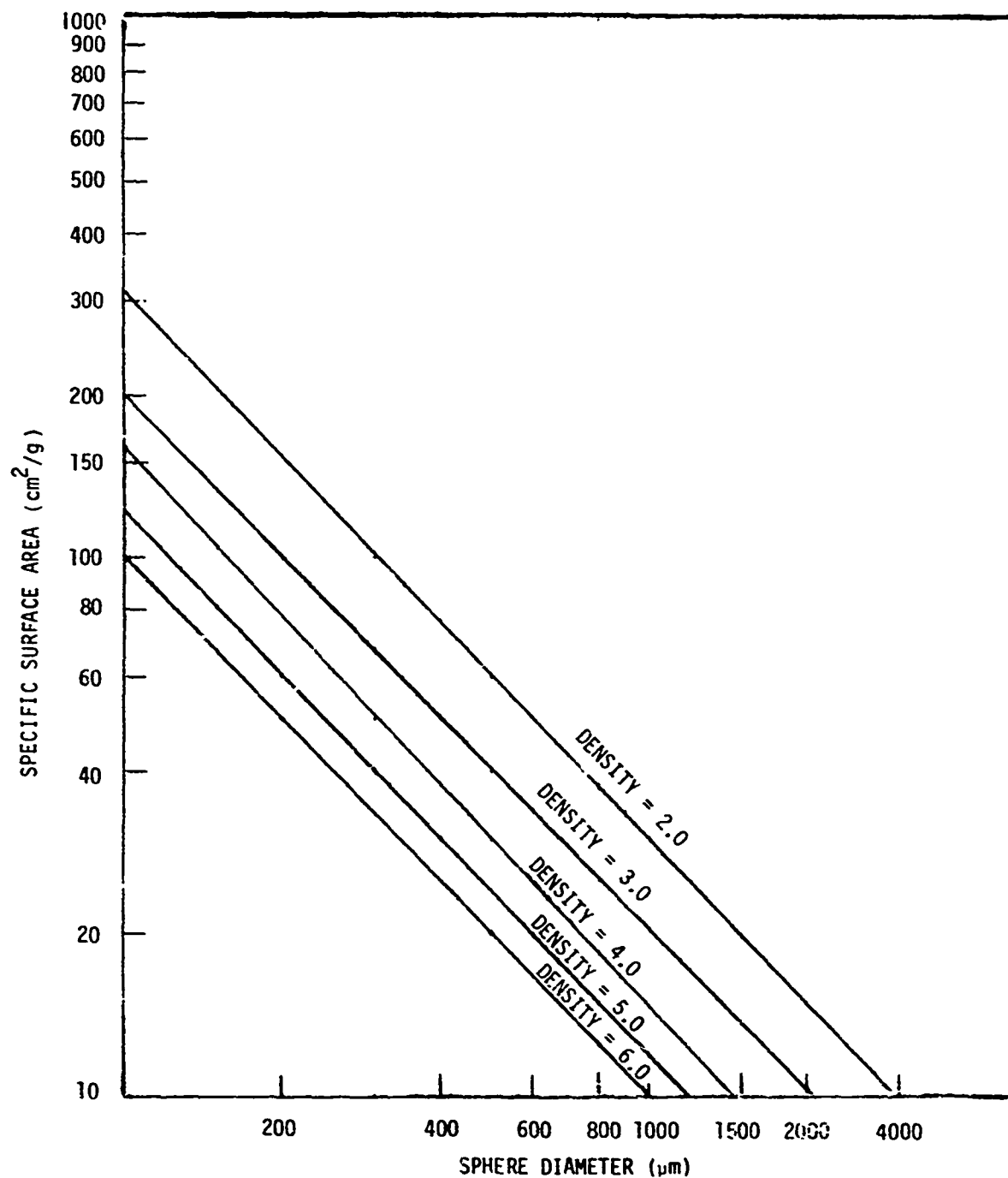
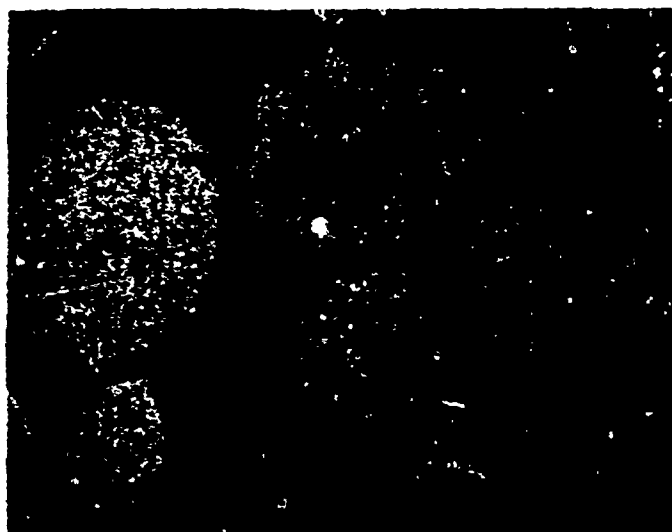


Fig. 5. Plot of specific surface area as a function of sphere diameter for various particle densities



Random sample

50X

Fig. 6. Photomicrograph of  $ZrO_2$  particles used as fluidized bed. Particle density is 98% (of theoretical). Broad-cut sieve analysis yields the following: 100% < 495  $\mu m$ , 95% > 350  $\mu m$ , 5% < 350  $\mu m$ , 100% > 210  $\mu m$ . Surface area  $\approx 30$   $cm^2/g$ . Bulk density = 3.3  $g/cm^3$ .

TABLE 1  
GASES AND ADDITIVES USED TO DEPOSIT COATINGS IN STEADY-STATE BEDS

| Gas                                    | Purity or Grade | Supplier                   |
|--|-----------------|----------------------------|
| Propane ( $C_3H_8$ )                   | C.P. grade      | Phillips Petroleum         |
| Methane ( $CH_4$ )                     | C.P. grade      | Matheson Scientific Co.    |
| Boron trichloride ( $BCl_3$ )          | Reagent grade   | Kerr-McGee Corp.           |
| Titanium tetrachloride ( $TiCl_4$ )    | 99.5%           | Matheson, Coleman and Bell |
| Methyltrichlorosilane ( $CH_3SiCl_3$ ) | 97%             | General Electric           |
| Hydrogen                               | Lab. grade      | Liquid Carbonic            |
| Chlorine ( $Cl_2$ )                    | Research grade  | Matheson Scientific Co.    |

### 3.3. DEPOSIT CHARACTERIZATION

The deposits are characterized by measuring their density, microstructure, microhardness, apparent crystallite size ( $L_c$ ), and apparent droplet size and performing chemical analysis (if applicable). Metallographic evaluation consists of mounting a disc sectioned along a diameter in resin, polishing through 1/2- $\mu$ m diamond, and viewing metallographically using bright field and polarized light. Experience has shown that deposits with Bacon anisotropy factors<sup>(35)</sup> of less than 1.1 are dark and unresponsive optically when viewed in this manner under polarized light at approximately 100X. The porosity of the coatings is visible under bright field illumination.

The density of the deposits is measured by suspending the pyrolytic carbon discs in a density gradient column. By using a 48-hr stabilization period, the density values can be determined accurately to four significant figures.

The samples used for density determinations are also used for X-ray diffraction and chemical analysis. The apparent crystallite sizes ( $L_c$ ) are determined from the broadening of the carbon (002) diffraction peaks, correcting only for instrument broadening.<sup>(40,41)</sup> Chemical analysis for co-deposited elements other than boron is performed using X-ray fluorescence techniques. Boron concentrations are determined using wet-chemical methods.

Diamond pyramid hardness (DPH) measurements are made by coating the metallographic sample with a thin collodion film in order to obtain a permanent record of the indentation depth.<sup>(42)</sup> The stylus load is 50 g. A photomicrograph of typical stylus imprints is shown in Fig. 7.

The apparent droplet size is determined from scanning electron micrographs of as-deposited and fractured surfaces.



K90745

Fig. 7. Imprints of a diamond indenter recorded in a thin polymeric film on the surface of an LTI carbon

### 3.4. DEPOSITION CHARACTERIZATION

A true steady-state fluidized bed can be defined as a fluidized bed in which the mean surface area of the particulate bed is maintained at some relatively constant value. In the commonly used fluidized bed, the bed surface area progressively increases so that the average coating rate in the fluidized bed decreases rapidly as the particles in the bed grow in size. The magnitude of this effect can be demonstrated as follows.

The volume of a single particle at time  $t$  is

$$V_t = V_o + Ct,$$

$$V_o = \frac{\pi}{6} D_o^3 \text{ and } V_t = \frac{\pi}{6} D_t^3,$$

where  $V_t$  and  $D_t$  = volume and diameter at time =  $t$ ,

$V_o$  and  $D_o$  = initial volume and diameter,

$t$  = time,

$C$  = volume of carbon deposited per minute.

Substituting yields

$$\frac{\pi}{6} D_t^3 = \frac{\pi}{6} D_o^3 + Ct,$$

$$D_t = \left( D_o^3 + \frac{6Ct}{\pi} \right)^{1/3}$$

Differentiating yields the coating rate:

$$\frac{dD_t}{dt} = \frac{2C}{\pi} \left( D_o^3 + \frac{6Ct}{\pi} \right)^{-2/3} \quad (1)$$

From this the surface area is determined as

$$A = \pi D^2,$$

$$A_t = \pi D_t^2,$$

$$= \pi \left( D_o^3 + \frac{6Ct}{\pi} \right)^{2/3} . \quad (2)$$

Plots of Eqs. (1) and (2) for  $D_o$  of 200 and 530  $\mu\text{m}$  and  $C = 2.03 \text{ cm}^3/\text{min}$  are shown in Fig. 8. The deposition rate in microns per minute drops 50% in the first 15 min of a deposition run and 75% in an hour. Under these conditions, the maximum coating thickness is limited, for practical reasons, to about 330  $\mu\text{m}$  (0.013 in.). Since Bard, *et al.*,<sup>(43)</sup> have shown that the structure is often related to deposition rate, it is likely that the structure varies across the thickness of a carbon deposited in a conventional fluidized bed. Deposition in a steady-state fluidized bed, as mentioned previously, avoids these problems, greatly extending the thickness range and providing for more homogeneous structures.

Providing the particle size distribution is maintained constant during the deposition, steady-state coating conditions are established when the particle withdrawal rate is equal to the particle feed rate plus the deposition rate:

$$W_{\text{out}} = W_{\text{in}} + W_c ,$$

where  $W_{\text{out}}$  = particle withdrawal rate (g/min),

$W_{\text{in}}$  = feed rate (g/min),

and

$$W_c = E \cdot \frac{V}{22.4} \cdot f \cdot \frac{273^\circ\text{K}}{293^\circ\text{K}} ,$$

where  $E$  = overall efficiency,

$V$  = volumetric flow of hydrocarbon ( $\ell/\text{min}$ ),

$f$  = weight fraction of carbon per mole of hydrocarbon.

The efficiency value can vary depending on the temperature and the gas composition, but is generally in the range of 40% to 60% for most conditions encountered.

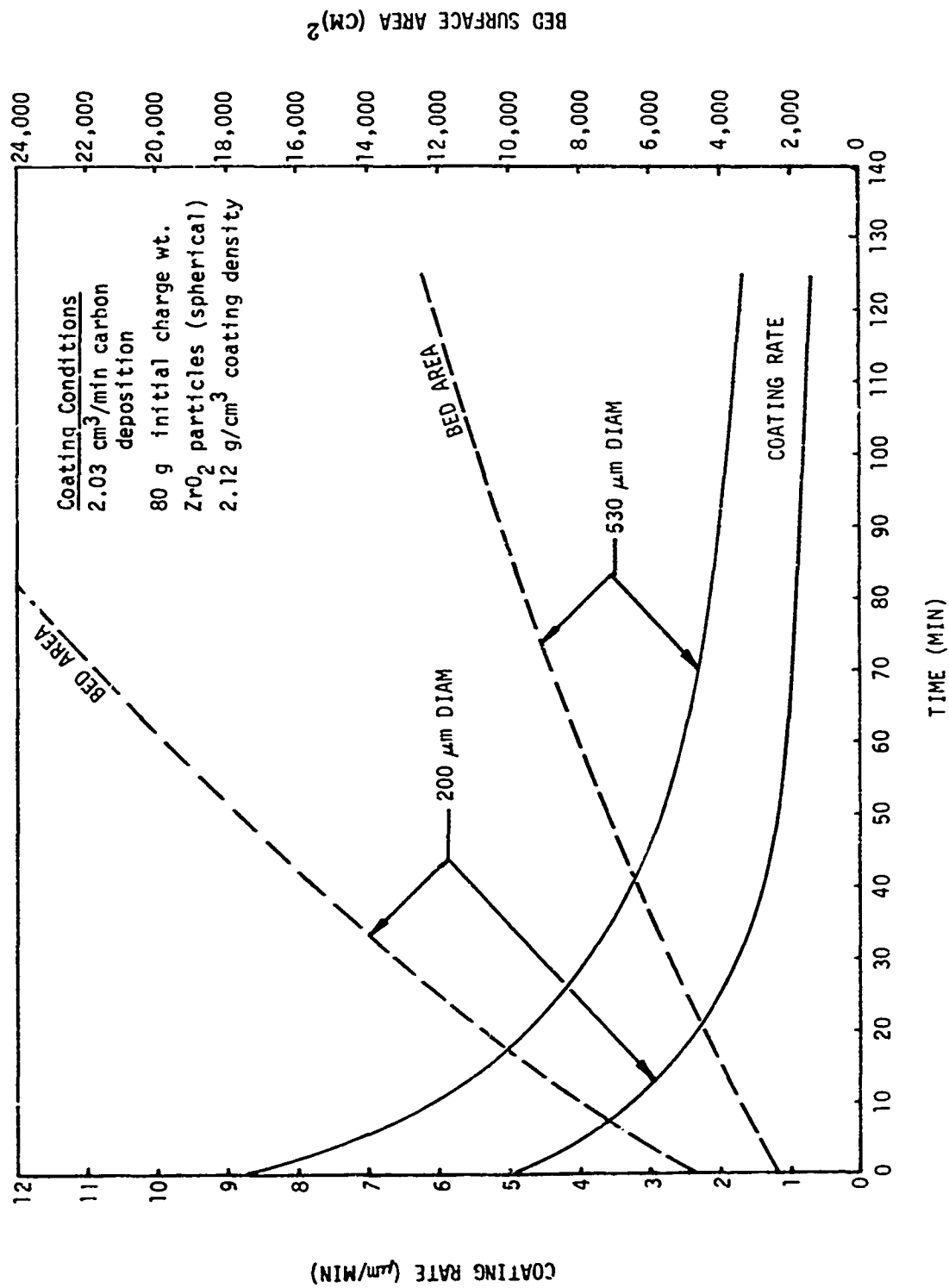


Fig. 8. Plots of coating rate ( $\mu\text{m}/\text{min}$ ) and bed surface area versus time for  $D_o = 200$  and  $530 \mu\text{m}$



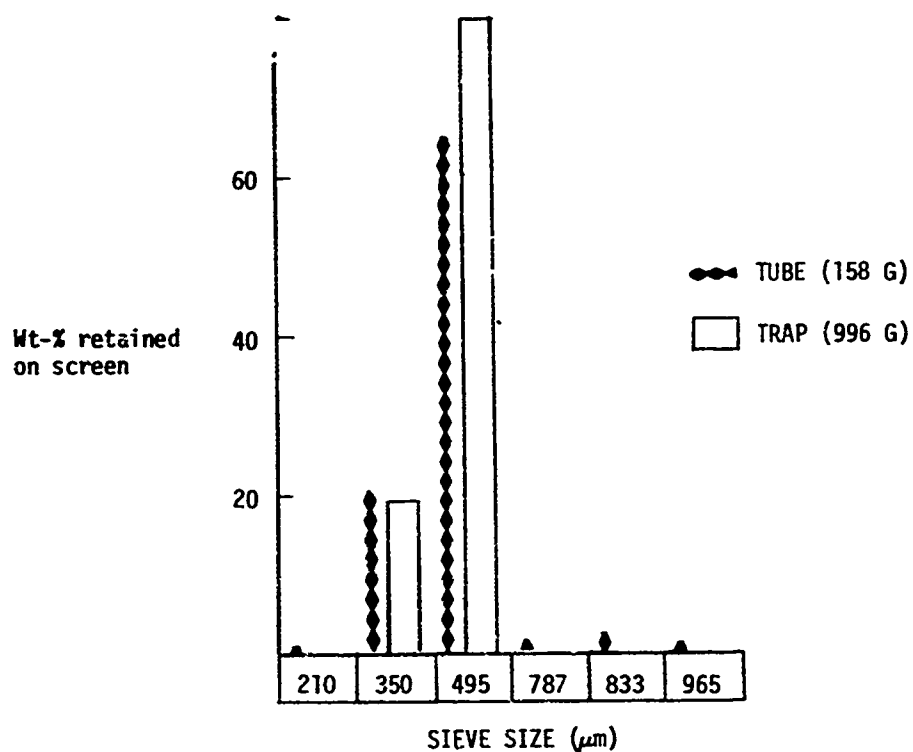
In the application of steady-state beds to the coating of large objects that are being levitated in the bed, it has been found preferable to allow the bed size to increase during the deposition to offset the increasing weight of the objects being coated. It is worth noting again that in any but routine cases, truly steady-state conditions are not maintained.

### 3.5. RESULTS FROM THE DEPOSITION STUDIES

At the outset, several exploratory runs were made so that the proper feed and withdrawal rates could be determined to obtain near-steady-state conditions and the flow conditions required to levitate the large substrate discs could be established. A feed rate of 4 g/min ( $124 \text{ cm}^2/\text{min}$ ) was selected for the initial runs along with a withdrawal rate that maintained a bed size about 40% larger than the initial bed. For an example, refer to the plot of the specific surface area versus sphere diameter for different sphere densities in Fig. 5. Using an initial bed of 100 g of 425- $\mu\text{m}$  particles with a density of  $5.5 \text{ g/cm}^3$  ( $2600 \text{ cm}^2$ ), the withdrawal rate was adjusted to remain  $4700 \text{ cm}^2$  (156 g of 750- $\mu\text{m}$  particles with a density of  $2.7 \text{ g/cm}^3$ ) when the desired conditions were established. Obviously, when different conditions are used, the withdrawal rates must be adjusted in accordance with the overall efficiency.

Typical particle size distributions for two of the runs that were made using steady-state beds are plotted in Figs. 9 and 10. Similar plots for all of the runs are presented in Appendix B.

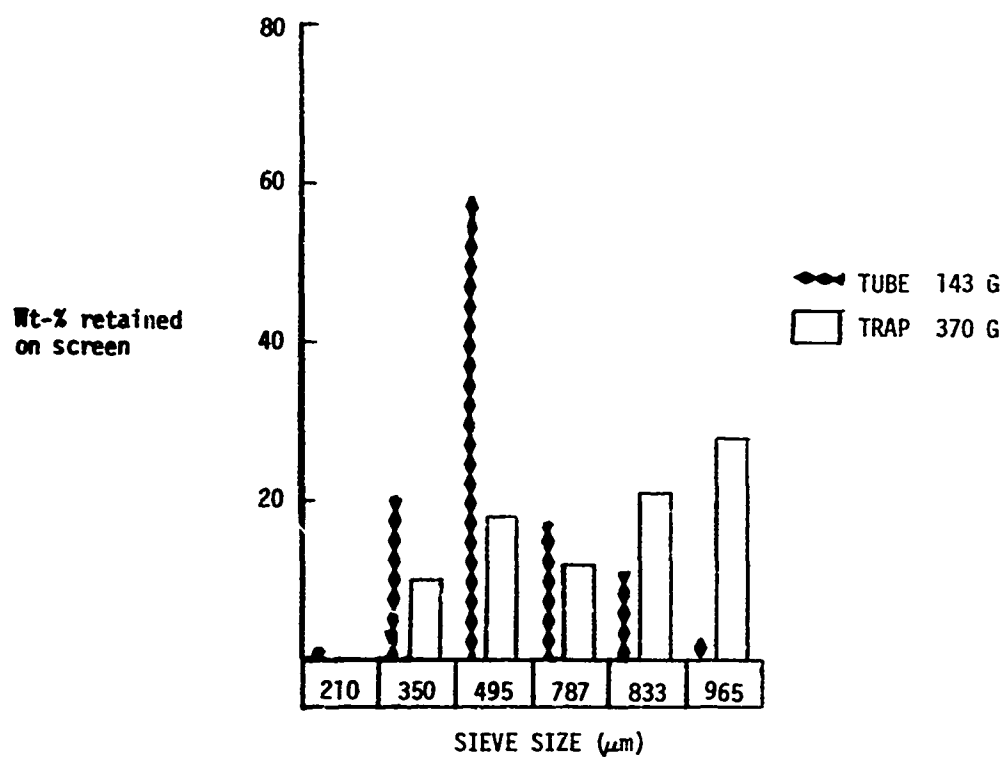
The approximate circulation time for the particles in the bed can be estimated by dividing the coating rate into the coating thickness corresponding to the largest sieve fraction. For example, batch 5408-23 had a deposition rate of  $1.4 \mu\text{m}/\text{min}$  and a mean particle diameter (from Fig. 9) that ranged from about 500 to about 750  $\mu\text{m}$  (625  $\mu\text{m}$  average), giving a residence time of about 100 min (compared with a total run time of 4 hr). Batch 5408-19 (Fig. 10), with a deposition rate of twice batch 5408-23, yields an estimated circulation time of 40 min (for a 1-hr run). Batches with high deposition rates tend to have higher weight fractions in the larger size ranges. Naturally, these are crude approximations, since many particles probably circulate in the bed from the start to the end of a deposition run.



Sample: 5408-23  
 $C_3H_8$  concentration: 7%  
 Bed temperature: 1280°C  
 Overall efficiency: 25%  
 Coating rate: 1.4 μm/min  
 Microhardness: 207-DPH  
 Density: 1.717 g/cm<sup>3</sup>  
 $L_c$ : 25 Å

85X

Fig. 5. Plot of particle size distributions in tube and trap for run 5804-23



Sample: 5408-19  
 $\text{C}_3\text{H}_8$  concentration: 60%  
 Bed temperature: 1140°C  
 Overall efficiency: 21%  
 Coating rate: 3.1  $\mu\text{m}/\text{min.}$   
 Microhardness: 215-DPH  
 Density: 2.008  $\text{g}/\text{cm}^3$   
 $L_c$ : 35 Å

85X

Fig. 10. Plot of particle size distributions in tube and trap for run 5408-19

### 3.5.1. Results for Depositions of Pure Carbons from Propane

The data relating deposition conditions for the unalloyed carbons deposited from propane are listed in Table 2. Corresponding data characterizing the structure of each of the carbons listed in Table 2 are presented in Table 3. Photomicrographs of all deposits are presented in Appendix B, including data for several exploratory coating runs using  $H_2$  and  $Cl_2$  additions. Hydrogen has been reported to inhibit pyrolysis, whereas chlorine catalyzes the decomposition by acting as a dehydrogenation agent.<sup>(36)</sup>

The density and  $L_c$  values that characterize the deposits listed in Table 3 have been plotted in Figs. 11 and 12 as a function of the deposition temperature and gas composition.

There is a significant difference between the data in Fig. 11 and similar data reported previously for depositions from propane with the conventional fluidized-bed process.<sup>(26,44)</sup> The present work indicates very little dependence of the sink-float density of the deposited carbon on gas composition for constant deposition temperatures. The discrepancy in the earlier work is likely an artifact that arises when the control temperature is assumed to be equal to the bed temperature. It can be noted in Table 3 that at a given control temperature, the density increases strongly with increasing propane concentration. A similar artifact may also exist in the data reported previously for depositions from methane in the same temperature range.<sup>(13,14)</sup> There may be a slight increase in the density when hydrogen, instead of helium, is used as the carrier gas, but the effect is surprisingly small. There is also very little effect due to the addition of 2% chlorine in the 25% propane experiment.

Very recent studies of the nature of the density of the low-density deposits have shown that for these materials, the sink-float density is an inadequate characterization of the density. For example, the data in Table 4 indicate very different pore structures for two carbons with densities near  $1.5 \text{ g/cm}^3$ . Efforts are in progress to improve the density characterization for low-density deposits.

TABLE 2  
COATING CONDITIONS AND COATING RESULTS FOR UNALLOYED LTI CARBONS DEPOSITED IN  
STEADY-STATE FLUIDIZED BEDS FROM PROPANE (a)

| Run Number | C <sub>3</sub> H <sub>8</sub> Conc. (%) | Control Temp (°C) | Bed Temp (°C) | Carbon Deposition Efficiency (%) | Average Coating Rate (μm/min) | Coating Thickness (in.) |
|------------|---|-------------------|---------------|----------------------------------|-------------------------------|-------------------------|
| 5408-23    | 7                                       | 1300              | 1280          | 25                               | 1.4                           | 0.013                   |
| 5408-21    | 25                                      | 1300              | 1190          | 55                               | 2.9                           | 0.014                   |
| 5408-19    | 60                                      | 1300              | 1140          | 21                               | 3.1                           | 0.013                   |
| 5408-17    | 3                                       | 1350              | 1330          | 79                               | 0.91                          | 0.013                   |
| 5408-11    | 7                                       | 1350              | 1330          | --                               | 1.4                           | 0.014                   |
| 5408-5     | 25                                      | 1350              | 1260          | 40                               | 4.9                           | 0.028                   |
| 5408-9     | 25                                      | 1350              | 1260          | 65                               | 4.2                           | 0.010                   |
| 5408-15    | 25                                      | 1350              | 1260          | 35                               | 2.3                           | 0.011                   |
| 5408-3     | 60                                      | 1350              | 1220          | 36                               | 5.5                           | 0.013                   |
| 5408-7     | 60                                      | 1350              | 1220          | 26                               | 5.9                           | 0.014                   |
| 5408-29    | 7                                       | 1420              | 1400          | 51                               | 1.3                           | 0.012                   |
| 5408-27    | 25                                      | 1400              | 1340          | 25                               | 5.7                           | 0.027                   |
| 5408-25    | 60                                      | 1400              | 1300          | 35                               | 8.1                           | 0.019                   |
| 5408-31    | 60                                      | 1380              | 1230          | 40                               | 6.8                           | 0.016                   |
| 5408-33    | 60                                      | 1440              | 1355          | 52                               | 9.8                           | 0.023                   |
| 5408-35    | 60                                      | 1475              | 1400          | 55                               | 8.5                           | 0.020                   |
| 5408-39    | 60 + 40% H <sub>2</sub>                 | 1400              | 1300          | 47                               | 8.0                           | 0.019                   |
| 5408-41    | 60 + 40% H <sub>2</sub>                 | 1300              | 1400          | 37                               | 3.8                           | 0.009                   |
| 5408-43    | 25 + 75% H <sub>2</sub>                 | 1300              | 1190          | 31                               | 1.7                           | 0.008                   |
| 5408-53    | 25 + 73% He<br>+ 2% Cl <sub>2</sub>     | 1350              | ~1240         | 30                               | 4.0                           | 0.019                   |

(a) Total flow rate was 15 l/min at room temperature.

TABLE 3  
COATING STRUCTURAL DATA FOR UNALLOYED LTI CARBONS DEPOSITED IN STEADY-STATE  
FLUIDIZED BEDS FROM PROPANE (a)

| Run Number | C <sub>3</sub> H <sub>8</sub> Conc. (%)         | Control Temp (°C) | Bed Temp (°C) | Microhardness (DPH, 50-g load) | Coating Density (g/cm <sup>3</sup> ) | Apparent Crystallite Height (Å) | Apparent Droplet Size (μm) |
|------------|---|-------------------|---------------|--------------------------------|--------------------------------------|---------------------------------|----------------------------|
| 5408-23    | 7   | 1300              | 1280          | 207                            | 1.717                                | 25                              | (b)                        |
| 5408-21    | 25  | 1300              | 1190          | 226                            | 1.914                                | 32                              | (b)                        |
| 5408-19    | 60  | 1300              | 1140          | 215                            | 2.008                                | 35                              | 0.48                       |
| 5408-17    | 3   | 1350              | 1330          | 153                            | 1.457                                | 20                              | 0.30                       |
| 5408-11    | 7   | 1350              | 1330          | 154                            | 1.553                                | 23                              | (b)                        |
| 5408-5     | 25  | 1350              | 1260          | 210                            | 1.775                                | 30                              | 0.35                       |
| 5408-9     | 25  | 1350              | 1260          | 192                            | (b)                                  | (b)                             | (b)                        |
| 5408-15    | 25  | 1350              | 1260          | 190                            | (b)                                  | (b)                             | (b)                        |
| 5408-3     | 60  | 1350              | 1220          | 214                            | 2.004                                | (b)                             | (b)                        |
| 5408-7     | 60  | 1350              | 1220          | 219                            | 1.974                                | 36                              | 0.35                       |
| 5408-29    | 7   | 1420              | 1400          | 100                            | 1.353                                | 26                              | (b)                        |
| 5408-27    | 25  | 1400              | 1340          | 156                            | 1.592                                | 24                              | (b)                        |
| 5408-25    | 60  | 1400              | 1300          | 170                            | 1.753                                | 29                              | 0.33                       |
| 5408-31    | 60  | 1390              | 1230          | 170                            | 1.823                                | 33                              | (b)                        |
| 5408-33    | 60  | 1440              | 1355          | 127                            | 1.535                                | 26                              | 0.28                       |
| 5408-35    | 60  | 1475              | 1400          | 92                             | 1.459                                | 26                              | 0.33                       |
| 5408-39    | 60 + 40% H <sub>2</sub>                         | 1400              | 1300          | 187                            | 1.813                                | 31                              | (b)                        |
| 5408-41    | 60 + 40% H <sub>2</sub>                         | 1300              | 1400          | 185                            | (b)                                  | (b)                             | (b)                        |
| 5408-43    | 25 + 75% H <sub>2</sub>                         | 1300              | 1190          | 203                            | 2.017                                | 32                              | 0.45                       |
| 5408-53    | 25 + 73% H <sub>2</sub><br>+ 2% Cl <sub>2</sub> | 1350              | ~1240         | 211                            | 1.782                                | 29                              | (b)                        |

(a) The Bacon anisotropy factor for all deposits from propane concentrations ≥25% was <1.1. Slight anisotropy was noted for deposits from 7% propane and moderate anisotropy for the 3% propane deposits.

(b) In progress.

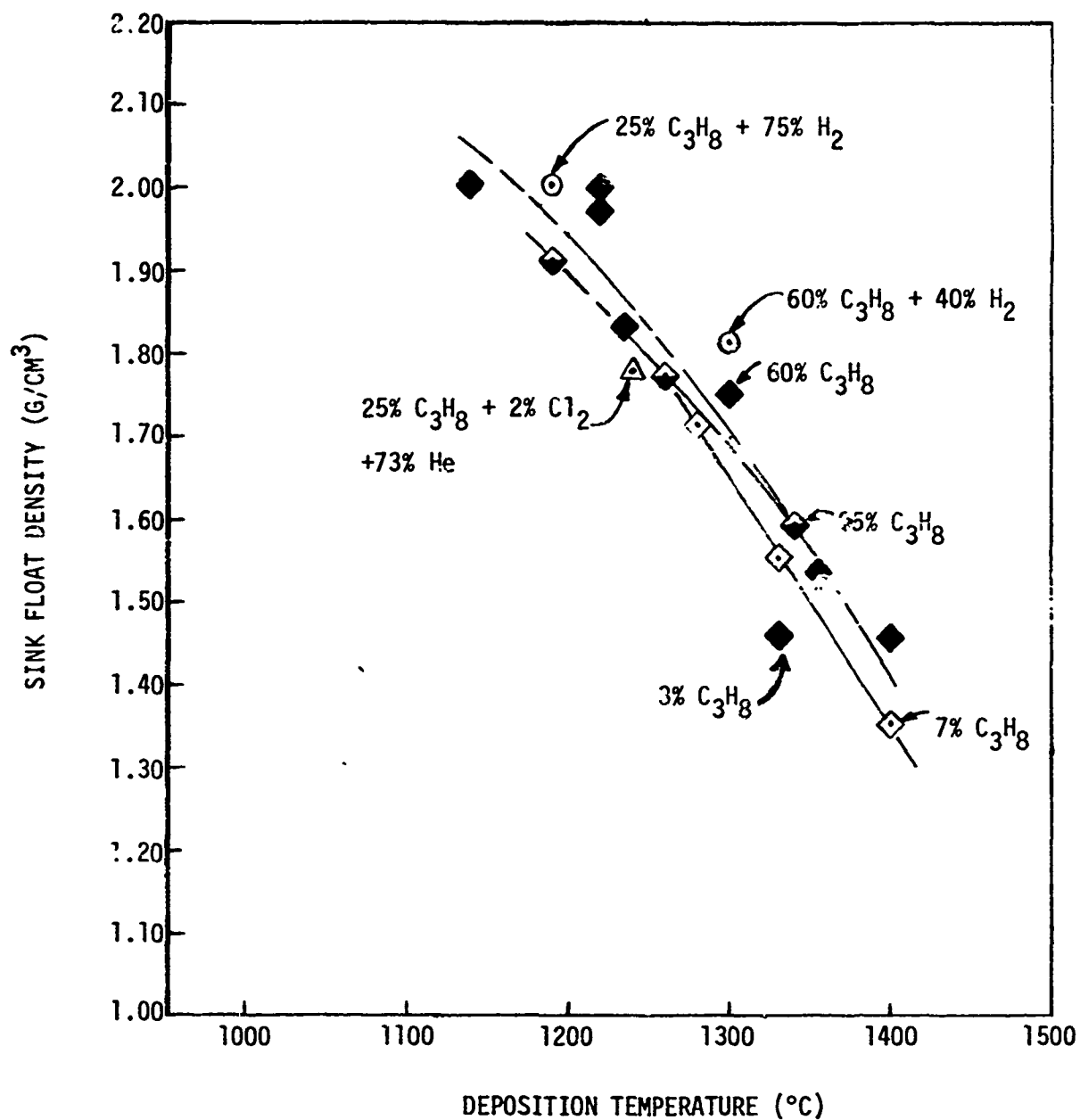


Fig. 11. Plot of coating density as a function of deposition temperature for coatings deposited from propane at 7%, 25%, and 60% concentrations

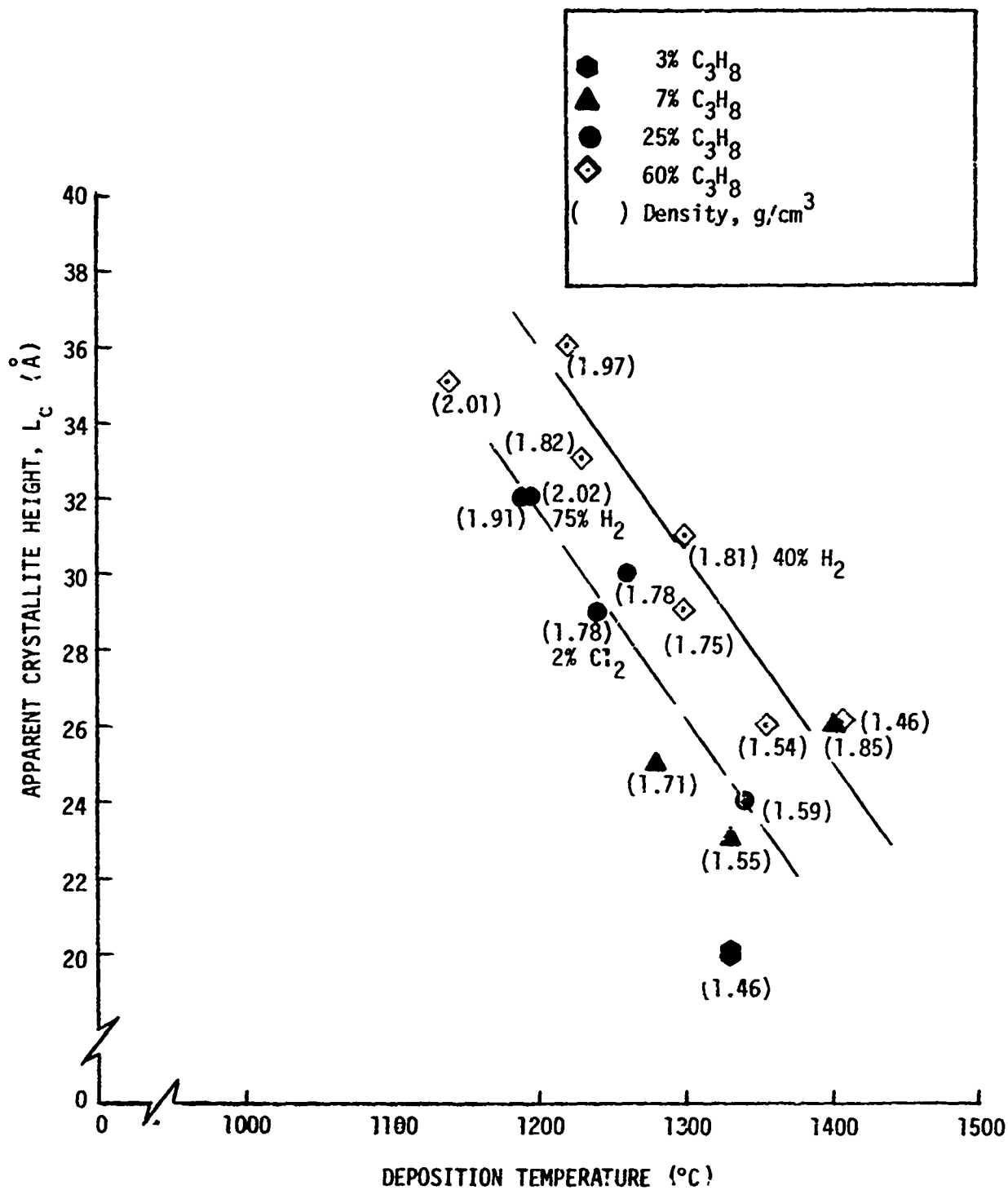


Fig. 12. Apparent crystallite height,  $L_c$ , as a function of deposition temperature for carbons deposited from various concentrations of propane



TABLE 4  
DATA COMPARING PORE STRUCTURES OF TWO CARBONS WITH  
SINK-FLOAT DENSITIES NEAR 1.5 G/CM<sup>3</sup>

|  | <u>5408-17</u> | <u>5408-33</u> |
|--|----------------|----------------|
| Sink-float density (g/cm <sup>3</sup> ). . . . .   | 1.46           | 1.54           |
| Apparent density (g/cm <sup>3</sup> ). . . . .     | 1.38           | 1.17           |
| Accessible porosity (%) . . . . .                  | 5.5            | 23.8           |
| Inaccessible porosity <sup>(a)</sup> (%) . . . . . | 32.6           | 23.6           |
| Total porosity (%) . . . . .                       | 38.5           | 47.8           |
| Coating rate (μm/min) . . . . .                    | 0.9            | 9.8            |

---

(a) Inaccessible porosity refers to all cellular porosity in addition to all density defect. It is calculated from the theoretical density of a perfect turbostratic crystal (2.22 g/cm<sup>3</sup>).

The data in Fig. 12 relating  $L_c$  values to deposition temperature indicate a rapid decrease in  $L_c$  with increasing deposition temperature and show that the  $L_c$  values are lower for the carbons deposited from lower propane concentrations. These data are in accord with data reported for methane (Ref. 14) and for propane (Ref. 26) but do not agree with the lack of dependence of  $L_c$  on methane and propane concentrations reported in other investigations.<sup>(13,44)</sup> There was no effect of hydrogen or chlorine additives on the  $L_c$  parameter. The lack of an important effect of these two elements is surprising in light of the large effects reported by Higgs and co-workers for deposition on a mandrel.<sup>(36)</sup>

The apparent droplet size as determined from scanning electron micrographs of as-deposited surfaces shows an interesting dependence on deposition temperature and propane concentration (representative photomicrographs are shown in Fig. 13). At constant propane concentration, the size of the droplets decreases with increasing bed temperature (Fig. 14) and, for a given gas composition, increases with increasing coating rate (Fig. 15). No comments will be made on the relevance of droplet size until more work has been performed in this area.

The microhardness data correlate very well with deposition temperature (Fig. 16). The hardness of the carbon, of course, cannot depend on the deposition temperature per se; rather it must be related to structural difference, which in turn depends on the deposition temperature. If the hardness is plotted as a function of the  $L_c$  parameter (Fig. 17), there is a rather poor correlation which suggests that the hardness increases with increasing  $L_c$  value. Intuitively, this seems unlikely. If, instead, the hardness is plotted as a function of coating density (Fig. 18), a good correlation results but the data group according to propane concentration. Examination of the  $L_c$  values for the data points in Fig. 18 shows that the hardness increases with density but there is a secondary effect of  $L_c$  parameter. These data indicate that the hardness increases with decreasing  $L_c$  value--not decreases as might be suggested by the general trend in Fig. 17. This is demonstrated more clearly by the fact that correlations between  $L_c$  and density for deposits with nearly constant hardness values (Fig. 19) show

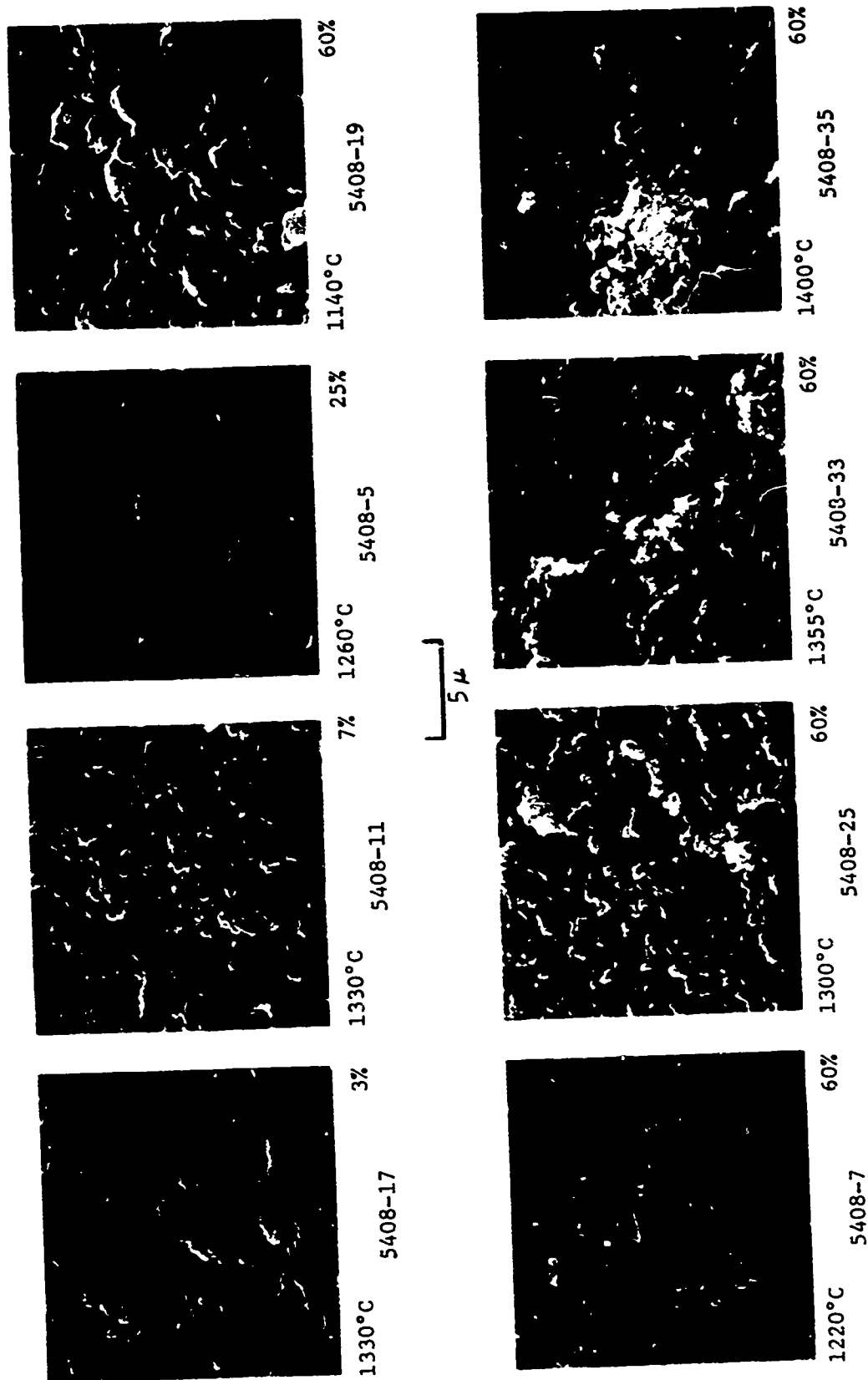


Fig. 13. Scanning electron micrographs of carbon surfaces deposited from propane at various temperatures; bed temperature (°C), propane concentration (%), and run number are given for each sample

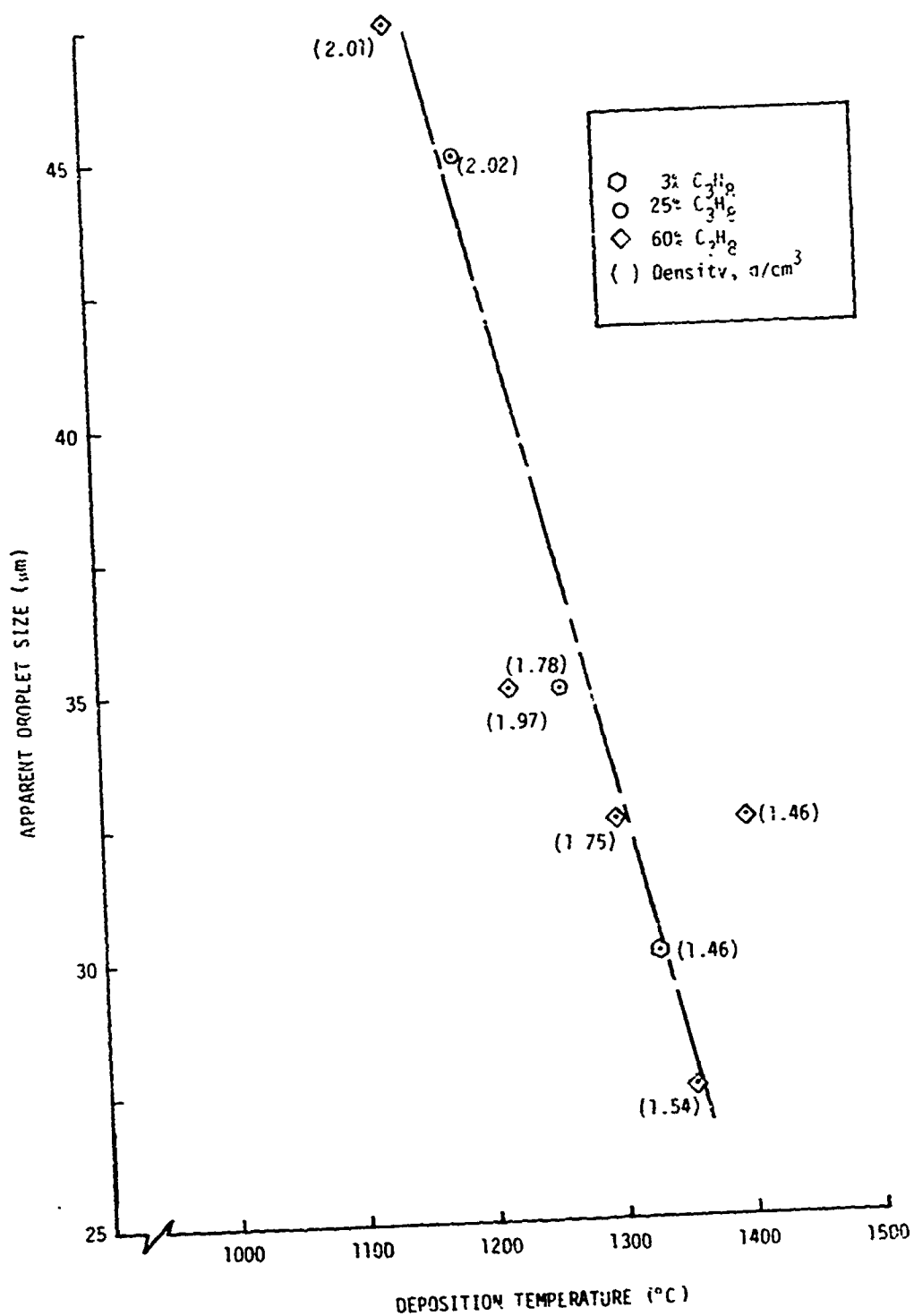


Fig. 14. Apparent droplet size versus deposition temperature for carbon deposited from various propane concentrations

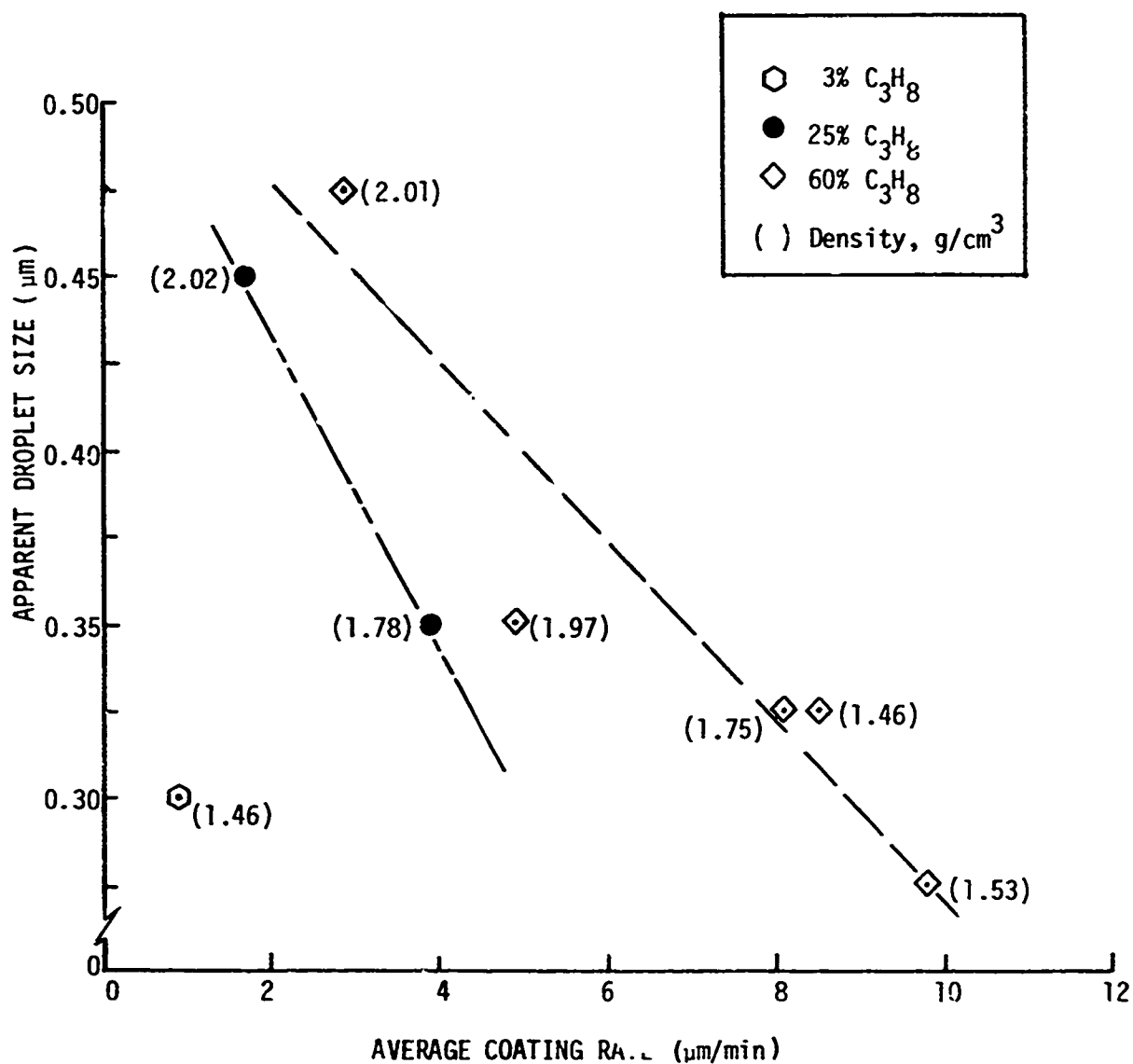


Fig. 15. Apparent droplet size versus coating rate for carbons deposited from propane

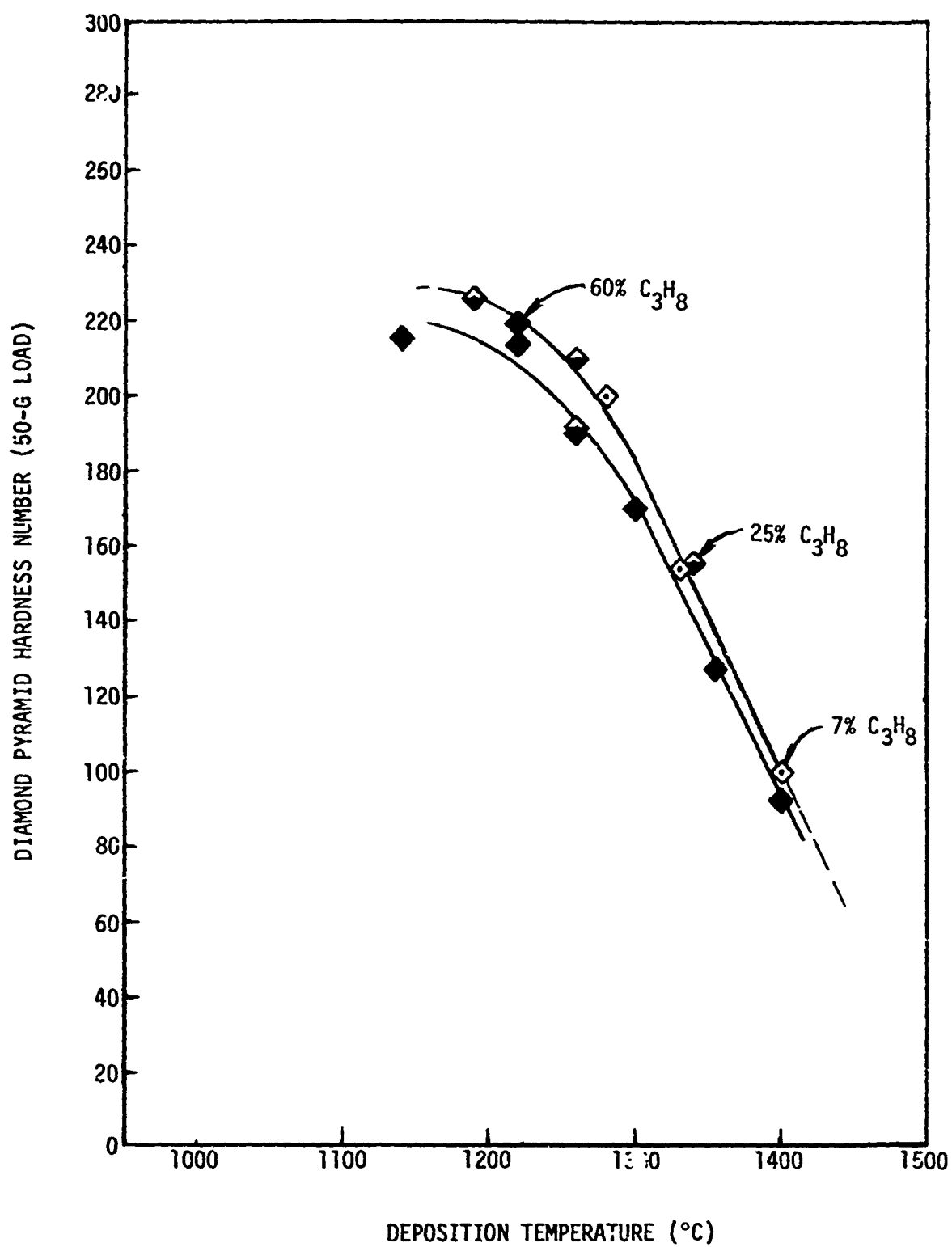


Fig. 16. Microhardness as a function of deposition temperature for carbons deposited from propane

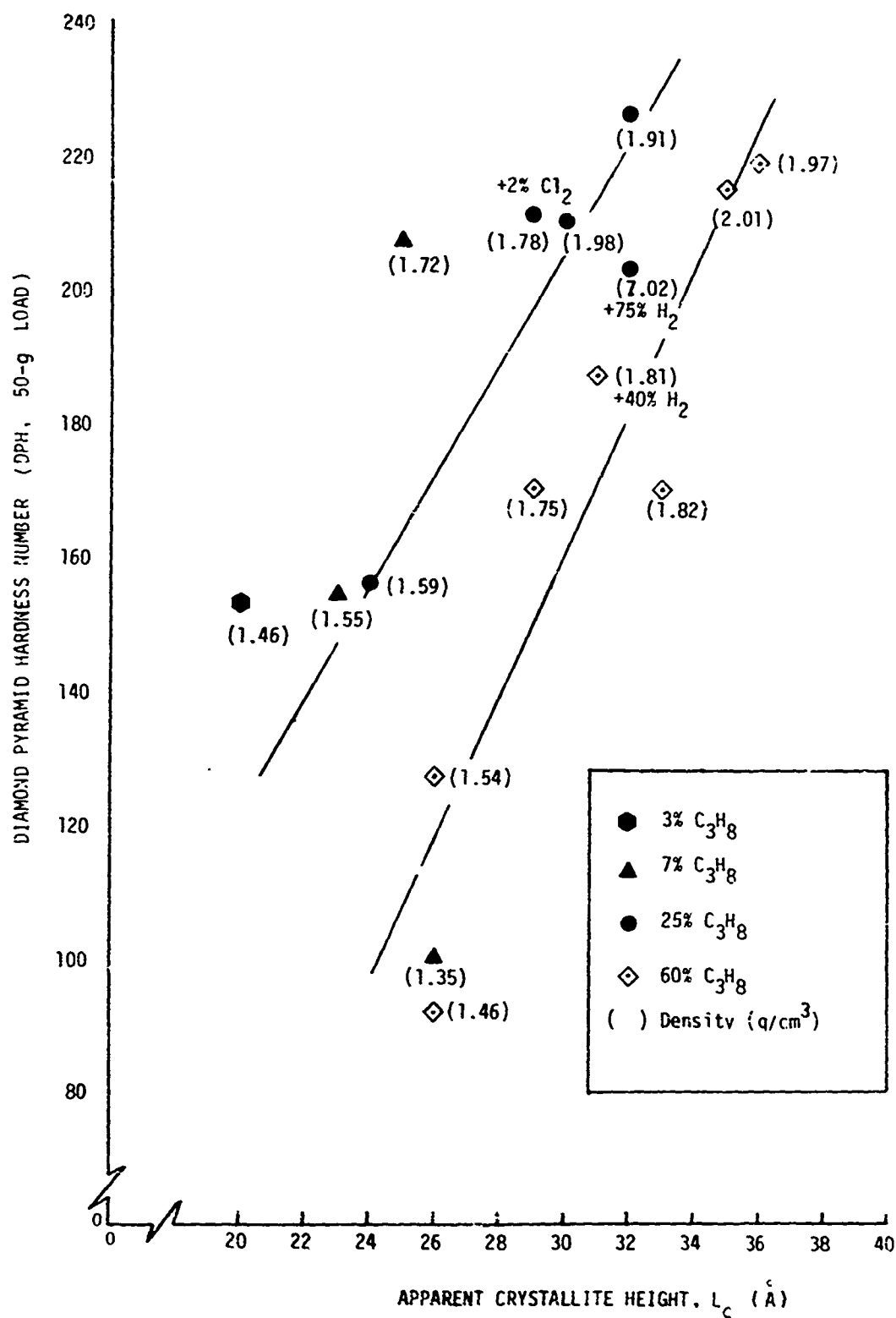


Fig. 17. Microhardness as a function of  $L_c$  parameter for carbons deposited from propane

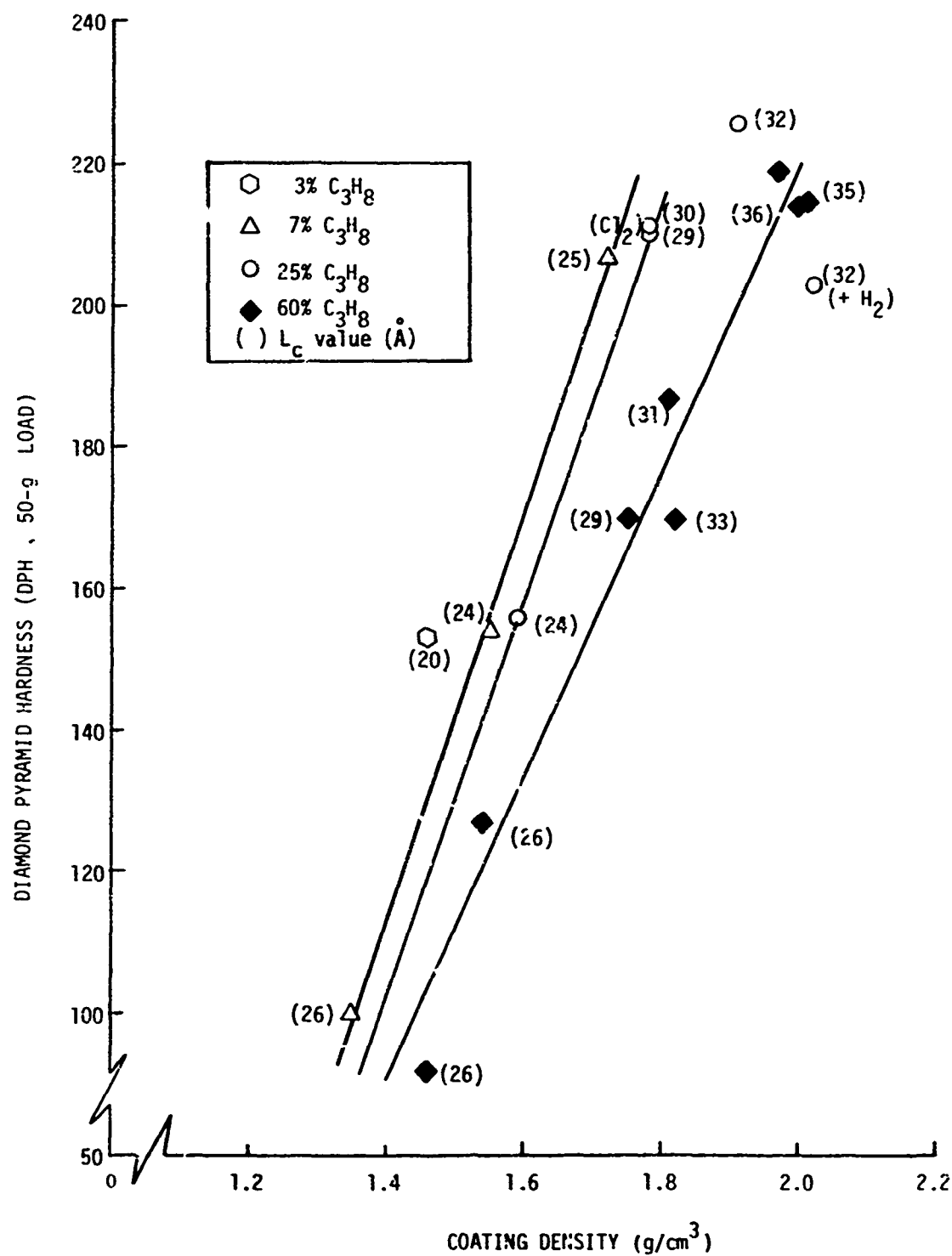


Fig. 18. Microhardness versus coating density for carbons deposited from propane



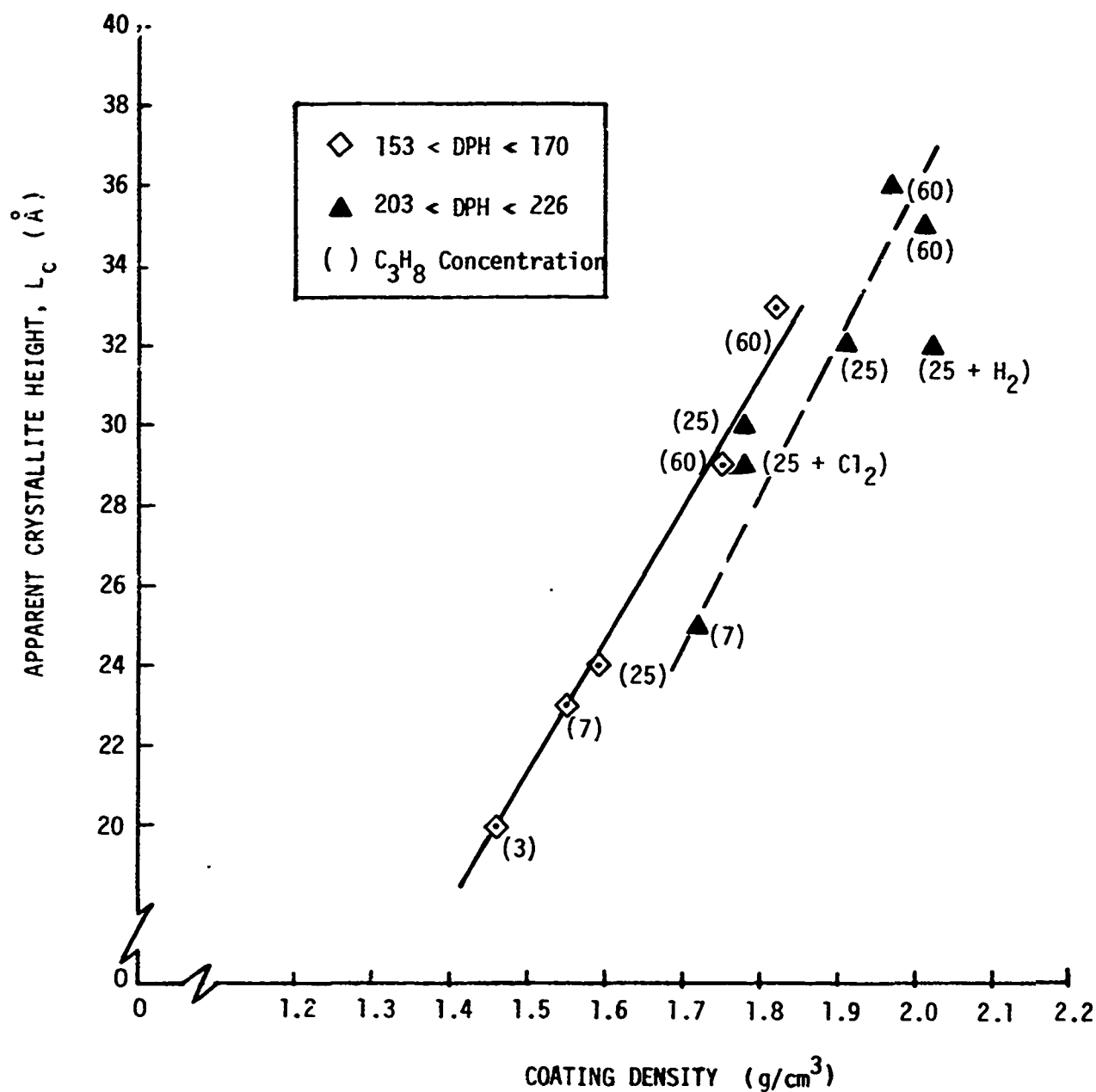


Fig. 19. Correlation of  $L_c$  and density for carbons with nearly the same microhardness value

that carbons with hardness values between 153 and 170 DPH units may have a low density with a low  $L_c$  value or a higher density with a higher  $L_c$  value. The same is true for the carbons with hardnesses in the range 203 to 226 DPH units. Therefore, the carbons can be made harder by shifting toward higher densities or lower  $L_c$  values. The data show that to obtain harder (and probably stronger) carbons, one should seek carbons with high densities combined with small  $L_c$  values, which are possibly obtainable by using higher propane concentrations and depositing at still lower temperatures.

Bard has shown that the coating rate can be a significant parameter for process control.<sup>(43)</sup> Bard's data indicate that at a given deposition temperature (below 1500°C), the same structure (as characterized by anisotropy and density) may be obtained from any hydrocarbon as long as the concentration used in the deposition is adjusted to yield the same deposition rate.

By using the data in Fig. 20 and those in Fig. 11, the relationships between density, gas composition, deposition temperature, and deposition rate can be explored. The plot in Fig. 21 indicates the surprising result that in spite of an order of magnitude range of deposition rates, at a given temperature the carbons deposited have nearly the same density, and that the density, if anything, increases slightly with increasing rate (at constant deposition temperature). This sort of dependence probably results from differences in the character of the droplets that form in carbon-rich and carbon-poor environments. An explanation for this dependence is being sought.

A plot similar to that in Fig. 21 for density is given in Fig. 22 for the  $L_c$  parameter. These data indicate that, at a given temperature, in spite of the order of magnitude increase in the deposition rate, the  $L_c$  value increases substantially. In other words, as shown by Figs. 20 and 21, increasing the deposition rate several fold at a given temperature in the range 1200° to 1400°C results in more crystalline, denser deposits. The explanation offered regarding a similar dependence for methane<sup>(15)</sup> may apply. Namely, at temperatures below about 1500°C, polymerization reactions produce planar arrays of carbon atoms in various states of dehydrogenation.<sup>(45)</sup>

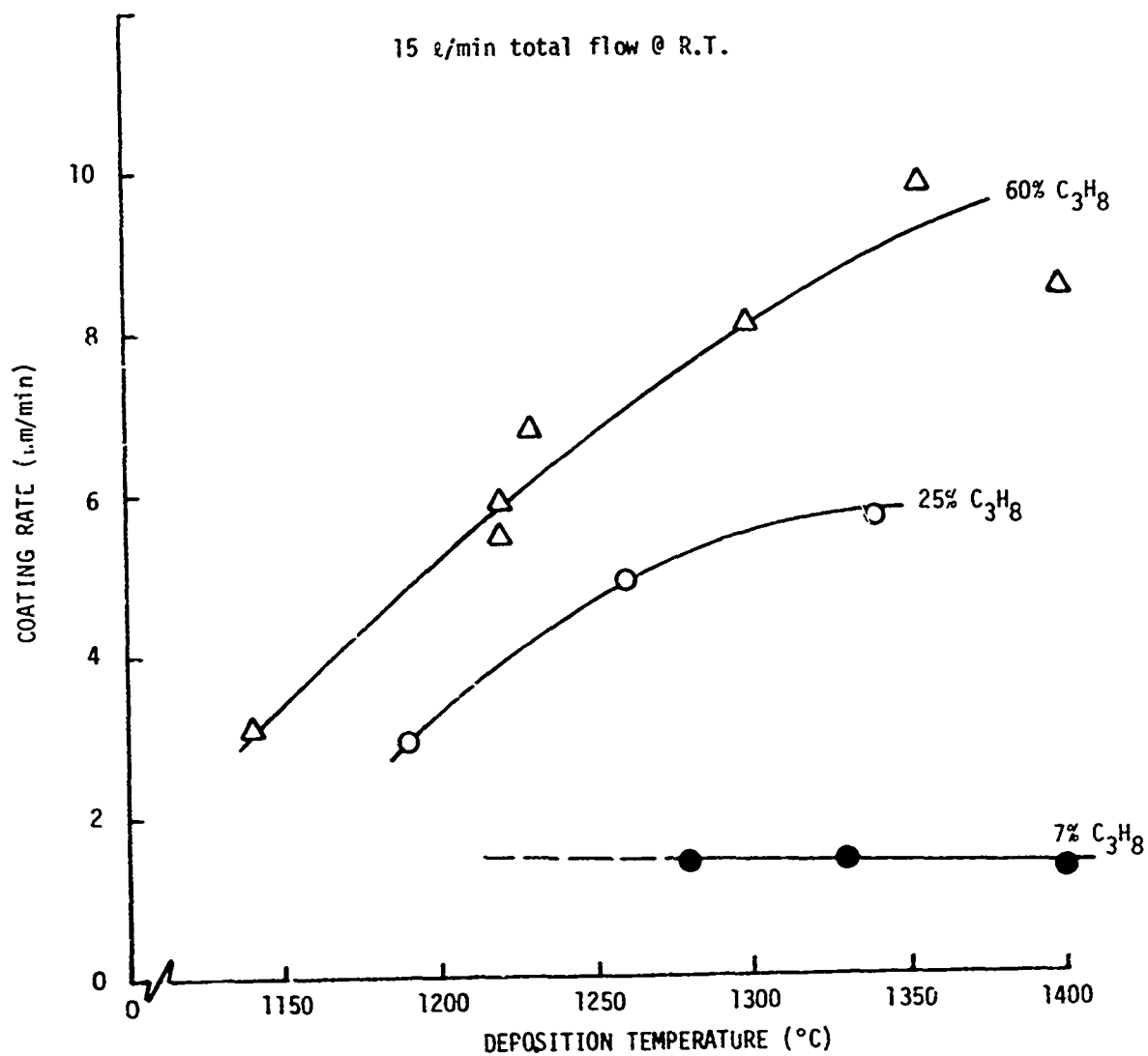


Fig. 20. Coating rate versus deposition temperature for carbons deposited from propane

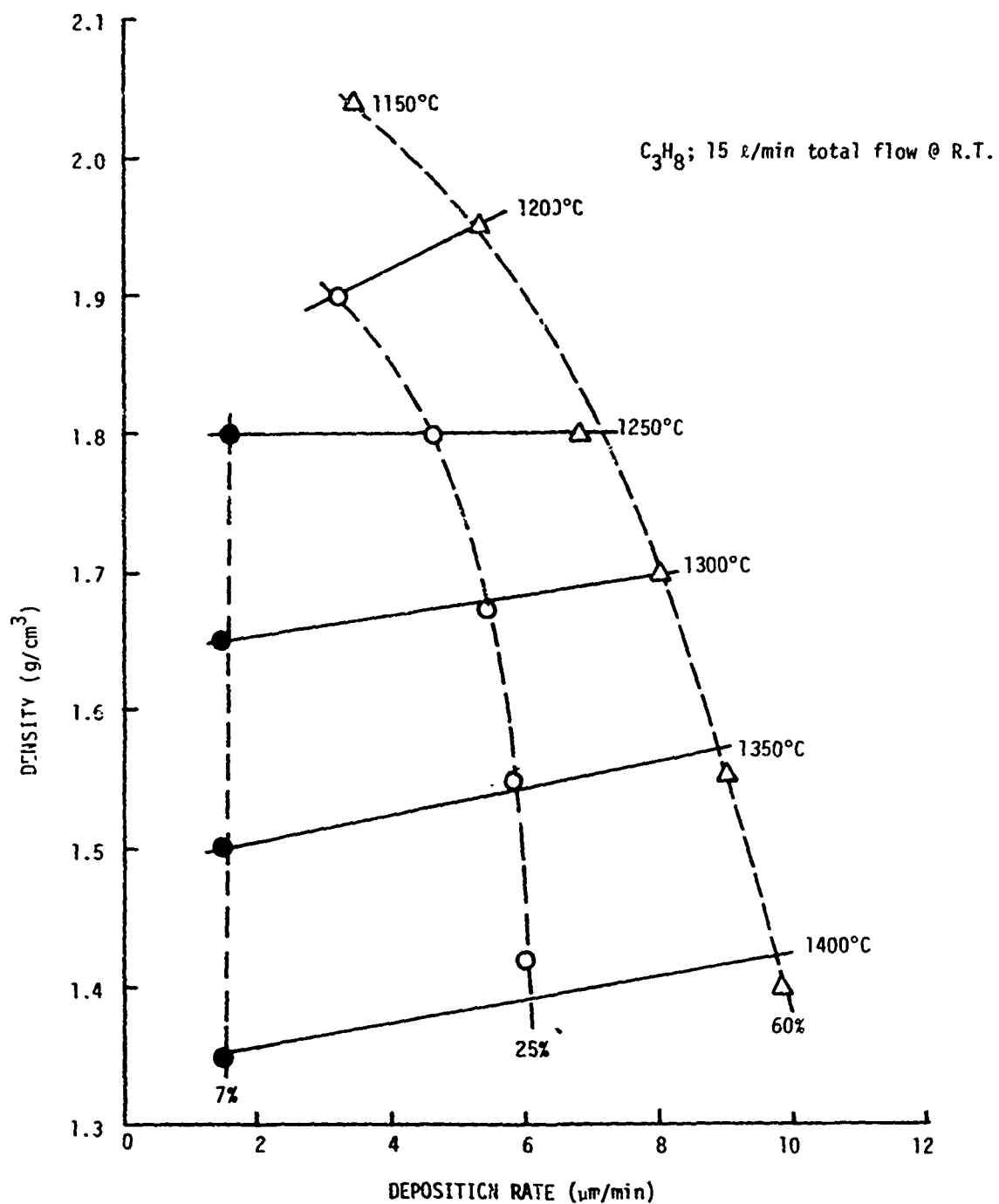


Fig. 21. Density versus deposition rate for carbons deposited from 7%, 25%, and 60% propane at temperatures in the range 1150° to 1400°C

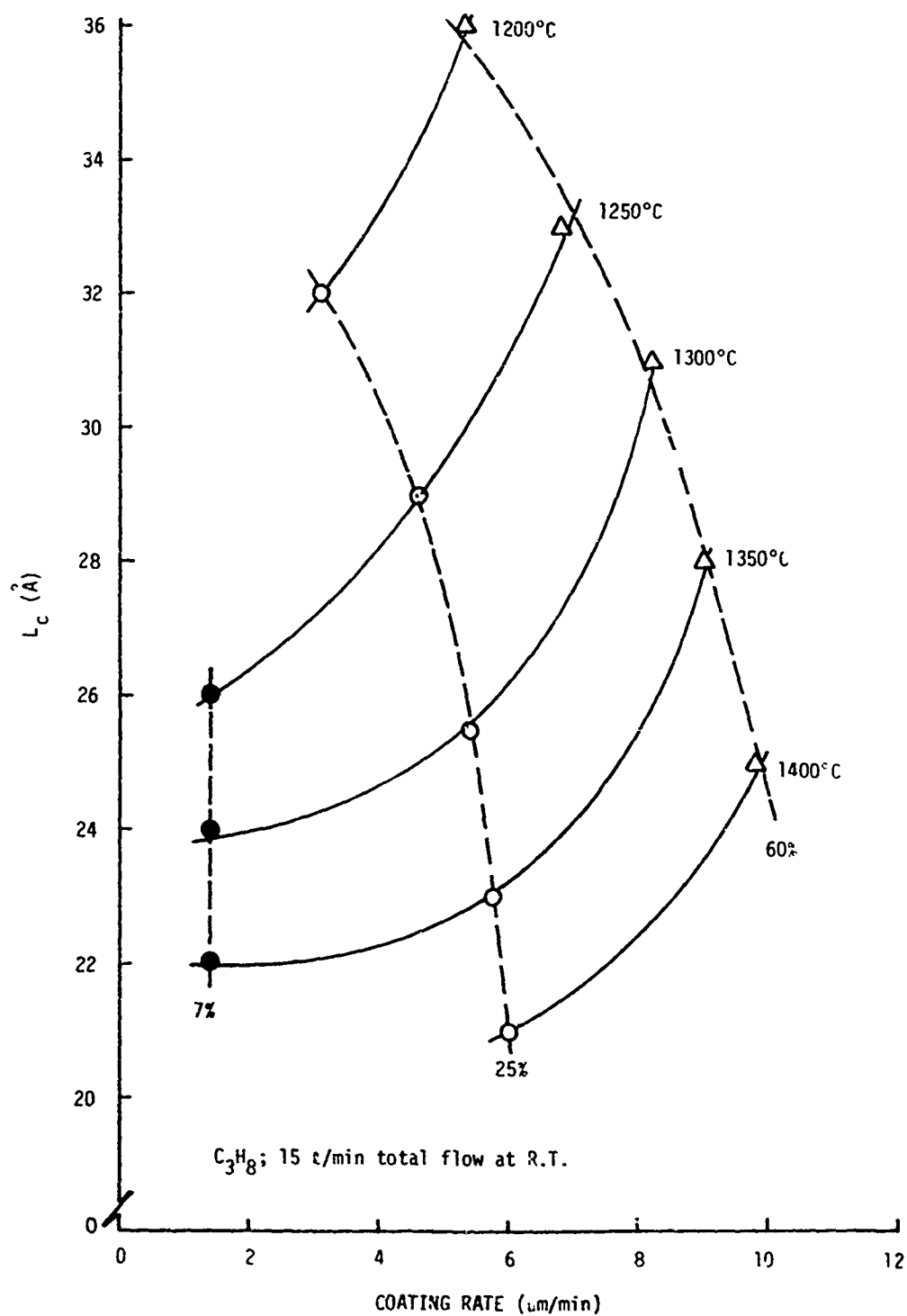


Fig. 22.  $L_c$  parameter versus deposition rate for carbons deposited from 7%, 25%, and 60% propane at temperatures in the range 1200° to 1400°C

It is thought that the higher the hydrocarbon concentrations used, the faster the polymerization and the larger the planar molecules that eventually make up the droplets. Since large planar molecules naturally are better able to align themselves parallel to one another, denser, more crystalline deposits result. Because it is less stable than methane and contains more carbon, propane produces high enough concentrations of carbon-bearing species in the gas to form droplets at much lower concentrations than methane. Accordingly, isotropic carbons formed by the droplet mechanism are much easier to form from propane at 1300°C, for example, than from methane. (31)

As a final point in this section, the relationships between the DPH property and the coating rate (Fig. 23) will be rationalized in terms of the data in Figs. 21 and 22 for density and the  $L_c$  parameter. The data in Fig. 23 for the DPH indicates that at constant deposition temperature, there is a slight drop with increasing deposition rate. Since in the same range the density is constant or rises slightly, the drop in DPH is taken to be a consequence of the concomitant rise in the  $L_c$  parameter. The data in Fig. 23 indicate that the hardest carbons (with as high a density and as low a  $L_c$  value as possible) should be formed at propane concentrations >60% and at temperatures below about 1200°C. This region will be explored further.

### 3.5.2. Results for Co-Deposited Carbon-Silicon Alloys

The data describing the deposition conditions and the parameters that characterize the co-deposited carbon-silicon materials are given in Tables 5 and 6, respectively. The microstructures of these deposits are shown in Fig. C-5 of Appendix C.

A comparison of the deposition rates for the carbon co-deposited with silicon (Fig. 24) with the rates for carbons deposited from propane alone (Fig. 20) in the same temperature range shows that for 7% propane, the deposition rate is increased by the addition of  $\text{CH}_3\text{SiCl}_3$ , but for 25% and

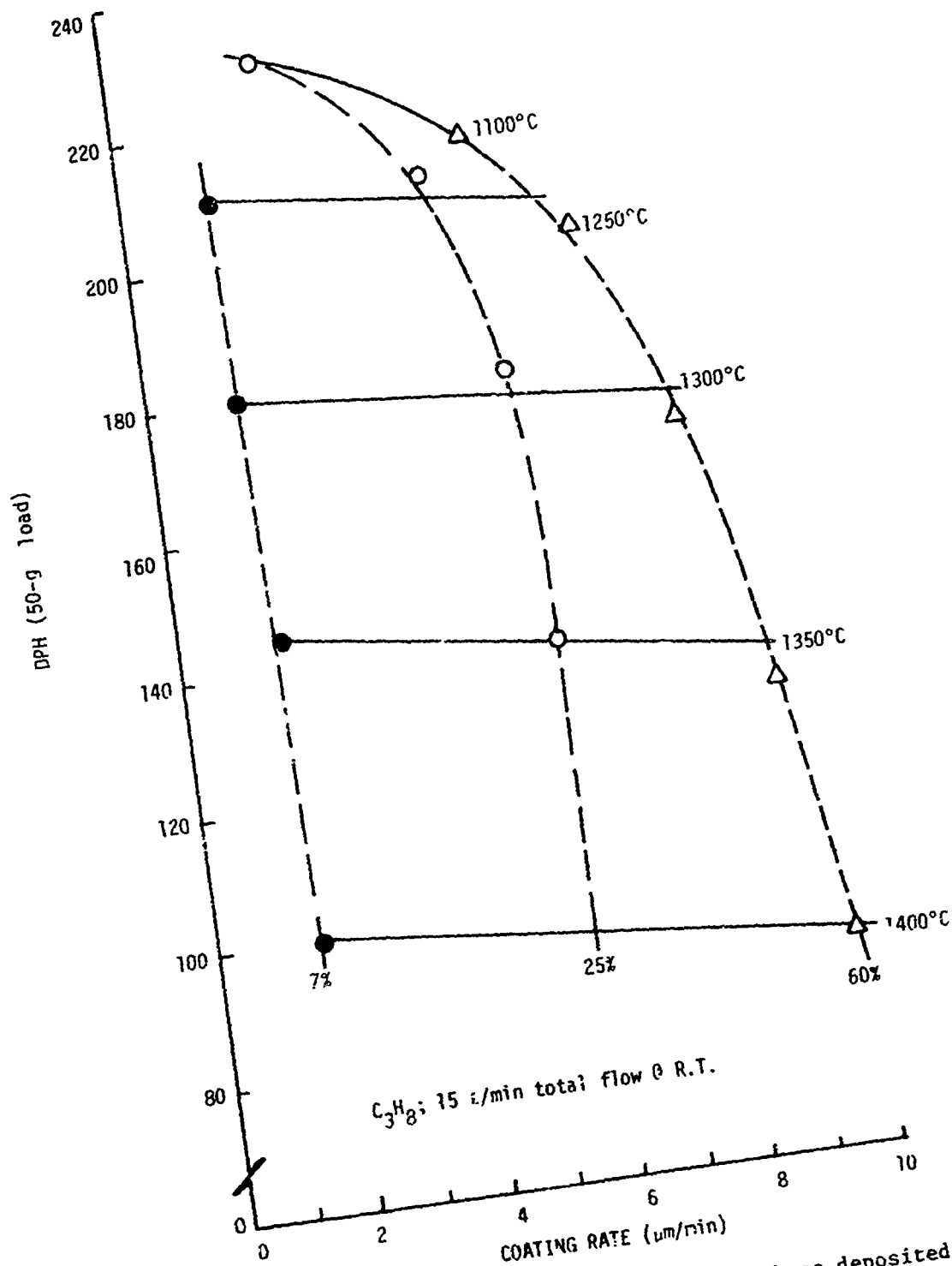


Fig. 23. Microhardness versus deposition rate for carbons deposited from 7%, 25%, and 60% propane at temperatures in the range 1200° to 1400°C

TABLE 5  
DEPOSITION CONDITIONS FOR CO-DEPOSITED CARBON-SILICON ALLOYS DEPOSITED IN STEADY-STATE  
BEDS USING PROPANE AND METHYLTRICHLOROSILANE (a)

| Run Number | C <sub>3</sub> H <sub>8</sub> Conc. (%) | Control Temp (°C) | Bed Temp (°C) | CH <sub>3</sub> SiCl <sub>3</sub> Feed Rate (g/min) | CH <sub>3</sub> SiCl <sub>3</sub> Volumetric Flow Rate (R.T.) (cm <sup>3</sup> /min) | Carbon Deposition Efficiency (%) | Average Deposition Rate (μm/min) | Coating Thickness (in.) |
|------------|---|-------------------|---------------|---|--|----------------------------------|----------------------------------|-------------------------|
| 5408-87    | 7                                       | 1300              | 1290          | 8.7   | 1360   | 44.5                             | 2.1                              | 0.020                   |
| 5408-69    | 25                                      | 1300              | 1270          | 8.7   | 1360   | 55.4                             | 3.6                              | 0.017                   |
| 5408-65    | 60                                      | 1300              | 1235          | 5.9   | 950  | 42.5                             | 5.5                              | 0.013                   |
| 5408-61    | 7                                       | 1350              | 1340          | 7.2   | 1150   | 36.3                             | 2.3                              | 0.022                   |
| 5408-59    | 25                                      | 1350              | 1335          | 9.5   | 1520   | 65.2                             | 4.8                              | 0.017                   |
| 5408-57    | 60                                      | 1350              | 1295          | 6.0   | 960  | 54.5                             | 5.9                              | 0.014                   |
| 5408-85    | 7                                       | 1400              | 1390          | 9.2   | 1470   | 40.0                             | 3.0                              | 0.022                   |
| 5408-83    | 25                                      | 1400              | 1370          | 9.8   | 1560   | 55.0                             | 6.8                              | 0.024                   |
| 5408-67    | 60                                      | 1400              | 1350          | 5.0   | 800  | 58.4                             | 5.9                              | 0.014                   |

(a) Total flow rate was 15 l/min (C<sub>3</sub>H<sub>8</sub> and He) at room temperature.



TABLE 6  
STRUCTURAL DATA FOR CO-DEPOSITED CARBON-SILICON DEPOSITS FORMED IN STEADY-STATE  
FLUIDIZED BEDS USING PROPANE AND METHYLTRICHLOROSILANE<sup>(a)</sup>

| Run<br>Number | C <sub>3</sub> H <sub>8</sub><br>Conc.<br>(%) | Control<br>Temp<br>(°C) | Bed<br>Temp<br>(°C) | Apparent<br>Droplet<br>Size<br>( $\mu$ m) | Silicon<br>Content<br>(wt-%) | Micro-<br>hardness<br>(DPH,<br>50-g load) | Carbon<br>Deposition<br>Efficiency<br>(g/cm <sup>3</sup> ) | Calculated<br>Carbon<br>Matrix<br>Density<br>(g/cm <sup>3</sup> ) | Vol-%<br>SiC     |
|---------------|---|-------------------------|---------------------|---|------------------------------|---|--|---|------------------|
| 5408-87       | 7   | 1300                    | 1290                | 0.14                                      | 23.0                         | 430                                       | 2.178  | 1.88  | 22.5             |
| 5408-69       | 25  | 1300                    | 1270                | 0.20                                      | 15.0                         | 352                                       | 2.105  | 1.92  | 14.2             |
| 5408-65       | 60  | 1300                    | 1235                | 0.22                                      | 8.0                          | 295                                       | 2.064  | 1.97  | 7.4              |
| 5408-61       | 7   | 1350                    | 1340                | (b)                                       | 28.0                         | 397                                       | 2.158  | 1.77  | 27.2             |
| 5408-59       | 25  | 1350                    | 1335                | 0.16                                      | 16.0                         | 212                                       | 2.062  | 1.87  | 14.9             |
| 5408-57       | 60  | 1350                    | 1295                | (b)                                       | 9.5                          | 201                                       | 2.085  | 1.98  | 8.8              |
| 5408-35       | 7   | 1400                    | 1390                | 0.10                                      | 34.0                         | 378                                       | 2.149  | 1.64  | 32. <sup>c</sup> |
| 5408-83       | 25  | 1400                    | 1370                | (b)                                       | 13.5                         | 279                                       | 2.063  | 1.92  | 12.6             |
| 5408-67       | 60  | 1400                    | 1350                | (b)                                       | 4.0                          | 179                                       | 2.031  | 1.98  | 3.7              |

(a) The Bacon anisotropy factor for all deposits was <1.1.

(b) In progress.

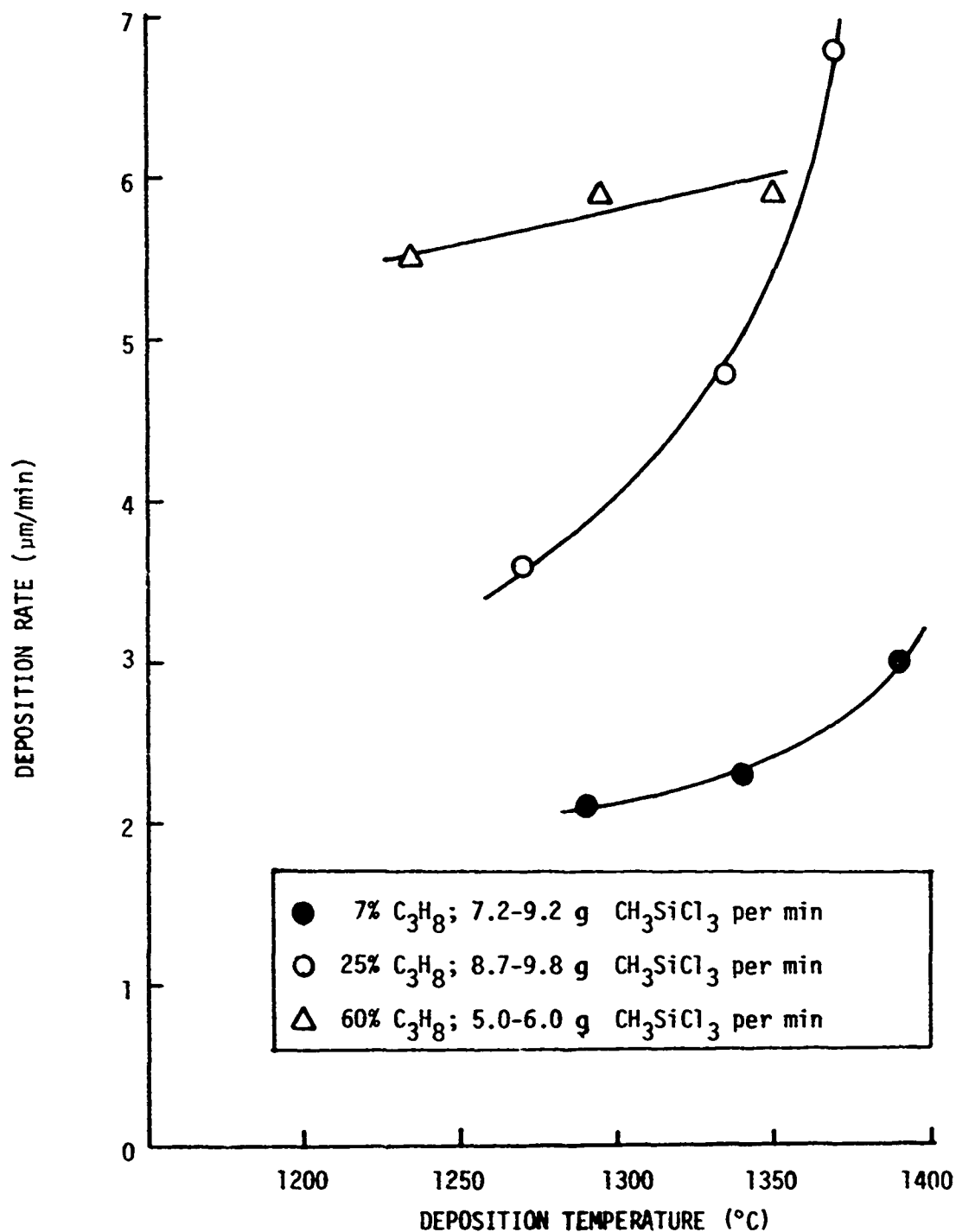


Fig. 24. Deposition rates for depositions from propane with a  $\text{CH}_3\text{SiCl}_3$  additive for temperatures in the range  $1250^{\circ}$  to  $1400^{\circ}\text{C}$  and propane concentrations in helium in the range 7% to 60%

60% propane, the rate is decreased. Surprisingly, no catalytic effect of the added chloride is evident. The increase in rate for the 7% propane case may be due to the significant amounts of SiC deposited from the  $\text{CH}_3\text{SiCl}_3$ .

Scanning electron micrographs such as those in Fig. 25 indicate that there is a correlation between the apparent droplet size and the silicon concentration (plotted in Fig. 26), but more data are required to substantiate this trend.

The relationships between the density of the carbon matrix (calculated from the bulk density and the silicon concentration assuming a theoretical density of  $3.21 \text{ g/cm}^3$  for SiC), the apparent droplet size, the silicon concentration, and the deposition temperature are plotted in Fig. 27. The data in Fig. 27a that relate the carbon matrix density to the deposition temperature and the gas composition indicate that the materials deposited from the highest concentrations of propane have the highest matrix density. Comparison of these data with corresponding data in Fig. 11 for carbons deposited without  $\text{CH}_3\text{SiCl}_3$  indicates that the latter all have substantially lower densities for the same deposition temperature. Even the carbon-silicon material co-deposited from gas with 7% propane at substantially higher rates than for the corresponding carbons deposited without  $\text{CH}_3\text{SiCl}_3$  have higher matrix densities. Comparison of the data in Fig. 27a with the silicon concentrations plotted in Fig. 27c shows that the carbons with the lowest carbon matrix density also have the highest silicon concentration. The correlation plotted in Fig. 28 has been reported for depositions in conventional fluidized beds. (46,47)

It is not yet understood why carbon-silicon alloys that have high carbon matrix densities with high silicon concentrations have not been observed. The explanation may be simply that the  $\text{C}_2\text{SiCl}_3$  has always been added with a bubble-contactor using all the helium carrier gas. Since the helium volume flow rate is lower when high propane concentrations are used, less  $\text{CH}_3\text{SiCl}_3$  is introduced. It may be that all that is required to

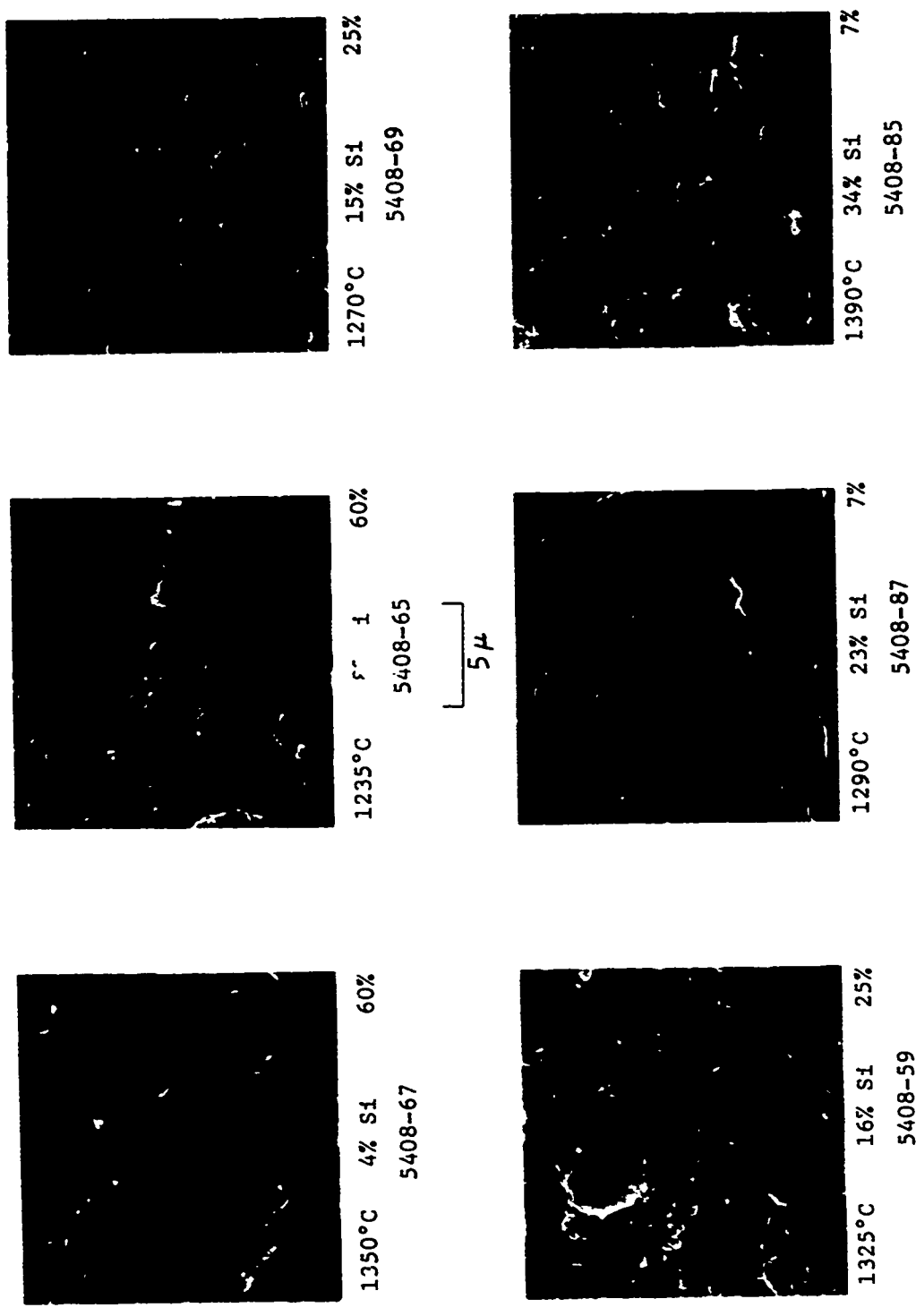


Fig. 25. Scanning electron micrographs of as-deposited surfaces of co-deposited silicon-carbon materials

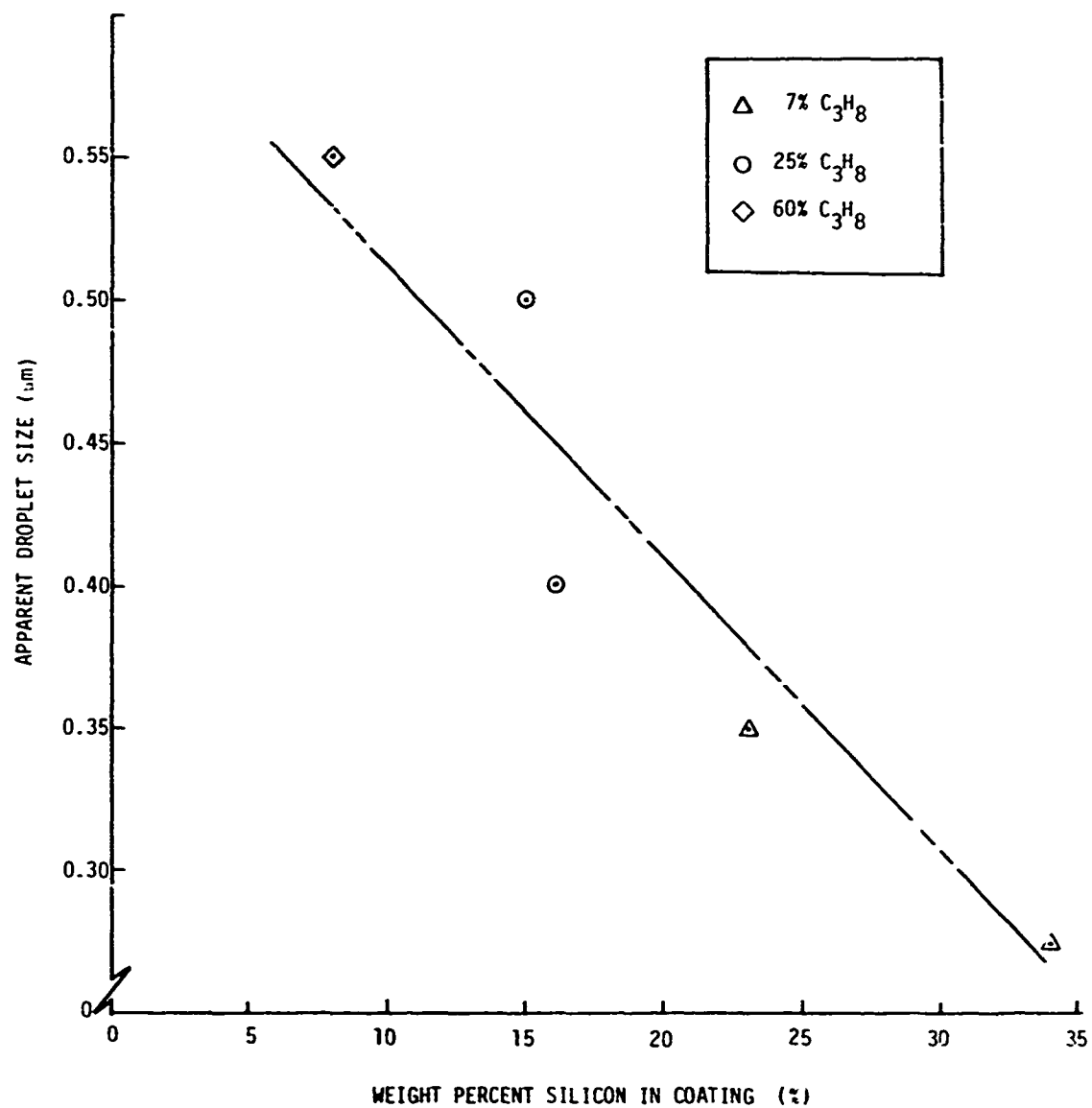


Fig. 26. Apparent droplet size versus weight percent silicon in coating for carbon-silicon materials co-deposited at 1200° to 1400°C from 7%, 25%, and 60% propane in helium with a  $\text{CH}_3\text{SiCl}_3$  additive

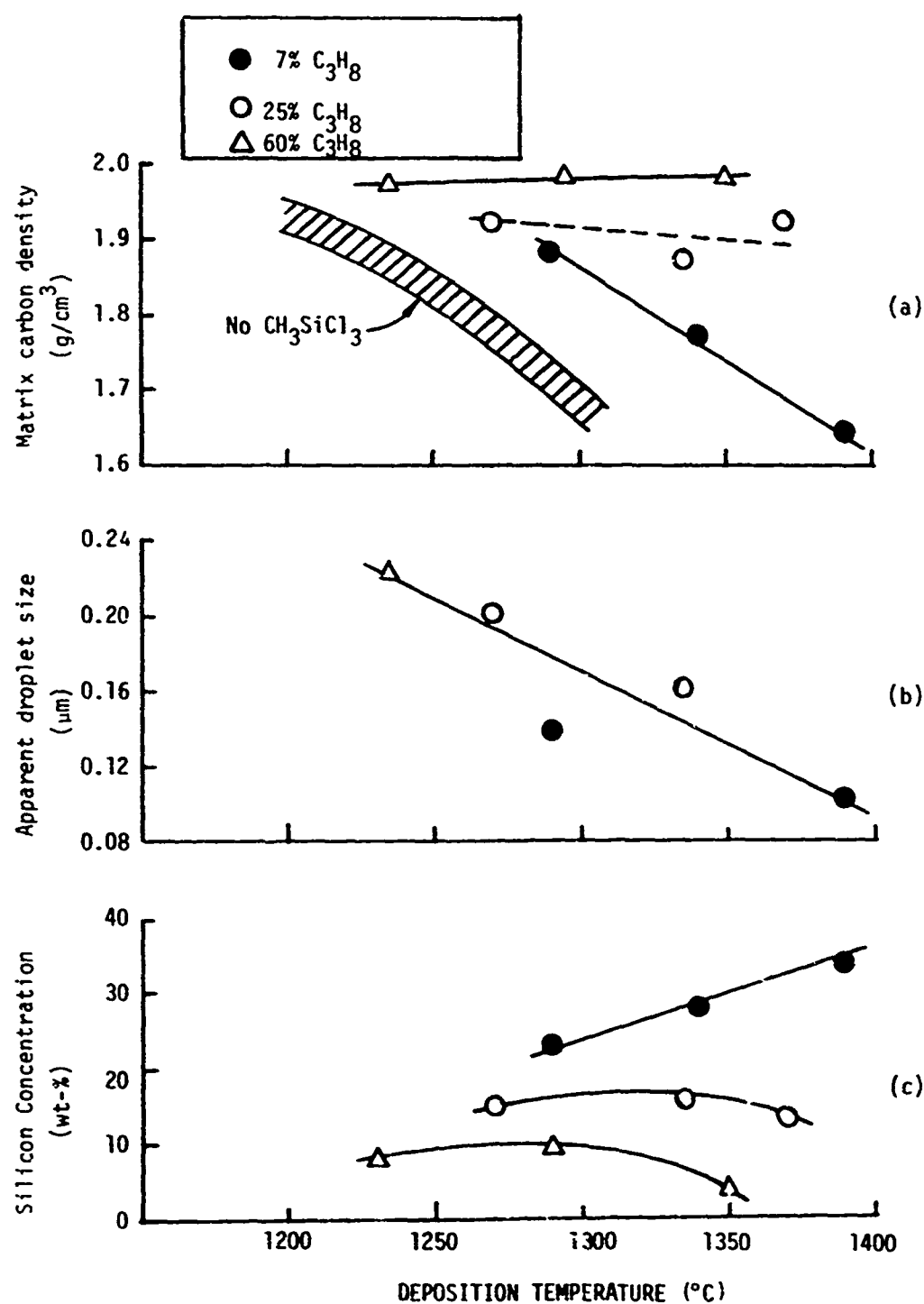


Fig. 27. Plots of matrix density (a), apparent droplet size (b), and silicon concentration (c) versus deposition temperature for materials co-deposited in the range 1200° to 1400°C from 7%, 25%, and 60% propane in helium with a  $\text{CH}_3\text{SiCl}_3$  additive

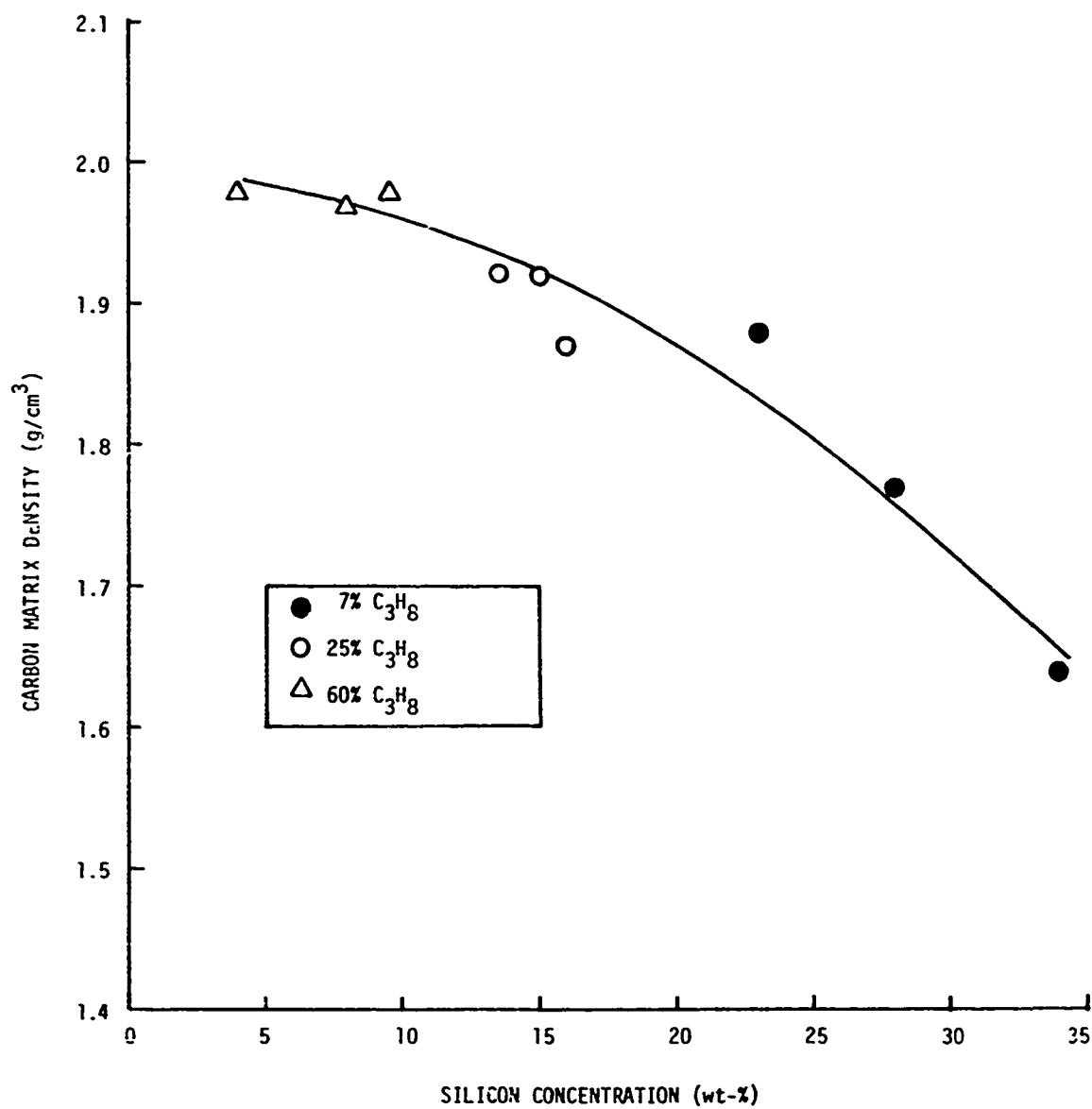


Fig. 28. Carbon matrix density versus silicon concentration for carbon-silicon materials deposited at temperatures in the range 1200° to 1400°C from 7%, 25%, and 60% propane with CH<sub>3</sub>SiCl<sub>3</sub> additive

obtain high silicon concentrations and high carbon matrix densities is to increase the amount of  $\text{CH}_3\text{SiCl}_3$  carried into the coater with high propane concentration, for example, by heating the  $\text{CH}_3\text{SiCl}_3$  bubbler. Another approach might use a more stable hydrocarbon like methane instead of propane.

The hardness of the carbon-silicon alloys correlates best with silicon concentrations (Fig. 29), but there appears to be a secondary dependence which causes carbons with the same silicon concentration to be harder if they are deposited at lower temperatures. This may prove to be a dependence on the  $L_c$  parameter (yet to be measured) which is likely to decrease with decreasing temperature in this range of temperatures.

### 3.5.3. Results for Co-Deposited Boron-Carbon Alloys

Fourteen exploratory depositions of boron-carbon alloys have been carried out. The first seven runs (5408-91 through 5408-105) had very sooty microstructures (see Figs. B-27 through B-33 in Appendix B). The amount of  $\text{BCl}_3$  added and the deposition temperature were both reduced, but the sooty microstructures persisted (see Figs. B-34 through B-36 in Appendix B) and the deposits cracked on cooling after coating. At this point the hydrocarbon was changed to methane and a crack-free deposit with a microstructure relatively free of soot inclusions was obtained (run 5408-137; see Fig. B-39 in Appendix B).

The deposition conditions and the parameters used to deposit the coatings are listed in Tables 7 and 8, respectively. Until a more promising field of structures is obtained, no detailed analysis of the data will be made. It is worth noting, however, that the  $L_c$  values listed in Table 8 are unusually high for this range of deposition temperatures. Unlike silicon, boron exhibits a considerable solubility in carbon (0.5 at.-% at  $1550^\circ\text{C}$ )<sup>(48)</sup> and is a potent catalyst for graphitization.<sup>(37,49-52)</sup> Work will continue using methane and low  $\text{BCl}_3$  injection rates.



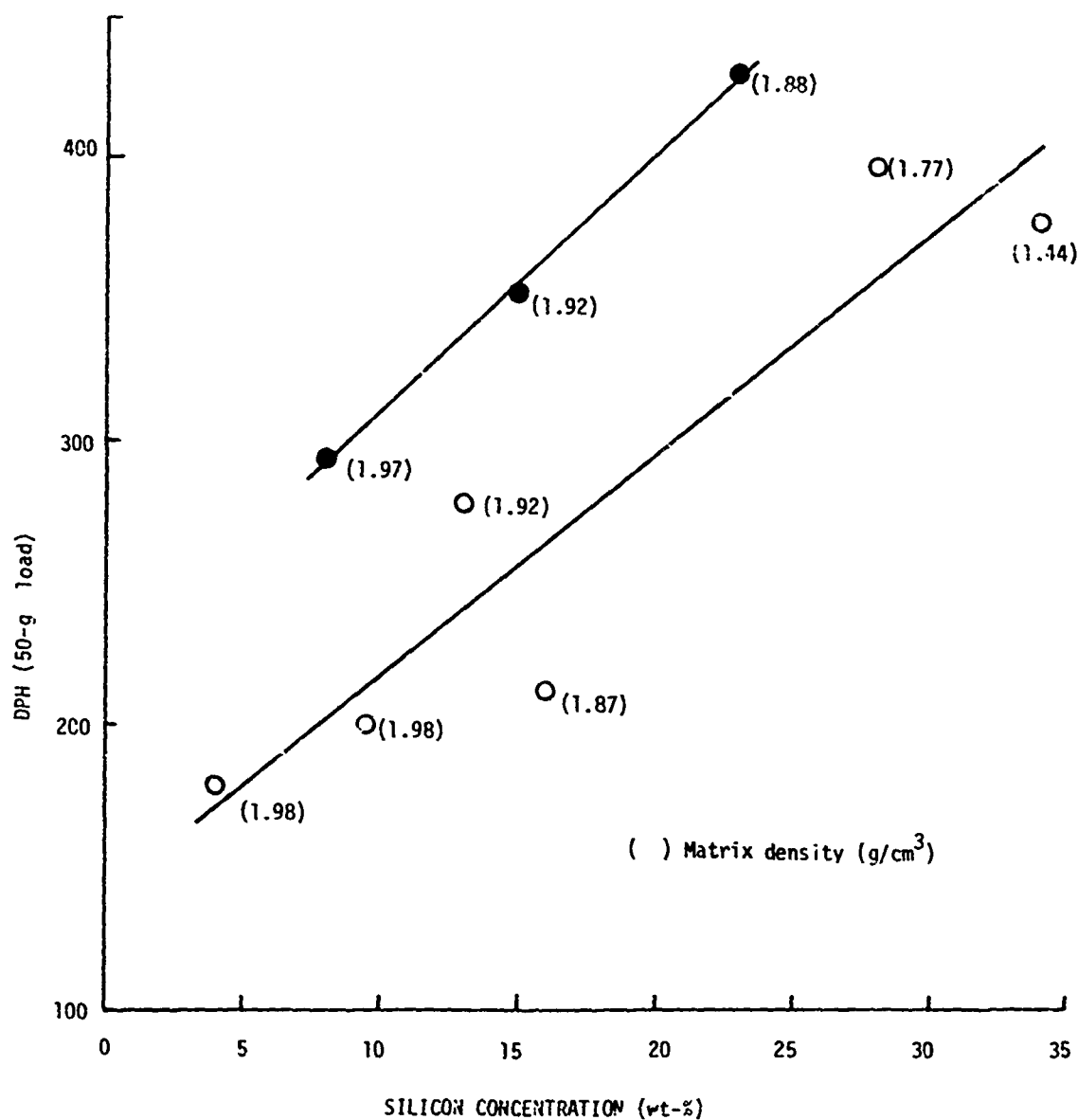


Fig. 29. Microhardness versus silicon concentration for carbons co-deposited with silicon in the range 1200° to 1400°C from propane in helium with added  $\text{CH}_3\text{SiCl}_3$ . The values in parentheses are the corresponding matrix carbon densities. Filled circles: bed temperatures = 1235° to 1290°C. Open circles: bed temperatures = 1295° to 1390°C.

TABLE 7  
DEPOSITION CONDITIONS FOR CO-DEPOSITED BORON-CARBON ALLOYS DEPOSITED IN STEADY-STATE  
FLUIDIZED BEDS USING PROPANE, METHANE, AND BORON TRICHLORIDE<sup>(a)</sup>

| Run Number | C <sub>3</sub> H <sub>8</sub> Conc. (%) | Control Temp (b) (°C) | BCl <sub>3</sub> Feed Rate (g/min) | BCl <sub>3</sub> Volumetric Flow Rate (R.T.) (cm <sup>3</sup> /min) | Carbon Deposition Efficiency (%) | Average Coating Rate (μm/min) | Coating Thickness (in.) |
|------------|---|-----------------------|------------------------------------|---|----------------------------------|-------------------------------|-------------------------|
| 5408-115   | 25                                      | 1150                  | 0.27                               | 56  | 13.6                             | 1.8                           | 0.013                   |
| 5408-113   | 25                                      | 1150                  | 0.30                               | 62  | 12.4                             | 1.9                           | 0.014                   |
| 5408-105   | 25                                      | 1200                  | 5.30                               | 1090  | 18.5                             | 2.8                           | 0.011                   |
| 5408-99    | 25                                      | 1200                  | 3.45                               | 710   | 48.0                             | 3.2                           | 0.015                   |
| 5408-111   | 25                                      | 1250                  | 0.33                               | 68  | 37.2                             | 3.0                           | 0.014                   |
| 5408-103   | 25                                      | 1250                  | 3.38                               | 695   | 60.7                             | 3.4                           | 0.016                   |
| 5408-93    | 25                                      | 1300                  | 3.75                               | 770   | 68.7                             | 5.5                           | 0.013                   |
| 5408-95    | 25                                      | 1350                  | 3.42                               | 703   | 70.5                             | 3.4                           | 0.008                   |
| 5408-109   | 25                                      | 1350                  | 0.28                               | 58  | 48.0                             | 5.1                           | 0.024                   |
| 5408-97    | 25                                      | 1400                  | 3.58                               | 735   | 74.4                             | 4.2                           | 0.010                   |
| 5408-91    | 60                                      | 1400                  | 2.50                               | 514   | 74.8                             | 23.0                          | 0.019                   |
| 5408-137   | 25 <sup>(c)</sup>                       | 1200                  | 0.30                               | 62  | 27.9                             | 0.85                          | 0.010                   |
| 5408-133   | 25 <sup>(c)</sup>                       | 1350                  | 0.35                               | 72  | 37.6                             | 1.7                           | 0.012                   |
| 5408-135   | 60 <sup>(c)</sup>                       | 1350                  | 0.30                               | 62  | 57.5                             | 2.1                           | 0.010                   |

(a) Total flow rate was 15 l/min at room temperature for all gases.

(b) Bed temperature measurements are in progress.

(c) CH<sub>4</sub> concentration (%).

TABLE 8  
STRUCTURAL DATA FOR CO-DEPOSITED BORON-CARBON ALLOYS DEPOSITED IN STEADY-STATE FLUIDIZED BEDS USING PROPANE, METHANE, AND METHYLTRICHLOROSILANE(a)

| Run Number   | C <sub>3</sub> H <sub>8</sub> Conc. (%) | Control Temp (°C) | Boron Content (wt-%) | Micro-hardness (DPH) | Bulk Coating Density (g/cm <sup>3</sup> ) | Apparent Crystallite Height (Å) |
|--------------|---|-------------------|----------------------|----------------------|---|---------------------------------|
| 5408-115     | 25                                      | 1150              | 0.71                 | ---                  | 1.990                                     | 31                              |
| 5408-113     | 25                                      | 1150              | 0.1                  | 217                  | 2.204                                     | 40-162                          |
| 5408-105     | 25                                      | 1200              | (c)                  | 216                  | 2.095                                     | 99                              |
| 5408-99      | 25                                      | 1200              | 5.5                  | 186                  | 2.128                                     | 111                             |
| 5408-111     | 25                                      | 1250              | 0.81                 | 223                  | 1.928                                     | 34                              |
| 5408-103     | 25                                      | 1250              | 4.3                  | 161                  | 2.053                                     | 83                              |
| 5408-93      | 25                                      | 1300              | 4.6                  | 150                  | 2.074                                     | 99                              |
| 5408-95      | 25                                      | 1350              | 4.5                  | 136                  | 2.114                                     | 107                             |
| 5408-109     | 25                                      | 1350              | 1.3                  | 170                  | 1.628                                     | 29                              |
| 5408-97      | 25                                      | 1400              | 3.6                  | 122                  | 2.060                                     | 83                              |
| 5408-91 (d)  | 60(e)                                   | 1400              | 1.8                  | 89                   | 1.964                                     | 71                              |
| 5408-137 (d) | 25(e)                                   | 1200              | 0.86                 | 214                  | 2.039                                     | 62                              |
| 5408-133 (d) | 25(e)                                   | 1350              | 2.3                  | 150                  | 1.843                                     | 49                              |
| 5408-135     | 60                                      | 1350              | 6.0                  | 215                  | 1.797                                     | 33                              |

(a) The Bacon anisotropy factor for all deposits was <1.1 unless otherwise indicated.

(b) Sink float.

(c) In progress.

(d) Slightly anisotropic.

(e) CH<sub>4</sub> concentration (%), >1.1 BAF noted.

#### 4. MECHANICAL PROPERTIES

##### 4.1. YOUNG'S MODULUS AND MODULUS OF RUPTURE (J. L. Kaae)

The mechanical properties of pyrolytic carbons are very structure sensitive and their control is important in developing useful load-bearing components. In this section, the variations observed thus far for propane-derived carbons will be reported.

##### 4.1.1. Experimental

Young's modulus and the modulus of rupture, or the fracture stress in bending, of the pure carbons have been measured in four-point bending. Previous measurements of these moduli for the fluidized-bed carbons have been carried out in three-point bending. (21,23,26,53) Four-point bending is generally preferred over three-point bending because the region of the specimen between the center knife edges is loaded with a constant bending moment and thus a constant outer fiber stress as opposed to a continuously varying bending moment along the length of the specimen in three-point bending, which applies the maximum stress to a very small, and probably not representative, volume of material. Until now it has not been possible to obtain sufficiently thick specimens with the fluidized-bed pyrolytic carbons to make the four-point loading configuration practical.

The four-point bending fixture used (see Fig. 30) has the capability of a wide range of inner and outer knife-edge spacings. The knife edges are razor blades, and the center knife edges are suspended on a thin reed to allow self-adjustment. To ensure alignment the knife-edge spacings and the final set-up were checked with a machinist's microscope. The outer knife-edge spacing used in the present tests was 0.2969 in. and the inner knife-edge spacing was 0.1484 in., both accurate to  $\pm 0.0001$  in.



Fig. 30. Four-point bending fixture constructed to test carbon specimens. A 0.040-in.-wide carbon strip is suspended across the outer knife edges.

In bending carbon specimens, the deflections are large and the specimens slide over the knife edges, so the small-deflection bending expressions which ignore frictional effects at the knife edges are no longer valid. A computer program valid for large-deflection expressions and including frictional effects is being used to analyze the data obtained in the tests. The expressions employed are similar to those of Schile and Sierakowski<sup>(53)</sup> except that frictional effects at the knife edges are included.

Specimens for testing were obtained by sectioning graphite discs which had been introduced into the bed of fluidized particles and coated with carbon. The graphite was ground away, and the remaining carbon discs were polished on an arbor to ensure that no taper was introduced. The final polishing compound was 0.25- $\mu$ m diamond powder. Strips 0.040 in. wide were then cut from the polished discs with a mechanically controlled diamond sectioning wheel. All specimens were examined for defects under a microscope. The specimens were free of chips and scratches. Before testing the width of each specimen was measured in the machinist's microscope to an accuracy of  $\pm 0.0001$  in., and after testing the thickness was measured at the position of fracture on an optical gage to an accuracy of  $\pm 0.00004$  in.

The testing fixture was mounted in a table model Instron testing machine, and the specimens were deflected to fracture at a cross-head speed of 0.02 in. per minute while the load and the deflection were simultaneously recorded. At least twelve specimens were tested from each coating run.

#### 4.1.2. Results

The Young's modulus and the modulus of rupture of the pure carbons are shown as a function of the density in Figs. 31 and 32 along with the values measured in three-point bending on thin specimens with similar X-ray crystallite sizes deposited in non-steady-state beds.<sup>(53)</sup> Two observations are noteworthy:

1. The Young's moduli of the present carbons agree with those of the previous carbons.

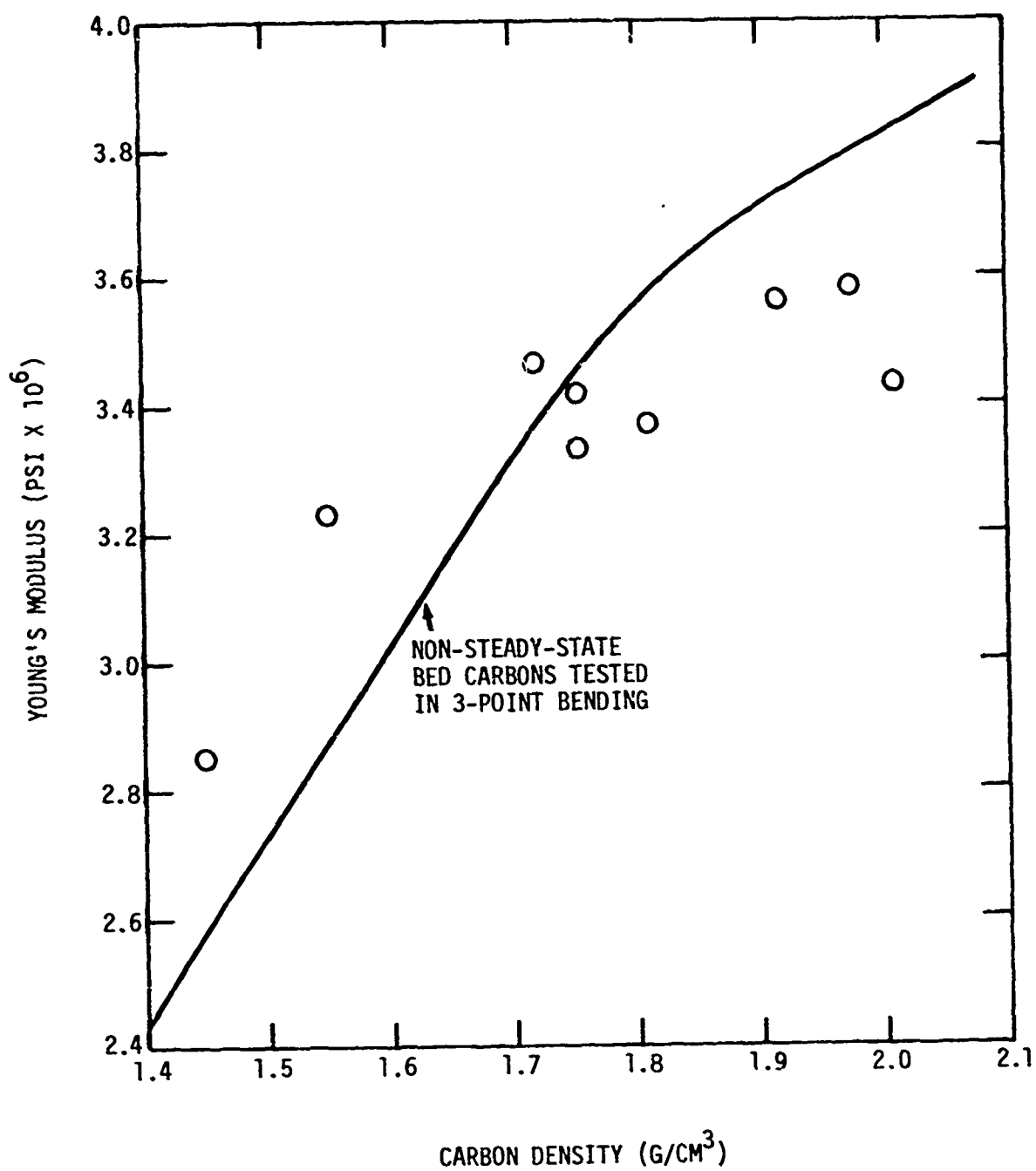


Fig. 31. Young's modulus of pure carbons as a function of carbon density

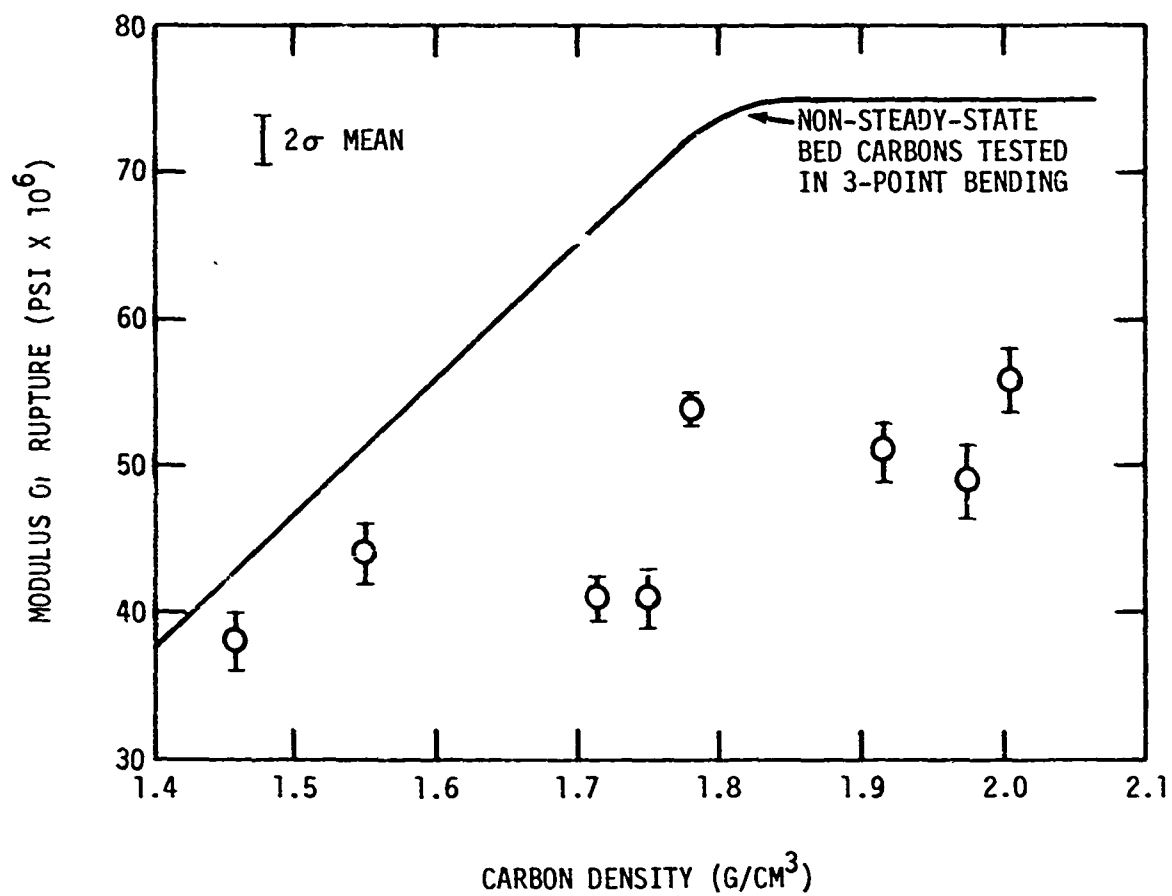


Fig. 32. Modulus of rupture of pure carbons as a function of carbon density



2. The moduli of rupture of the present carbons fall below those of the previous carbons.

The first observation was expected and shows that the elastic response of the steady-state bed carbons is similar to that of the non-steady-state carbons.

The magnitude in the decrease in the moduli of rupture was unexpected and requires further investigation. It was expected that the modulus of rupture might decrease a small amount as a result of changing from three-point to four-point bending but not nearly to the extent that occurred. In order to determine if the decrease is due solely to the different methods of testing, one coating run will be tested in three-point bending with the usual thickness and also after grinding down to a thickness comparable to that of the non-steady-state bed carbons. The results will be compared with the four-point bending results.

Another possible source of the decrease in the modulus of rupture is a structural difference between the steady-state bed carbons and the non-steady-state bed carbons. One difference which is present and could account for the decrease in strength is soot inclusions. These inclusions, which were apparent on the polished surface of the present test specimens and were not present in the non-steady-state bed carbons, could have acted as flaws which would be expected to cause a reduction in strength. The effect of the soot inclusions on the strength will be investigated by measuring the properties of steady-state bed carbons produced under conditions which eliminate the soot inclusions.

The mechanical properties of a carbon deposited with chlorine as an additive to the coating atmosphere and a carbon deposited with hydrogen as an additive to the coating atmosphere were also measured. The properties of these carbons are shown in Table 9 along with the deposition conditions and the carbon structures. The additives apparently did not change the mechanical properties of the deposits, since when these properties are compared with the mechanical properties of carbons of similar densities (shown in Figs. 2 and 3), they fall within the scatter of the data.

TABLE 9  
DEPOSITION CONDITIONS AND STRUCTURE AND MECHANICAL  
PROPERTIES OF CARBONS DEPOSITED WITH CHLORINE  
AND HYDROGEN ADDITIVES TO THE ATMOSPHERE

| Bed<br>Temp<br>(°C) | C <sub>3</sub> H <sub>8</sub><br>Conc.<br>(%) | Additive<br>and<br>Conc.<br>(%) | Density<br>(g/cm <sup>3</sup> ) | Young's<br>Modulus<br>(psi x 10 <sup>6</sup> ) | Modulus of<br>Rupture<br>(psi x 10 <sup>3</sup> ) |
|---------------------|---|---------------------------------|---------------------------------|--|---|
| ~1240               | 25  | Cl <sub>2</sub> , 2             | 1.78                            | 3.55   | 45.5  |
| 1140                | 60  | H <sub>2</sub> , 40             | 1.81                            | 3.37   | 41.9  |

The fracture surfaces of a number of these carbons were examined by scanning electron microscopy. These fracture surfaces, photographs of which are shown in Fig. 33 and in Fig. C-4 of Appendix C, were not greatly different from those of the carbons deposited in non-steady-state beds. Structural differences which might have accounted for the lower strengths of the present carbons are not obvious in the photographs.

#### 4.2. FATIGUE (F. J. Schoen)

The fatigue properties of carbon are important in assessing the performance of carbon load-bearing devices. Very little work has been devoted to the study of fatigue of carbonaceous bodies, and none has been reported for pyrolytic carbon. The fatigue data that are available will be presented and discussed in this section.

##### 4.2.1. Methods

The fatigue behavior of pyrolytic carbon is being tested in a cantilever beam configuration on small strip specimens having the same geometry as those being used for static mechanical property measurements. The testing device, pictured in Fig. 34, consists of a Delrin specimen holder and knife edge with driving cams and motor. There are two vertical and one horizontal degrees of freedom in aligning the specimen to the knife edge. All specimens, prepared as described in Section 4.1, were tested at a frequency of approximately 1800 cpm, measured exactly through the use of a stroboscopic light calibrated to  $\pm 1\%$ . Specimen orientation was such that the substrate side was always in tension. Deflections are measured to  $\pm 0.0002$  with a Gaertner cathetometer. A gage length of 0.223 in. was used for all the tests (except two, for which 0.212 in. was used). Time, and hence number of cycles to failure, was determined by a clock which was shut off by a relay when specimen breakage occurred. During normal operation the relay was kept closed by a small current running through the specimen.

Gage length was measured by the following method. The static Young's tensile modulus, fracture strength, and strain to fracture were determined



(a)  
 $\rho = 1.91 \text{ g/cm}^3$ ,  $T = 1790^\circ\text{C}$ ,  
 60%  $\text{C}_3\text{H}_8$



(b)  
 $\rho = 1.75 \text{ g/cm}^3$ ,  $T = 1300^\circ\text{C}$ ,  
 60%  $\text{C}_3\text{H}_8$



(c)  
 $\rho = 1.55 \text{ g/cm}^3$ ,  $T = 1330^\circ\text{C}$ ,  
 7%  $\text{C}_3\text{H}_8$

Fig. 33. Scanning electron micrographs typical of fracture surfaces of carbons studied



(a)



(b)

Fig. 34. Fatigue tester with specimen indicating stressed configuration:  
(a) overall view, (b) close-up of specimen

for a particular coating run using a miniature three-point test rig whose knife-edge spacings may be quite accurately determined.<sup>(23)</sup> This testing was performed in a table model Instron mechanical testing machine. The same coating run was then tested in the cantilever beam device in the Instron machine, and the modulus obtained here was matched to that previously obtained by three-point bending by treating the gage length as an independent variable. The exact gage length was chosen as that at which the moduli were identical. All calibrations were performed with the aid of a computer program which calculated the mechanical properties from input data from the Instron machine and specimen geometry. This program has corrections for large deflections and friction at the knife edges. At least 10 specimens were used in each statistical determination of mechanical properties.

An additional computer program (with the above corrections) was devised to calculate the specimen stress (maximum fiber stress) from input consisting of specimen geometry, modulus, and deflection. In Fig. 35, the specimen stress for coating run 5408-5 is shown as a function of deflection and specimen thickness for a gage length of 0.223 in.

#### 4.2.2. Results and Discussion

Fatigue behavior results to date for coating run 5408-5 are given in Fig. 36. While the data are not sufficient at this point for drawing statistical conclusions, a number of inferences may be made. At stresses near the fracture stress, some specimens are exceeding  $10^5$  cycles prior to breaking. Some specimens are not fracturing at these stress levels, even after  $10^7$  cycles. It thus appears that the endurance limit (stress below which the material can endure an infinite number of cycles without failure) is quite close to, if not as high as, the single cycle fracture stress. This is in contrast to the fatigue behavior of a high-density graphite, for which the endurance limit has been determined to correspond to a homologous stress of about 47%.<sup>(54)</sup>

The high endurance limit near the fracture stress is consistent with the observed immobility of dislocations in pyrolytic carbons<sup>(55,56)</sup> and also

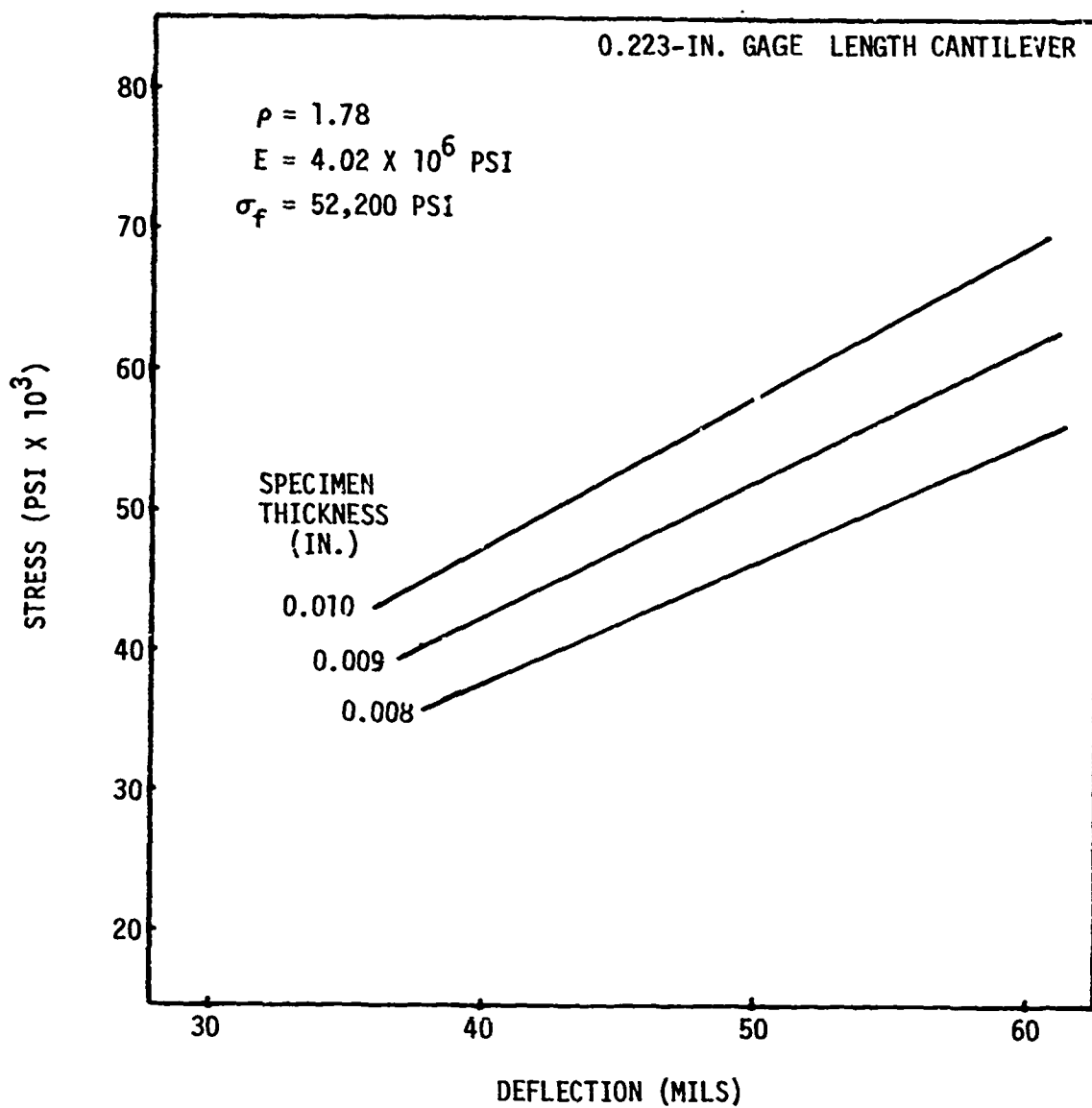


Fig. 35. Calculated stress-deflection curves for cantilever beam bending of run 5408-5

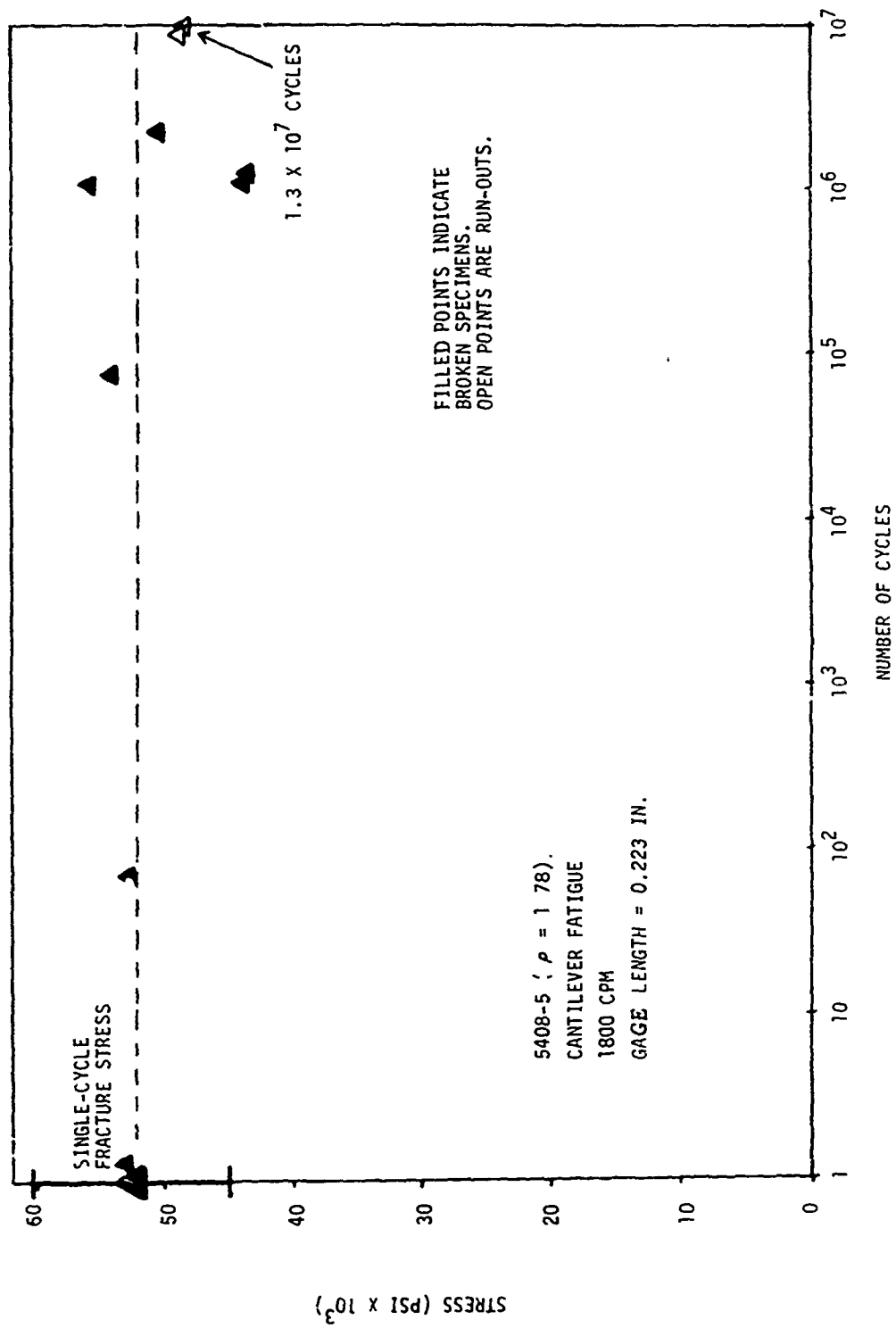


Fig. 36. Fatigue behavior of pure LTI carbon (5408-5) in cantilever beam bending



with a fracture mechanism described by a Griffith failure criterion, whose application to pyrolytic carbons is described in Refs. 26 and 27. It is possible that the specimens fracturing after many cycles initially have flaws which are subcritical and which propagate in a stable manner until the critical size is reached and catastrophic propagation occurs. The existence of run-outs at high stress levels indicates that critical flaws are not formed in certain specimens. The statistical nature of fatigue behavior is evident, and leads to a large amount of scatter around the endurance limit.

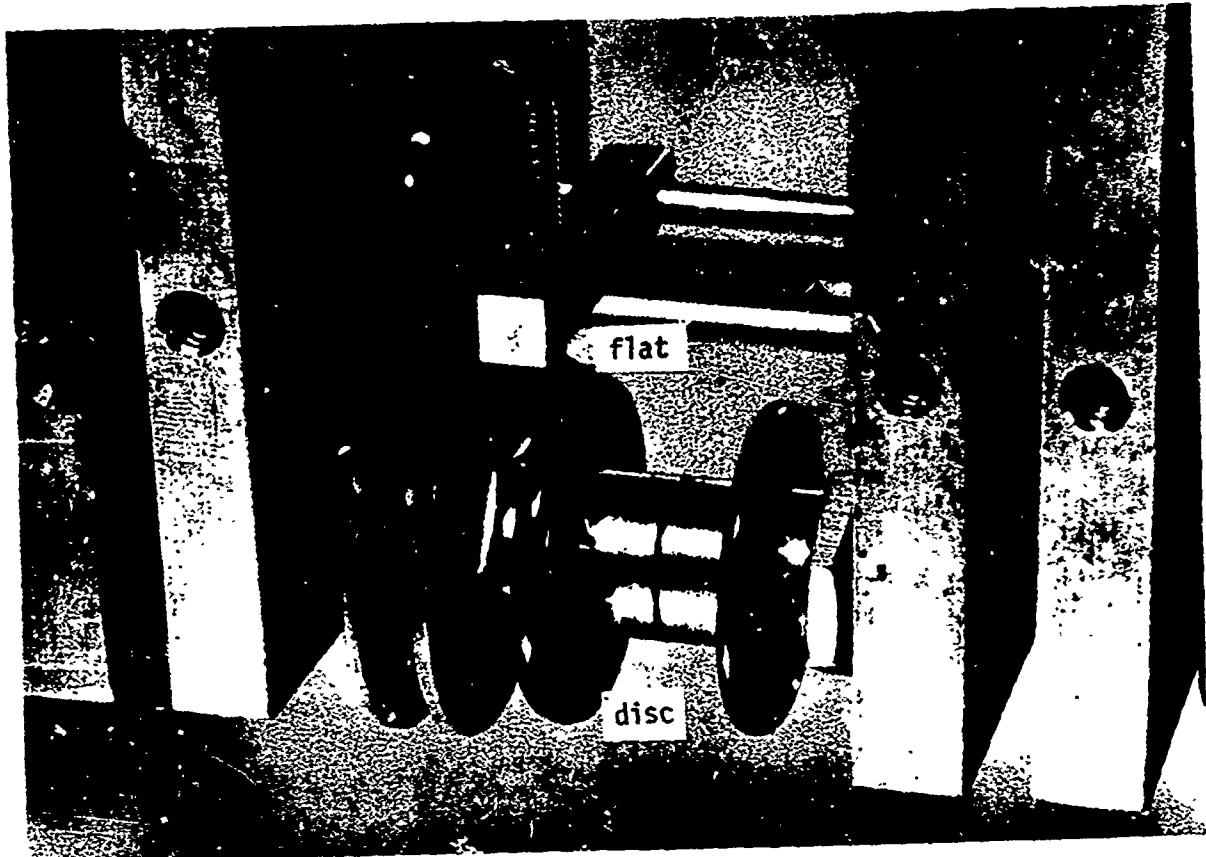
Additional tests on this (5408-5) and other coating runs are in progress as well as microscopic investigations of the morphology of cyclic stress damage.

#### 4.3. WEAR (F. J. Schoen)

Although the applications of carbons on bearing are extensive, there has been little work reported describing wear properties of pyrolytic carbons and no studies relating friction and wear to structure have been carried out. In this section, the results from initial studies are reported.

##### 4.3.1. Methods

A device was constructed for the rapid comparative evaluation of pyrolytic carbon containing wear couples. As shown in Fig. 37, operation of the device involves a small (approximately 1/8-in. by 1/8-in.) polished square of test material (flat) bearing against a rotating disc of known material characteristics. Initially, pure LTI pyrolytic carbons were used as the discs and both pure and silicon-doped carbons as the flat, as well as one specimen of a Co-Cr-Mo alloy, Stellite 21. The disc is polished with a double radius (see Fig. 37) while on its shaft, so that no wobble of any sort occurs. Both the shaft holding the paddle with the flat and that holding the disc are supported by low-friction bearings. The bearings holding the paddle shafts are sapphire vee-jewels mounted in screws which are advanced slightly to allow the same specimen to be used for obtaining numerous data points.



ME92683

Fig. 37. Close-up view of one cell of wear testing machine

After a number of wear marks for a particular couple were produced for various times, the flat was removed and photographed along with a microscopic scale. A typical set of wear marks obtained in this way is shown in Fig. 38. Measurements were made as the length of the major axis of the mark. At small depths of penetration, the surface of wear may be approximated by an ellipsoid, and thus the projection of the wear surface on the surface of the flat is an ellipse. The volume of wear (V) may then be given as a function of the length of the major axis (c):

$$V = 2\pi \left( R - \frac{1}{2} \sqrt{4R^2 - c^2} \right)^2 \sqrt{rR} ,$$

where R and r are the large and small radii of the rotating disc, respectively.

In all the tests to be described, the radii of the discs were 0.750 and 0.378 in., the fluid medium was distilled water, and the speed of revolution was 60 rpm. Both discs and flats were polished through 1/2- $\mu$ m diamond grit. All loads were  $2.2 \pm 0.1$  g except in the series determining the effect of load, where 12.4 and 22.9 g were also used.

#### 4.3.2. Results

Raw data are taken as the length of the wear mark as a function of time for the various material couples (see Fig. C-1 in Appendix C). The data are then reduced to volume of wear as a function of sliding distance. The effect of material combination on the wear of pure LTI pyrolytic carbons is illustrated by Fig. 39, which shows that the wear rates are constant with time and thus independent of contact area. Characteristics of both adhesive and abrasive wear are present, and it is not yet possible to mechanistically separate the two. Wear is seen to increase with increasing density of the disc and to decrease with increasing density of the flat. Data for silicon-doped LTI carbons are similarly plotted in Fig. 40.

These data are summarized in Fig. 41, where the volume wear rates (slopes of Figs. 39 and 40) are plotted as a function of the density of the disc bearing on the specimen flat. Included in this figure are the diamond pyramid

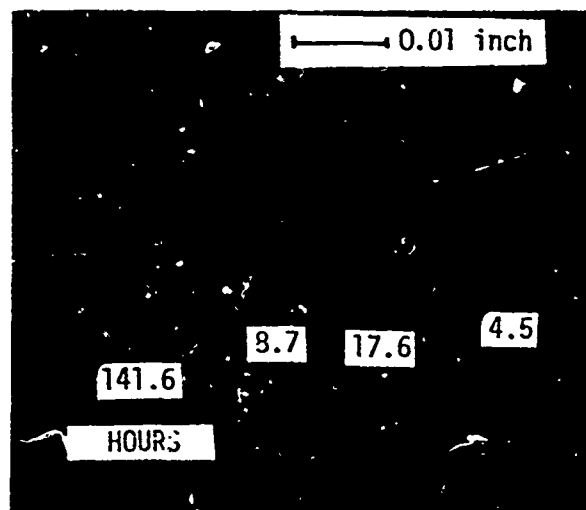


Fig. 38. Typical set of wear marks (specimen 5408-17)

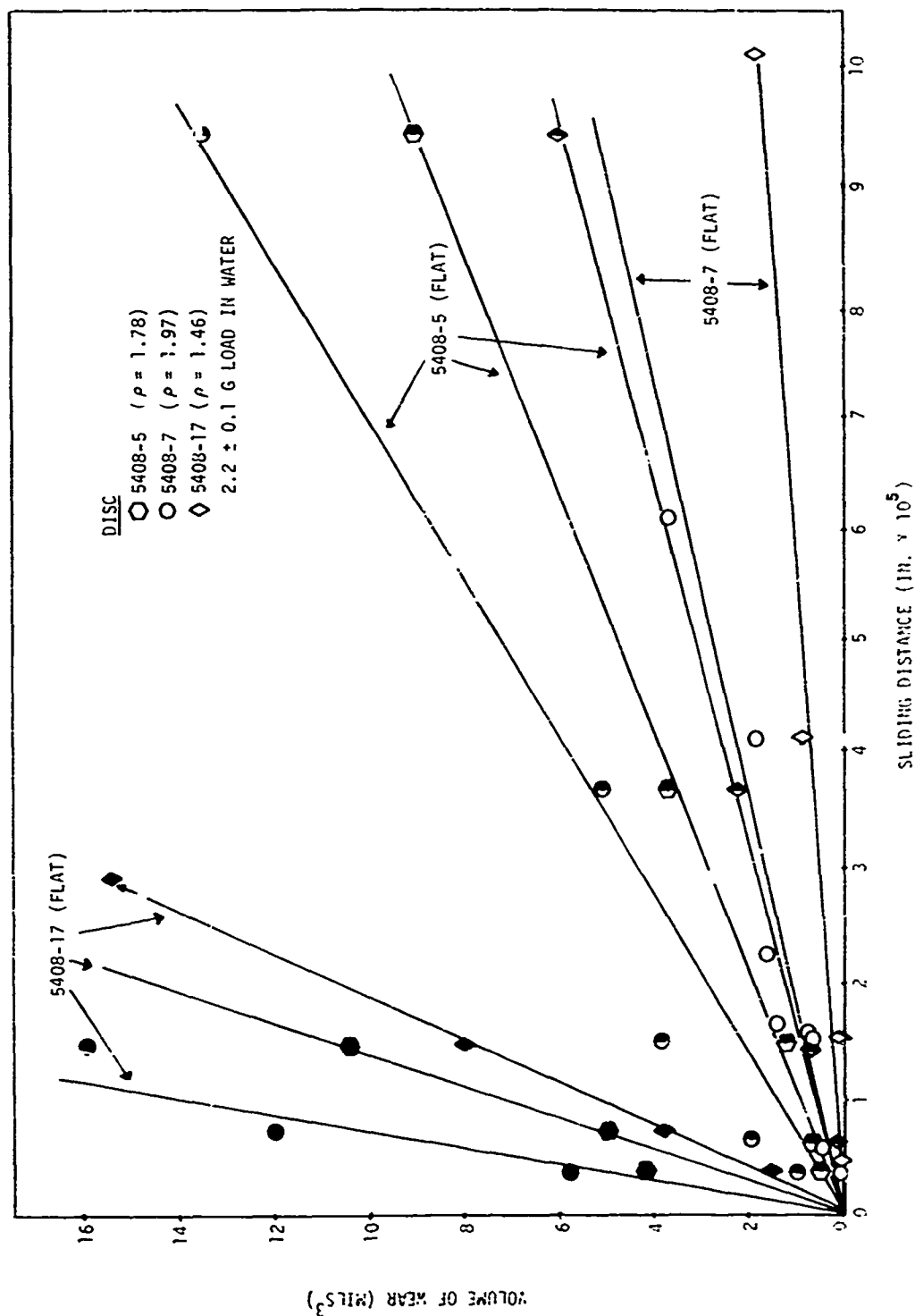


Fig. 39. Volume of wear measured on flat as a function of sliding distance for pure LTI carbon discs bearing on pure LTI carbon flats. Densities of carbons in g/cm<sup>3</sup> are given in parentheses. DPH values are as follows: 5408-7, 219; 5408-5, 210; and 5408-17, 153. Flat 5408-7, open points; 5408-5, half-filled points; 5408-17, filled points.

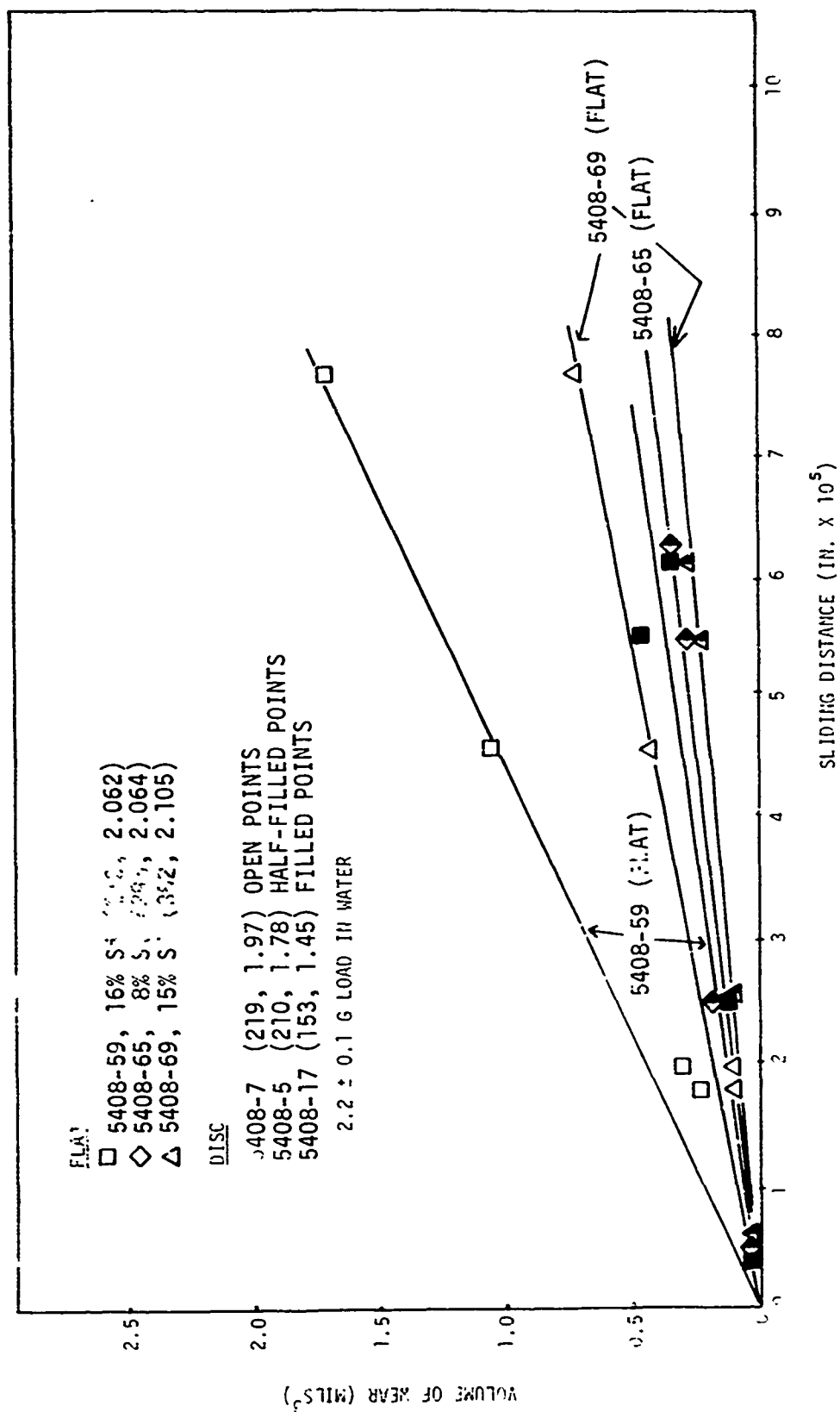


Fig. 40. Volume of wear measured on flat as a function of sliding distance for silicon-alloyed LTI carbon flats bearing on pure LTI carbon discs. DPH values and densities in g/cm<sup>3</sup> are given in parentheses.

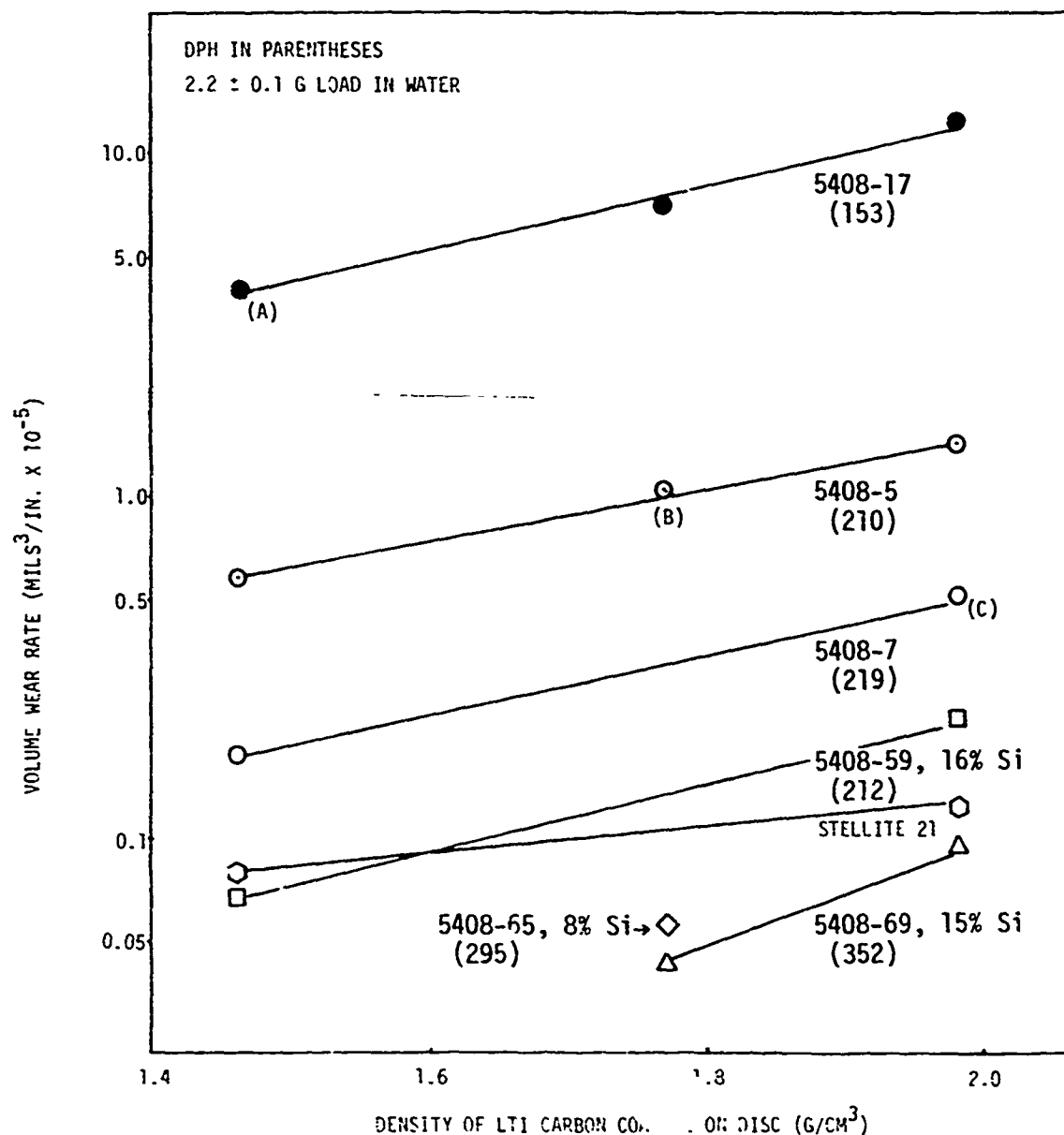


Fig. 41. Volume wear rate as measured from wear on flat versus density of pure LTI carbon disc for various flat materials. Points (A), (B), and (C) represent situations where flat and disc are of identical material.

hardness values for the various carbons. There is a definite correlation between minimal wear and high hardness. Also included in Fig. 41 are the data for Stellite 21, a Co-Cr-Mo alloy (see Fig. C-2 of Appendix C). It appears that a suitable correlation may possibly be made between wear resistance and fracture strength. The applicability of such a correlation awaits further data.

An interesting observation may be made from Fig. 41 when points (A), (B), and (C) are compared. These are the data obtained when both the disc and flat are of identical material. It is seen that the wear resistance increases as the density of both the disc and flat increases. Thus, the material of the flat appears to be a more controlling factor than that of the disc. The implications of this observation are under consideration.

It was desired to determine the effect of load on the volume wear rate for a particular wear couple. From the slopes of the wear/sliding distance curves for these combinations (see Fig. C-1 of Appendix C), the wear rates were obtained and then plotted against load on a log-log scale as shown in Fig. 42. The slope of this curve is 0.33, in contrast to a slope of 1.00 for metals.<sup>(57)</sup> The implications of this fact with respect to mechanism of wear are presently under consideration.

Most theories of abrasive and adhesive wear lead to equations of the form<sup>(57-61)</sup>

$$V \propto \frac{KLd}{T} ,$$

where V is the wear volume, K is a constant, L is the load, d is the sliding distance, and T is the hardness,<sup>(59)</sup> tensile yield strength,<sup>(58,60)</sup> or other mechanical property.<sup>(58,60,61)</sup> In Archard's model,<sup>(57)</sup> K is a probability of wear fragment formation referred to as the adhesive wear coefficient, a widely accepted parameter which correlates with most conventional wear measurement data. The model predicts wear to be independent of nominal area of contact, and K is a dimensionless coefficient varying for different wear



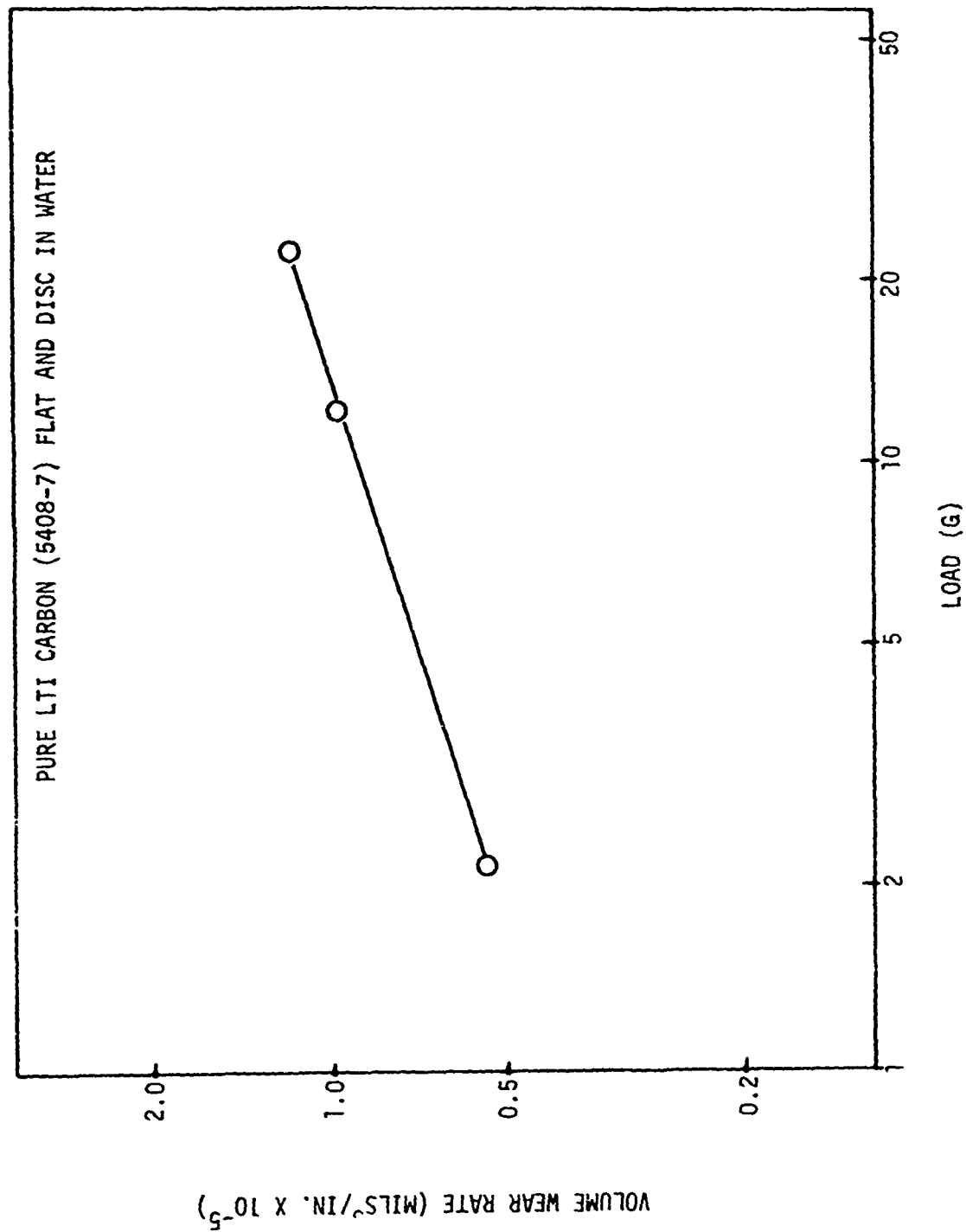


Fig. 42. Effect of bearing load on volume wear rate as measured from wear on flat for pure LTI carbon wear couple (flat 5408-7, disc 5408-7)

systems from  $10^{-1}$  to  $10^{-8}$ , the first representing excessive wear and the latter minimal wear. For LTI carbons, K appears to be around  $10^{-7}$ , indicating that on the basis of this model, carbon/carbon makes an excellent wear couple.

## 5. PHYSICAL PROPERTIES

(R. J. Price and K. Koyama)

### 5.1. THERMAL EXPANSIVITY

The thermal expansivity of pyrolytic carbon is an important property in determining the thermal stresses developed in pyrolytic-carbon-coated bodies both during service and on cooling from the coating temperature. In addition, the relationships between thermal expansivity and structural parameters are interesting from a fundamental point of view, because they provide information on the way thermal strains in individual crystallites are transmitted to the bulk.

During the present reporting period, thermal expansion measurements parallel to the deposition plane were made on a series of undoped isotropic pyrolytic carbons deposited from propane at temperatures between 1200° and 1400°C. Samples were prepared by stripping carbon coatings from graphite discs levitated in the steady-state fluidized bed coater in the same manner as described in Section 3.1 of this report. Three rectangular strips of carbon, measuring 0.7 in. x 0.05 in. x ~0.01 in., were placed in longitudinal slots cut at 120° intervals around a cylinder of Poco graphite and held in position by a Poco graphite sleeve. This assembly was placed in a conventional silica dilatometer with the ends of the three carbon strips bearing on silica buttons that transmit the expansion to the pushrods. This arrangement provides stability and prevents the thin carbon strips from buckling under the pushrod load. Thermal expansion measurements were made between room temperature and 1000°C.

Deposition conditions, structural parameters, and the mean coefficient of thermal expansion (between 22° and 1000°C) are listed in Table 10 for the carbons tested so far. When complete, this group of tests will include a series of carbons deposited from 60% propane at bed temperatures ranging from

TABLE 10  
DEPOSITION CONDITIONS, STRUCTURAL PARAMETERS, AND THERMAL EXPANSIVITY OF PYROLYTIC CARBONS

| Run Number | CTE Run Number | Deposition Conditions |               |                                 | Structural Parameters        |   | CTE (22°-1000°C) |
|------------|----------------|-----------------------|---------------|---------------------------------|------------------------------|---|------------------|
|            |                | Propane Conc. (%)     | Bed Temp (°C) | Average Coating Rate (mils/min) | Density (g/cm <sup>3</sup> ) | Apparent Crystallite Height, L <sub>c</sub> (Å) |                  |
| 5408-7     | J 0476         | 60                    | 1180          | 0.234                           | 1.974                        | 36  | 5.95             |
| 5408-11    | J 0477         | 7                     | 1330          | 0.058                           | 1.553                        | 23  | 4.40             |
| 5408-23    | J 0478         | 7                     | 1280          | 0.054                           | 1.717                        | 25  | 4.56             |
| 5408-25    | J 0479         | 60                    | 1300          | 0.317                           | 1.753                        | 29  | 5.36             |
| 5408-27    | J 0480         | 25                    | 1340          | 0.225                           | 1.59?                        | 24  | 4.68             |
| 5408-31    | J 0481         | 60                    | 1230          | 0.267                           | 1.823                        | 33  | 5.62             |
| 5408-33    | J 0482         | 60                    | 1355          | 0.384                           | 1.535                        | 26  | 4.50             |
| 5408-35    | J 0483         | 60                    | 1400          | 0.333                           | 1.459                        | 26  | 4.08             |

1140° to 1400°C, a series deposited from 7% propane at temperatures between 1280° and 1400°C, and a series deposited at 1330° to 1350°C with propane concentrations ranging from 3% to 60%.

A typical thermal expansivity curve is shown in Fig. 43. (All the curves are shown in Appendix C.) The plot shows a slight upward curvature between room temperature and approximately 300°C. This behavior is typical of carbonaceous materials and reflects the change in the crystallite a-axis expansivity over this temperature range. The mean coefficient of thermal expansion (CTE) between 22° and 1000°C is plotted as a function of carbon density in Fig. 44. There is a clear correlation between the two properties, with the coefficient of thermal expansion increasing from about  $4 \times 10^{-6} \text{ }^{\circ}\text{C}^{-1}$  for carbon with a density around  $1.4 \text{ g/cm}^3$  to about  $6 \times 10^{-6} \text{ }^{\circ}\text{C}^{-1}$  for carbon with a density of  $2.0 \text{ g/cm}^3$ .

These figures compare well with values of  $\sim 3.5 \times 10^{-6} \text{ }^{\circ}\text{C}^{-1}$  for a density of  $1.2 \text{ g/cm}^3$  and  $6 \times 10^{-6} \text{ }^{\circ}\text{C}^{-1}$  for a density of  $2.0 \text{ g/cm}^3$  reported by Auriol, *et al.*,<sup>(62)</sup> for two isotropic fluidized-bed carbons deposited from acetylene at 1200°C. Previous work<sup>(18)</sup> on isotropic pyrolytic carbons deposited from methane at 1650° to 1800°C (HTI carbons) showed slightly lower expansivities ( $3.5 \times 10^{-6} \text{ }^{\circ}\text{C}^{-1}$  for a density of  $1.55 \text{ g/cm}^3$  and  $5.4 \times 10^{-6} \text{ }^{\circ}\text{C}^{-1}$  for a density of  $1.87 \text{ g/cm}^3$ ), but this apparent difference may not be significant in view of the lower accuracy of the earlier work.

At 400°C, the coefficient of thermal expansion in the a-direction of a graphite crystal ( $\alpha_a$ ) is zero. The coefficient of thermal expansion of isotropic polycrystalline carbon or graphite at 400°C [ $\alpha_{P(400)}$ ] is therefore given by<sup>(16,63)</sup>

$$\alpha_{P(400)} = \frac{1}{3} \alpha_{C(400)} \gamma \quad , \quad (3)$$

where  $\alpha_{C(400)}$  is the single-crystal c-axis expansivity at 400°C, and  $\gamma$  is an "accommodation coefficient" representing the extent to which the crystallite expansion is absorbed by internal cracks, porosity, or intercrystalline restraints. Recent work by Pellegrini<sup>(64)</sup> has shown that for fluidized-bed

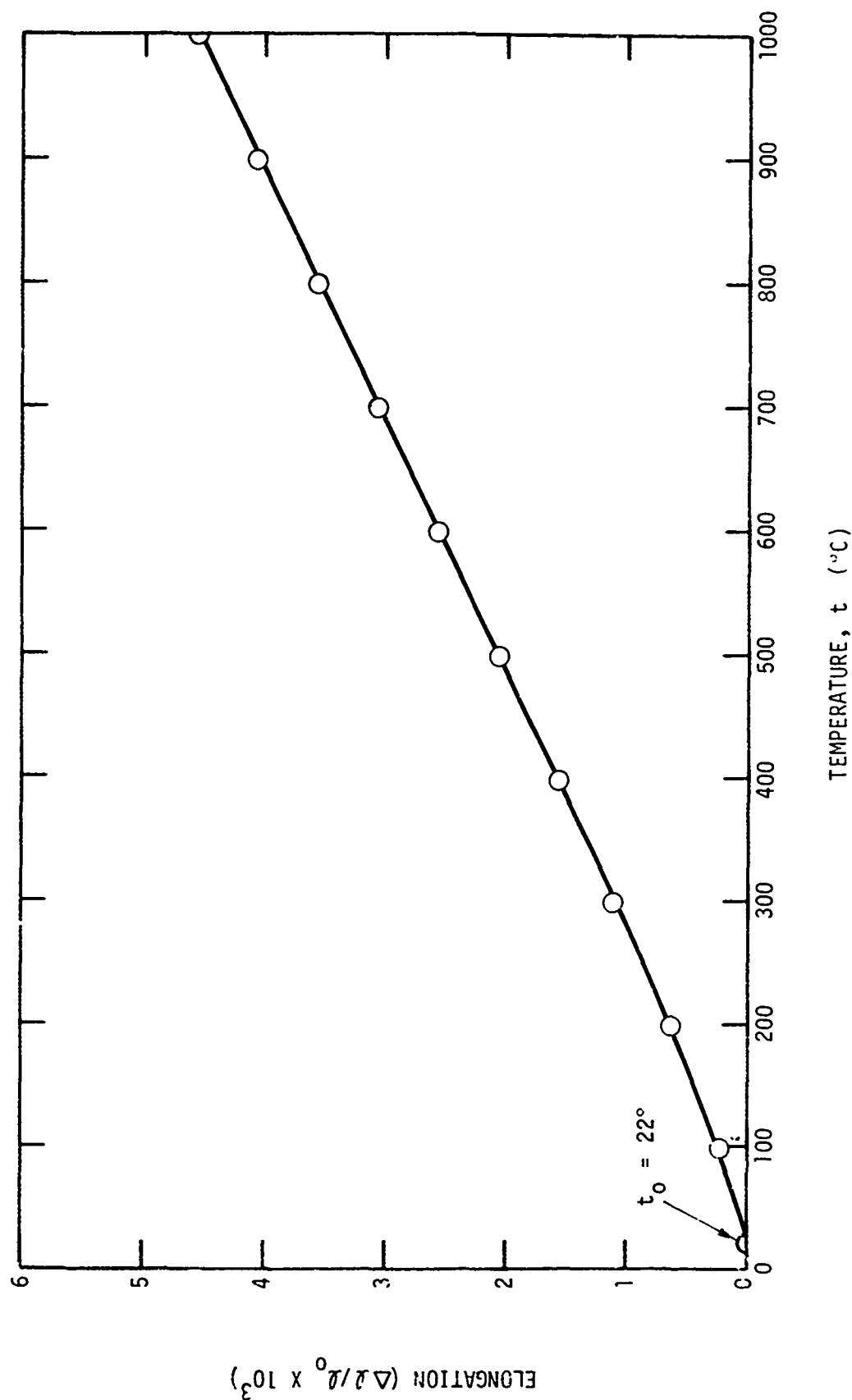


Fig. 43. Typical thermal expansion curve for isotropic pyrolytic carbon (5408-27) measured parallel to deposition plane. Carbon density = 1.592 g/cm<sup>3</sup>;  $L_c = 24 \text{ \AA}$ .

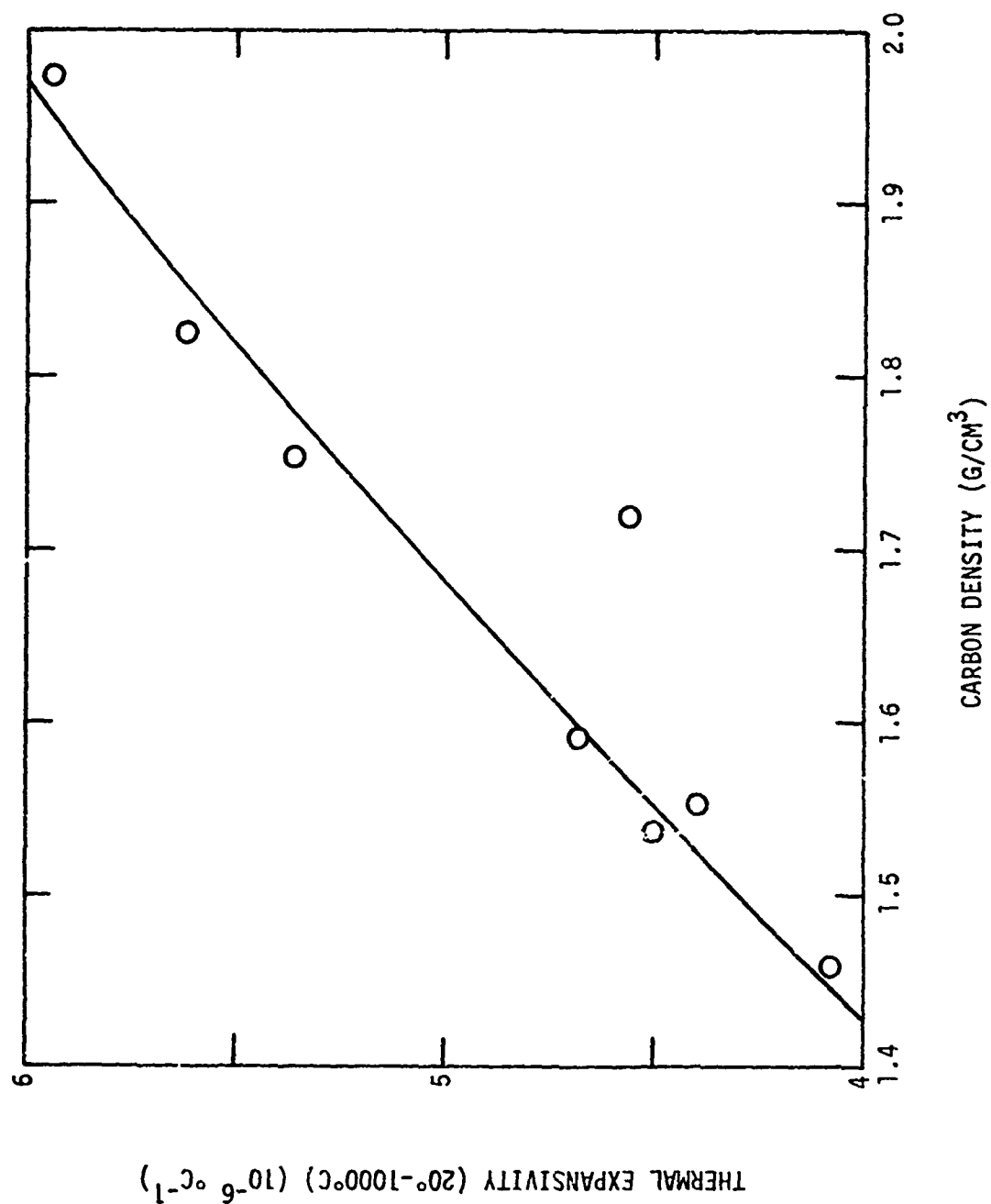


Fig. 44. Mean thermal expansivity (22° to 1000°C) parallel to the deposition plane of isotropic pyrolytic carbons deposited from propane at 1200° to 1400°C as a function of carbon density

pyrolytic carbons, the lattice c-axis coefficient of thermal expansion,  $\alpha_c$ , increases with increasing apparent crystallite height,  $L_c$ , from  $17.7 \times 10^{-6} \text{ }^\circ\text{C}^{-1}$  for carbons with  $L_c = 20 \text{ \AA}$  to  $22.8 \times 10^{-6} \text{ }^\circ\text{C}^{-1}$  for carbons with  $L_c = 150 \text{ \AA}$ . (The value for near-perfect crystalline graphite is  $28 \times 10^{-6} \text{ }^\circ\text{C}^{-1}$ .) Using Pellegrini's results to estimate  $\alpha_c$ , Eq. (3) yields values for  $\gamma$  ranging from 0.68 for the lowest-density carbon ( $\rho = 1.46 \text{ g/cm}^3$ ) to 0.97 for the highest-density carbon ( $\rho = 1.97 \text{ g/cm}^3$ ). For polycrystalline graphites,  $\gamma$  ranges from about 0.3 for needle-coke graphites to about 0.8 for the fine-grained Poco-type graphites. Thus, the results indicate that the high-density carbons in the present series have thermal expansivities approaching the theoretical maximum. In the lower-density carbons, some of the crystallite is evidently absorbed by the pores.

## 5.2. THERMAL CONDUCTIVITY

A knowledge of the thermal conductivity of pyrolytic carbons is important for those applications (such as nuclear fuel particle coatings) where a significant heat flux passes through the carbon. The shape of the thermal conductivity versus temperature curve additionally gives information about the crystal defects present in the carbon.

Measurements of the thermal conductivity perpendicular to the deposition plane are being made on the same series of pyrolytic carbons as used for thermal expansivity measurements. The heat-pulse method<sup>(65)</sup> was used to measure the thermal diffusivity of rectangular pieces of carbon measuring about 0.75 in. x 0.5 in. x 0.01 in. In this method a pulse of radiant energy from a xenon flash tube is flashed onto the front face of the sample while the temperature of the rear face is monitored with a thermocouple. The time for the rear face temperature to reach 0.5 of its terminal value is related to the thermal diffusivity of the material, the sample thickness, and the pulse shape and length.<sup>(66)</sup> The measured thermal diffusivity was converted to the thermal conductivity by multiplying by the measured sample density and the literature value for the heat capacity of pyrolytic carbon. Measurements were taken at 100°C intervals between room temperature and 800°C.



The results on the carbons tested so far are given in Table 11. The full curves showing the dependence of thermal conductivity on measurement temperature are given in Appendix D. A typical example is shown in Fig. 45. All the curves show a downward slope between room temperature and approximately 500°C.

For a given temperature, the absolute value of the thermal conductivity increases with density. This dependence is illustrated in Fig. 46. The conductivity of a given carbon is approximately proportional to the sample density, suggesting that all the carbons have about the same inherent conductivity but the effective cross-sectional area is reduced in proportion to the porosity. The conductivity values (0.014 to 0.020 cal/cm-sec-°C at room temperature) average approximately 30% lower than those for isotropic pyrolytic carbons of similar density deposited from methane at 1650° to 2000°C (HTI pyrolytic carbons.)<sup>(34)</sup>

A downward slope to the temperature dependence curve normally results from a significant contribution from phonon-phonon interactions to the total thermal resistivity. Since this requires a relatively large spacing between phonon-scattering crystallite boundaries, this type of behavior is very unexpected in poorly crystalline carbons. Confirmatory work on the present carbons is therefore needed before the data are further analyzed.

TABLE 11  
DEPOSITION CONDITIONS, STRUCTURAL PARAMETERS, AND THERMAL CONDUCTIVITY OF PYROLYTIC CARBONS

| Run Number | Thermal Diffus. Run Number | Deposition Conditions |               |                                 | Structural Parameters        |  | Thermal Conductivity (cal/cm-sec-°C) |        |        |        |        |
|------------|----------------------------|-----------------------|---------------|---------------------------------|------------------------------|--|--------------------------------------|--------|--------|--------|--------|
|            |                            | Propane Conc. (%)     | Bed Temp (°C) | Average Coating Rate (mils/min) | Density (g/cm <sup>3</sup> ) | Apparent Crystallite Height, $l_c$ (Å) |                                      |        |        |        |        |
|            |                            |                       |               |                                 |                              |  | 22°C                                 | 200°C  | 400°C  | 600°C  | 800°C  |
| 5408-7     | K 0001                     | 60                    | 1180          | 0.234                           | 1.974                        | 36                                     | 0.020                                | 0.0158 | 0.0140 | 0.0142 | 0.0144 |
| 5408-25    | K 0002                     | 60                    | 1300          | 0.317                           | 1.753                        | 29                                     | 0.0170                               | 0.0135 | 0.0113 | 0.0106 | 0.0110 |
| 5408-27    | K 0003                     | 25                    | 1340          | 0.225                           | 1.592                        | 24                                     | 0.0150                               | 0.0130 | 0.0110 | 0.0105 | 0.0103 |
| 5408-31    | K 0004                     | 60                    | 1230          | 0.267                           | 1.823                        | 33                                     | 0.0170                               | 0.0145 | 0.0120 | 0.0117 | 0.0115 |
| 5408-33    | K 0005                     | 60                    | 1355          | 0.384                           | 1.535                        | 26                                     | 0.0142                               | 0.0113 | 0.0105 | 0.0098 | 0.0095 |

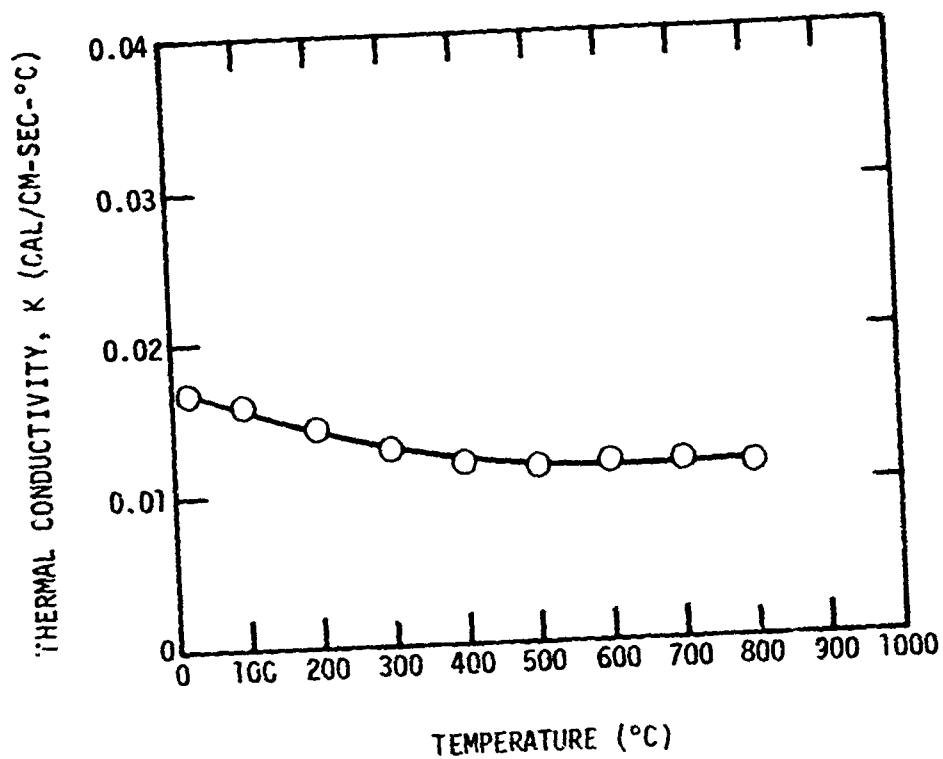


Fig. 45. Typical curve of thermal conductivity versus temperature for isotropic pyrolytic carbon (5408-31) measured perpendicular to deposition plane. Carbon density =  $1.823 \text{ g/cm}^3$ ;  $L_c = 33 \text{ \AA}$ .

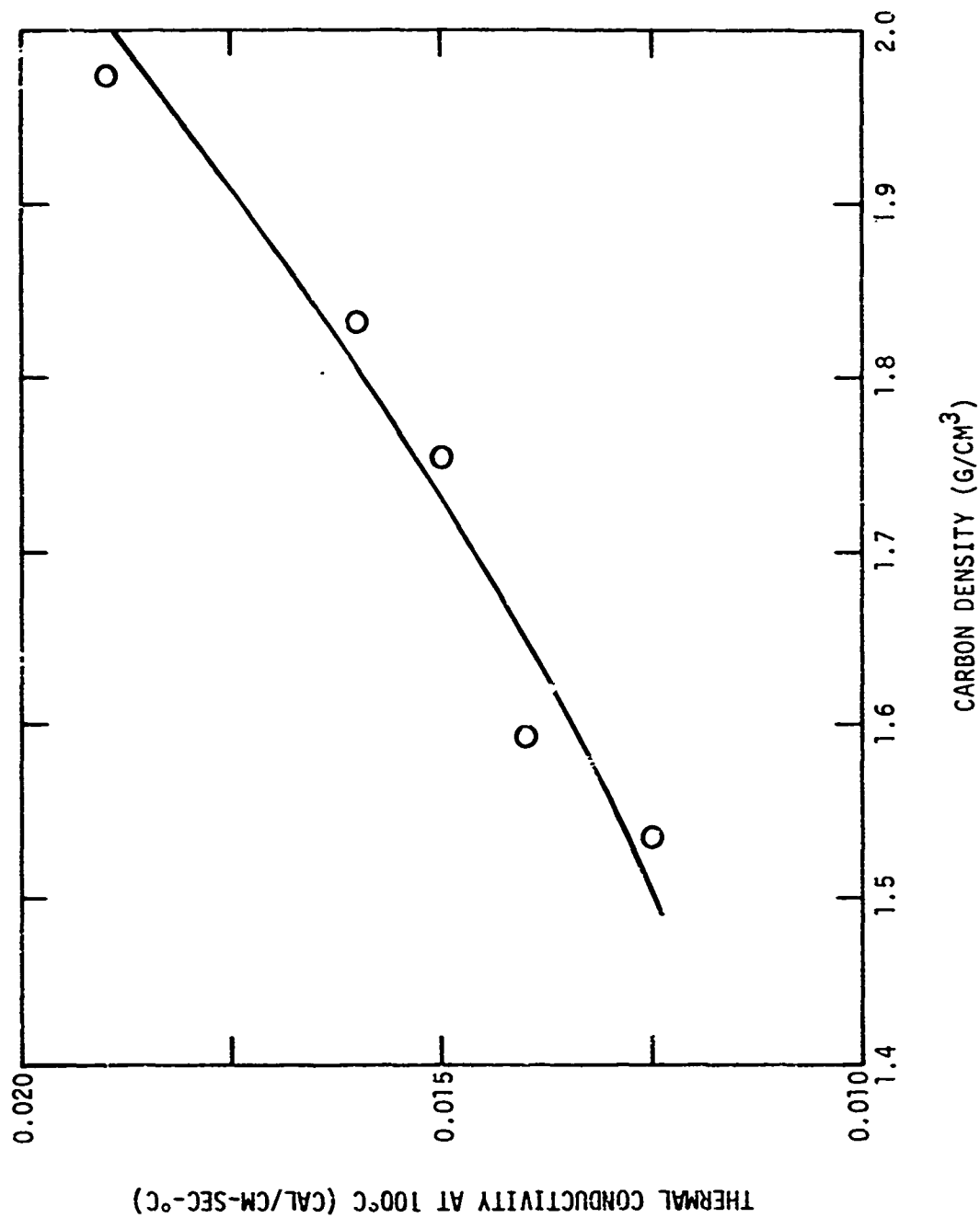


Fig. 46. Thermal conductivity at 100°C of isotropic pyrolytic carbons as a function of carbon density

## REFERENCES

1. Dayton, R. W., J. H. Oxley, and C. W. Townley, in Ceramic-Matrix Fuels Containing Coated Particles. Proceedings of a Symposium Held at Battelle Memorial Institute, November 5 and 6, 1962," USAEC Report TID-7654, Division of Reactor Development, pp. 10-68.
2. Goeddel, W. V., ibid., pp. 142-219.
3. Auriol, A., et al., ibid., pp. 462-481.
4. Lepie, M. P., ibid., pp. 319-333.
5. Huddle, R.A.U., J. R. Gough, and H. Beutler, ibid., pp. 349-374.
6. Nucl. Sci. Eng. 20, 153 (1964) entire issue.
7. Dayton, R. W., J. H. Oxley, and C. W. Townley, J. Nucl. Mater. 11, 1 (1964).
8. Sayers, J. B., et al., in Carbides in Nuclear Energy. Proceedings of a Symposium held at Harwell, November 1963, L. E. Russell, et al., eds., Vol. 2, MacMillan and Company, Ltd., London, 1964, pp. 919-962.
9. Carley-Macaulay, K. W., J. W. Myles, and G. H. Williams, ibid., pp. 826-848.
10. Oxley, J. H., in Vapor Deposition, Carroll F. Powell, J. H. Oxley, and J. M. Blocher, Jr., eds., John Wiley & Sons, Inc., New York, 1966, pp. 434-511.
11. Bokros, J. C., Nature 202, 1004 (1964).
12. Bokros, J. C., R. J. Price, and T. A. Trozera, Nature 204, 371 (1964).
13. Beatty, R. L., F. L. Carlsen, Jr., and J. L. Cook, Nucl. Appl. 1, 560 (1965).
14. Bokros, J. C., Carbon 3, 17 (1965).
15. Bokros, J. C., Carbon 3, 201 (1965).
16. Price, R. J., and J. C. Bokros, J. Appl. Phys. 36, 1897 (1965).
17. Price, R. J., Phil. Mag. 12, 561 (1965).
18. Price, R. J., J. C. Bokros, and K. Koyama, Carbon 5, 423 (1967).
19. Bokros, J. C., and A. S. Schwartz, Carbon 5, 90 (1967).
20. Bokros, J. C., Carbon 3, 167 (1965).

21. Price, R. J., et al., Carbon 4, 263 (1966).
22. Beutler, H., R. L. Beatty, and J. H. Coobs, Electrochem. Technol. 5, 191 (1967).
23. Bokros, J. C., and R. J. Price, Carbon 3, 503 (1966).
24. Bokros, J. C., R. J. Price, and K. Koyama, Carbon 4, 293 (1966).
25. Lonsdale, H. K., and J. N. Graves, J. Appl. Phys. 38, 3620 (1967).
26. Kaae, J. L., J. Nucl. Mater. 38, 42 (1971).
27. Kaae, J. L., Carbon 9, 291 (1971).
28. Kaae, J. L., "Effect of Annealing on the Microstructures and the Mechanical Properties of Poorly Crystalline Isotropic Pyrolytic Carbon," Gulf General Atomic Report Gulf-GA-A10968, October 18, 1971 (to be published in Carbon).
29. Kaae, J. L., T. D. Gulden, and S. Liang, "Transmission Electron Microscopy of the Pyrolytic Carbons Deposited in a Bed of Fluidized Particles," Gulf General Atomic Report Gulf-GA-A10931 (to be published in Carbon).
30. Kaae, J. L., "The Mechanical Properties of Glassy and Isotropic Pyrolytic Carbons," Gulf General Atomic Report GA-10307, September 11, 1970 (to be published in J. Biomed. Mater. Res.).
31. Bokros, J. C., in Chemistry and Physics of Carbons, P. L. Walker, ed., vol. 5, Marcel Dekker, New York, 1969, Chapter 1.
32. Bokros, J. C., and K. Koyama, J. Appl. Phys. 11, 2146 (1970).
33. Bokros, J. C., and R. J. Akins, in Proceedings of the 4th Buhl International Conference on Materials, Pittsburgh, Pennsylvania, November 16-18, 1971, Carnegie Press, Carnegie-Mellon University, Pittsburgh, Pennsylvania, 1971, p. 243.
34. Price, R. J., K. Koyama, and J. C. Bokros, "Thermal Conductivity of Neutron-Irradiated Pyrocarbons," paper presented at 10th Biennial Conference on Carbon, Lehigh University, Bethlehem, Pennsylvania, June 27 - July 2, 1971 (to be published in Carbon).
35. Bacon, G. E., J. Appl. Chem. 6, 477 (1956).
36. Higgs, P. H., et al., USAF Report WADD-TR-61-72, Vol. XXXVII, National Carbon Company, May 1964.
37. Kotlenski, W. V., Carbon 5, 409 (1967).

38. Schwartz, A. S., and J. C. Bokros, Carbon 5, 325 (1967).
39. Kaae, J. L., and T. D. Gulden, "The Structure and Mechanical Properties of Co-deposited Pyrolytic Carbon-Silicon Carbide Alloys," Gulf General Atomic Report GA-10452, February 26, 1971 (to be published in J. Am. Ceram. Soc.).
40. Klug, H. P., and L. E. Alexander, X-ray Diffraction Procedures for Polycrystalline and Amorphous Materials, John Wiley & Sons, Inc., New York, 1954.
41. Short, M. A., and P. L. Walker, Jr., Carbon 1, 3 (1963).
42. Kegley, T. M., and B. C. Leslie, Nucleonics 21, 62 (1963).
43. Bard, R. J., et al., Carbon 6, 603 (1968).
44. Beatty, R. L., USAEC Report ORNL-TM-1649, Oak Ridge National Laboratory, January 1967.
45. Thomas, A., Combust. Flame 6, 46 (1962).
46. Bokros, J. C., D. W. Stevens, and R. J. Akins, Carbon 9, 439 (1971).
47. Kaae, J. L., J. C. Bokros, and D. W. Stevens, "Dimensional Changes and Creep of Poorly Crystalline Isotropic Carbons and Carbon-Silicon Alloys During Irradiation," Gulf General Atomic Report Gulf-GA-A10882, November 1971 (to be published in Carbon).
48. Lowell, C. E., J. Am. Ceram. Soc. 50, 142 (1967).
49. Gasparoux, H., A. Pacault, and E. Poquet, Carbon 3, 65 (1965).
50. Tombrel, F., Rev. Hautes Temp. Refractories 3, 79 (1966).
51. Delhaes, P., and A. Marchand, Carbon 3, 115, 125 (1965).
52. Albert, P., and J. Parisat, in Proc. 3rd Carbon Conf., Pergamon Press, New York, 1959, p. 476.
53. Schile, R. D., and R. L. Sierakowski, Int. J. Non-Linear Mech. 2, 61 (1967).
54. Leichter, H. L., and E. Robinson, J. Am. Ceram. Soc. 53, 197 (1970).
55. Tsuzuku, T., Carbon 1, 25 (1963).
56. Tsuzuku, T., Carbon 1, 51i (1964).
57. Archard, J. F., J. Appl. Phys. 24, 981 (1953).
58. Finkin, E. F., in Symposium on Evaluation of Wear Testing, American Society for Testing and Materials, Philadelphia, 1969, p. 55 (ASTM-STP-446).

59. Pritchard, C., Wear 17, 185 (1971).
60. de Laat, F. G. A., Tribophysics Inc., Northridge, California, private communication.
61. Oberle, T. L., J. Metals 3, 438 (1951).
62. Auriol, A., et al., Carbon 4, 509 (1966).
63. Sutton, A. L., and V. C. Howard, J. Nucl. Mater. 7, 58 (1962).
64. Pellegrini, G., M. Moulaert, and I. Zubani, paper presented at the 10th Biennial Conference on Carbon, Bethlehem, Pa., June 1971.
65. Parker, W. J., et al., J. Appl. Phys. 32, 1679 (1961).
66. Larson, K. B., and K. Koyama, J. Appl. Phys. 38, 465 (1967).



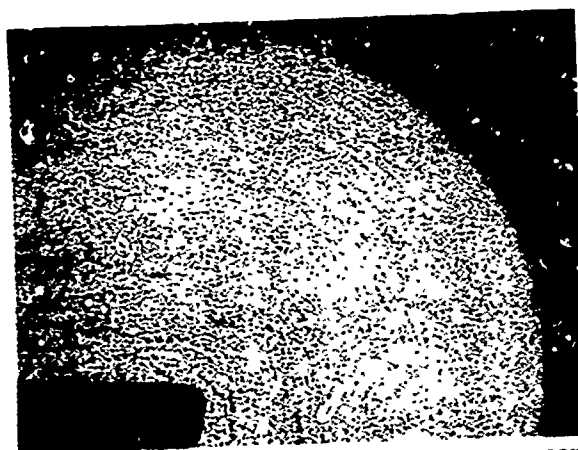
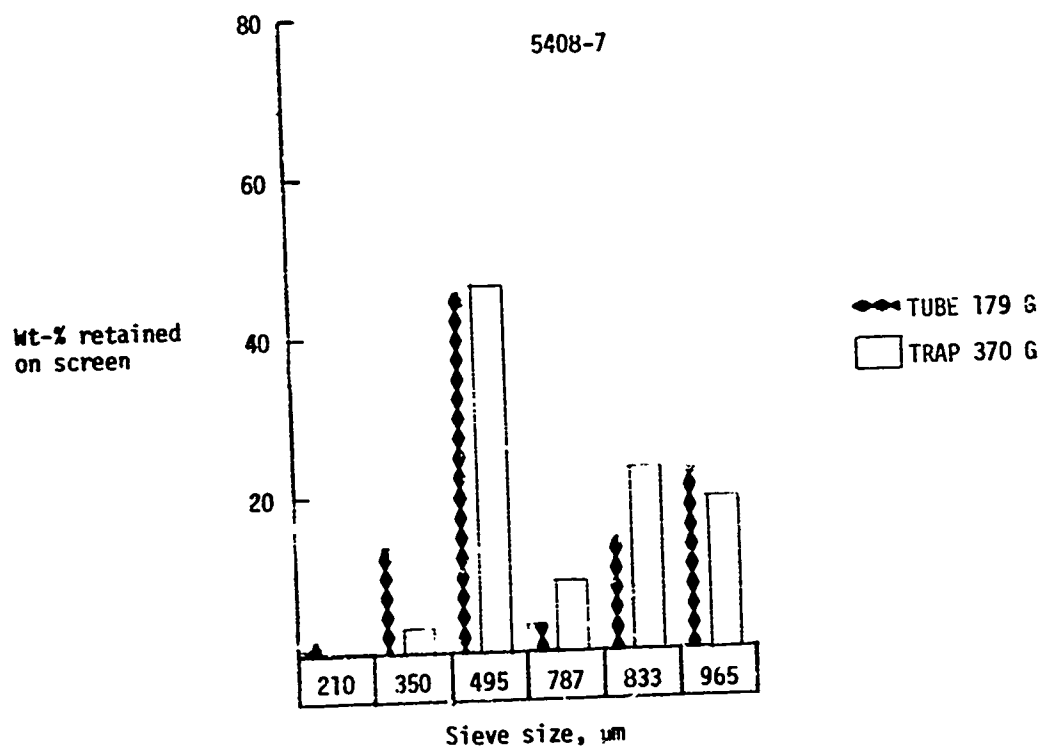
APPENDIX A  
WORK STATEMENT

The work statement for the current contract year is:

- "a. The Contractor shall use its best efforts to investigate the control of the structure of carbonaceous materials in the basic deposition process in fluid beds. Catalysts will be used to manipulate the deposition process and additional materials will be co-deposited with the carbon to expand the number of structures attainable. The structure of the deposited carbon will be related to the deposition conditions and variations in properties will be interpreted in terms of the structure.
- b. During this contract term, major emphasis will be devoted to investigating deposition in steady-state beds and characterizing the structures that are formed. The primary goal will be to develop an understanding of the deposition mechanism and the structures formed so that the structure deposited may be controlled at will through appropriate adjustments of the pyrolysis conditions.
- c. In determining whether or not the Contractor has performed with due diligence hereunder, it is agreed and understood that the Contracting Officer may measure the amount and quality of the Contractor's efforts against the representations made by the Contractor in negotiation of this contract and as contained in the Contractor's Proposal GGAP 1'-043, dated 9 February 1971, a copy of which is on file in the office of the Contracting Officer."

APPENDIX B  
PHOTOMICROGRAPHS AND PARTICLE SIZE DISTRIBUTION DATA

B-1

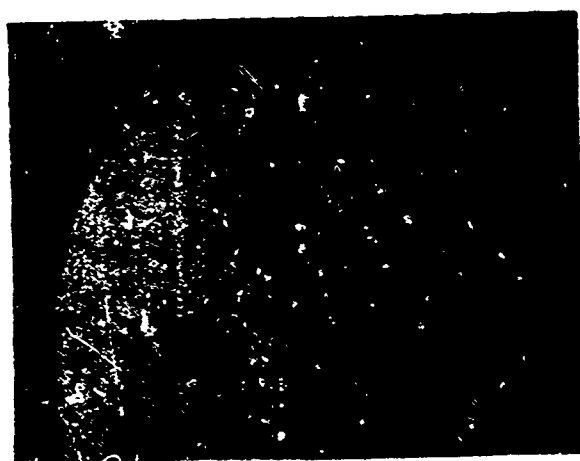
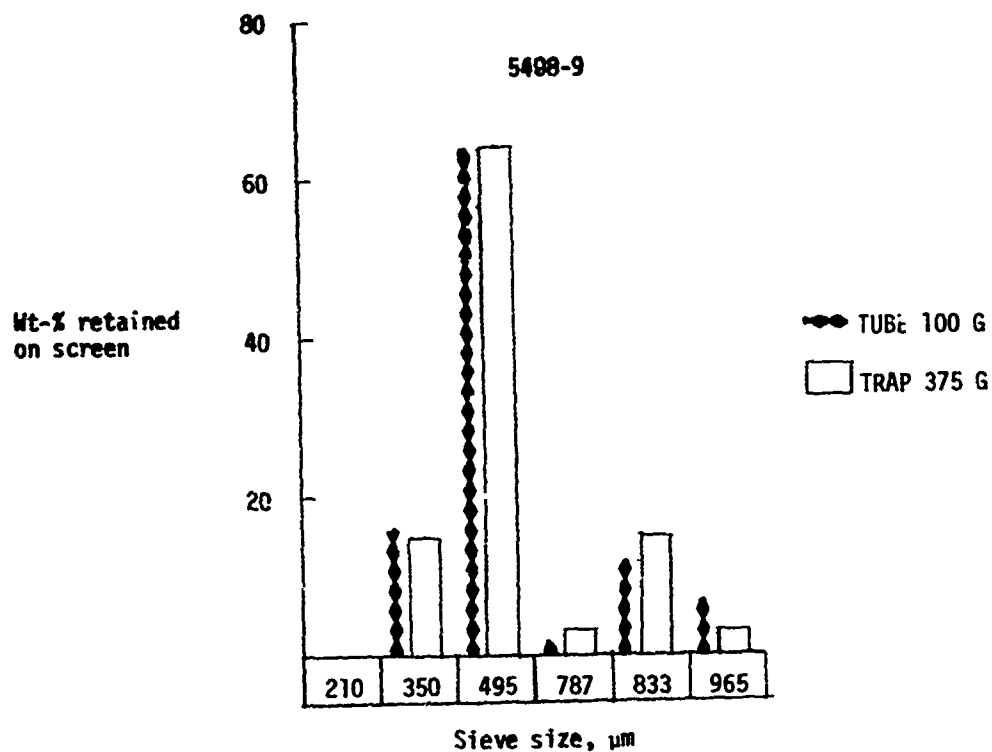


Sample: 5408-7  
 $\text{C}_3\text{H}_8$  concentration: 60%  
 Bed temperature: 1220°C  
 Overall efficiency: 26%  
 Coating rate: 5.9  $\mu\text{m}/\text{min.}$   
 Microhardness: 219-DPH  
 Density: 1.974  $\text{g}/\text{cm}^3$   
 $L_c$ : 36 Å

85X

Fig. B-1

B-3

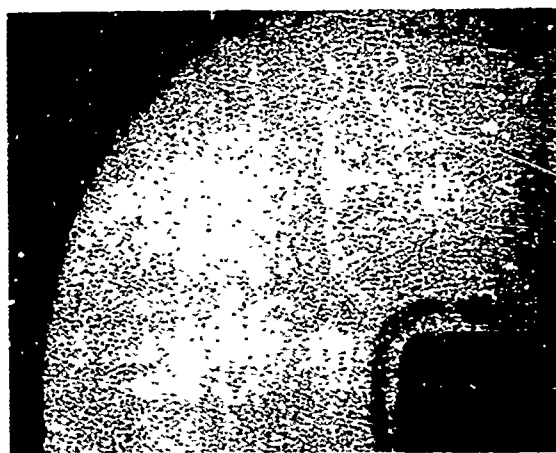
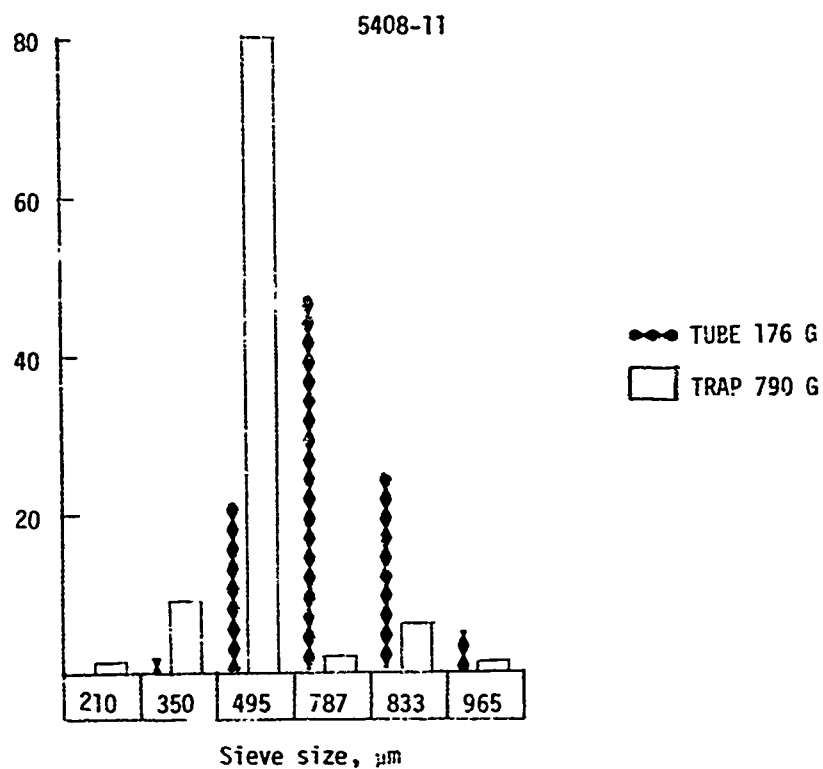


85X

Sample: 5408-9  
 $\text{C}_3\text{H}_8$  concentration: 25%  
 Bed temperature: 1260°C  
 Overall efficiency: 40%  
 Coating rate: 4.2  $\mu\text{m}/\text{min}$   
 Microhardness: 192 DPH  
 Density: N.D.  
 $L_c$ : N.D.

Fig. B-2

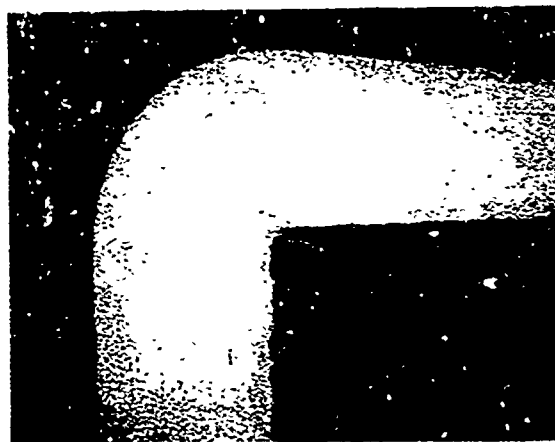
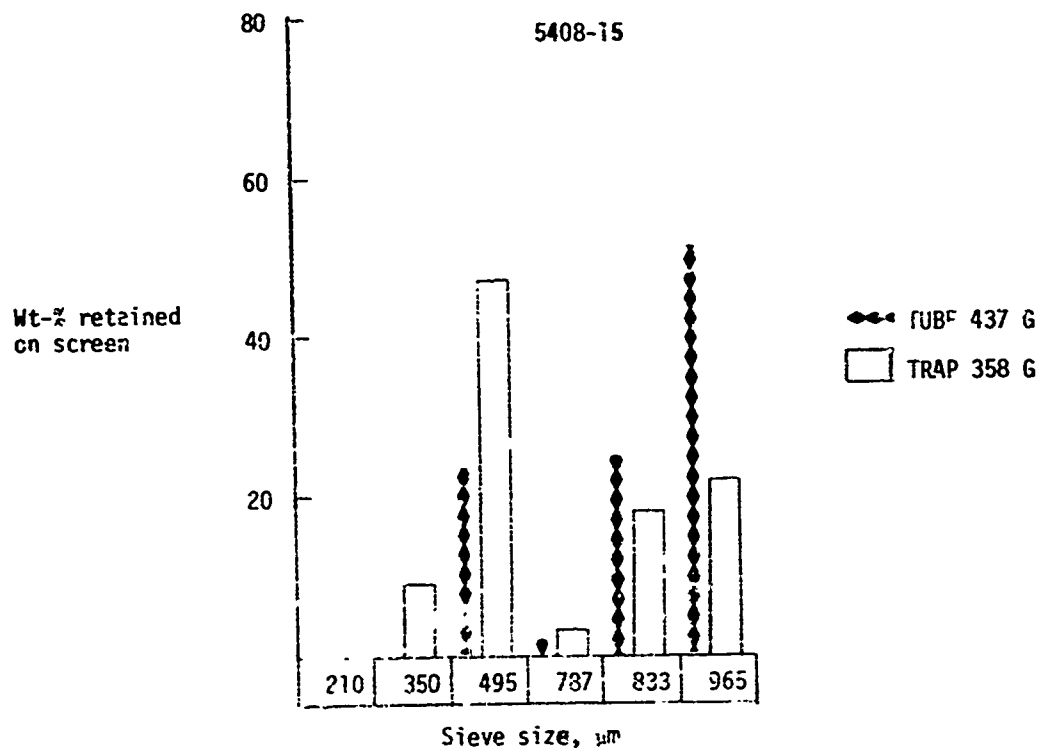
B-4



85X

Sample: 5408-11  
 $\text{C}_3\text{H}_8$  concentration: 7%  
 Bed temperature: 1330°C  
 Overall efficiency: N.D.  
 Coating rate: 1.4  $\mu\text{m}/\text{min}$ .  
 Microhardness: 154-DPH  
 Density: 1.553  $\text{g}/\text{cm}^3$   
 $L_c$ : 23 Å

Fig. B-3

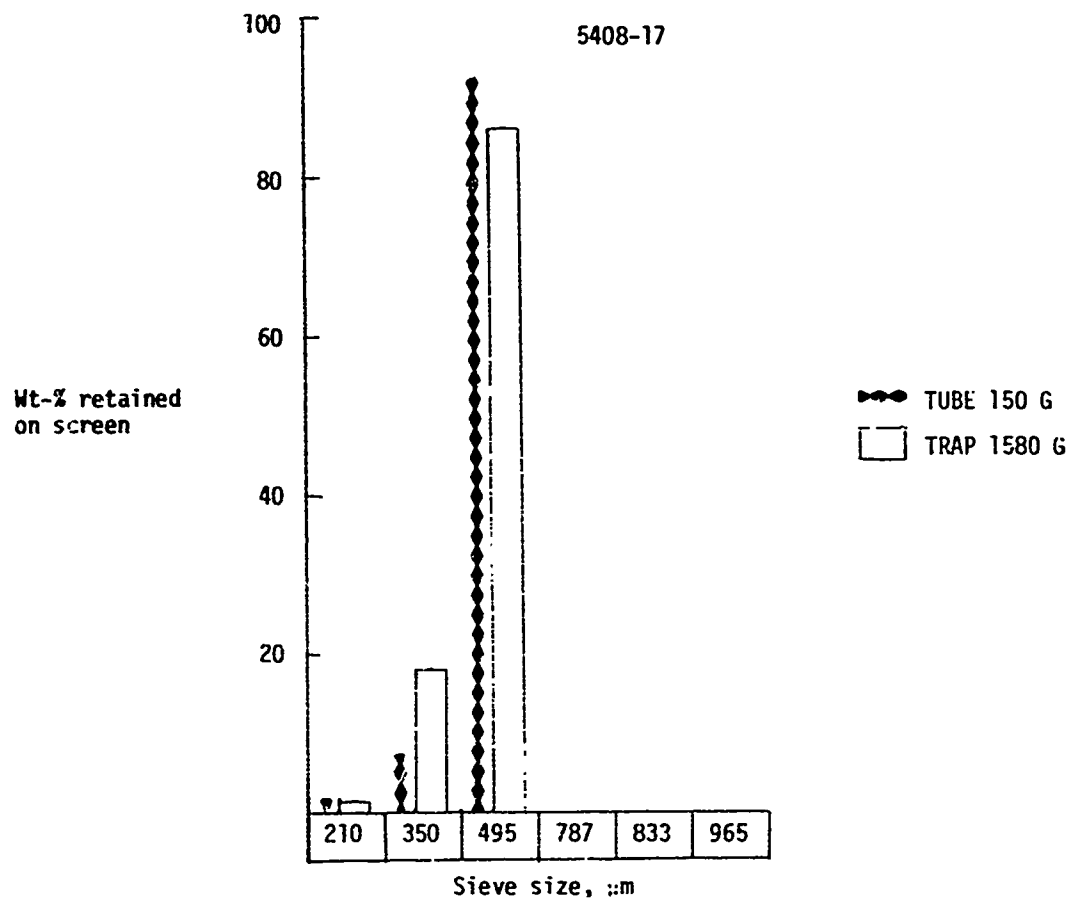


Sample: 5408-15  
 $\text{C}_3\text{H}_8$  concentration: 25%  
 Bed temperature: 1260°C  
 Overall efficiency: 33%  
 Coating rate: 1.3  $\mu\text{m}/\text{min}$ .  
 Microhardness: 190-DPH  
 Density: N.D.  
 $L_c$ : N.D.

42X

Fig. E-4

B-6

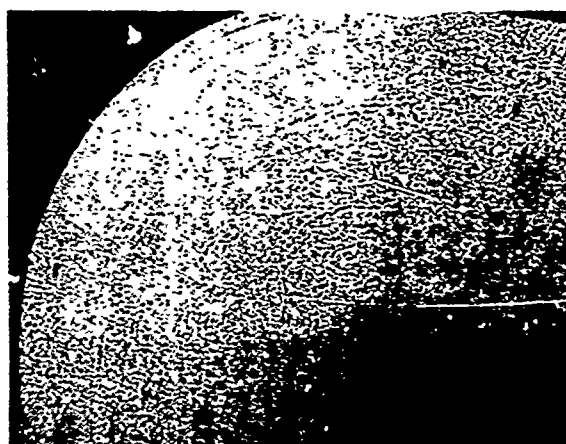
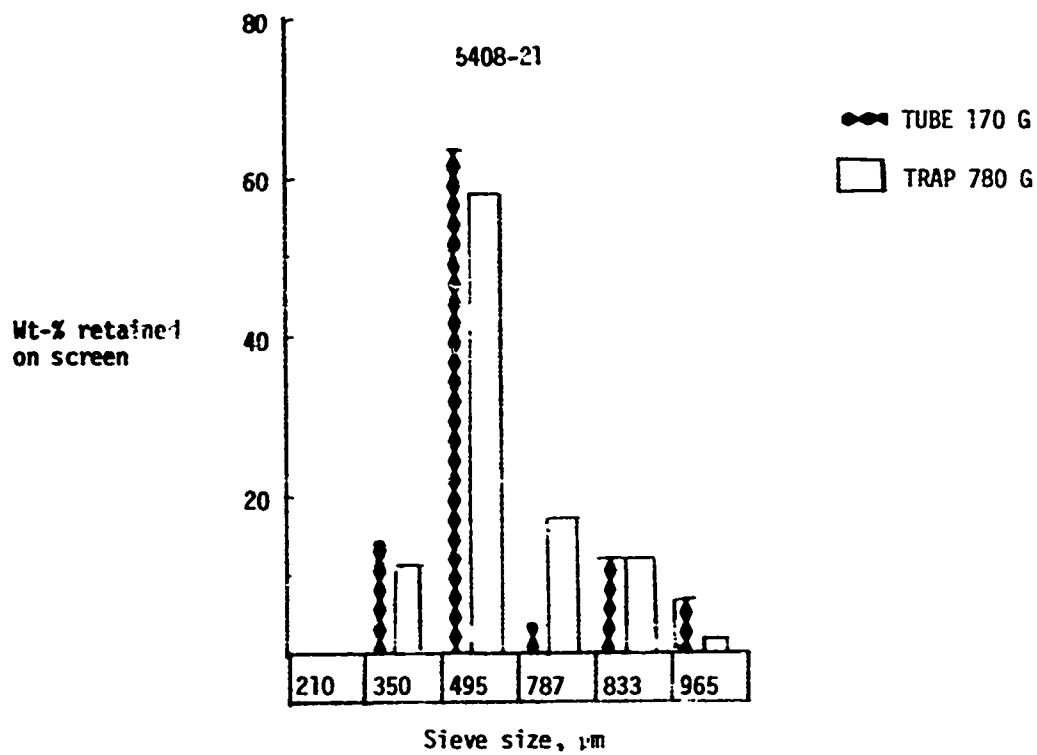


Sample: 5408-17  
 $\text{C}_2\text{H}_8$  concentration: 3%  
 Bed temperature: 1330°C  
 Overall efficiency: 73%  
 Coating rate: 0.91  $\mu\text{m}/\text{min}$ .  
 Microhardness: 153-DPH  
 Density: 1.457  $\text{g}/\text{cm}^3$   
 $L_c$ : 20 Å

85X

Fig. B-5

B-7



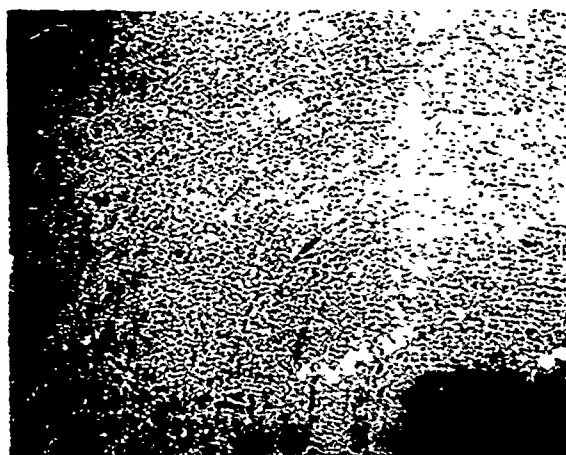
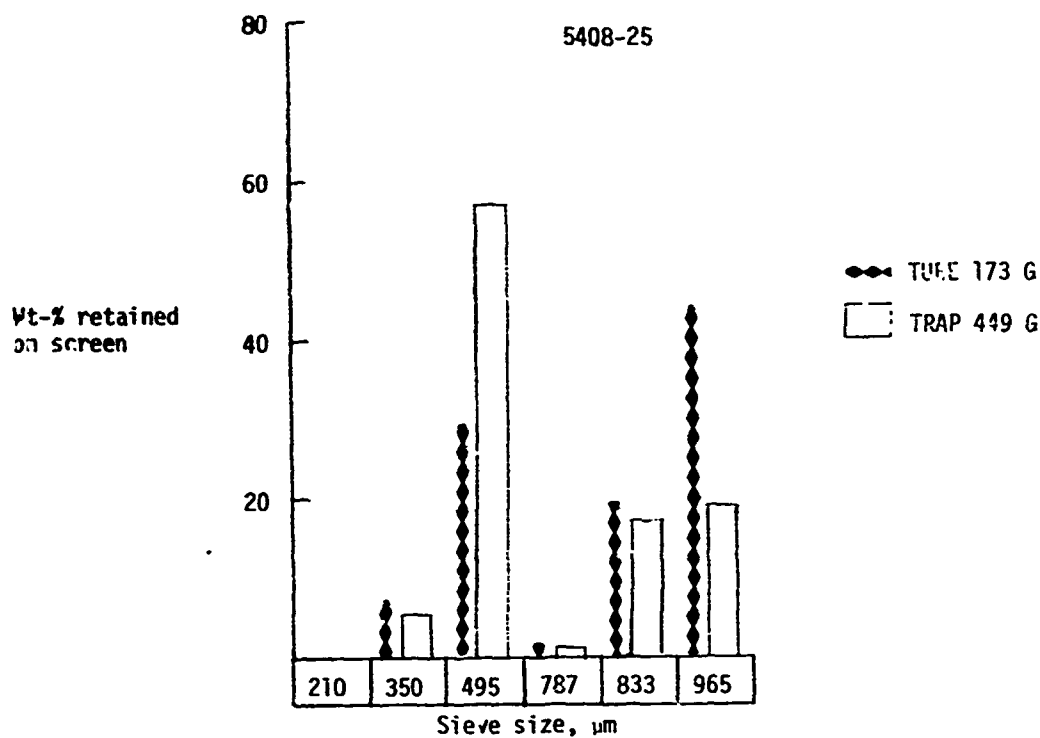
85X

Sample: 5408-21  
 Bed temperature: 1190°C  
 Propane concentration: 25%  
 Overall efficiency: 55%  
 Coating ratio: 2.9  $\mu\text{m}/\text{min}$ .  
 Microhardness: 226-DPH  
 Density: 1.914  
 $L_c$ : 32 Å

Fig. B-6

B-8



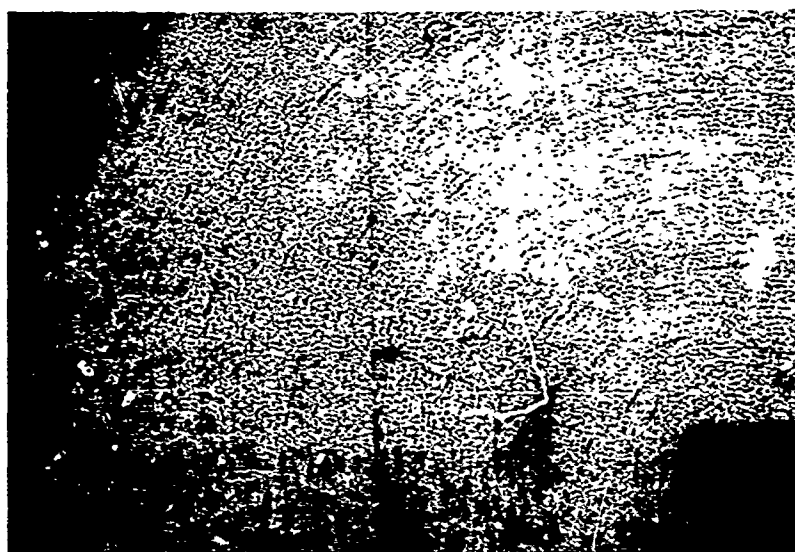
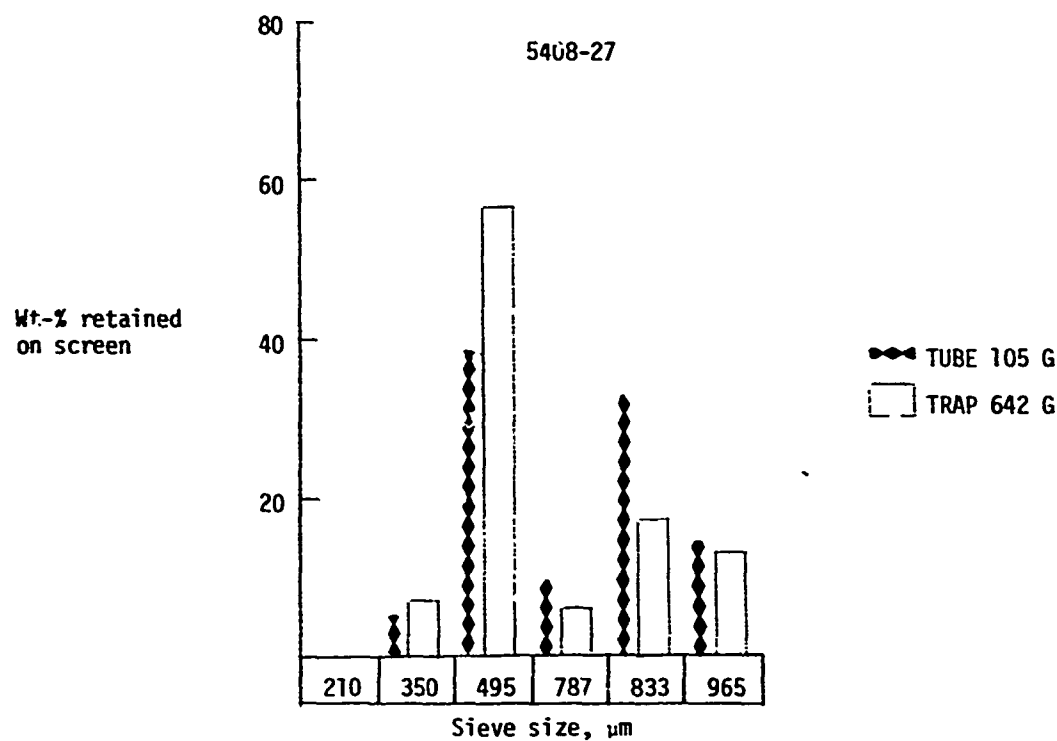


Sample: 5408-25  
 $\text{C}_3\text{H}_8$  concentration: 60%  
 Bed temperature: 1300°C  
 Overall efficiency: 35%  
 Coating rate: 8.1  $\mu\text{m}/\text{min}$ .  
 Microhardness: 170-DPH  
 Density: 1.753  $\text{g}/\text{cm}^3$   
 $L_c$ : 29 Å

85X

Fig. B-7

B-9

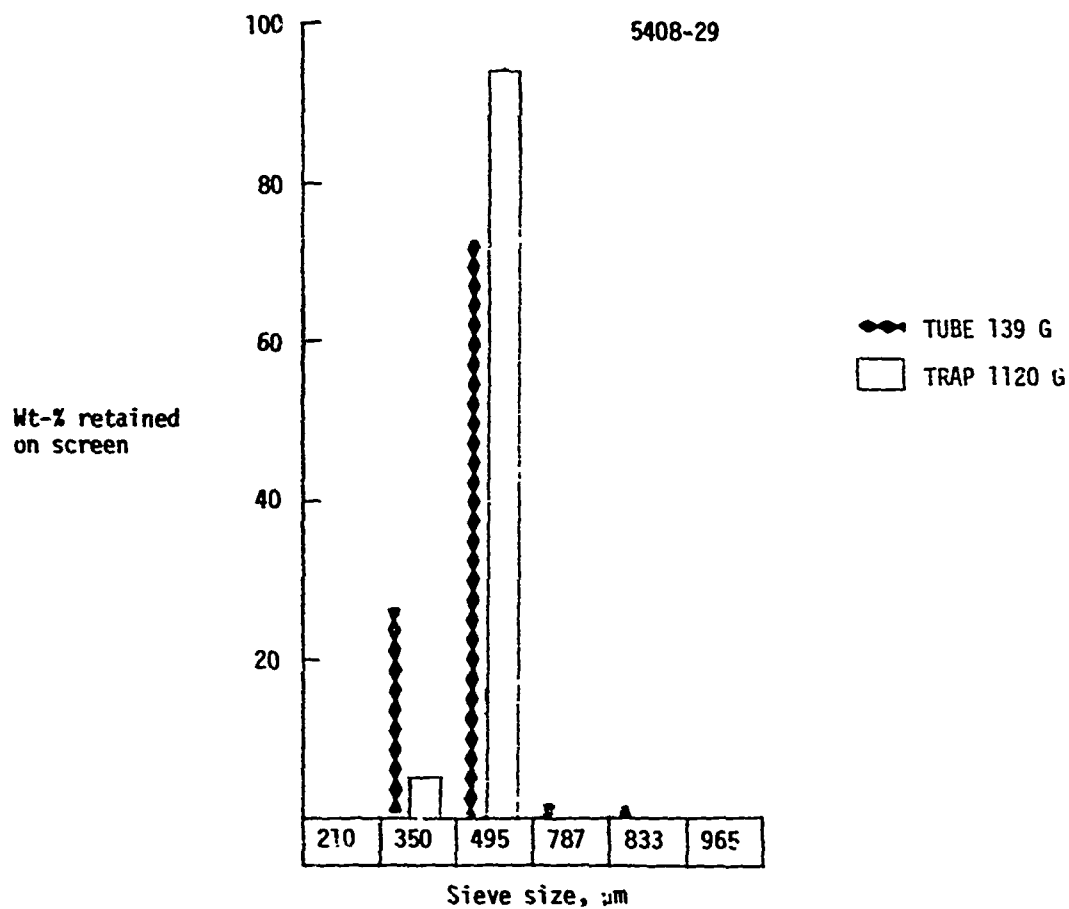


Sample: 5408-27  
 $\text{C}_3\text{H}_8$  concentration: 25%  
 Bed temperature: 1340°C  
 Overall efficiency: 25%  
 Coating rate: 5.7  $\mu\text{m}/\text{min}$ .  
 Microhardness: 156-DPH  
 Density: 1.592  $\text{g}/\text{cm}^3$   
 $L_c$ : 24 Å

85X

Fig. B-8

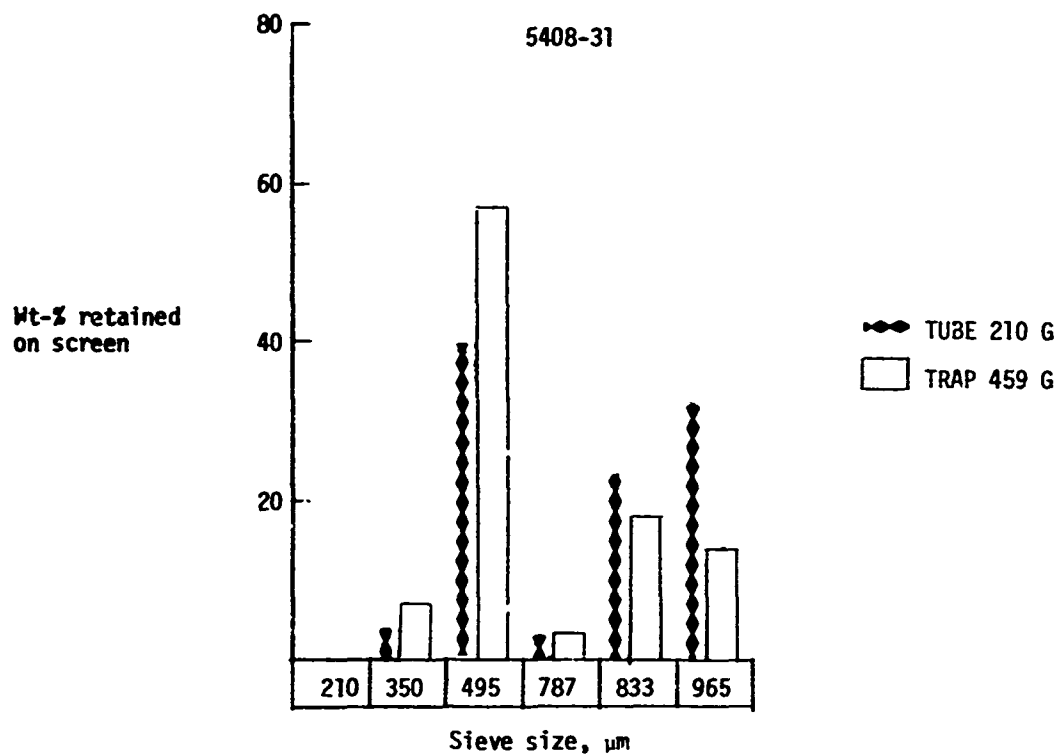
B-10



Sample: 5408-29  
 $\text{C}_3\text{H}_8$  concentration: 7%  
 Bed temperature: 1400°C  
 Overall efficiency: 51%  
 Coating rate: 1.3  $\mu\text{m}/\text{min}$ .  
 Microhardness: 100-DPH  
 Density: 1.353  $\text{g}/\text{cm}^3$   
 $L_c$ : 26 Å

Fig. B-9

B-11

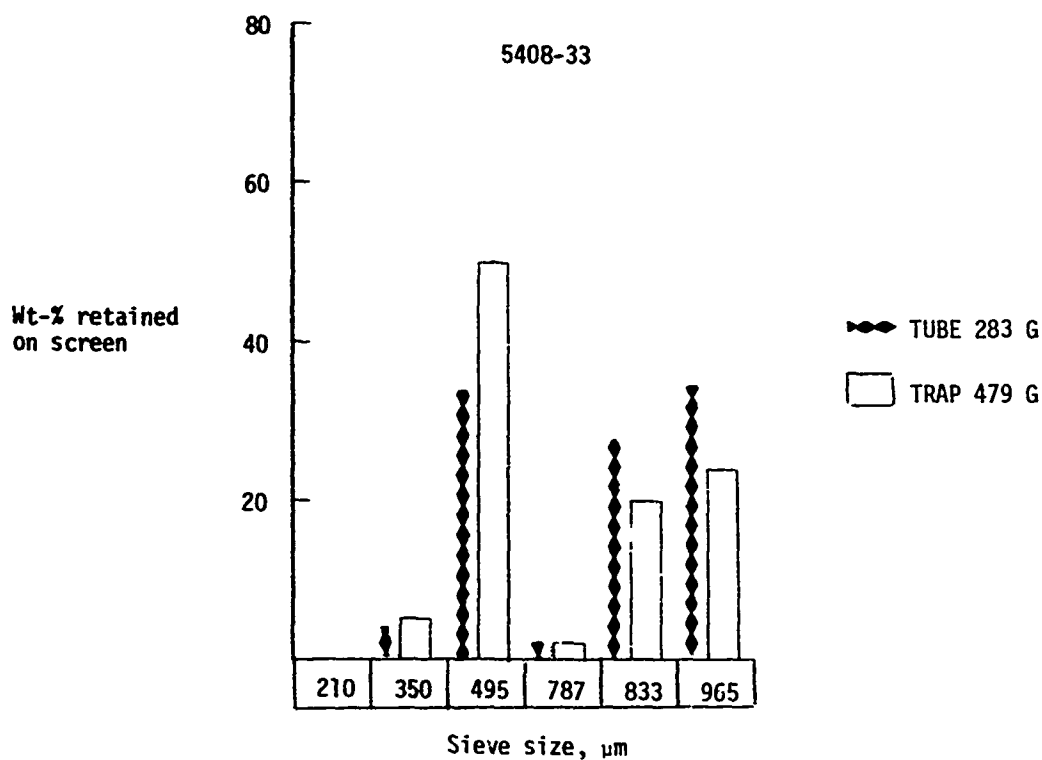


Sample: 5408-31  
 $\text{C}_2\text{H}_8$  concentration: 60%  
 Bed temperature: 1230°C  
 Overall efficiency: 40%  
 Coating rate: 6.8  $\mu\text{m}/\text{min}$ .  
 Microhardness: 170-DPH  
 Density: 1.823  $\text{g}/\text{cm}^3$   
 $L_c$ : 33 Å

42X

Fig. B-10

B-12

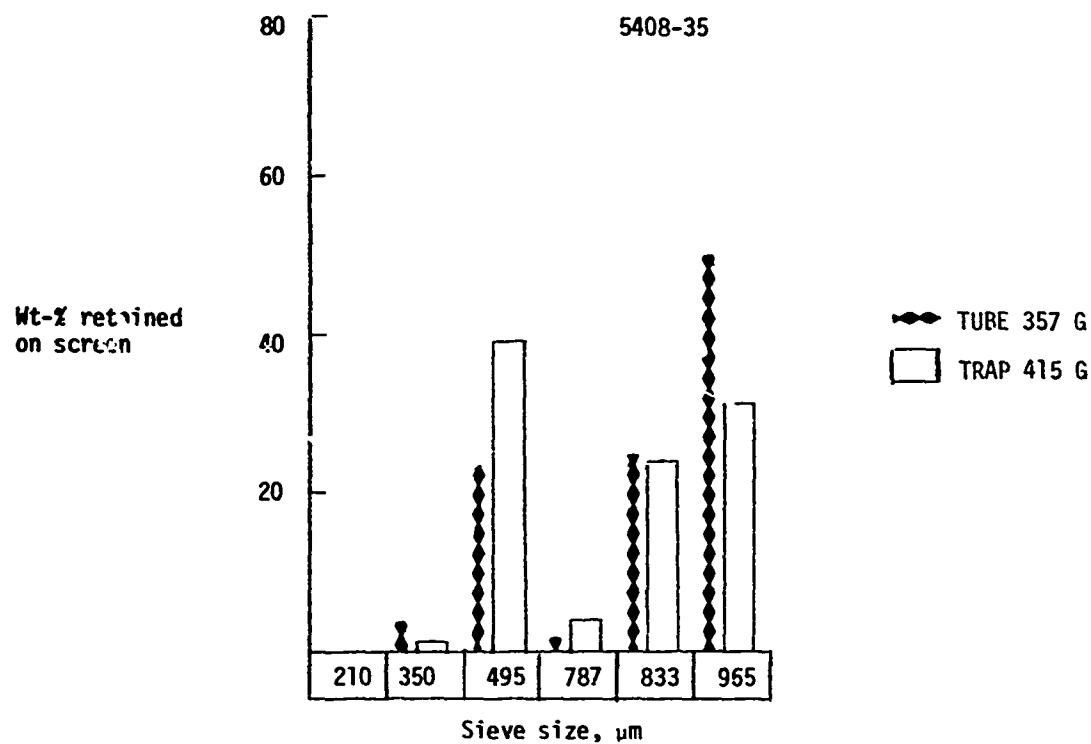


Sample: 5408-33  
 $\text{C}_3\text{H}_8$  concentration: 60%  
 Bed temperature: 1355°C  
 Overall efficiency: 52%  
 Coating rate: 9.8  $\mu\text{m}/\text{min.}$   
 Microhardness: 127-DPH  
 Density: 1.535  $\text{g}/\text{cm}^3$   
 $L_c$ : 26 Å

42X

Fig. B-11

B-13

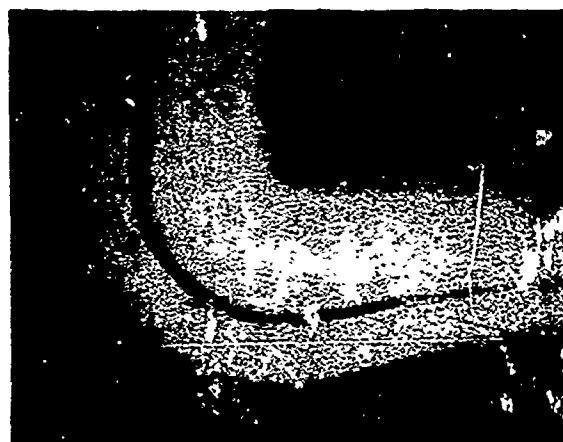
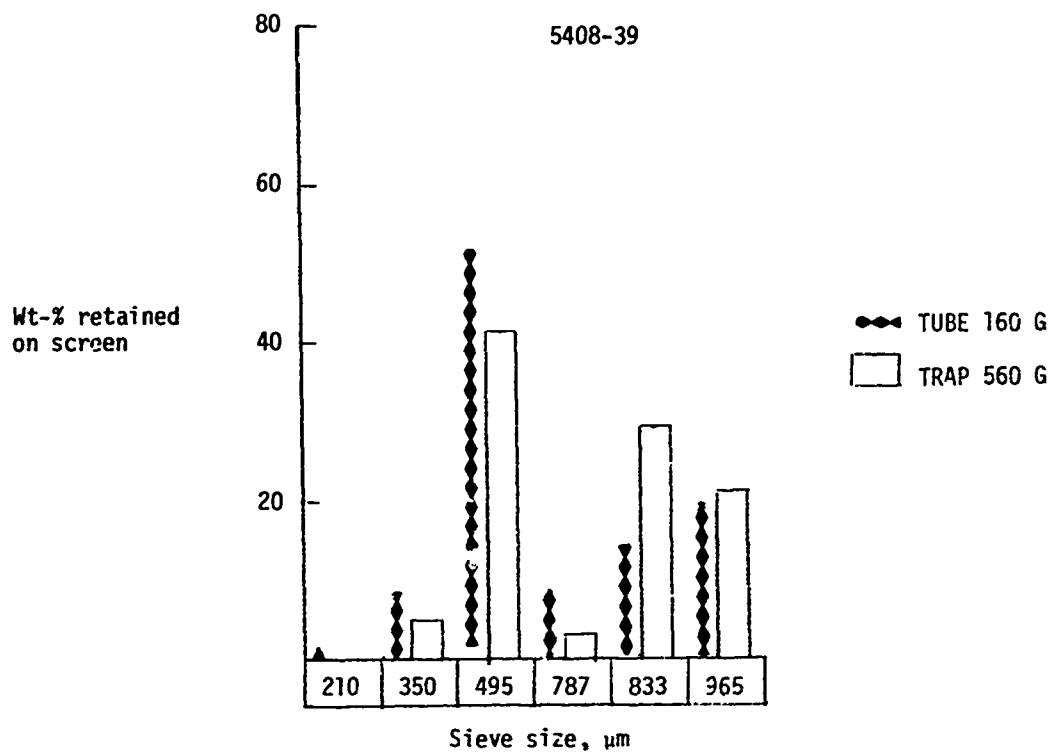


Sample: 5408-35  
 $\text{C}_3\text{H}_8$  concentration: 60%  
 Bed temperature: 1400°C  
 Overall efficiency: 55%  
 Coating rate: 8.5  $\mu\text{m}/\text{min.}$   
 Microhardness: 92-DPH  
 Density: 1.459  $\text{g}/\text{cm}^3$   
 $L_c$ : 26 Å

85X

Fig. B-12

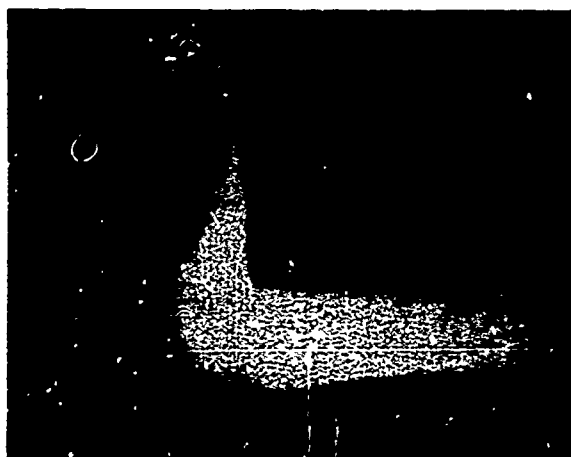
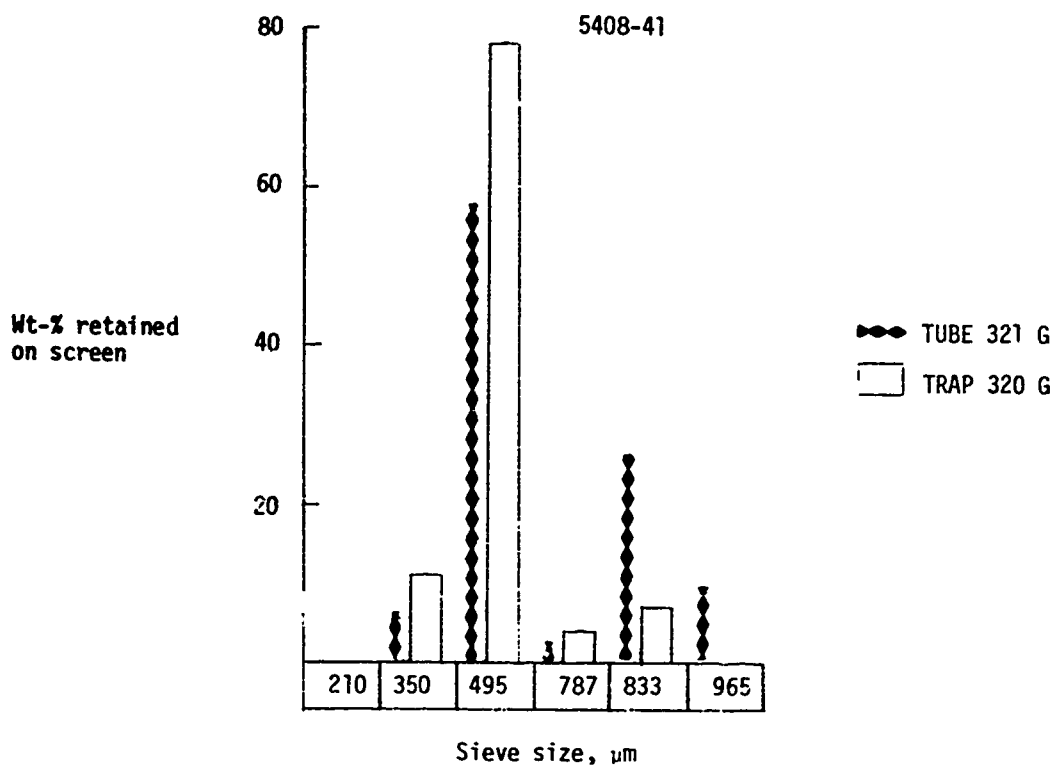
B-14



42X

Sample: 5408-39  
 $\text{C}_3\text{H}_8$  concentration: 60% + 40%  $\text{H}_2$   
 Bed temperature: 1300°C  
 Overall efficiency: 47%  
 Coating rate: 8.0  $\mu\text{m}/\text{min}$ .  
 Microhardness: 187-DPH  
 Density: 1.813  $\text{g}/\text{cm}^3$   
 $L_c$ : 31 Å

Fig. B-13



Sample: 5408-41  
 $\text{C}_3\text{H}_8$  concentration: 60% +  
 40%  $\text{H}_2$   
 Bed temperature: 1140°C  
 Overall efficiency: 37%  
 Coating rate: 3.8  $\mu\text{m}/\text{min}$ .  
 Microhardness: 185-DPH  
 Density: N.D.  
 $L_c$ : N.D.

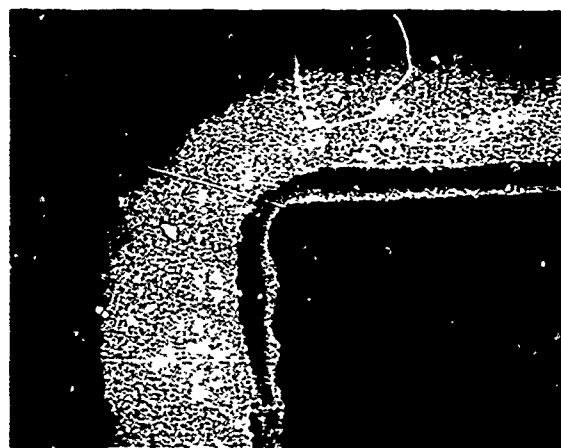
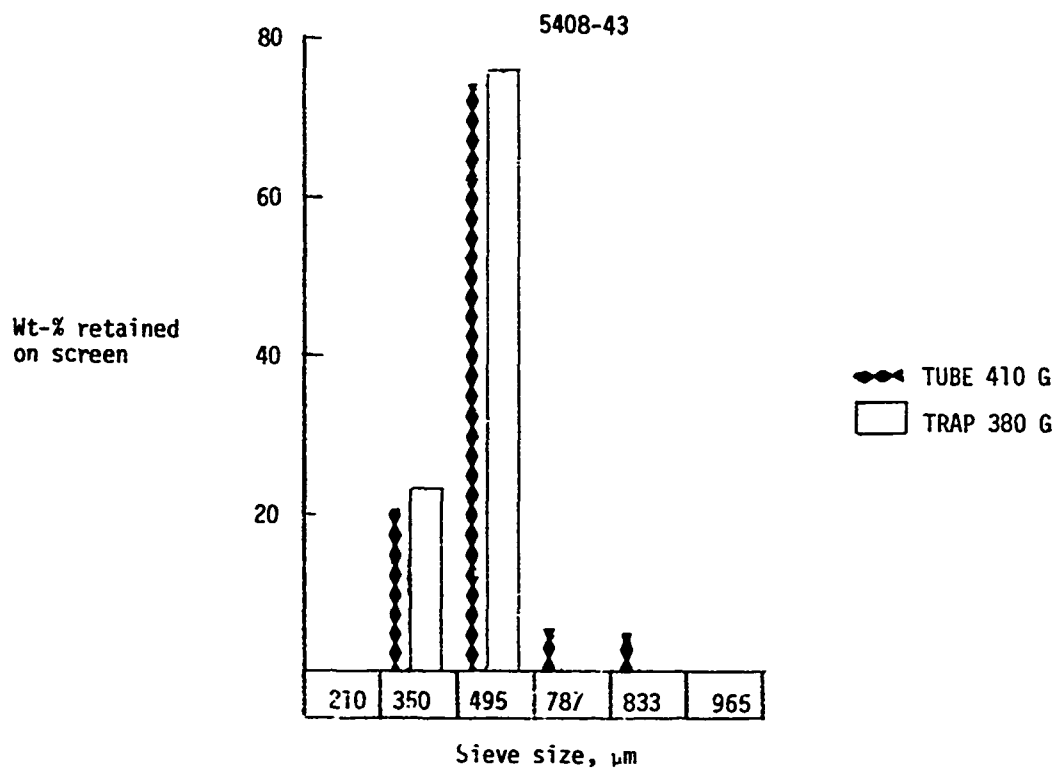
42X

Fig. B-14

B-16

107





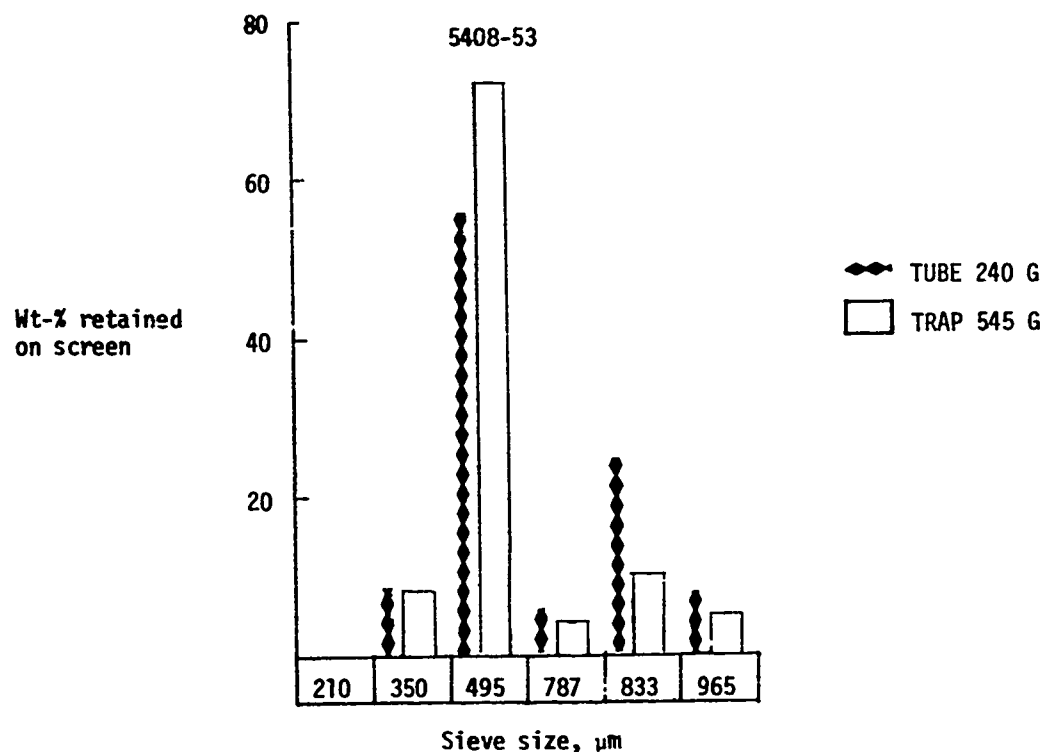
Sample: 5408-43  
 $\text{C}_3\text{H}_8$  concentration: 25% +  
 75%  $\text{H}_2$   
 Bed temperature: 1190°C  
 Overall efficiency: 31%  
 Coating rate: 1.7  $\mu\text{m}/\text{min}$ .  
 Microhardness: 203-DPH  
 Density: 2.017  $\text{g}/\text{cm}^3$   
 $L_c$ : 32 Å

85X

Fig. B-15

B-17

108



Sample: 5408-53

$\text{C}_3\text{H}_8$  concentration: 25% +  
2% Cl

Bed temperature:  $\sim 1240^\circ\text{C}$

Overall efficiency: 30%

Coating rate:  $4.0 \mu\text{m}/\text{min}$ .

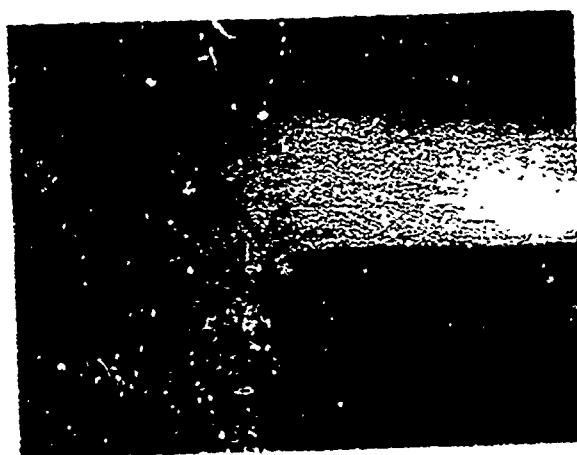
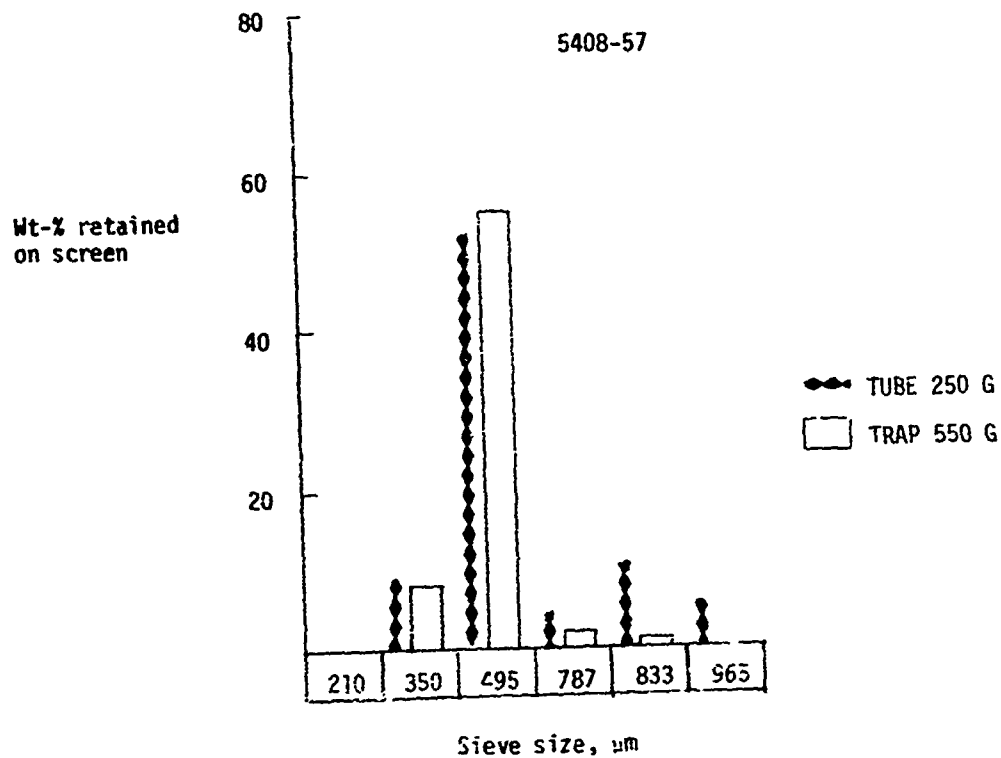
Microhardness: N.D.

Density:  $1.872 \text{ g}/\text{cm}^3$

$L_c$ : 29 Å

Fig. B-16

B-18

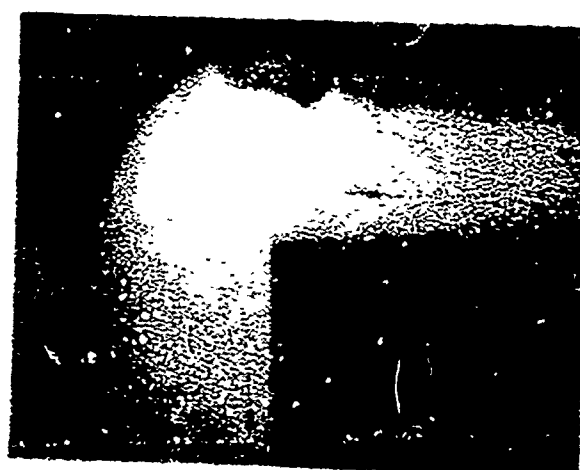
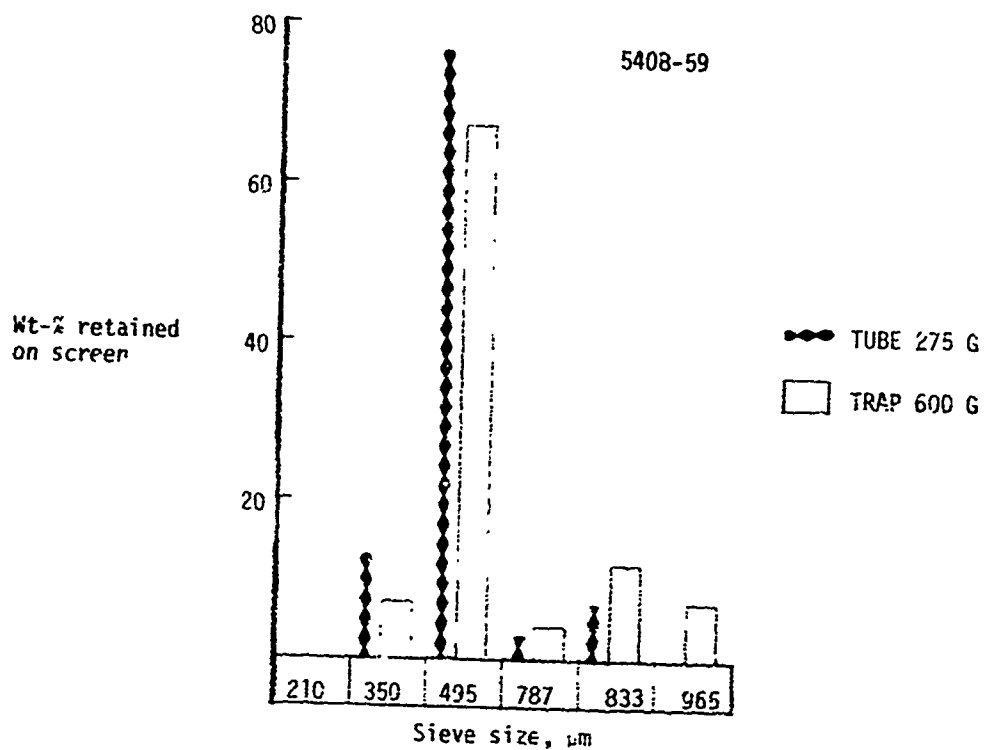


Sample: 5408-57  
 $\text{C}_3\text{H}_8$  concentration: 60%  
 $\text{CH}_3\text{SiCl}_3$  flux: 6.0 g/min.  
 Bed temperature: 1295°C  
 Overall efficiency: 54.5%  
 Coating rate: 5.9  $\mu\text{m}/\text{min}$ .  
 Microhardness: 201-DPH  
 Si content: 9.5%  
 Density: 2.085 g/cm<sup>3</sup>  
 Carbon density: 1.98 g/cm<sup>3</sup>

85X

Fig. B-17

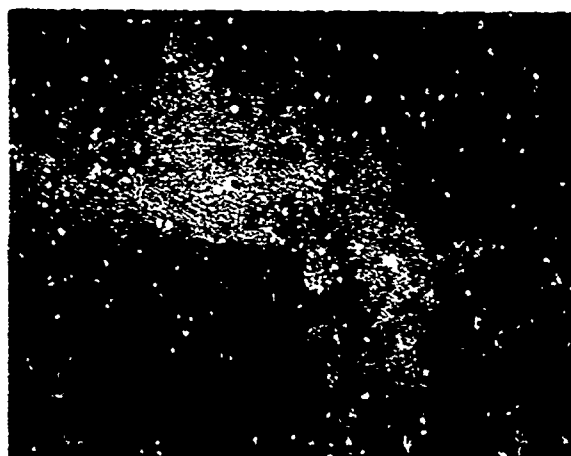
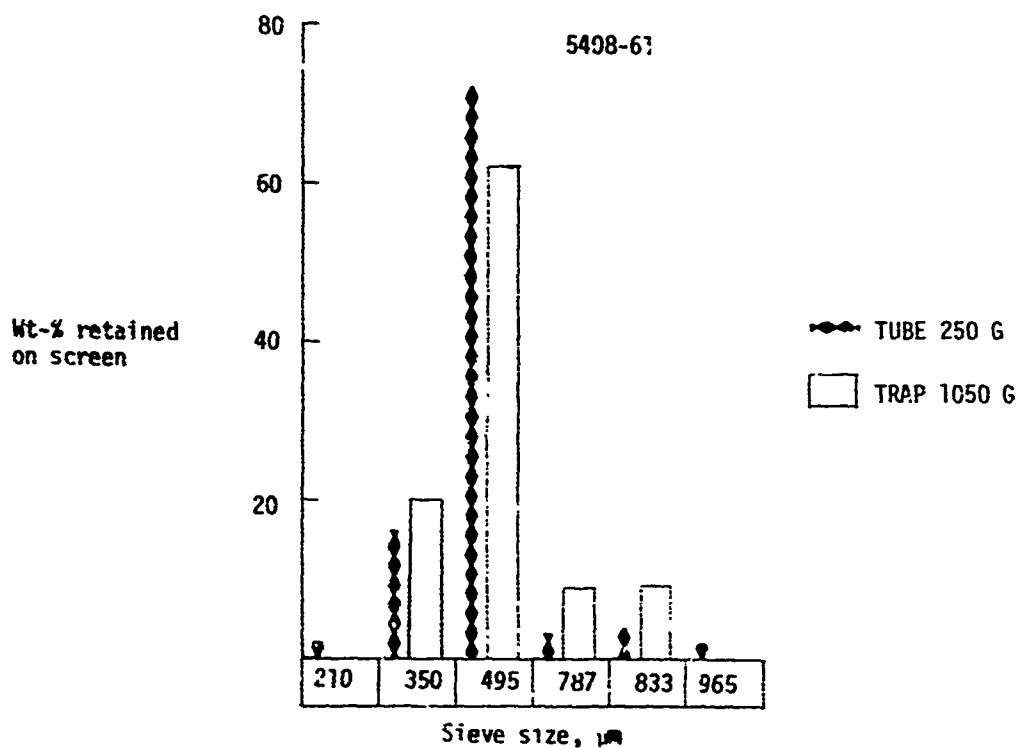
B-19



Sample: 5408-59  
 $\text{C}_3\text{H}_8$  concentration: 25%  
 $\text{CH}_3\text{SiCl}_3$  flux: 9.5 g/min.  
 Bed temperature: 1235°C  
 Overall efficiency: 65%  
 Coating rate: 4.8  $\mu\text{m}/\text{min}$ .  
 Microhardness: 212-DPH  
 Si content: 16%  
 Density: 2.062  $\text{g}/\text{cm}^3$   
 Carbon density: 1.87  $\text{g}/\text{cm}^3$

42X

Fig. B-18

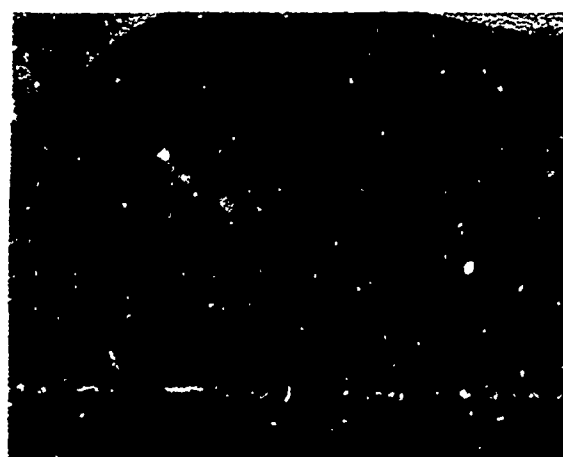
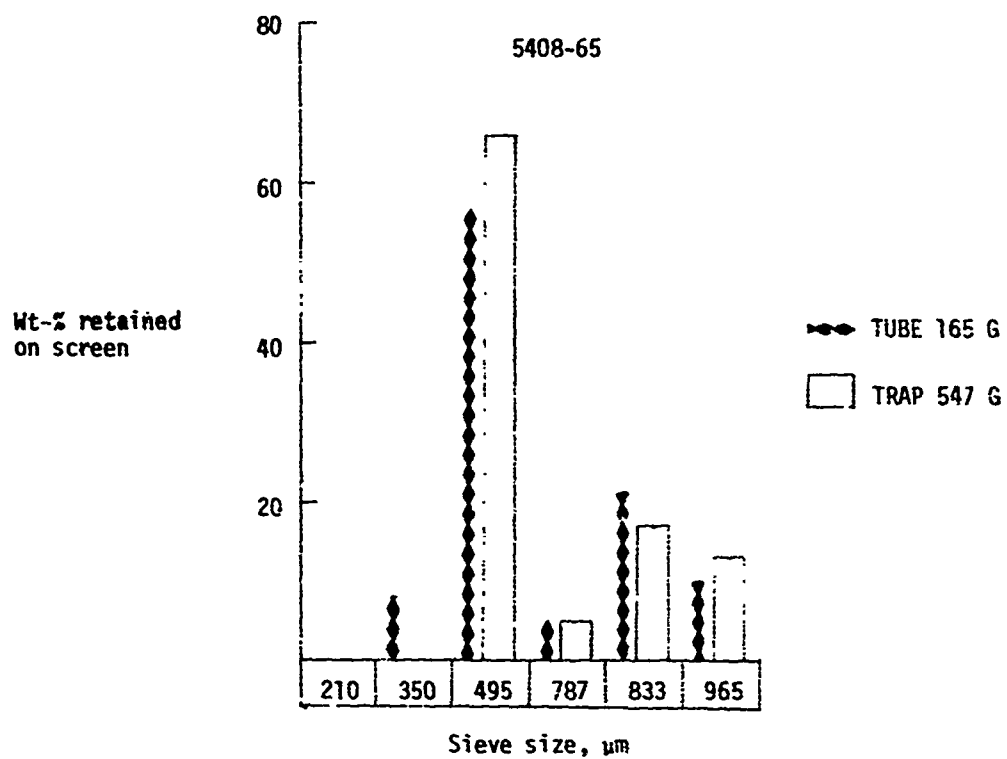


85X

Sample: 5408-61  
 $\text{C}_3\text{H}_8$  concentration: 7%  
 $\text{CH}_3\text{SiCl}_3$  flux: 7.2 g/min.  
 Bed temperature: 1340°C  
 Overall efficiency: 36%  
 Coating rate: 2.3  $\mu\text{m}/\text{min}$   
 Microhardness: 397-DPH  
 Si content: 28%  
 Density: 2.158  $\text{g}/\text{cm}^3$   
 Carbon density: 1.77  $\text{g}/\text{cm}^3$

Fig. B-19

B-21

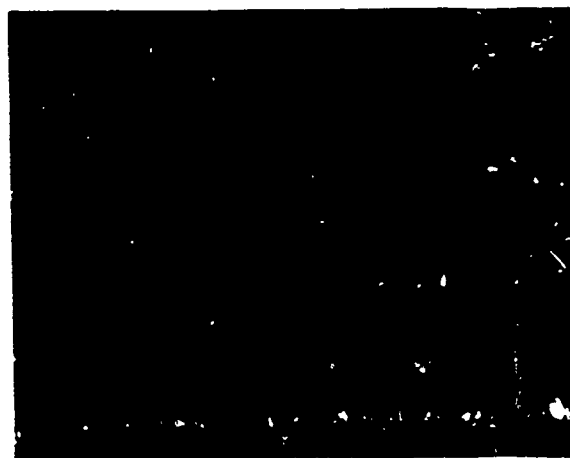
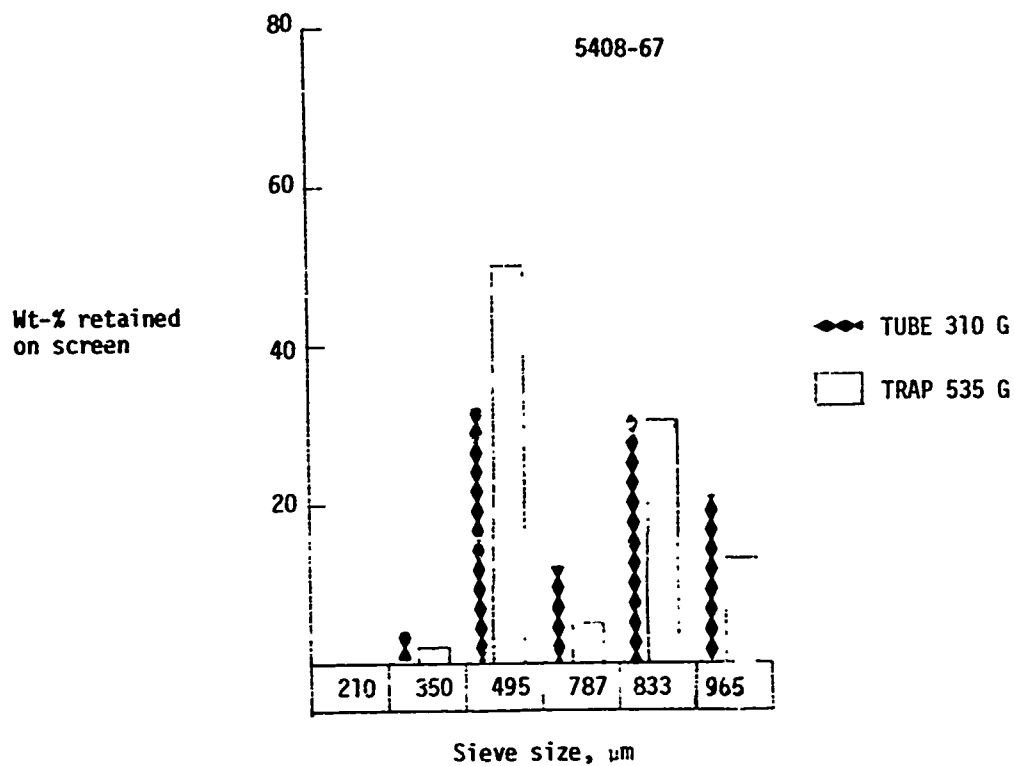


170X

Sample: 5408-65  
 $\text{C}_3\text{H}_8$  concentration: 60%  
 $\text{CH}_3\text{SiCl}_2$  flux: 5.9 g/min.  
 Bed temperature: 1235°C  
 Overall efficiency: 42%  
 Coating rate: 5.5  $\mu\text{m}/\text{min}$ .  
 Microhardness: 295-DPH  
 Si content: 8%  
 Density: 2.064  $\text{g}/\text{cm}^3$   
 Carbon density: 1.97  $\text{g}/\text{cm}^3$

Fig. 3-20

B-22

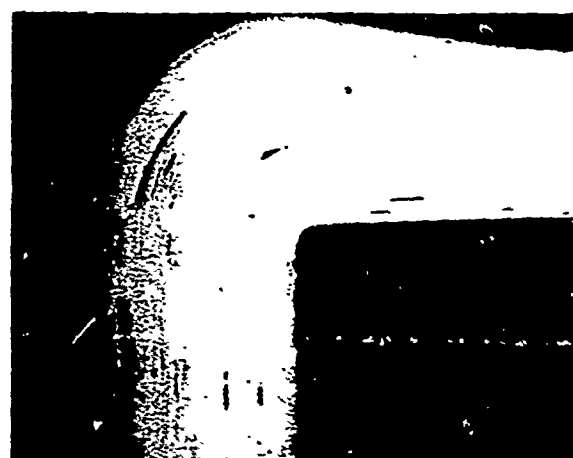
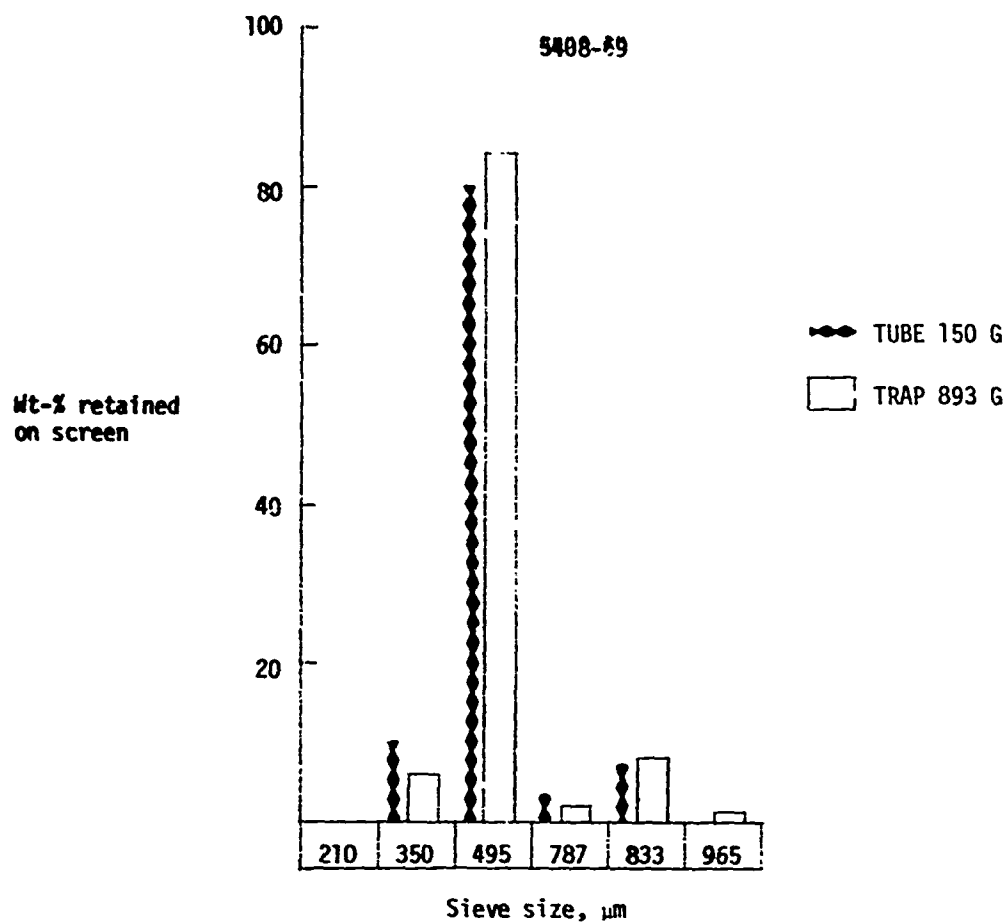


170X

Sample: 5408-67  
 $\text{C}_3\text{H}_8$  concentration: 60%  
 $\text{CH}_3\text{SiCl}_3$  flux: 5.0 g/min  
 Bed temperature: 1350°C  
 Overall efficiency: 58.4%  
 Coating rate: 5.9  $\mu\text{m}/\text{min}$ .  
 Microhardness: 179-DPH  
 Si content: 4.0%  
 Density: 2.031  $\text{g}/\text{cm}^3$   
 Carbon density: 1.98  $\text{g}/\text{cm}^3$

Fig. B-21

B-23



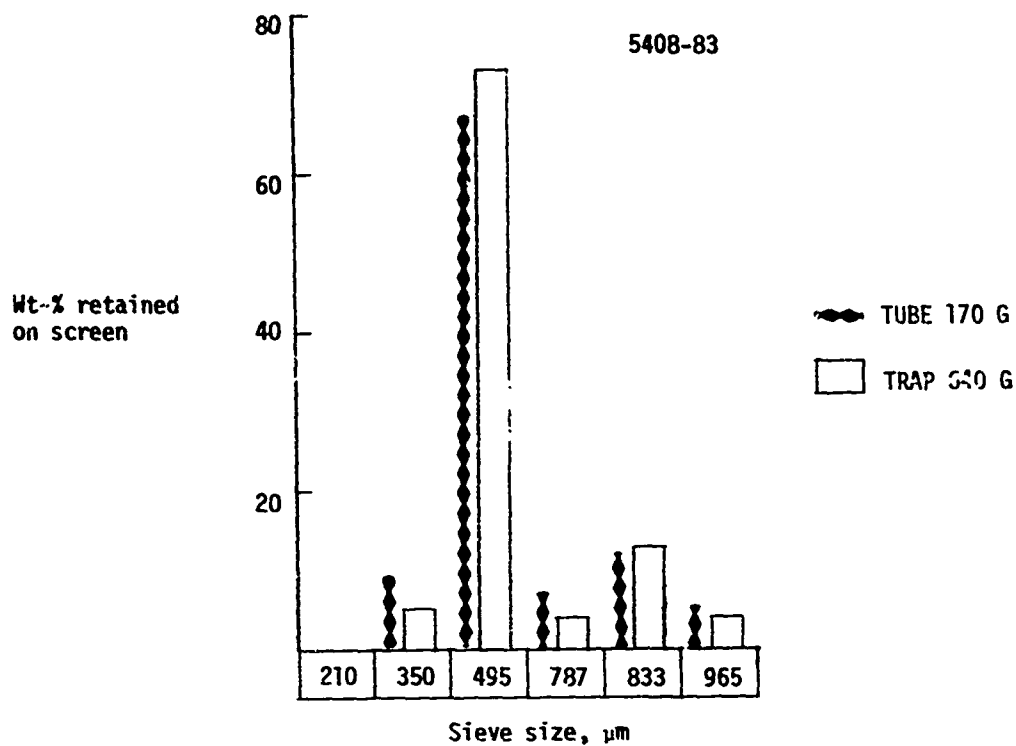
85X

Sample: 5408-69  
 $\text{C}_3\text{H}_8$  concentration: 25%  
 $\text{CH}_3\text{SiCl}_3$  flux: 8.7 g/min  
 Bed temperature: 1270°C  
 Overall efficiency: 55%  
 Coating rate: 3.6  $\mu\text{m}/\text{min}$ .  
 Microhardness: 352-NPH  
 Si content: 15%  
 Density: 2.105  $\text{g}/\text{cm}^3$   
 Carbon density: 1.92  $\text{g}/\text{cm}^3$

Fig. B-22

B-24



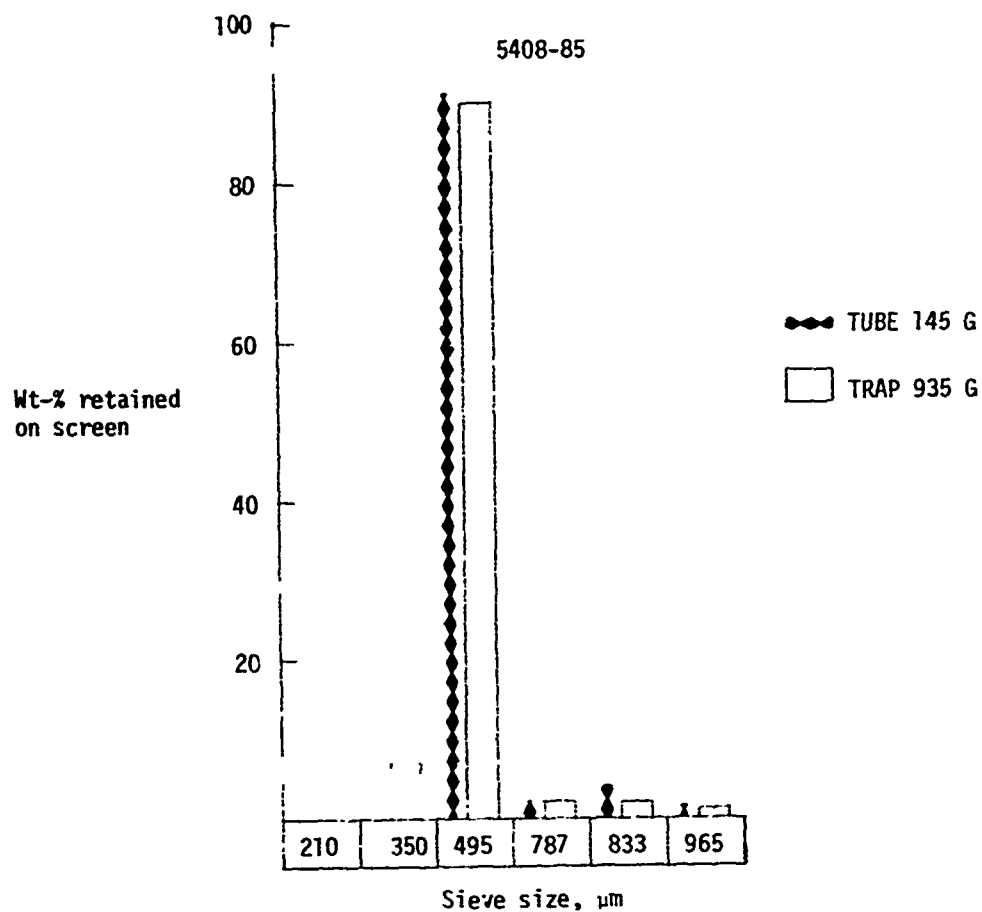


85X

Sample: 5408-83  
 $\text{C}_3\text{H}_8$  concentration: 25%  
 $\text{CH}_3\text{SiCl}_3$  flux: 9.8 g/min.  
 Bed temperature: 1370°C  
 Overall efficiency: 50%  
 Coating rate: 6.8  $\mu\text{m}/\text{min}$ .  
 Microhardness: 279-DPH  
 Si content: 13.5%  
 Density: 2.031  $\text{g}/\text{cm}^3$   
 Carbon density: 1.92  $\text{g}/\text{cm}^3$

Fig. B-23

B-25

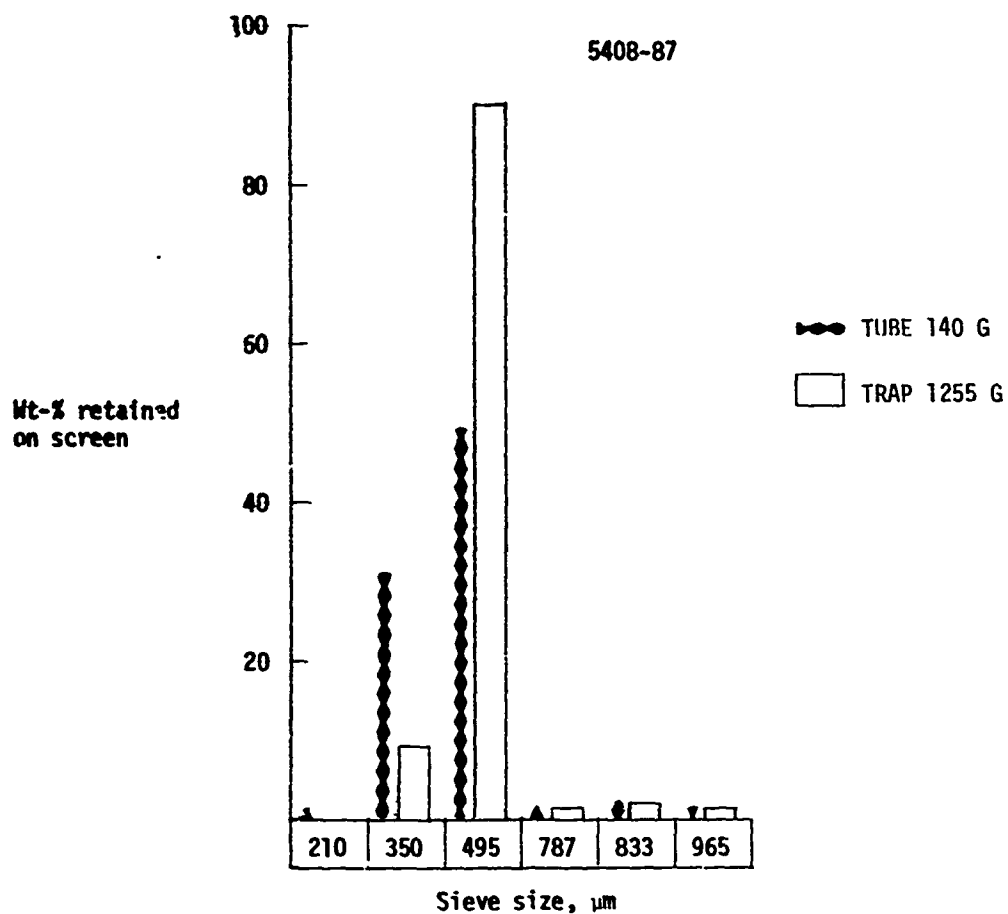


85X

Sample: 5408-85  
 $\text{C}_3\text{H}_8$  concentration: 7%  
 $\text{CH}_3\text{SiCl}_3$  flux: 9.2 g/min.  
 Bed temperature: 1390°C  
 Overall efficiency: 40%  
 Coating rate: 3.0  $\mu\text{m}/\text{min}$ .  
 Microhardness: 378-DPH  
 Si content: 34%  
 Density: 2.149  $\text{g}/\text{cm}^3$   
 Carbon density: 1.64  $\text{g}/\text{cm}^3$

Fig. B-24

B-26

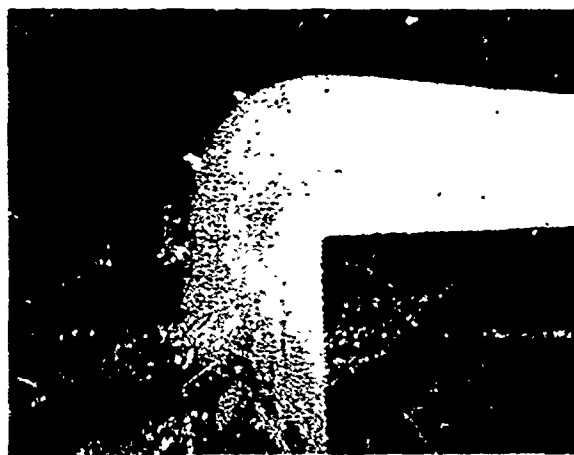
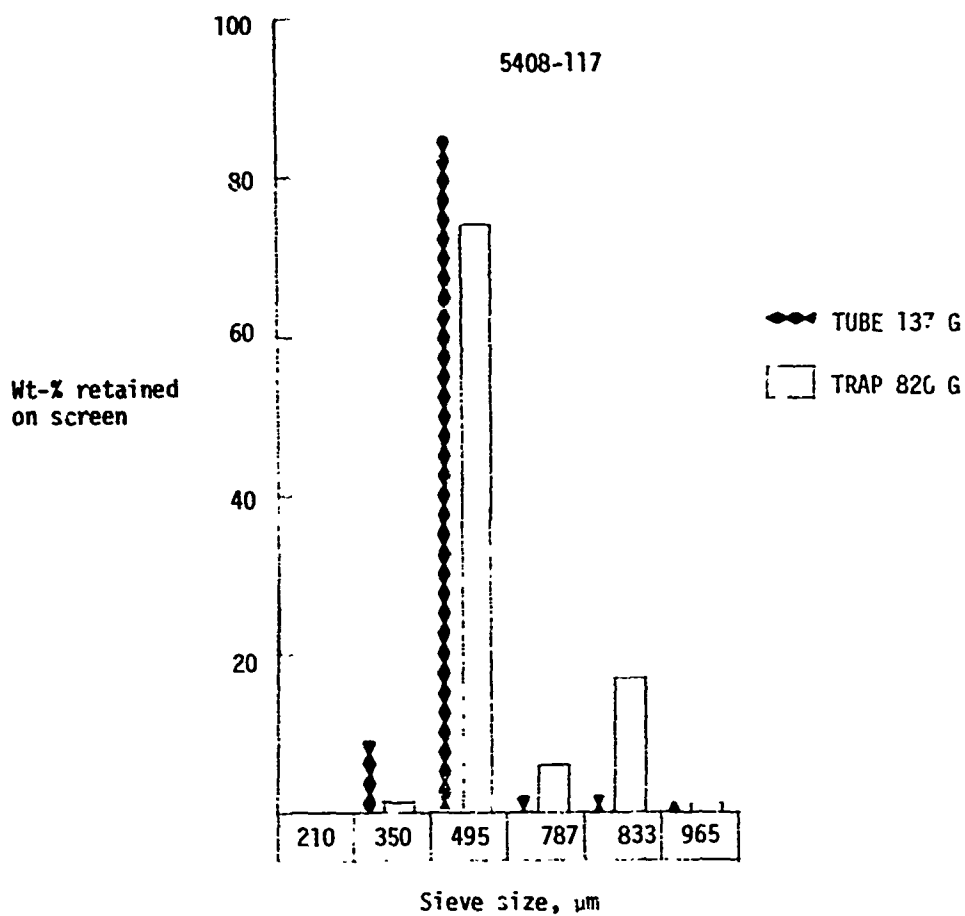


Sample: 5408-87  
 $\text{C}_3\text{H}_8$  concentration: 7%  
 $\text{CH}_3\text{SiCl}_3$  flux: 8.7 g/min.  
 Bed temperature: 1290°C  
 Overall efficiency: 44%  
 Coating rate: 2.1  $\mu\text{m}/\text{min}$ .  
 Microhardness: 430-DPH  
 Si content: 23%  
 Density: 2.178  $\text{g}/\text{cm}^3$   
 Carbon density: 1.88  $\text{g}/\text{cm}^3$

85X

Fig. B-25

B-27



85X

Sample: 5408-117  
 $\text{C}_3\text{H}_8$  concentration: 25%  
 $\text{TiCl}_4$  flux: 1.1 g/min.  
 Bed temperature: 1280°C  
 Overall efficiency: N.D.  
 Coating rate: 2.8  $\mu\text{m}/\text{min}$ .  
 Microhardness: 240-DPH  
 Titanium content: 3.4%  
 Density: 1.980  $\text{g}/\text{cm}^3$

Fig B-26

B-28

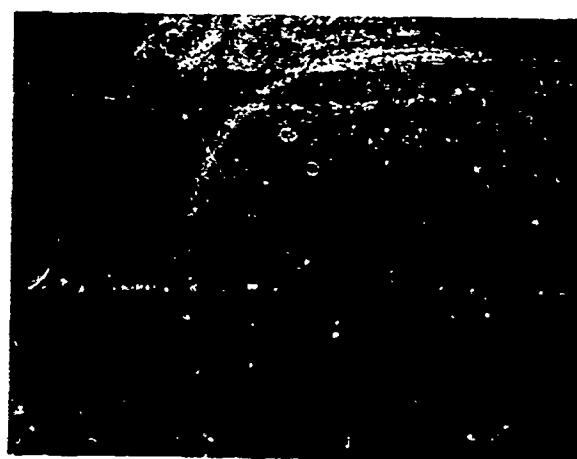
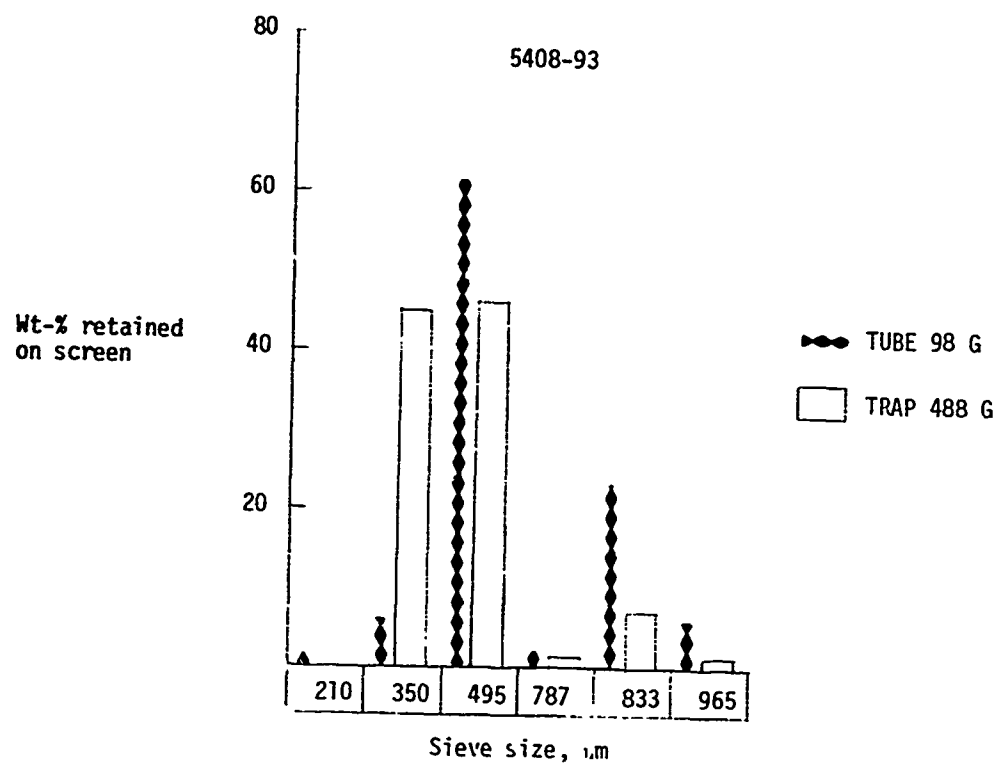
TUBE: 100 G  
TRAP: 300 G



85X

Sample: 5408-91  
 $C_3H_8$  concentration: 60%  
 $BCl_3$  flux: 2.50 g/min.  
Control temperature: 1400°C  
Overall efficiency: 74.8%  
Coating rate: 23.0  $\mu\text{m}/\text{min.}$   
Microhardness: 89-DPH  
Boron content: 1.8%  
Density: 1.964  $\text{g}/\text{cm}^3$

Fig. B-27

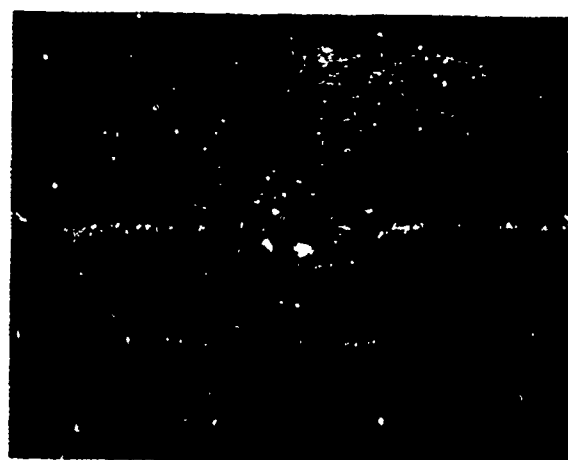
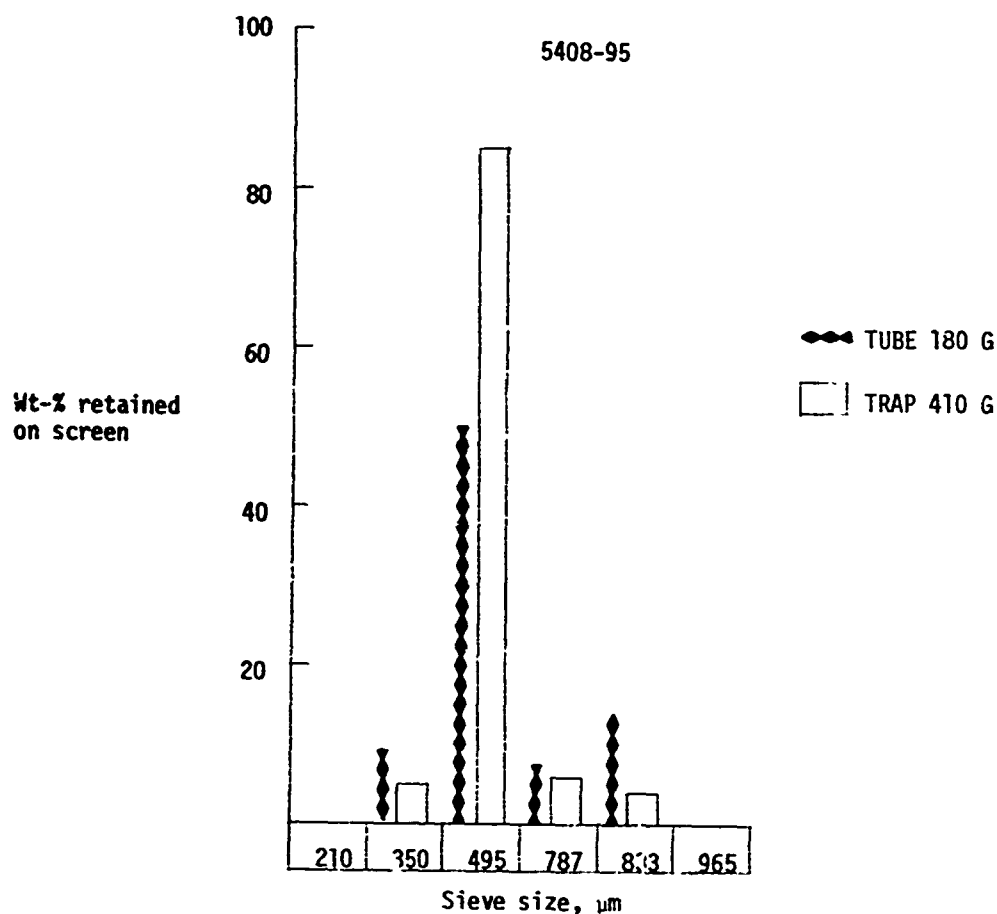


85X

Sample: 5408-93  
 $\text{C}_3\text{H}_8$  concentration: 25%  
 $\text{BCl}_3$  flux: 3.75 g/min.  
 Bed temperature: 1300°C  
 Overall efficiency: 68.7%  
 Coating rate: 5.5  $\mu\text{m}/\text{min}$ .  
 Microhardness: 150-DPH  
 Boron content: 4.6%  
 Density: 2.074  $\text{g}/\text{cm}^3$

Fig. B-28

B-30

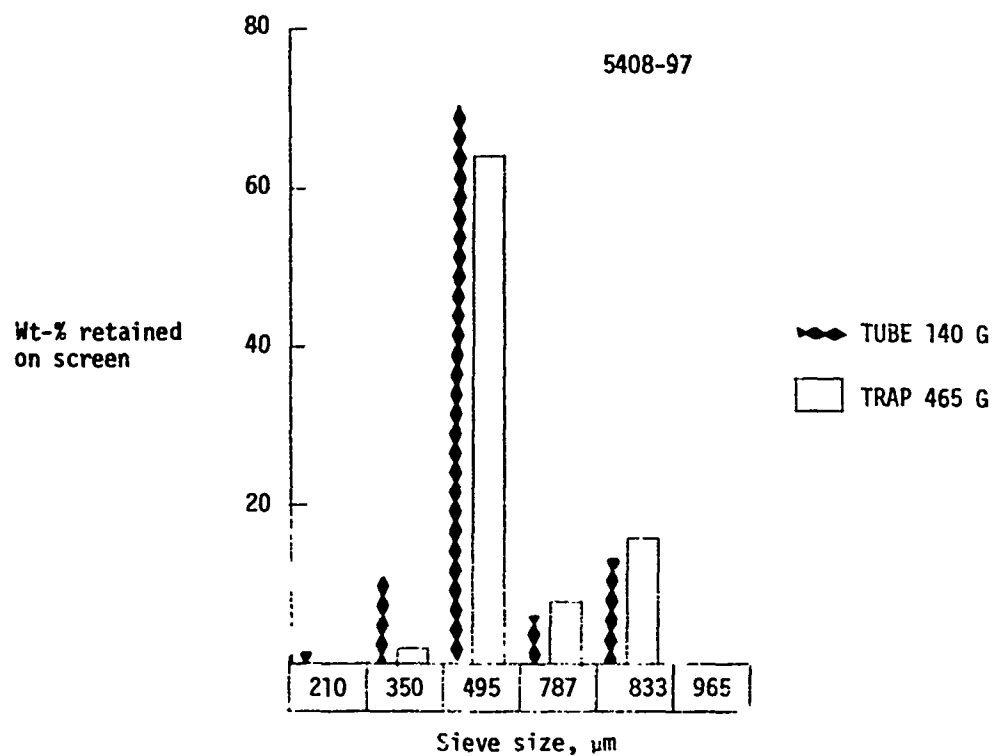


85X

Sample: 5408-95  
 $\text{C}_3\text{H}_8$  concentration: 25%  
 $\text{BCl}_3$  flux: 3.42 g/min.  
 Bed temperature: 1350°C  
 Overall efficiency: 71%  
 Coating rate: 3.4  $\mu\text{m}/\text{min}$ .  
 Microhardness: 136-DPH  
 Boron content: 4.5%  
 Density: 2.114  $\text{g}/\text{cm}^3$

Fig. B-29

B-31



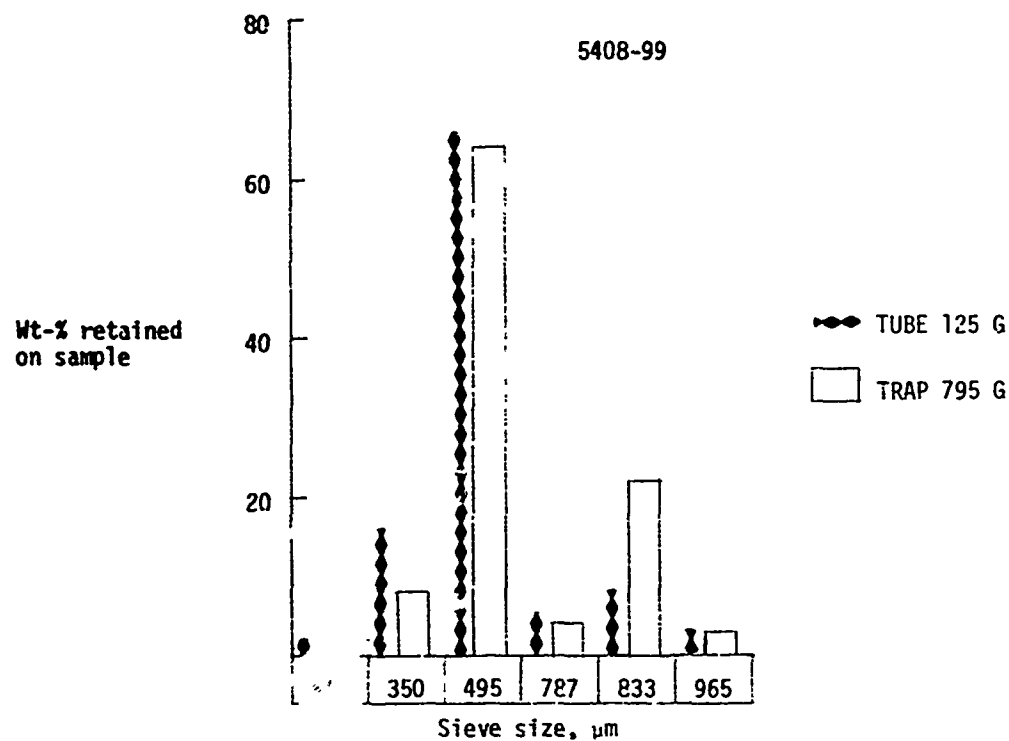
85X

Sample: 5408-97  
 $\text{C}_3\text{H}_8$  concentration: 25%  
 $\text{BCl}_3$  flux: 3.58 g/min.  
 Bed temperature: 1400°C  
 Overall efficiency: 74%  
 Coating rate: 4.2  $\mu\text{m}/\text{min}$ .  
 Microhardness: 122-UPH  
 Boron content: 3.6%  
 Density: 2.060 g/cm<sup>3</sup>

Fig. B-30

B-32



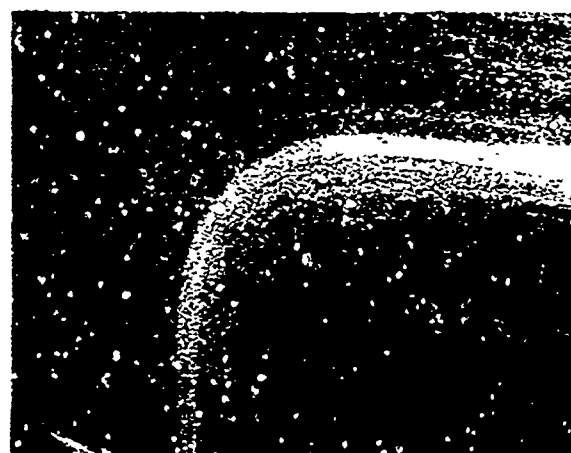
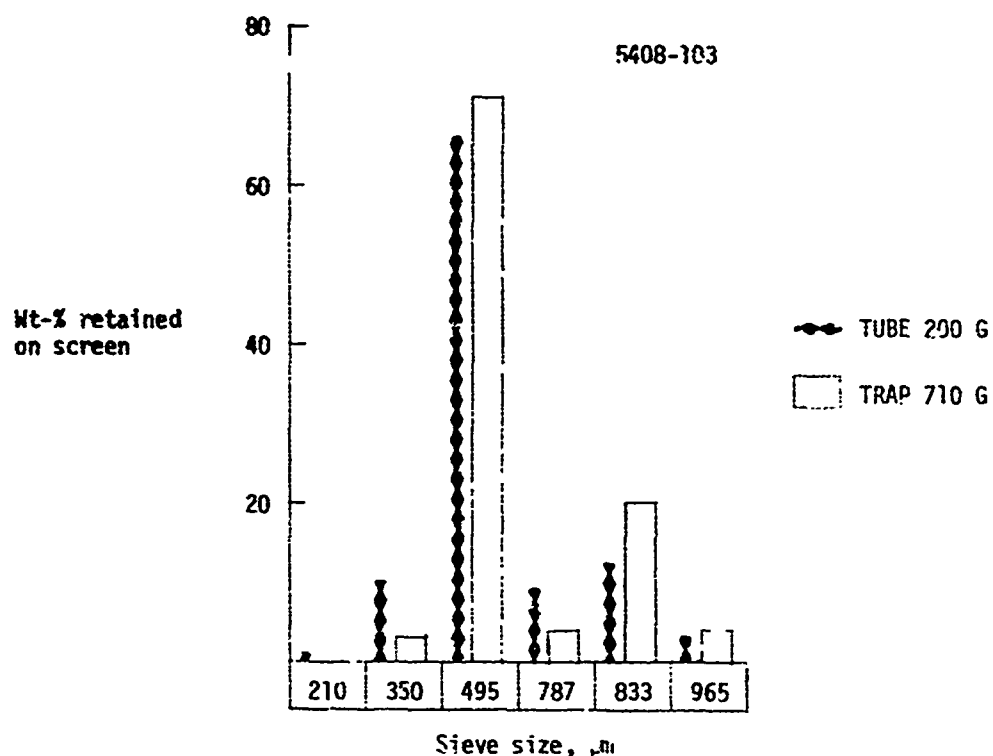


85X

Sample: 5408-99  
 $\text{C}_3\text{H}_8$  concentration: 25%  
 $\text{BCl}_3$  flux: 3.45 g/min.  
 Bed temperature: 1200°C  
 Overall efficiency: 48%  
 Coating rate: 3.2  $\mu\text{m}/\text{min}$ .  
 Microhardness: 186-DPH  
 Boron content: 5.5%  
 Density: 2.128 g/cm<sup>3</sup>

Fig. B-31

B-33

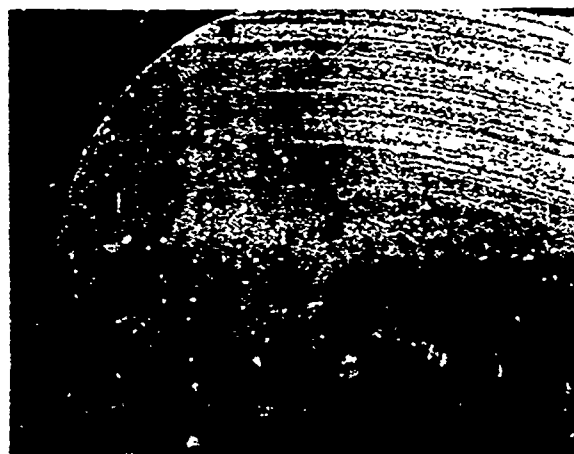
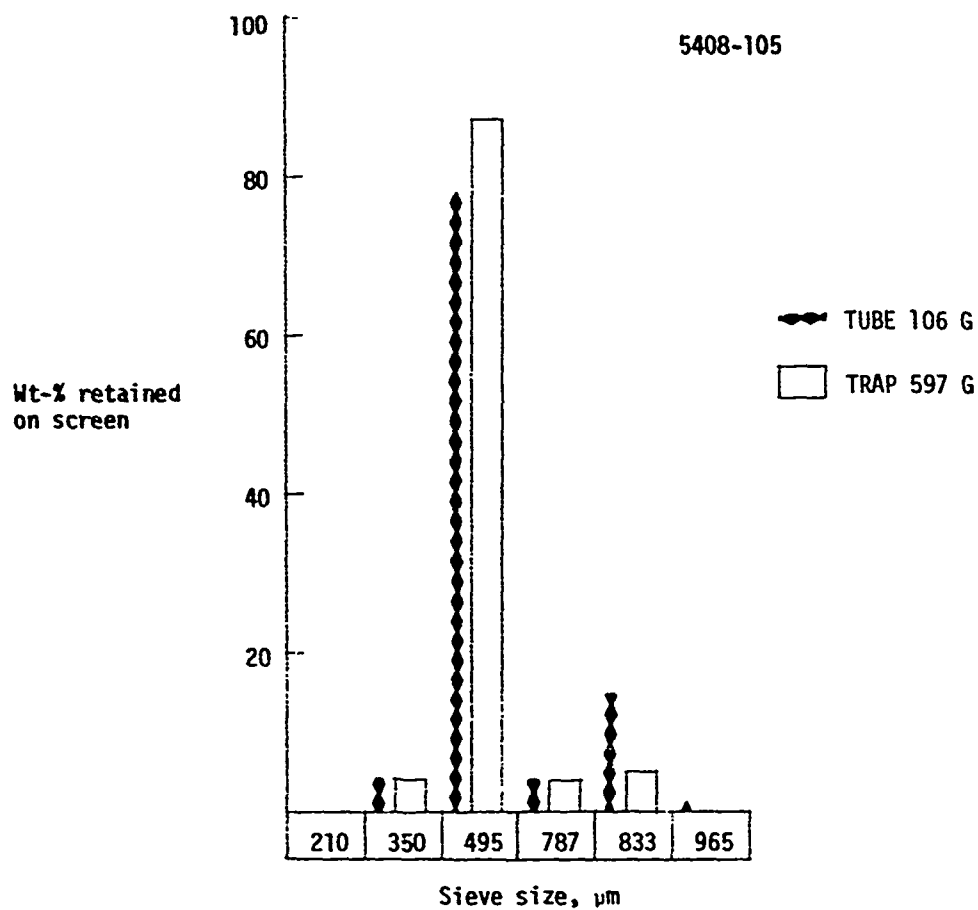


Sample: 5408-103  
 $\text{C}_3\text{H}_8$  concentration: 25%  
 $\text{BCl}_3$  flux: 3.38 g/min.  
 Bed temperature: 1250°C  
 Overall efficiency: 60%  
 Coating rate: 3.4  $\mu\text{m}/\text{min}$ .  
 Microhardness: 161-DPH  
 Boron content: 4.3%  
 Density: 2.053  $\text{g}/\text{cm}^3$

85X

Fig. B-32

B-32

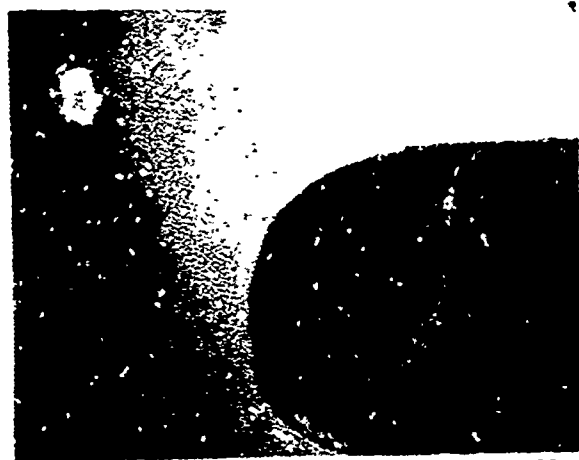
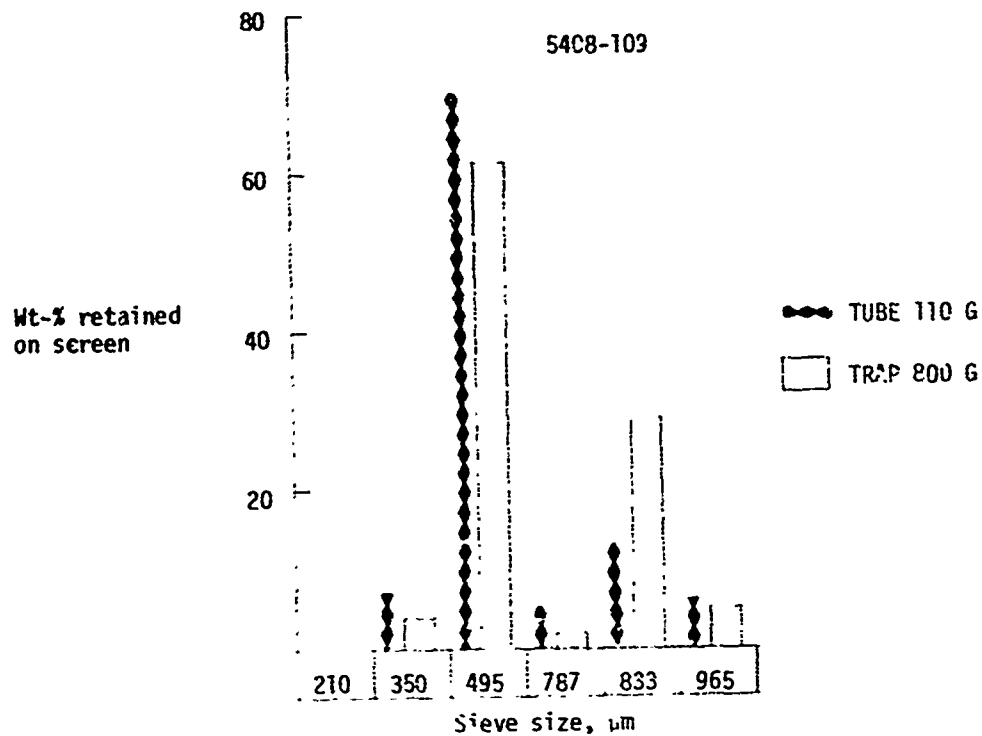


85X

Sample: 5408-105  
 $\text{C}_2\text{H}_8$  concentration: 25%  
 $\text{BCl}_3$  flux: 5.3 g/min.  
 Bed temperature: 1200°C  
 Overall efficiency: 18.5%  
 Coating rate: 2.8  $\mu\text{m}/\text{min}$ .  
 Microhardness: 216-DPH  
 Boron content: N.D.  
 Density: 2.095  $\text{g}/\text{cm}^3$

Fig. B-33

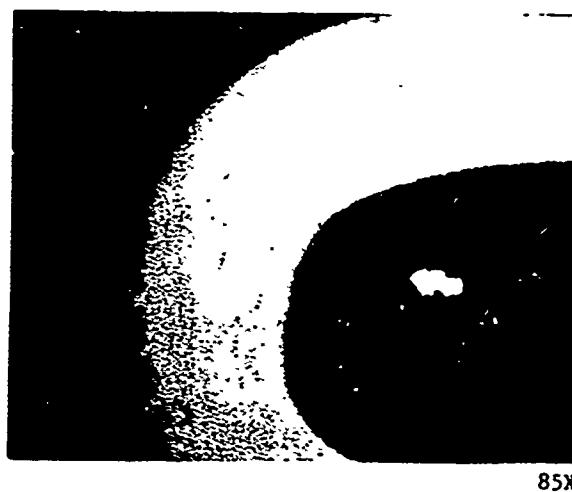
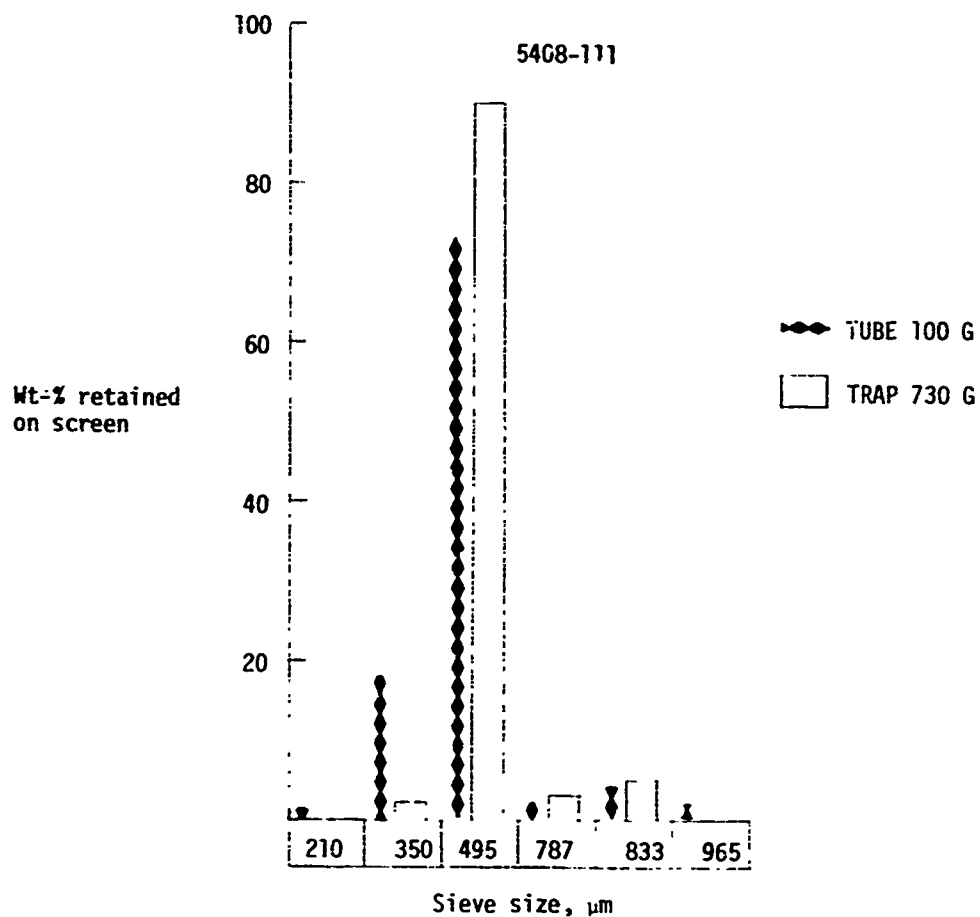
B-35



85X

Sample: 5408-109  
 $\text{C}_3\text{H}_8$  concentration: 25%  
 $\text{BCl}_3$  flux: 0.28 g/min.  
 Bed temperature: 1350°C  
 Overall efficiency: 48%  
 Coating rate: 5.1  $\mu\text{m}/\text{min}$ .  
 Microhardness: 170-DPH  
 Boron content: In progress  
 Density: 1.628  $\text{g}/\text{cm}^3$

Fig. B-34



Sample: 5408-111  
 $\text{C}_3\text{H}_8$  concentration: 25%  
 $\text{BCl}_3$  flux: 0.33 g/min.  
 Bed temperature: 1250°C  
 Overall efficiency: 37%  
 Coating rate: 3.0  $\mu\text{m}/\text{min}$ .  
 Microhardness: 223-DPH  
 Boron content: In progress  
 Density: 1.928 g/cm<sup>3</sup>

85X

Fig. B-35

B-37

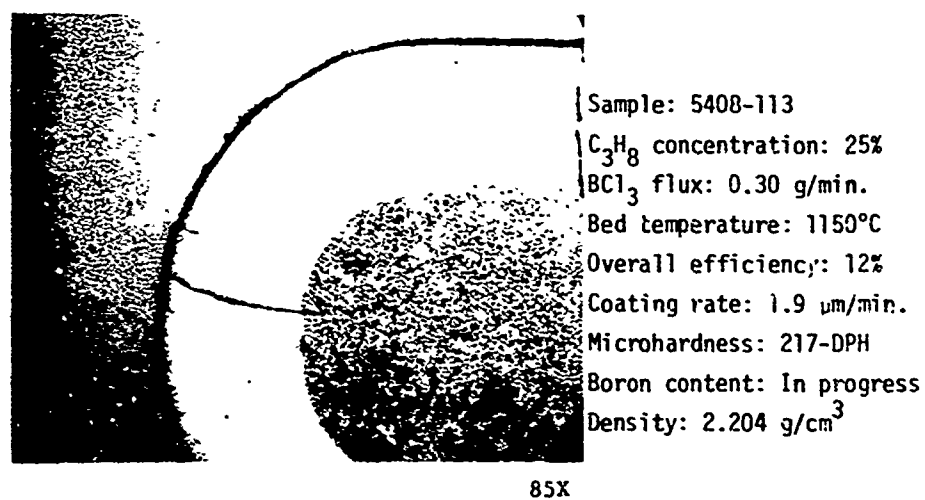
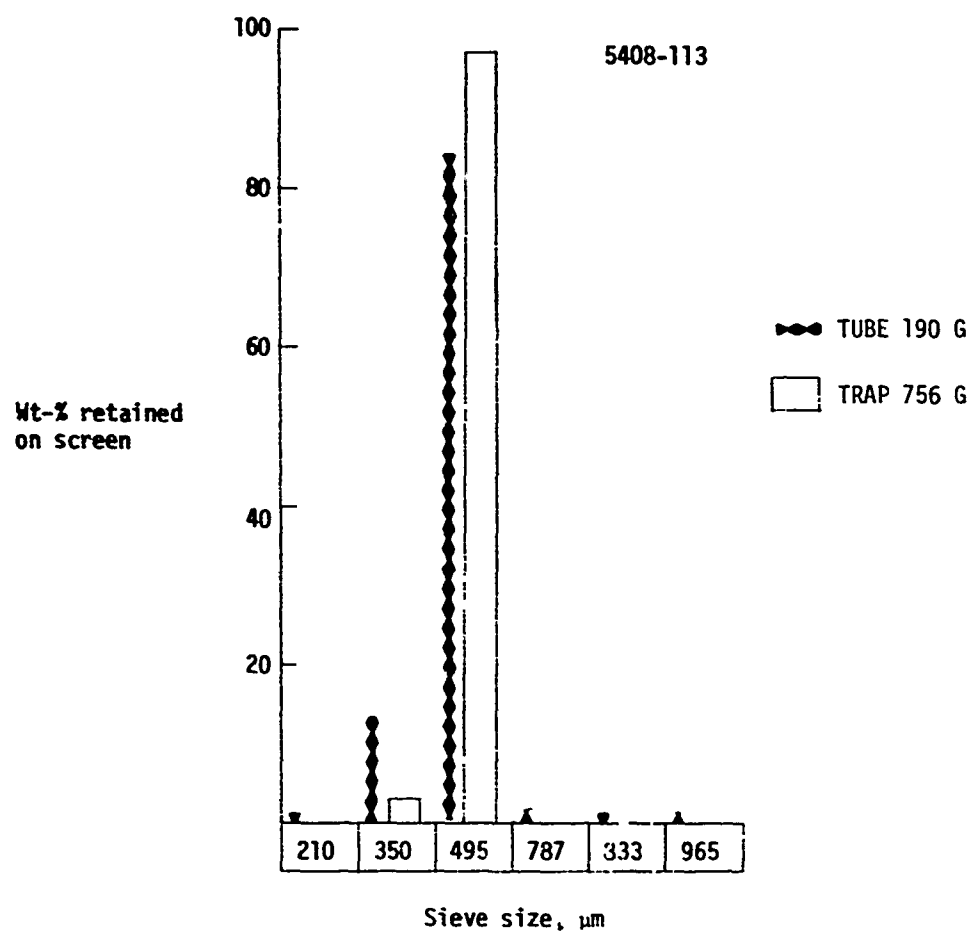
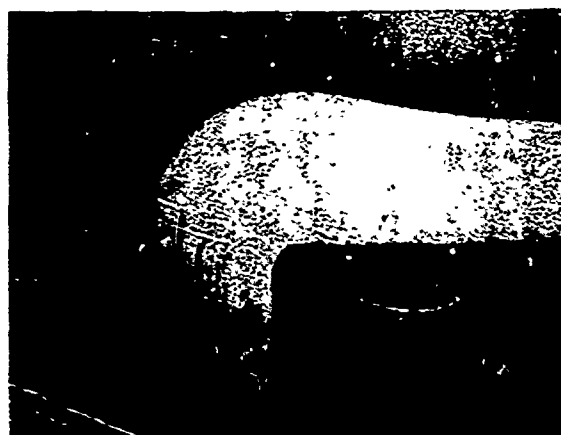
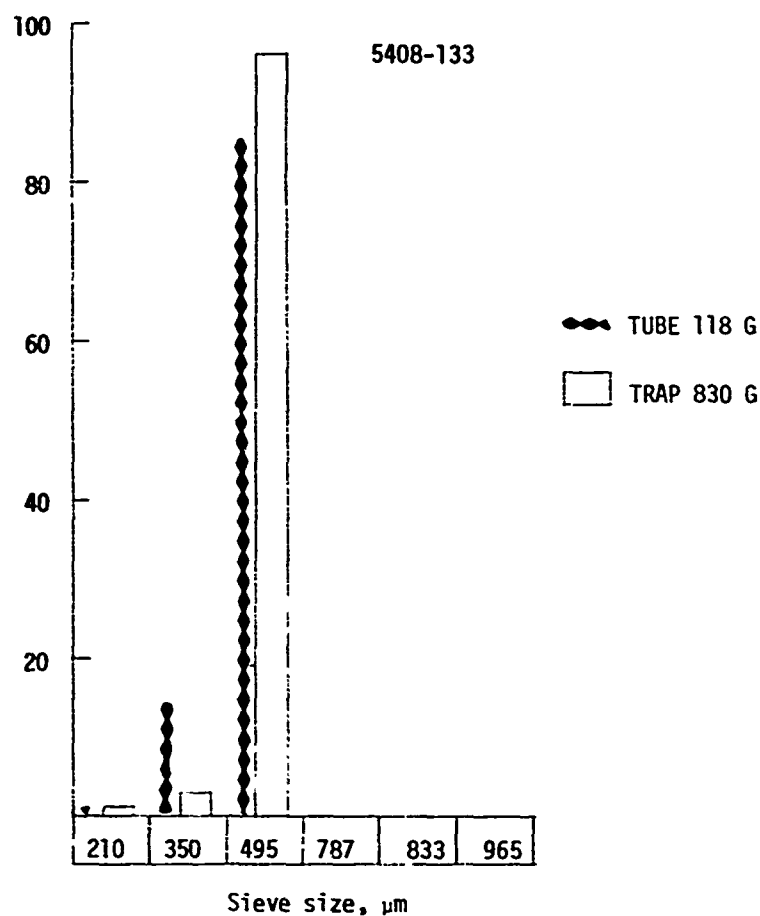


Fig. B-36

B-38

Wt-% retained  
on screen

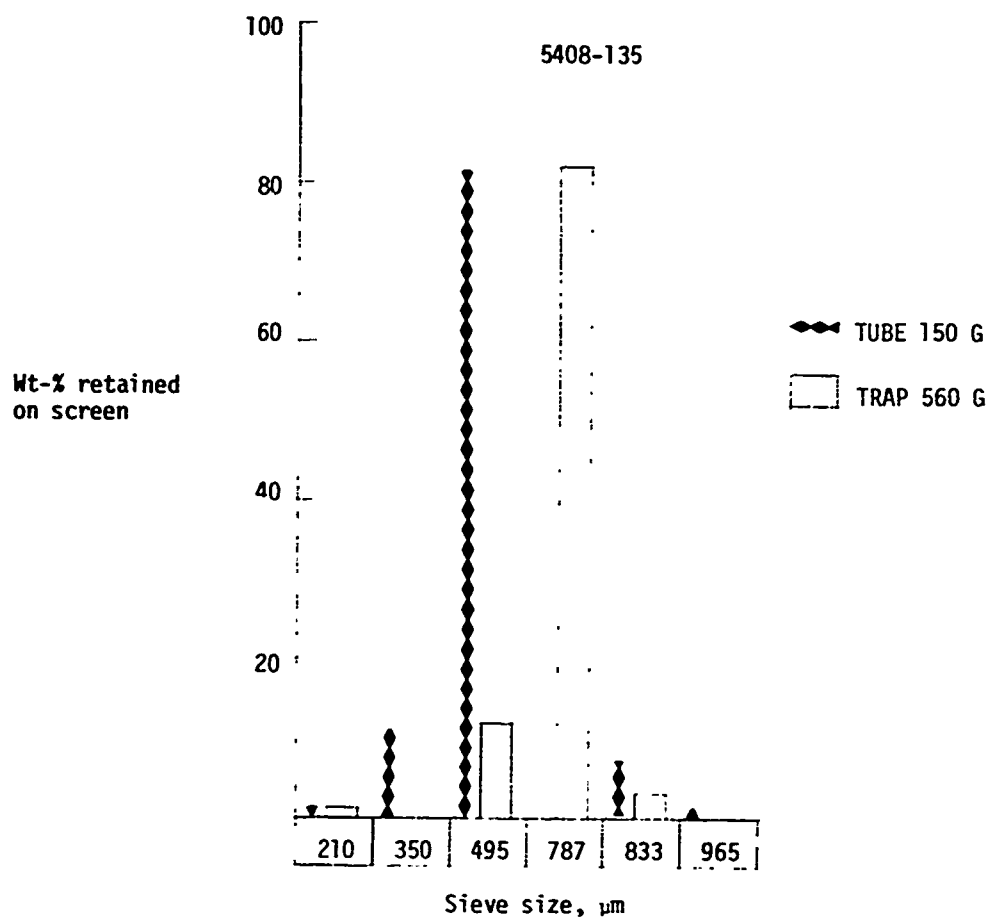


42X

Sample: 5408-133  
 $\text{CH}_4$  concentration: 25%  
 $\text{BCl}_3$  flux: 0.35 g/min.  
 Control temperature: 1350°C  
 Overall efficiency: 38%  
 Coating rate: 1.7  $\mu\text{m}/\text{min}$ .  
 Microhardness: 150-DPH  
 Boron content: In progress  
 Density: 1.843  $\text{g}/\text{cm}^3$

Fig. B-37

B-39



Sample: 5408-135  
 $\text{CH}_4$  concentration: 60%  
 $\text{BCl}_3$  flux: 0.30 g/min.  
 Bed temperature: 1350°C  
 Overall efficiency: 58%  
 Coating rate: 2.1  $\mu\text{m}/\text{min}$ .  
 Microhardness: 215-DPH  
 Boron content: In progress  
 Density: 1.737  $\text{g}/\text{cm}^3$

85X

Fig. B-38

B-40



TUBE: 125 G

TRAP: 705 G

Wt-% retained  
on screen



85X

Sample: 5408-137

CH<sub>4</sub> concentration: 25%

BCl<sub>3</sub> flux: 0.30 g/min.

Control temperature: 1200°C

Overall efficiency: 27.9%

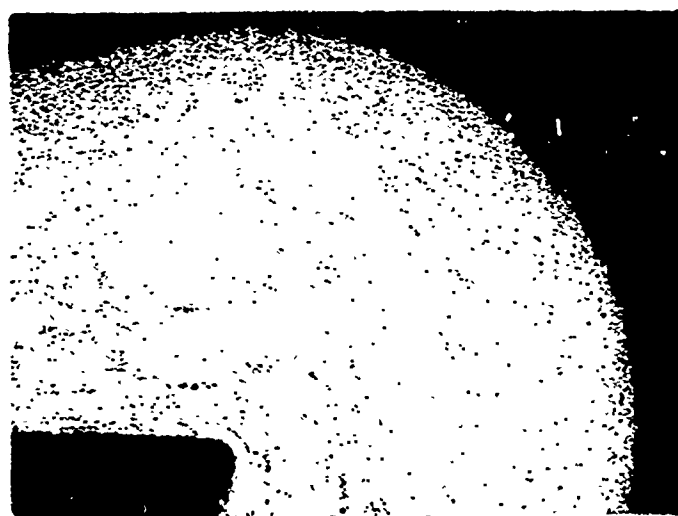
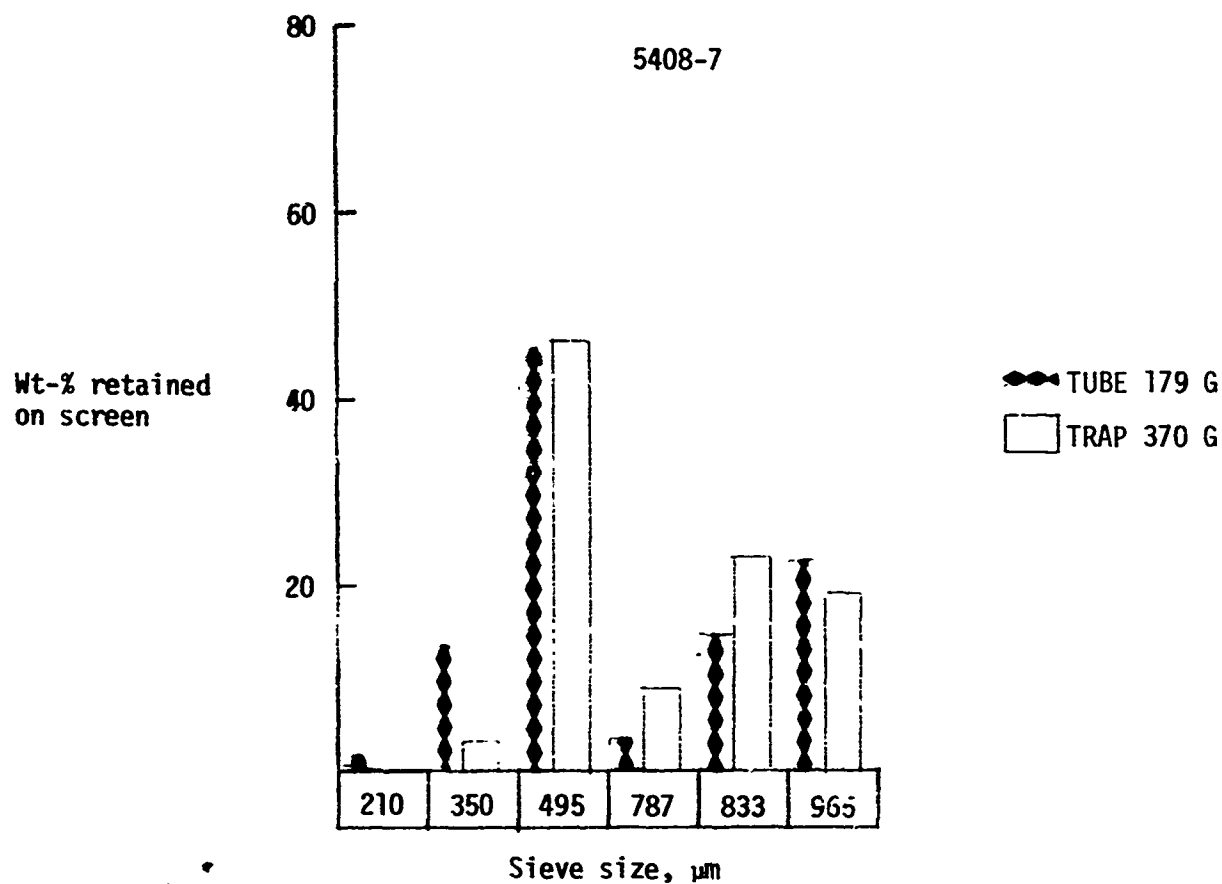
Coating rate: 0.85 μm/min.

Microhardness: 214-DPH

Density: 2.039 g/cm<sup>3</sup>

Fig. B-39

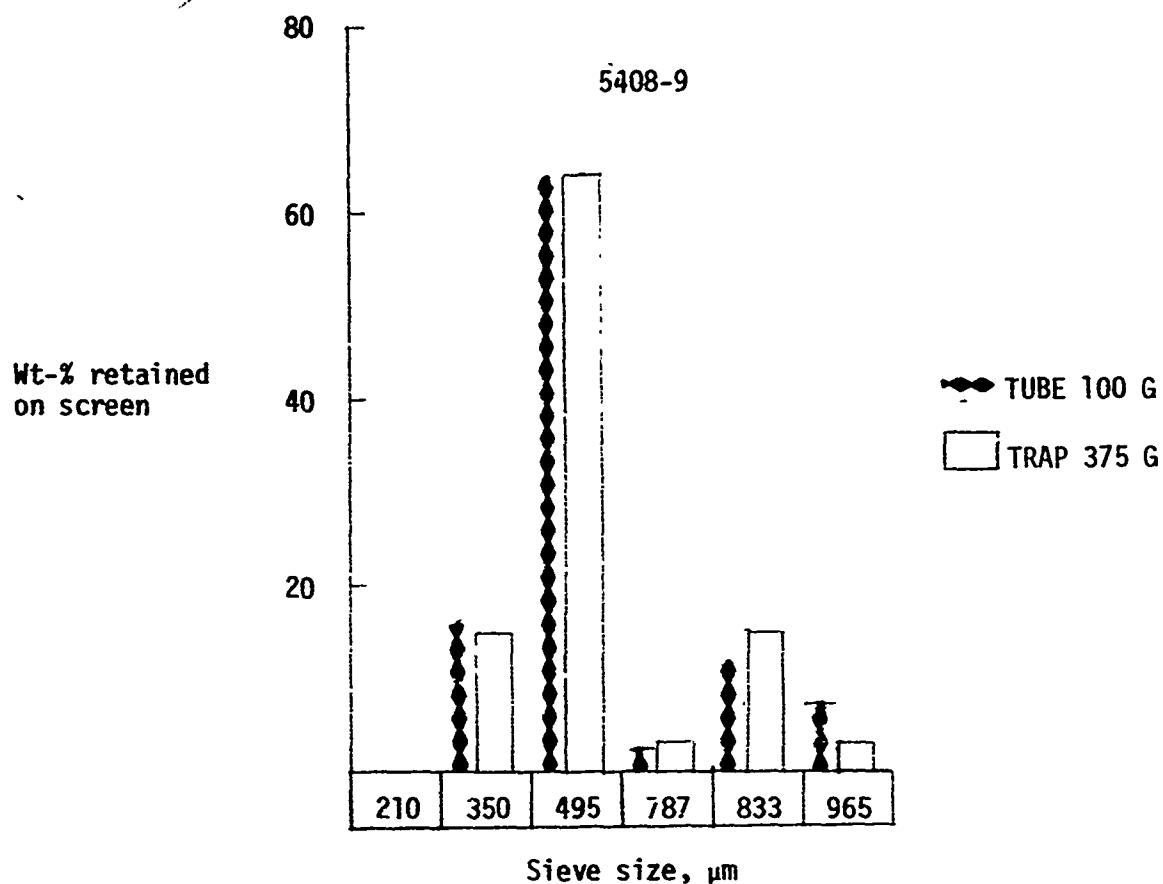
B-41



85X

Sample: 5408-7  
 $\text{C}_3\text{H}_8$  concentration: 60%  
 Bed temperature: 1220°C  
 Overall efficiency: 26%  
 Coating rate: 5.9  $\mu\text{m}/\text{min.}$   
 Microhardness: 219-DPH  
 Density: 1.974  $\text{g}/\text{cm}^3$   
 $L_c$ : 36 Å

Fig. B-1

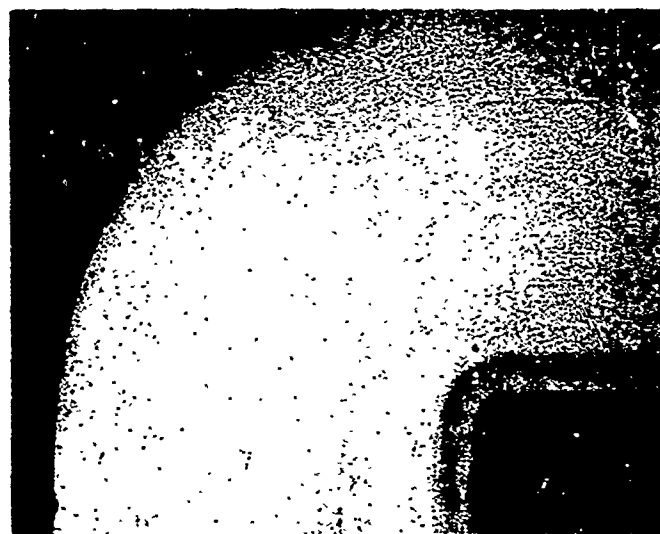
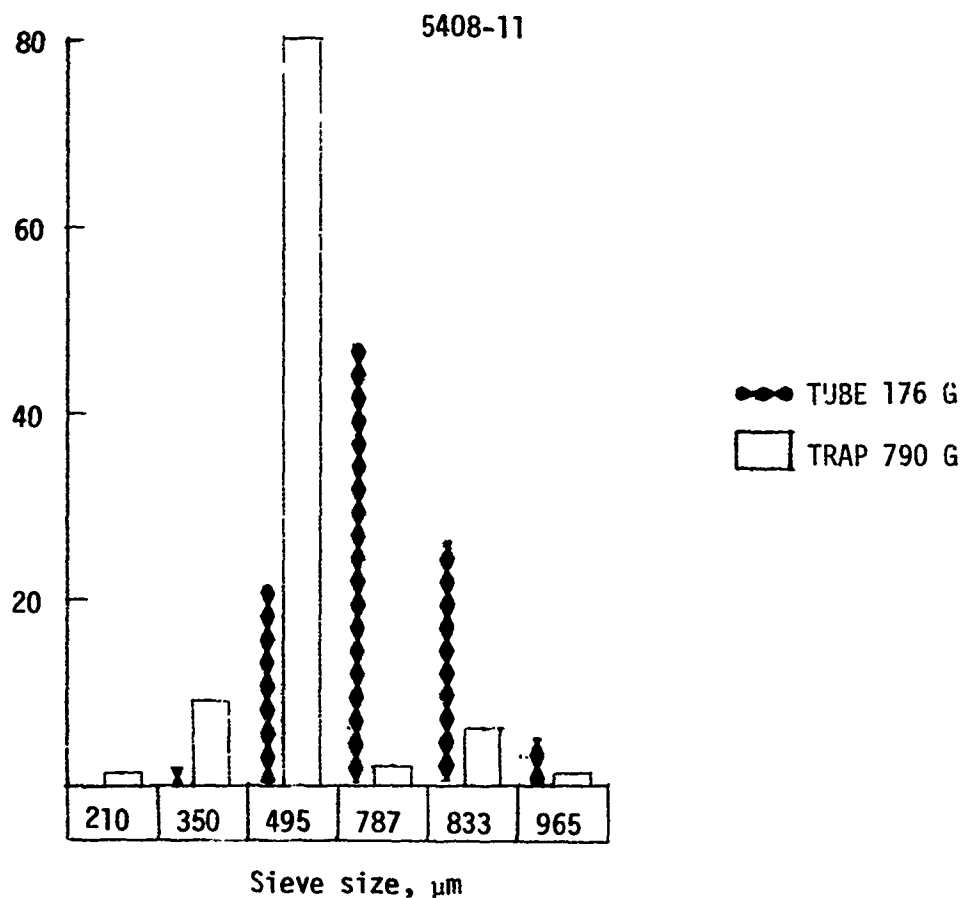


Sample: 5408-9  
 $\text{C}_3\text{H}_8$  concentration: 25%  
 Bed temperature: 1260°C  
 Overall efficiency: 40%  
 Coating rate: 4.2  $\mu\text{m}/\text{min.}$   
 Microhardness: 192 DPH  
 Density: N.D.  
 $L_c$ : N.D.

85X

Fig. B-2

Wt-% retained  
on screen

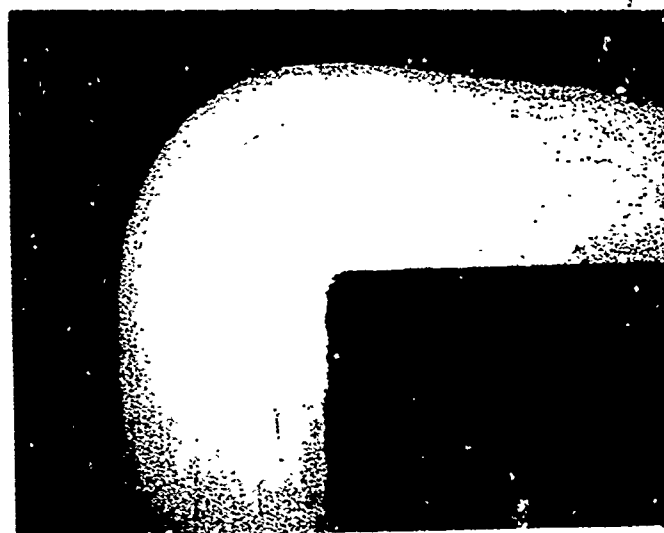
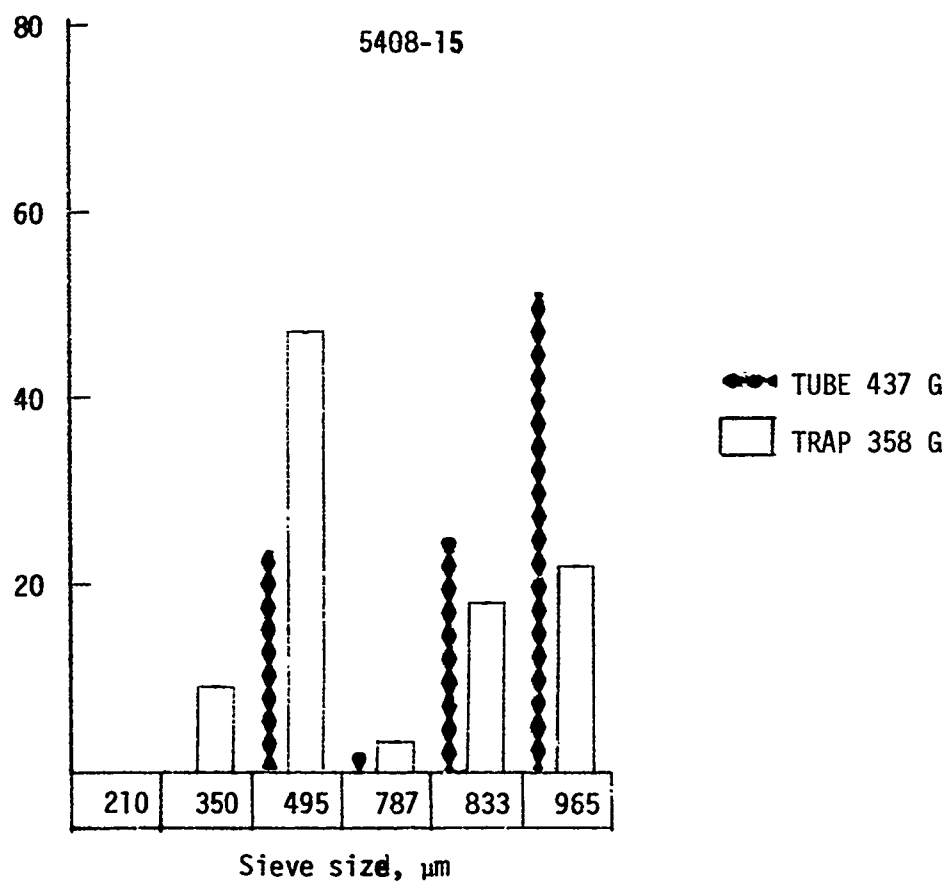


Sample: 5408-11  
 $\text{C}_3\text{H}_8$  concentration: 7%  
 Bed temperature: 1330°C  
 Overall efficiency: N.D.  
 Coating rate: 1.4  $\mu\text{m}/\text{min}$ .  
 Microhardness: 154-DPH  
 Density: 1.553  $\text{g}/\text{cm}^3$   
 $L_c$ : 23 Å

85X

Fig. B-3

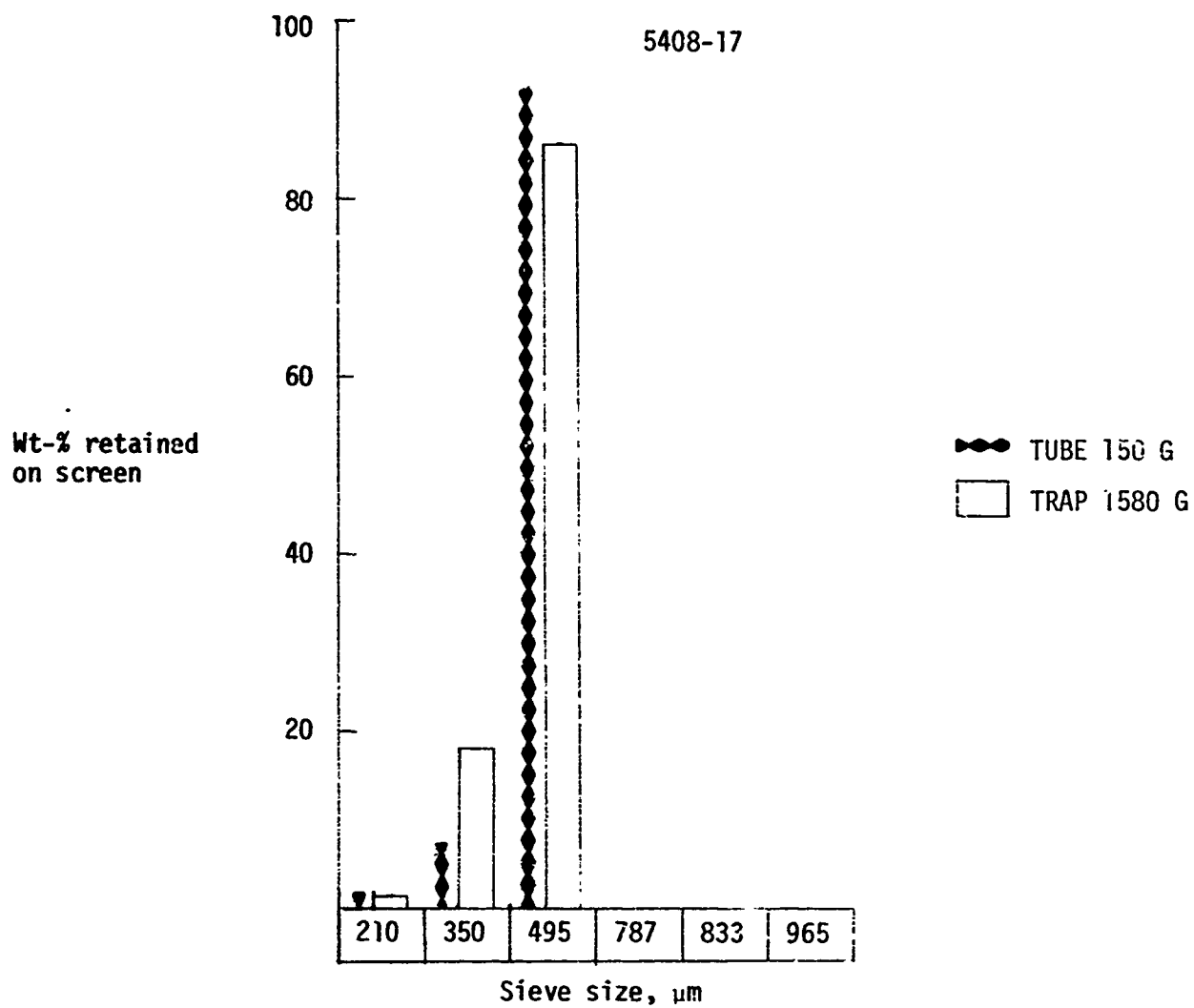
Wt-% retained  
on screen



Sample: 5408-15  
 $\text{C}_3\text{H}_8$  concentration: 25%  
 Bed temperature: 1260°C  
 Overall efficiency: 35%  
 Coating rate: 2.3  $\mu\text{m}/\text{min.}$   
 Microhardness: 190-DPH  
 Density: N.D.  
 $L_c$ : N.D.

42X

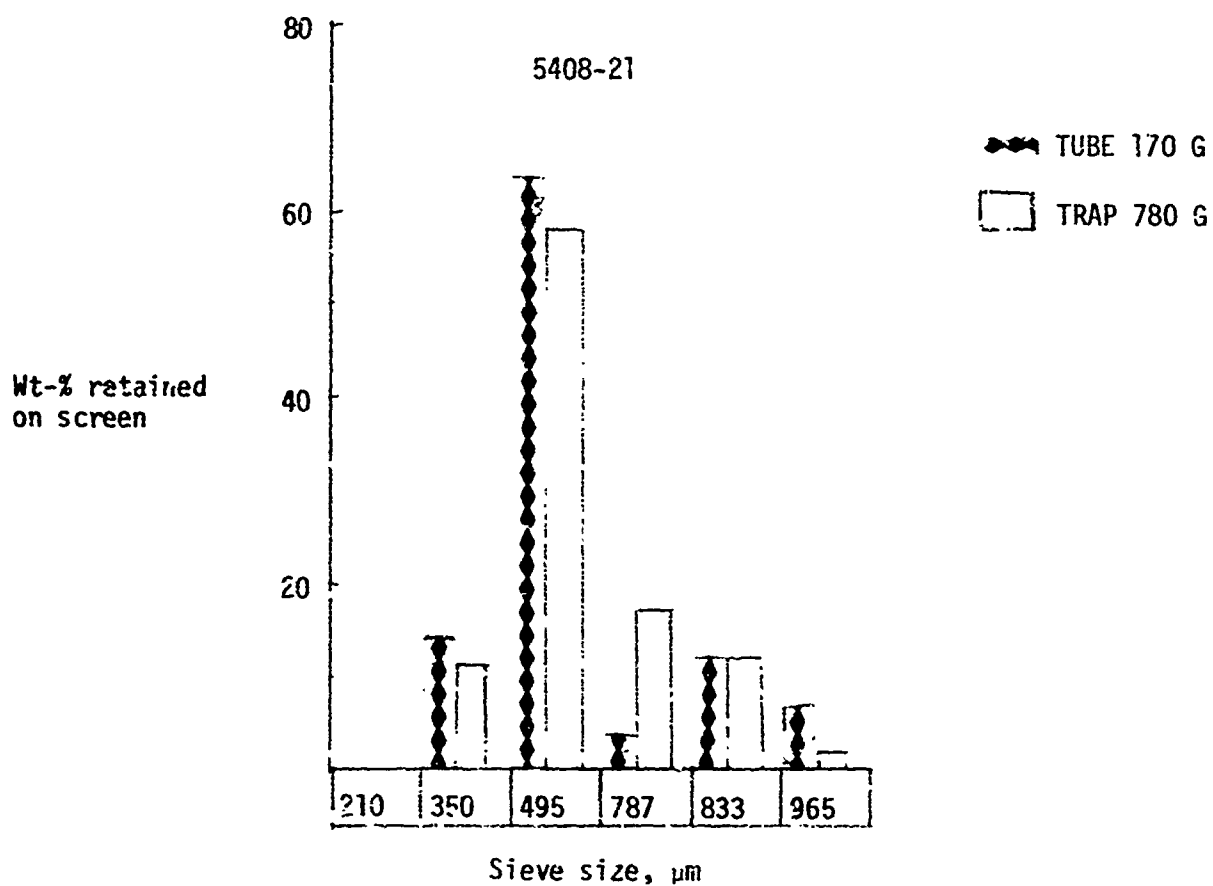
Fig. B-4



Sample: 5408-17  
 $\text{C}_3\text{H}_8$  concentration: 3%  
 Bed temperature:  $1330^\circ\text{C}$   
 Overall efficiency: 73%  
 Coating rate:  $0.91 \mu\text{m}/\text{min.}$   
 Microhardness: 153-DPH  
 Density:  $1.457 \text{ g}/\text{cm}^3$   
 $L_c$ : 20 Å

85X

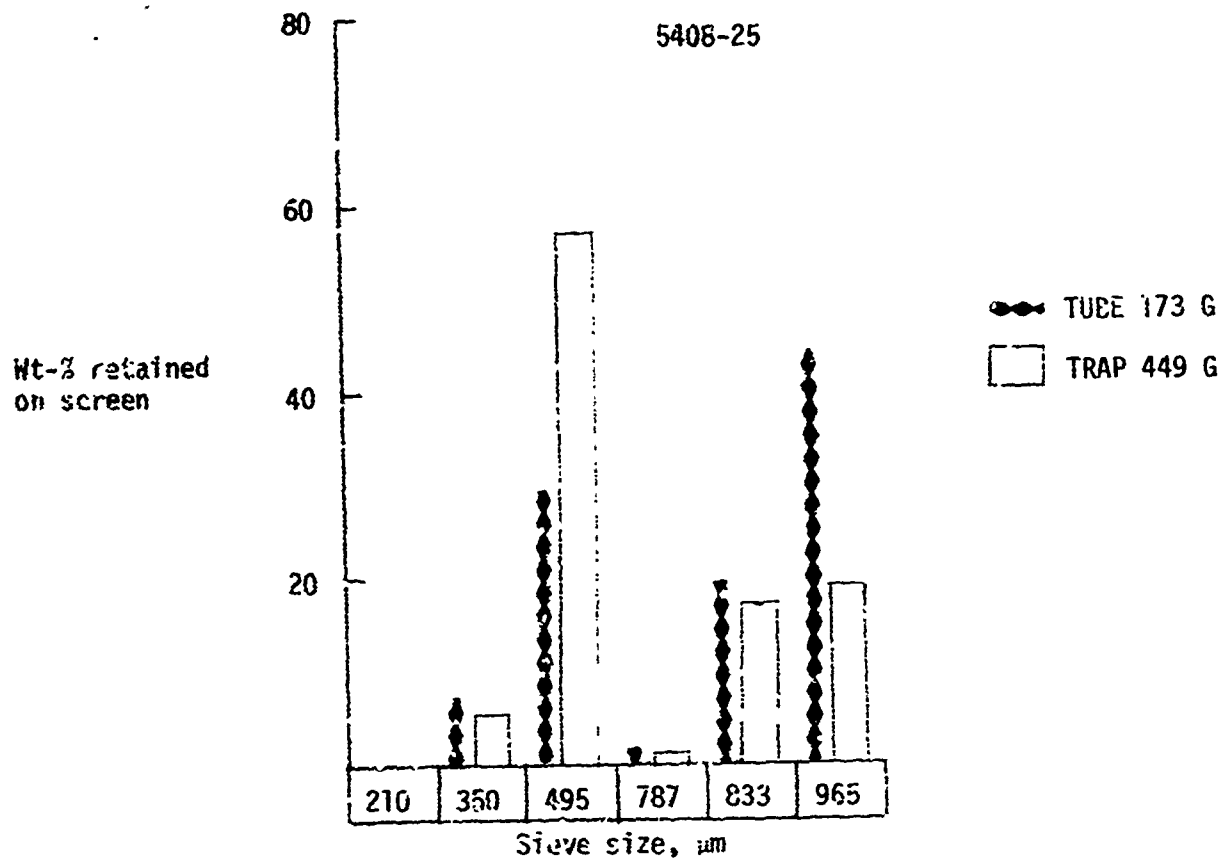
Fig. B-5



Sample: 5408-21  
 Bed temperature: 1190°C  
 Propane concentration: 25%  
 Overall efficiency: 55%  
 Coating ratio: 2.9  $\mu\text{m}/\text{min}$ .  
 Microhardness: 226-DPH  
 Density: 1.914  
 $L_c$ : 32 Å

85X

Fig. B-6

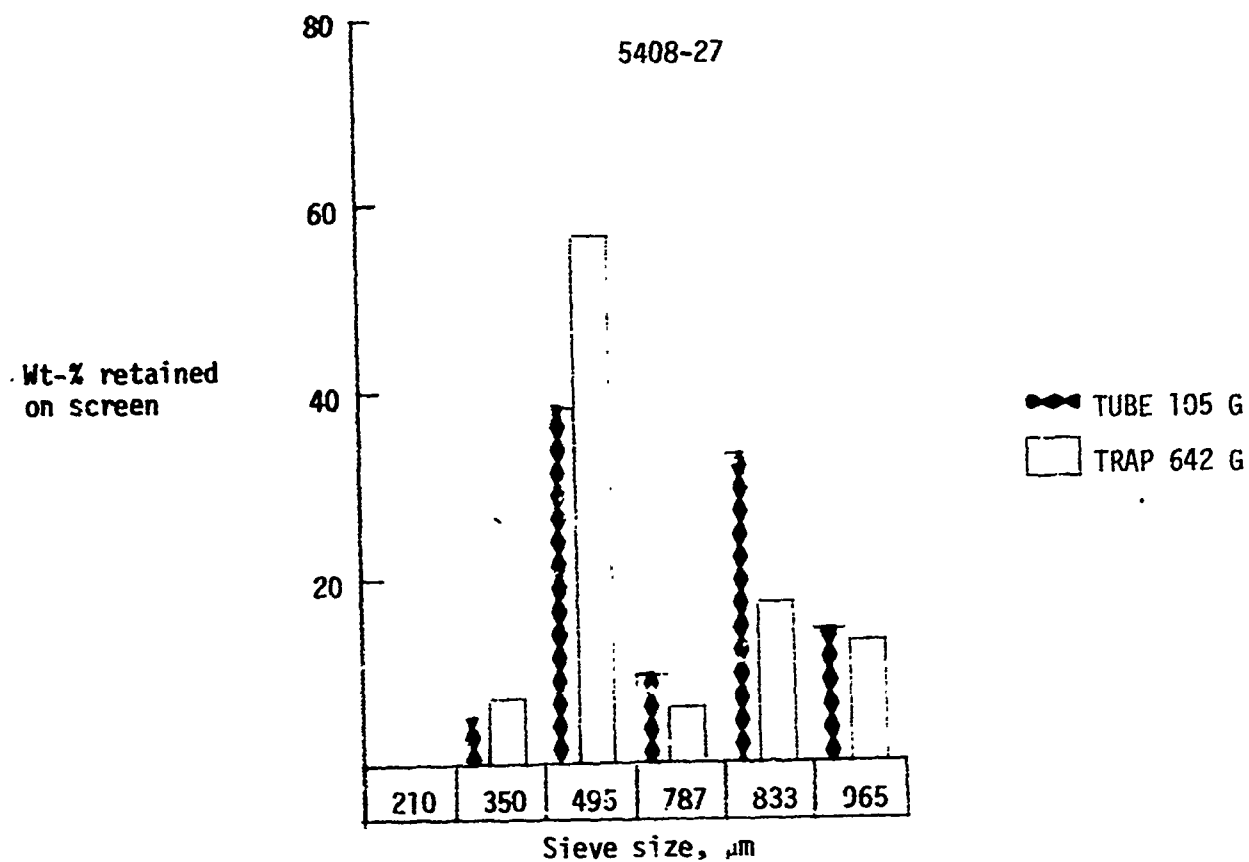


Sample: 5408-25  
 $\text{C}_3\text{H}_8$  concentration: 60%  
 Bed temperature: 1300°C  
 Overall efficiency: 35%  
 Coating rate: 8.1  $\mu\text{m}/\text{min.}$   
 Microhardness: 170-DPH  
 Density: 1.753  $\text{g}/\text{cm}^3$   
 $L_c$ : 29 Å

85X

Fig. B-7





85X

Sample: 5408-27

$\text{C}_3\text{H}_8$  concentration: 25%

Bed temperature: 1340°C

Overall efficiency: 25%

Coating rate: 5.7  $\mu\text{m}/\text{min.}$

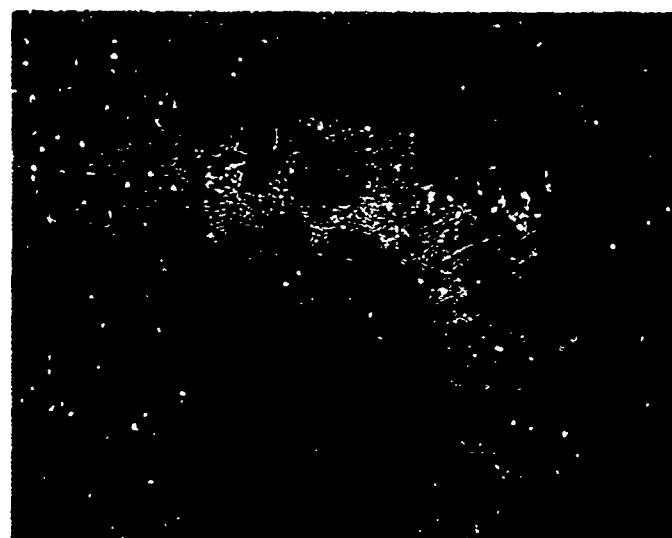
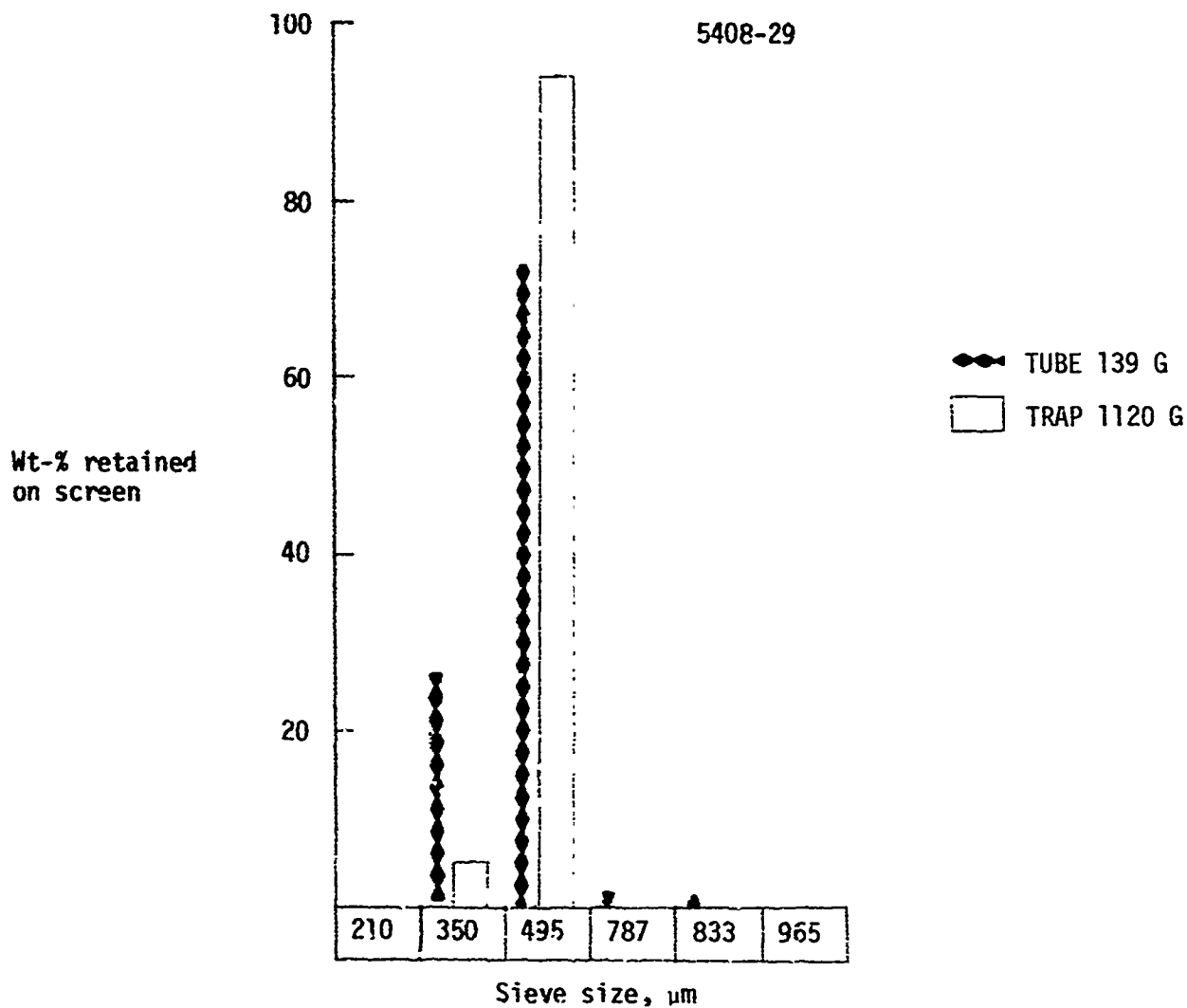
Microhardness: 156-DPH

Density: 1.592  $\text{g}/\text{cm}^3$

$L_c$ : 24 Å

Fig. B-8

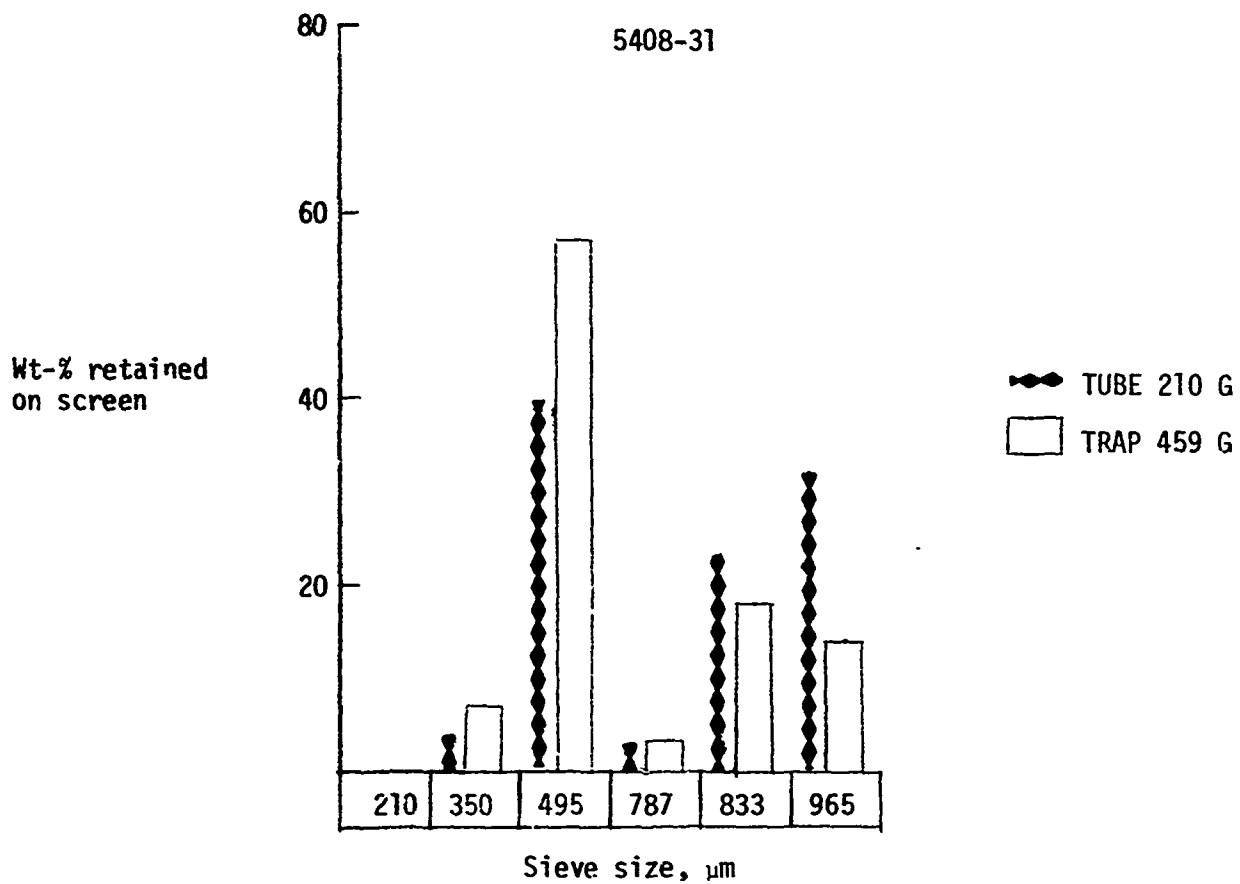
B-10



Sample: 5408-29  
 $\text{C}_3\text{H}_8$  concentration: 7%  
 Bed temperature: 1400°C  
 Overall efficiency: 51%  
 Coating rate: 1.3  $\mu\text{m}/\text{min}$ .  
 Microhardness: 100-DPH  
 Density: 1.353  $\text{g}/\text{cm}^3$   
 $L_c$ : 26 Å

42X

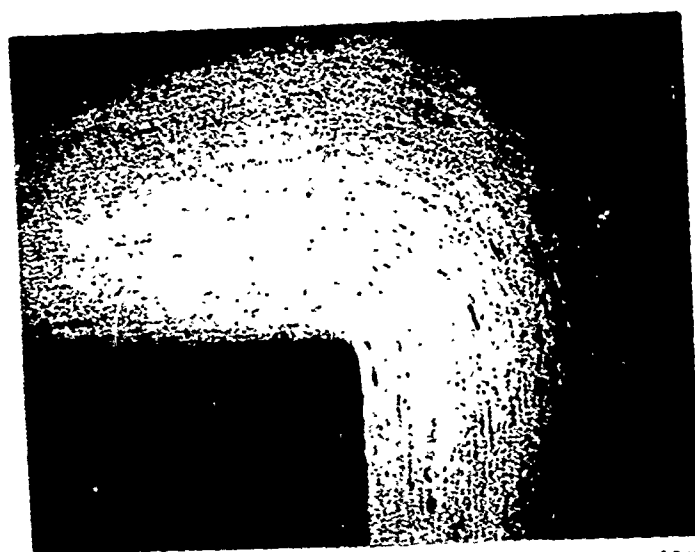
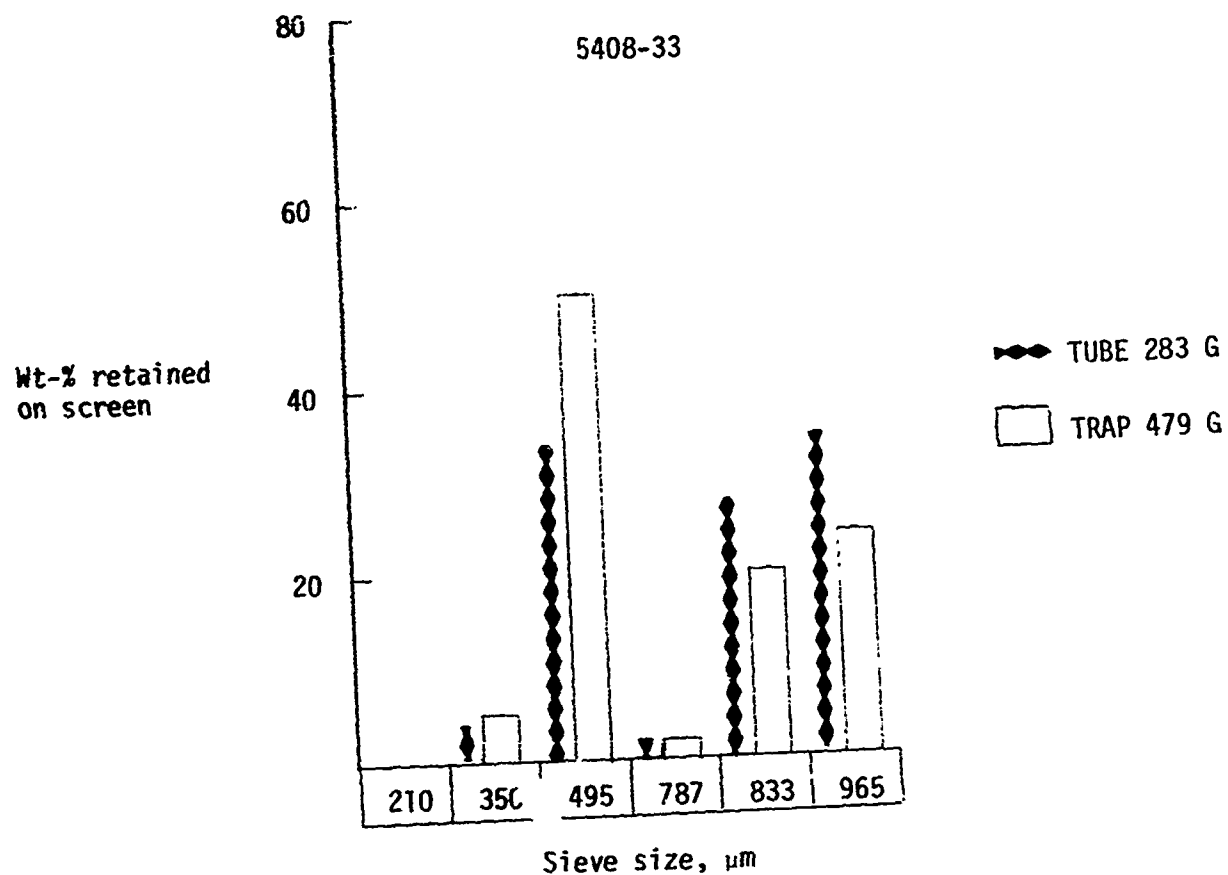
Fig. B-9



Sample: 5408-31  
 $\text{C}_3\text{H}_8$  concentration: 60%  
 Bed temperature: 1230°C  
 Overall efficiency: 40%  
 Coating rate: 6.8  $\mu\text{m}/\text{min.}$   
 Microhardness: 170-DPH  
 Density: 1.823  $\text{g}/\text{cm}^3$   
 $L_c$ : 33 Å

- 42X

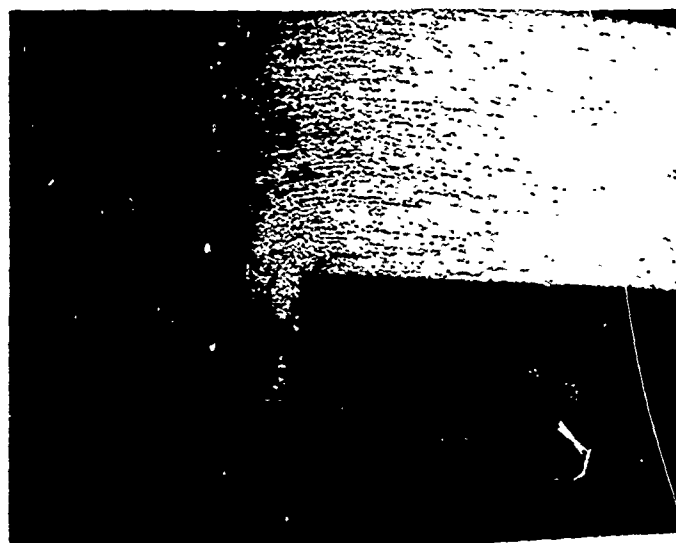
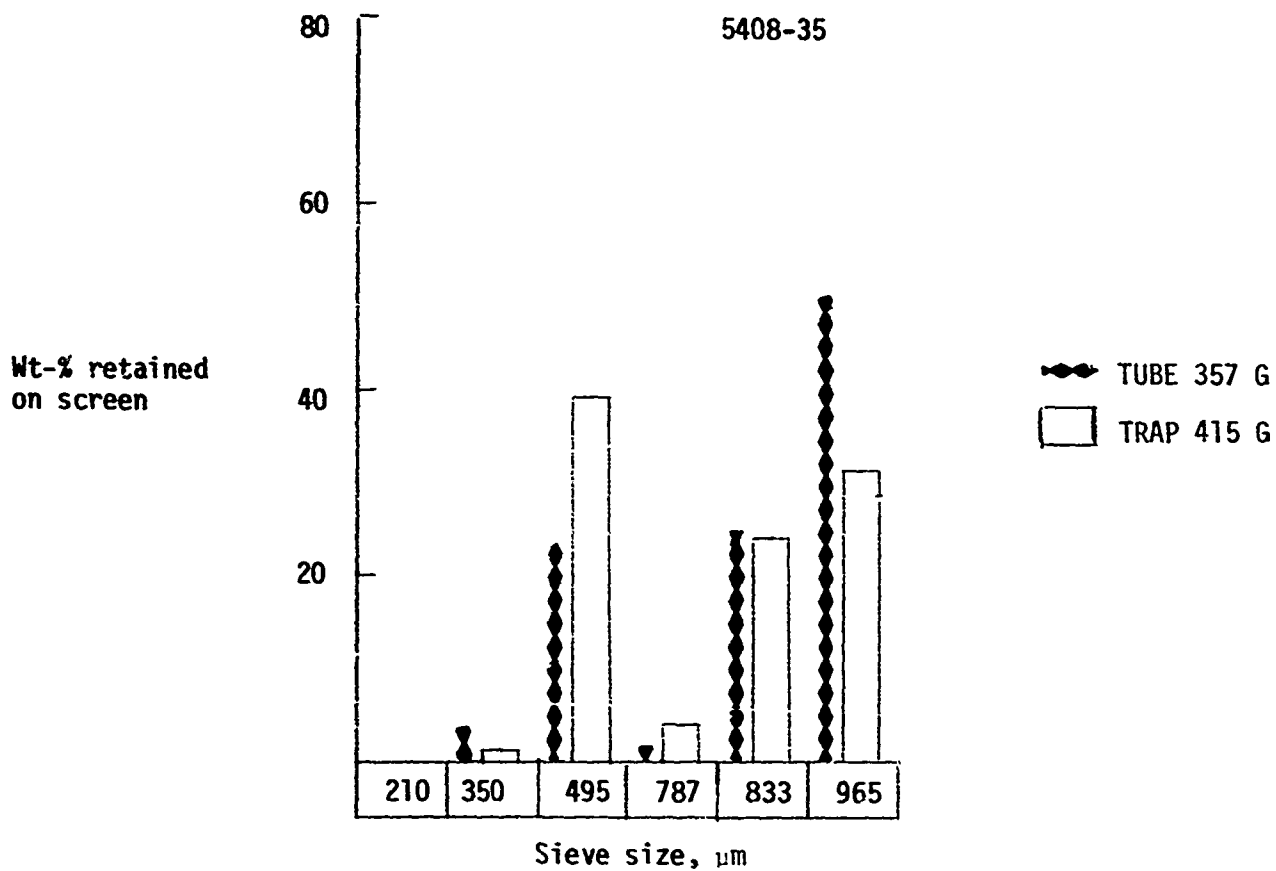
Fig. B-10



42X

Sample: 5408-33  
 $\text{C}_3\text{H}_8$  concentration: 60%  
 Bed temperature: 1355°C  
 Overall efficiency: 52%  
 Coating rate: 9.8  $\mu\text{m}/\text{min}$ .  
 Microhardness: 127-DPH  
 Density: 1.535  $\text{g}/\text{cm}^3$   
 $L_c$ : 26 Å

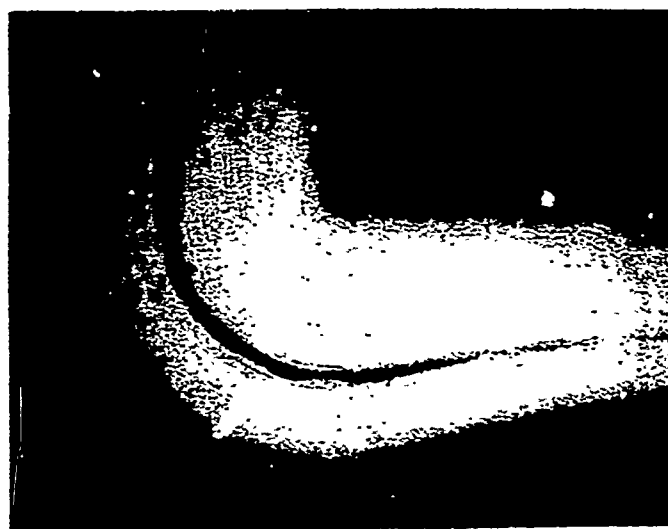
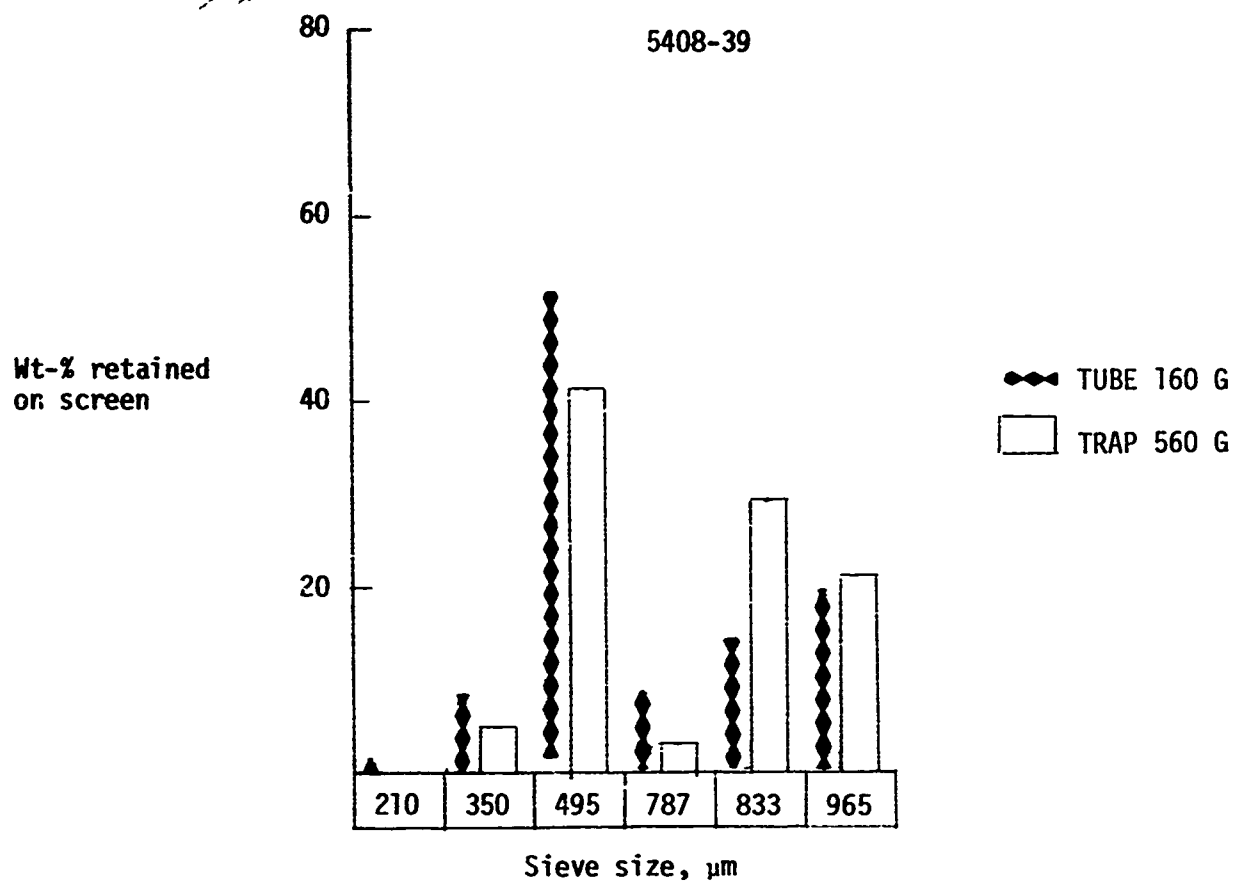
Fig. B-11



Sample: 5408-35  
 $\text{C}_3\text{H}_8$  concentration: 60%  
 Bed temperature: 1400°C  
 Overall efficiency: 55%  
 Coating rate: 8.5  $\mu\text{m}/\text{min.}$   
 Microhardness: 92-DPH  
 Density: 1.459  $\text{g}/\text{cm}^3$   
 $L_c$ : 26 Å

85X

Fig. B-12

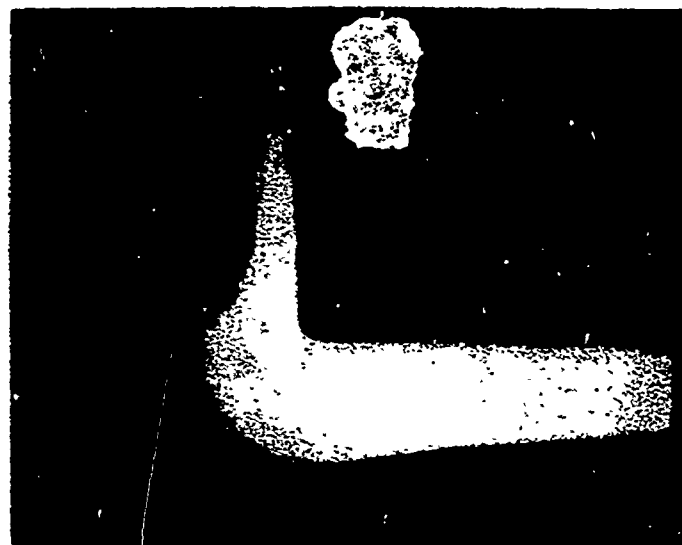
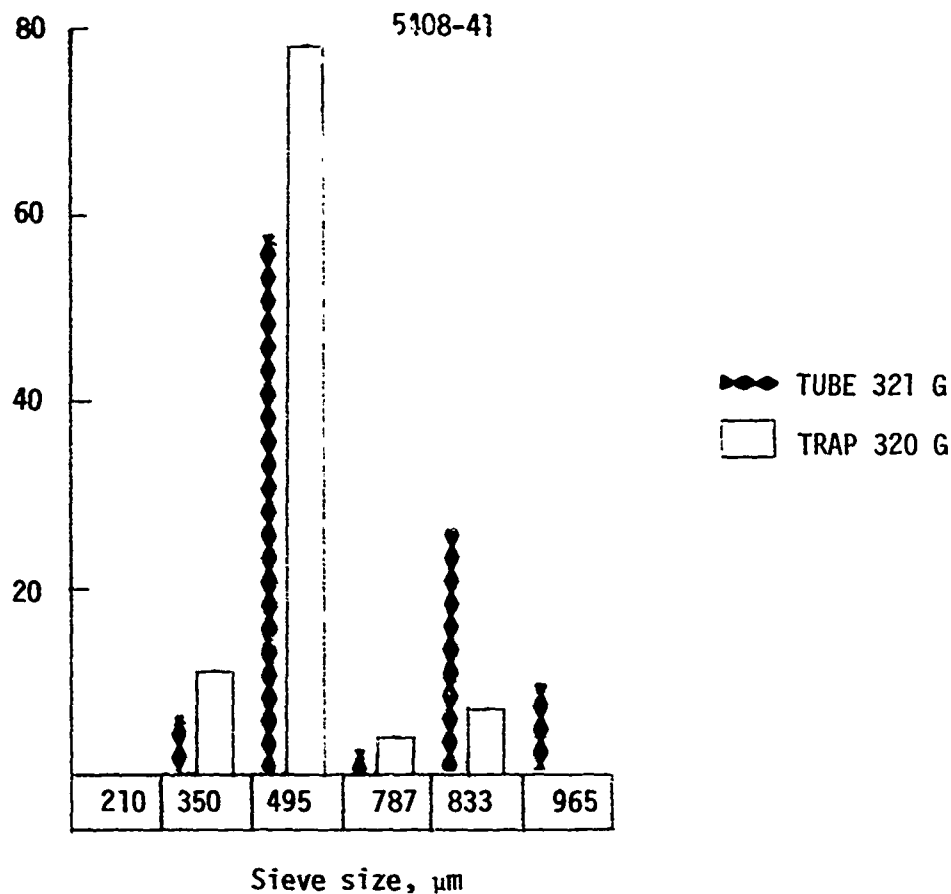


Sample: 5408-39  
 $\text{C}_3\text{H}_8$  concentration: 60% +  
 40%  $\text{H}_2$   
 Bed temperature: 1300°C  
 Overall efficiency: 47%  
 Coating rate: 8.0  $\mu\text{m}/\text{min}$ .  
 Microhardness: 187-DPH  
 Density: 1.813  $\text{g}/\text{cm}^3$   
 $L_c$ : 31 Å

42X

Fig. B-13

Wt-% retained  
on screen

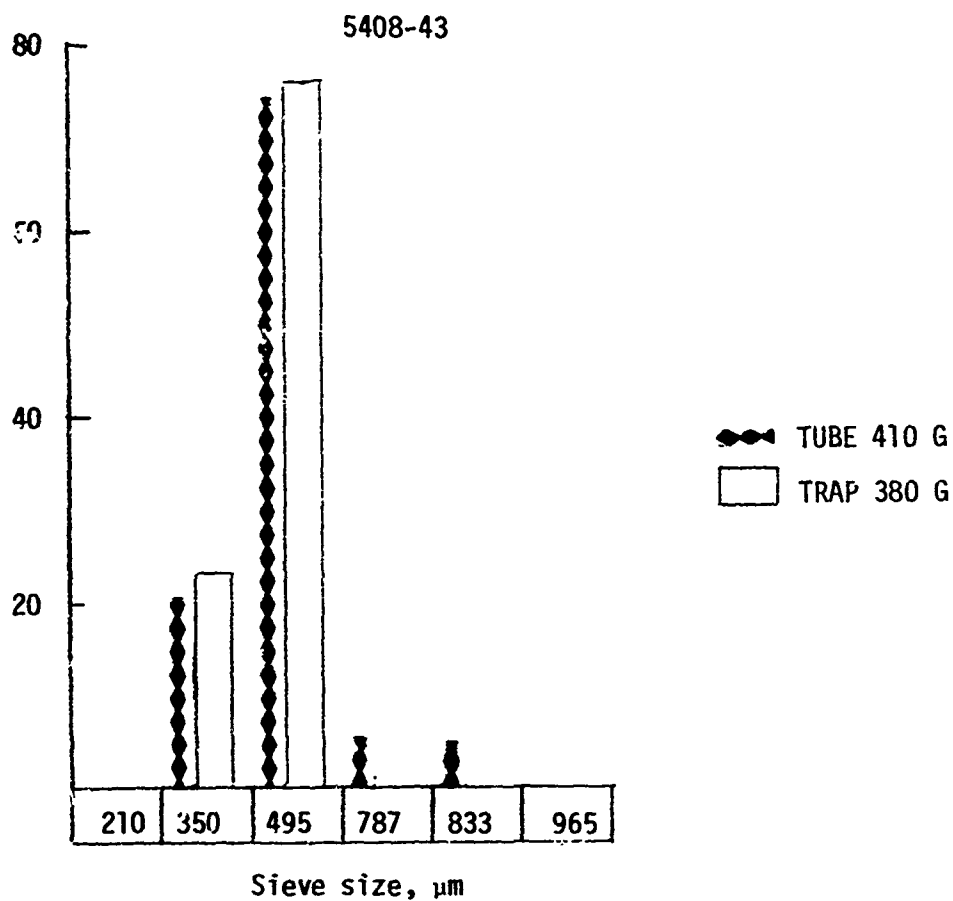


Sample: 5408-41  
 $\text{C}_3\text{H}_8$  concentration: 60% +  
 40%  $\text{H}_2$   
 Bed temperature: 1140°C  
 Overall efficiency: 37%  
 Coating rate: 3.8  $\mu\text{m}/\text{min}$ .  
 Microhardness: 185-DPH  
 Density: N.D.  
 $L_c$ : N.D.

42X

Fig. B-14

Wt-% retained  
on screen



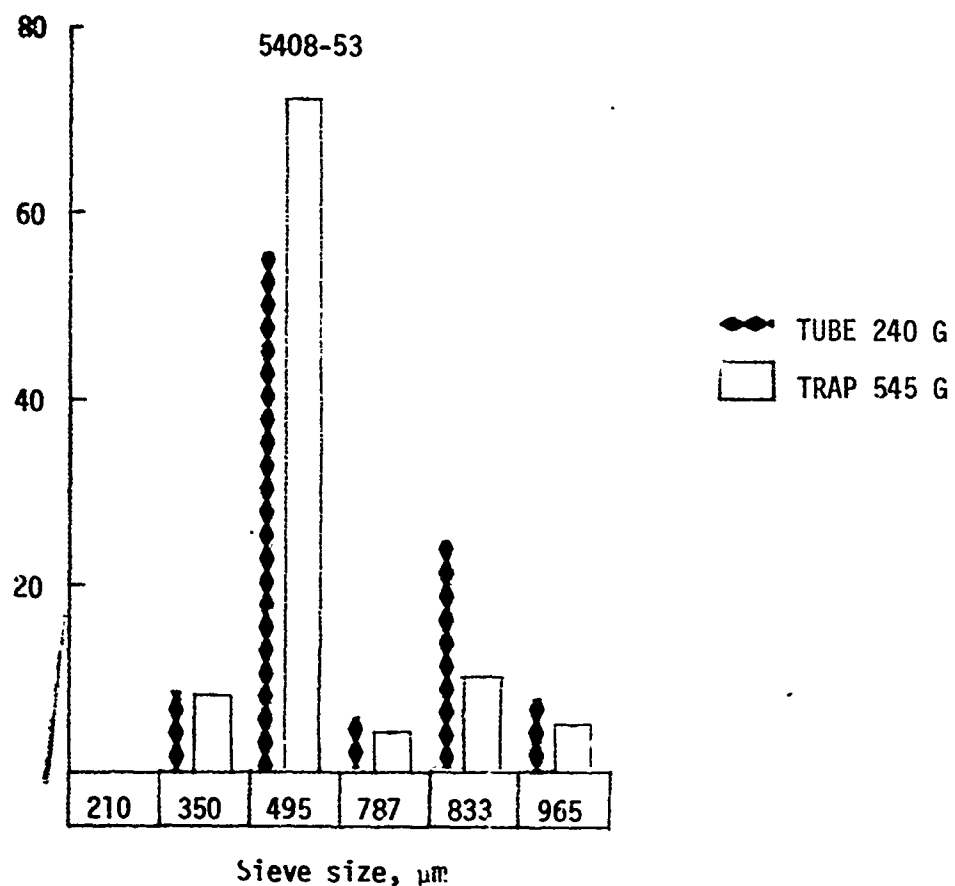
85X

Sample: 5408-43  
 $\text{C}_3\text{H}_8$  concentration. 25% +  
 75%  $\text{H}_2$   
 Bed temperature: 1190°C  
 Overall efficiency: 31%  
 Coating rate: 1.7  $\mu\text{m}/\text{min}$ .  
 Microhardness: 203-DPH  
 Density: 2.017  $\text{g}/\text{cm}^3$   
 $L_c$ : 32 Å

Fig. B-15



Wt-% retained  
on screen



Sample: 5408-53

$\text{C}_3\text{H}_8$  concentration: 25% +  
2%  $\text{Cl}$

Bed temperature:  $\sim 1240^\circ\text{C}$

Overall efficiency: 30%

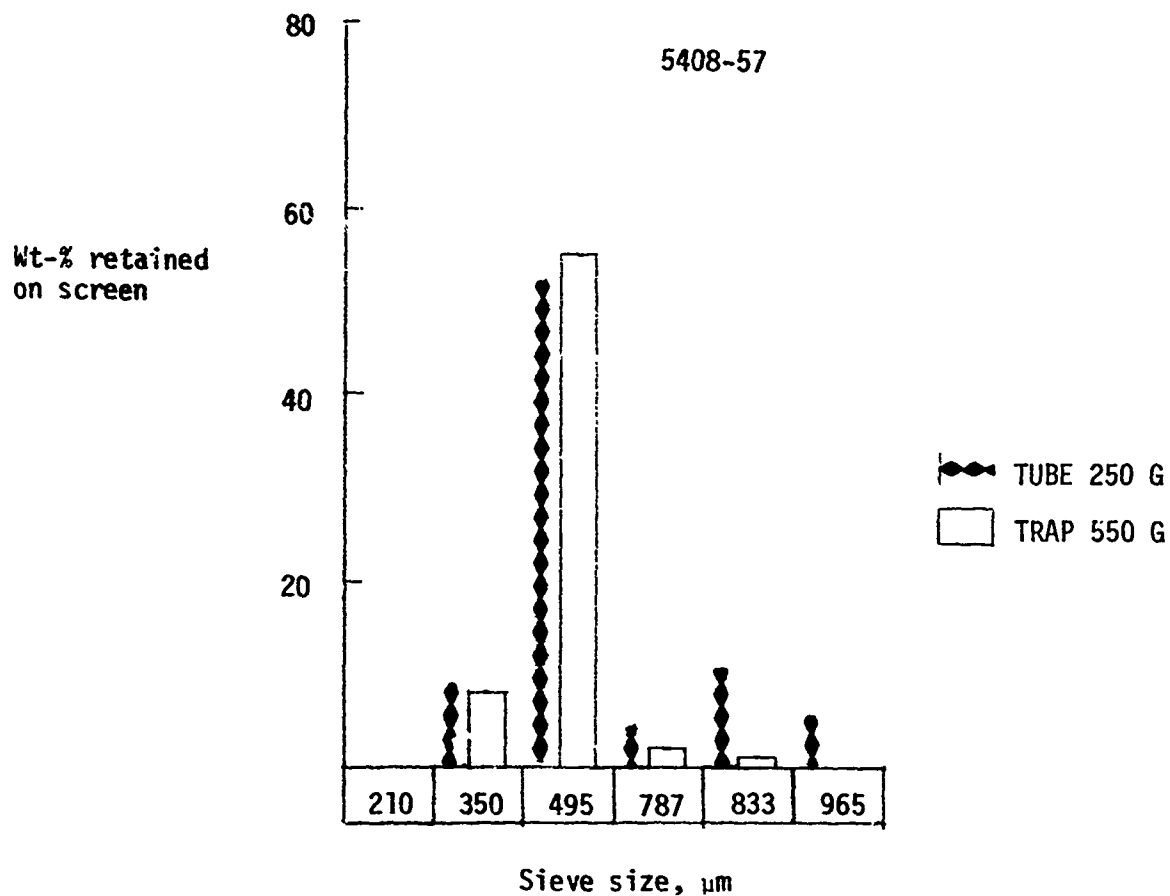
Coating rate:  $4.0 \mu\text{m}/\text{min}$ .

Microhardness: N.D.

Density:  $1.872 \text{ g}/\text{cm}^3$

$L_c$ : 29 Å

Fig. B-16



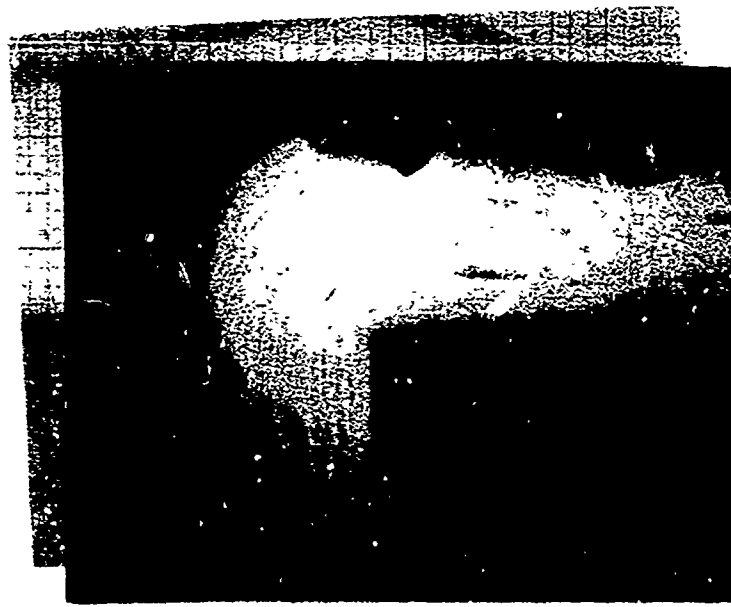
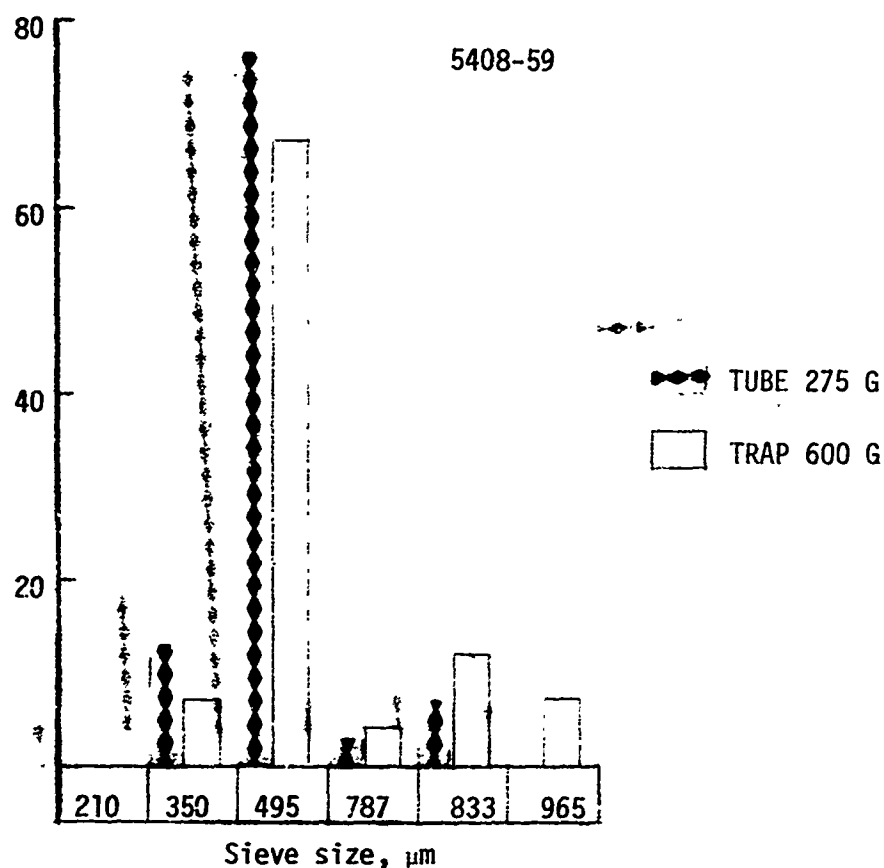
Sample: 5408-57  
 $\text{C}_3\text{H}_8$  concentration: 60%  
 $\text{CH}_3\text{SiCl}_3$  flux: 6.0 g/min.  
 Bed temperature: 1295°C  
 Overall efficiency: 54.5%  
 Coating rate: 5.9  $\mu\text{m}/\text{min}$ .  
 Microhardness: 201-DPH  
 Si content: 9.5%  
 Density: 2.085  $\text{g}/\text{cm}^3$   
 Carbon density: 1.98  $\text{g}/\text{cm}^3$

85X

Fig. B-17

8-7

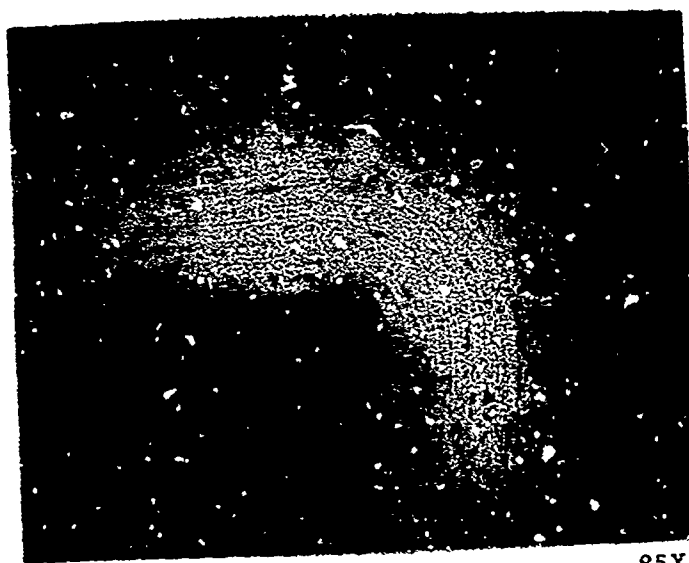
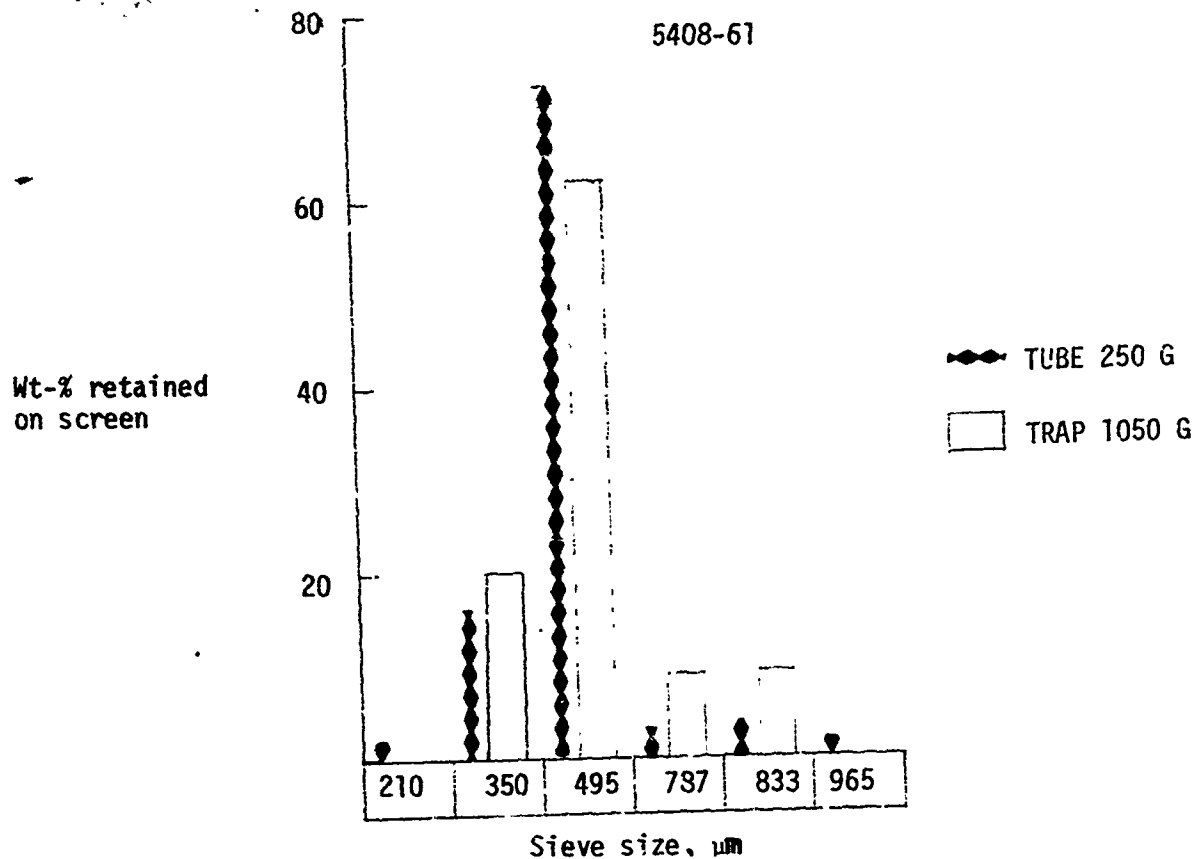
Wt-% Retained  
on screen



42X

Sample: 5408-59  
 $\text{C}_3\text{H}_8$  concentration: 25%  
 $\text{CH}_3\text{SiCl}_3$  flux: 9.5 g/min.  
 Bed temperature: 1235°C  
 Overall efficiency: 65%  
 Coating rate: 4.8  $\mu\text{m}/\text{min}$ .  
 Microhardness: 212-DPH  
 Si content: 16%  
 Density: 2.062  $\text{g}/\text{cm}^3$   
 Carbon density: 1.87  $\text{g}/\text{cm}^3$

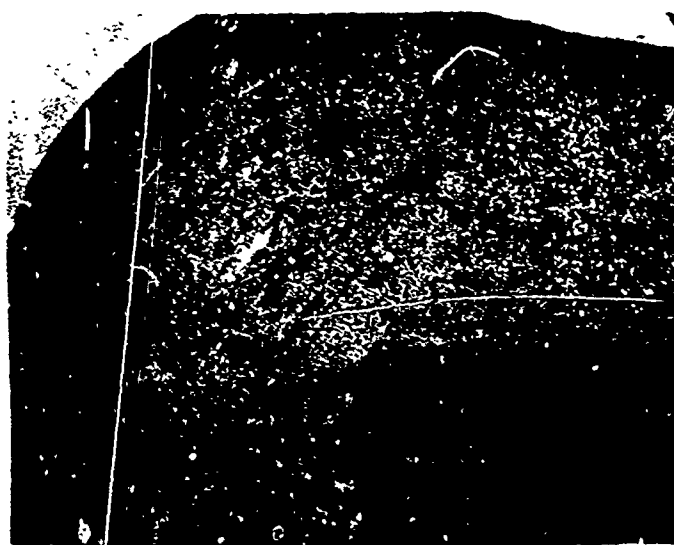
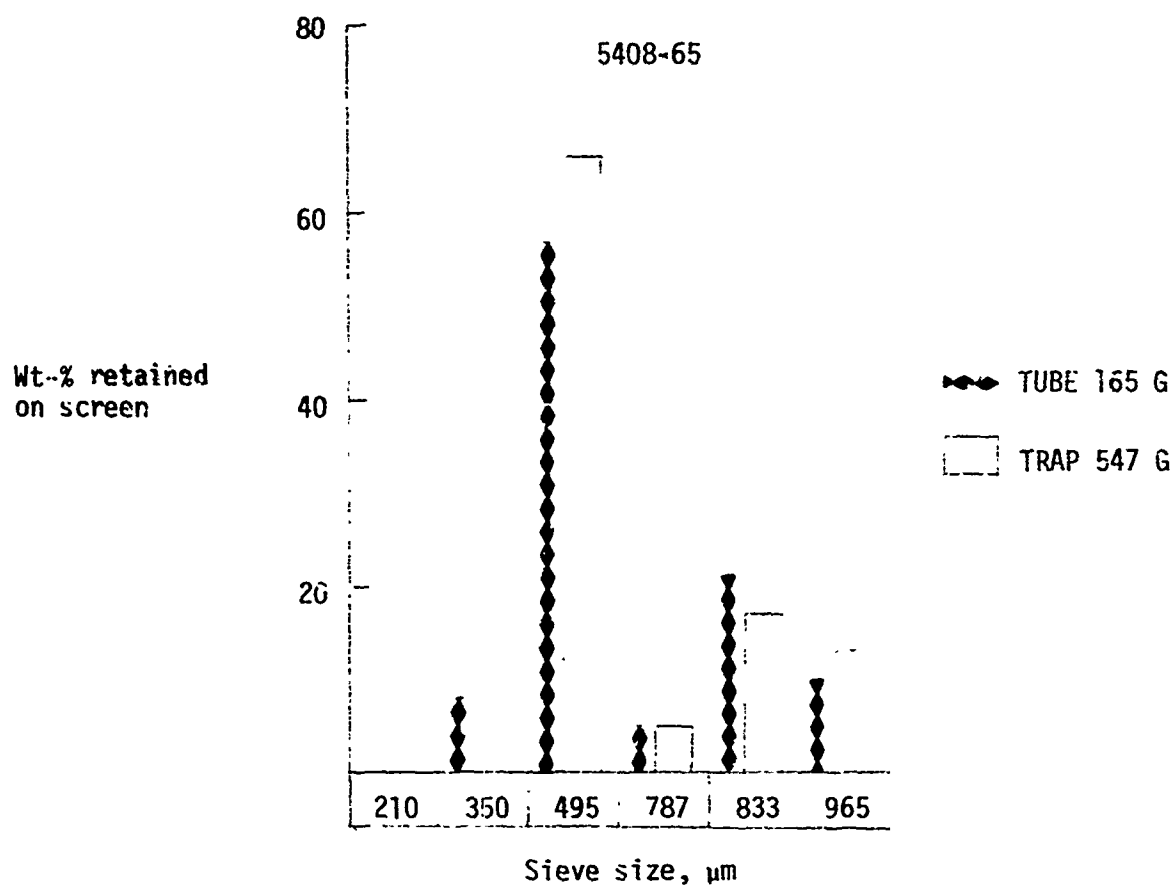
Fig. B-18



Sample: 5408-61  
 $\text{C}_3\text{H}_8$  concentration: 7%  
 $\text{CH}_3\text{SiCl}_3$  flux: 7.2 g/min.  
 Bed temperature: 1340°C  
 Overall efficiency: 36%  
 Coating rate: 2.3  $\mu\text{m}/\text{min}$   
 Microhardness: 397-DPH  
 Si content: 28%  
 Density: 2.158  $\text{g}/\text{cm}^3$   
 Carbon density: 1.77  $\text{g}/\text{cm}^3$

85X

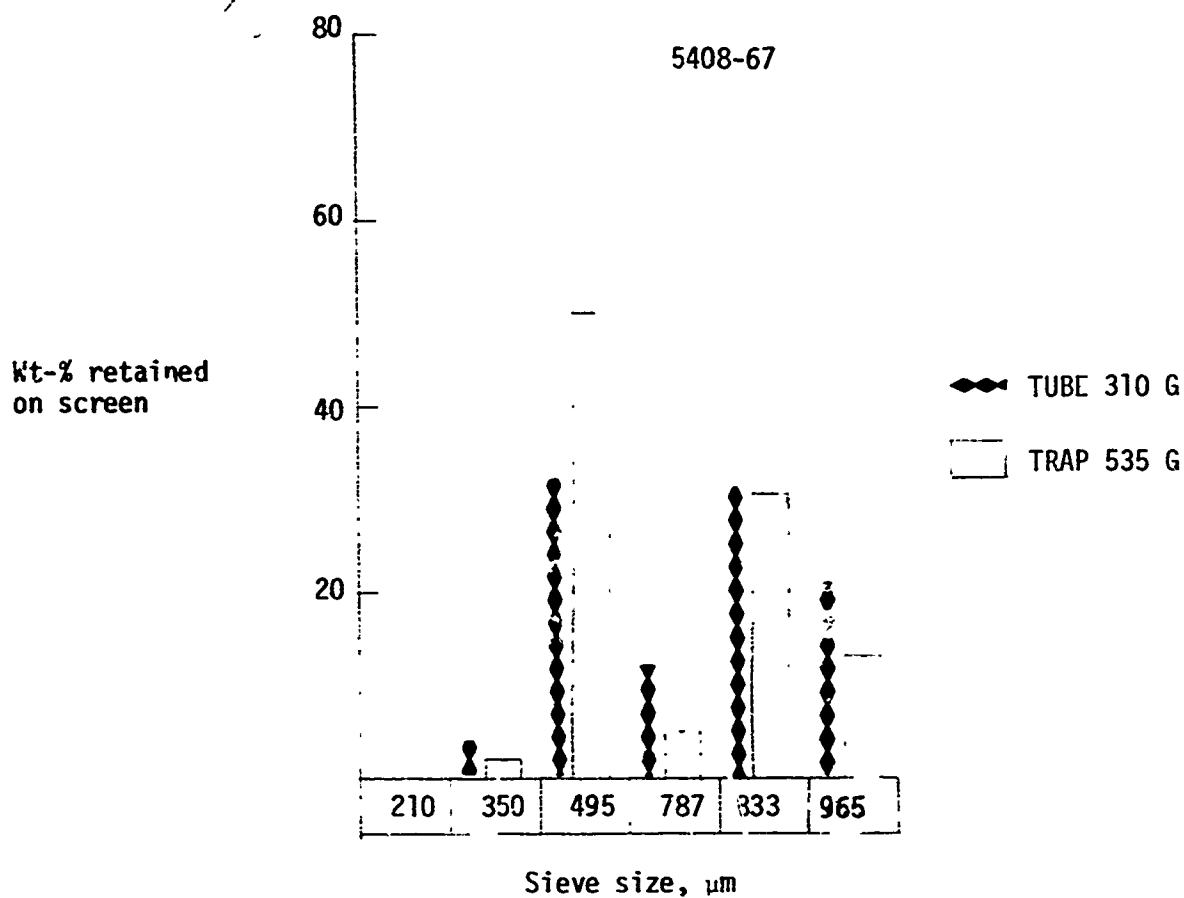
Fig. B-19



170X

Sample: 5408-65  
 $\text{C}_3\text{H}_8$  concentration: 60%  
 $\text{CH}_3\text{SiCl}_3$  flux: 5.9 g/min.  
 Bed temperature: 1235°C  
 Overall efficiency: 42%  
 Coating rate: 5.5  $\mu\text{m}/\text{min}$ .  
 Microhardness: 295-DPH  
 Si content: 8%  
 Density: 2.064  $\text{g}/\text{cm}^3$   
 Carbon density: 1.97  $\text{g}/\text{cm}^3$

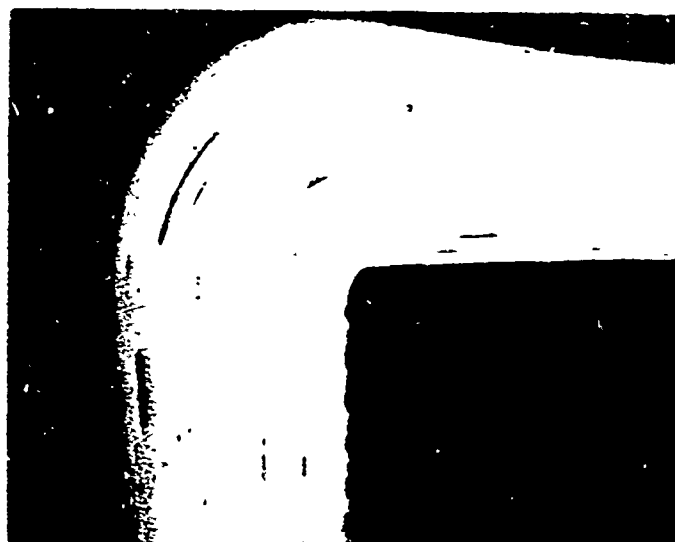
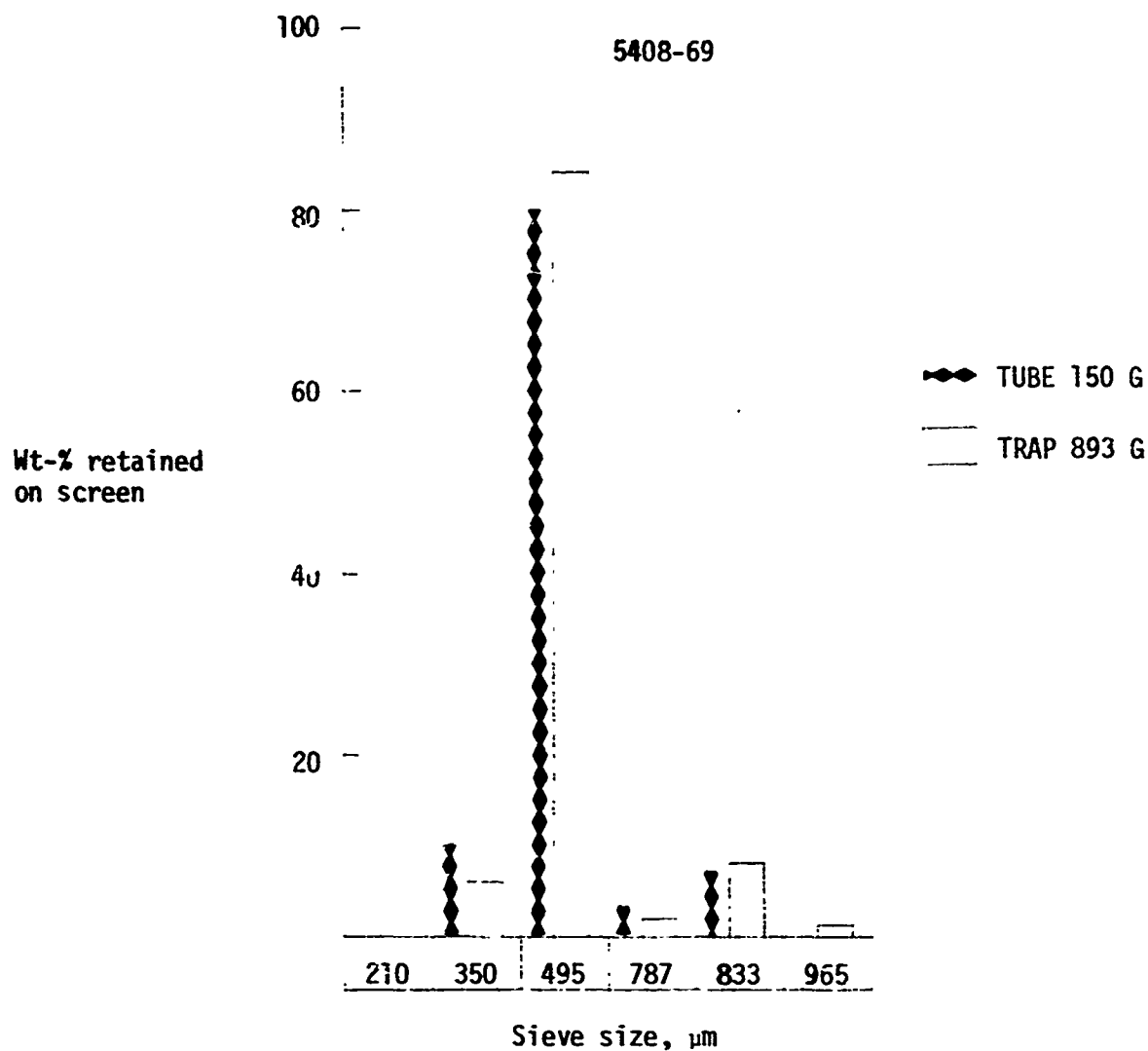
Fig. B-20



Sample: 5408-67  
 $\text{C}_3\text{H}_8$  concentration: 60%  
 $\text{CH}_3\text{SiCl}_3$  flux: 5.0 g/min  
 Bed temperature: 1350°C  
 Overall efficiency: 58.4%  
 Coating rate: 5.9  $\mu\text{m}/\text{min}$ .  
 Microhardness: 179-DPH  
 Si content: 4.0%  
 Density: 2.031  $\text{g}/\text{cm}^3$   
 Carbon density: 1.98  $\text{g}/\text{cm}^3$

170X

Fig. B-21



85X

Sample: 5408-69

$\text{C}_3\text{H}_8$  concentration: 25%

$\text{CH}_3\text{SiCl}_3$  flux: 8.7 g/min

Bed temperature: 1270°C

Overall efficiency: 55%

Coating rate: 3.6  $\mu\text{m}/\text{min}$ .

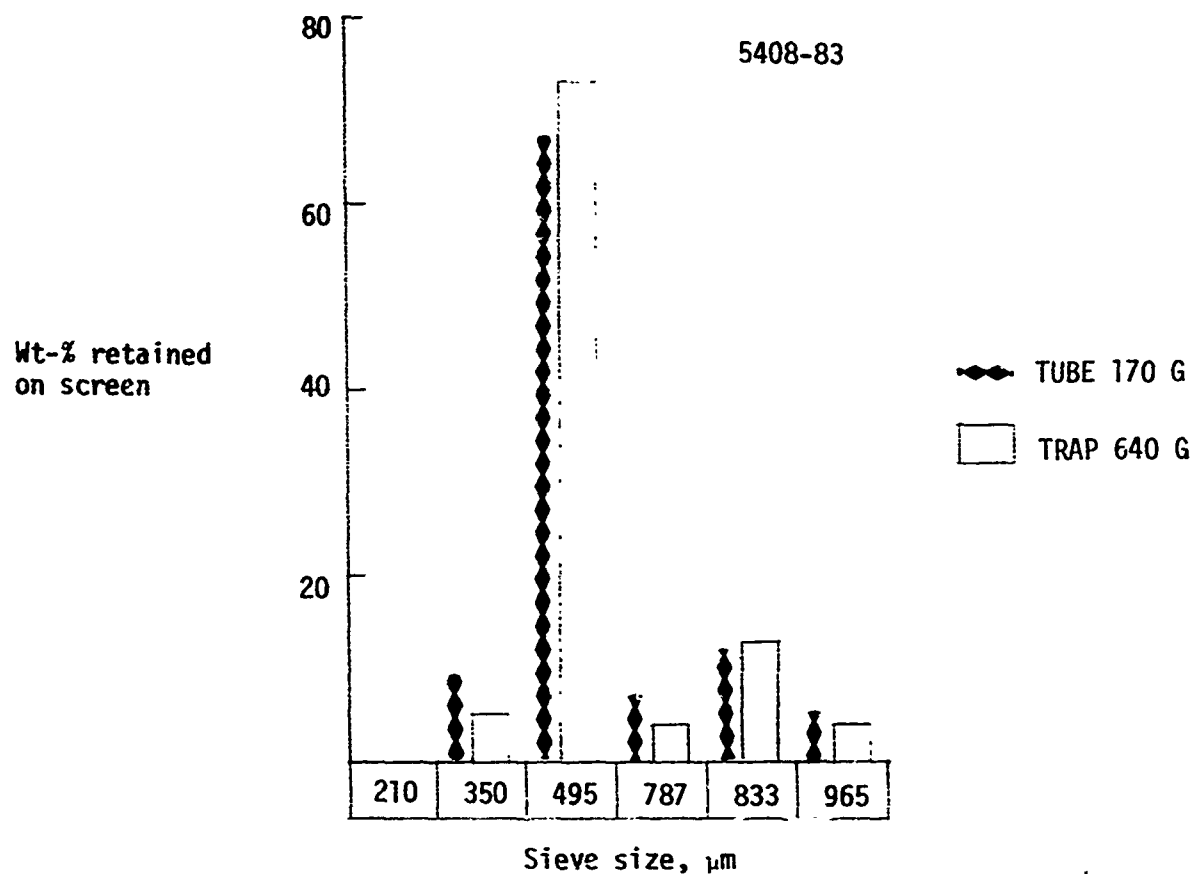
Microhardness: 352-DPH

Si content: 15%

Density: 2.105  $\text{g}/\text{cm}^3$

Carbon density: 1.92  $\text{g}/\text{cm}^3$

Fig. B-22

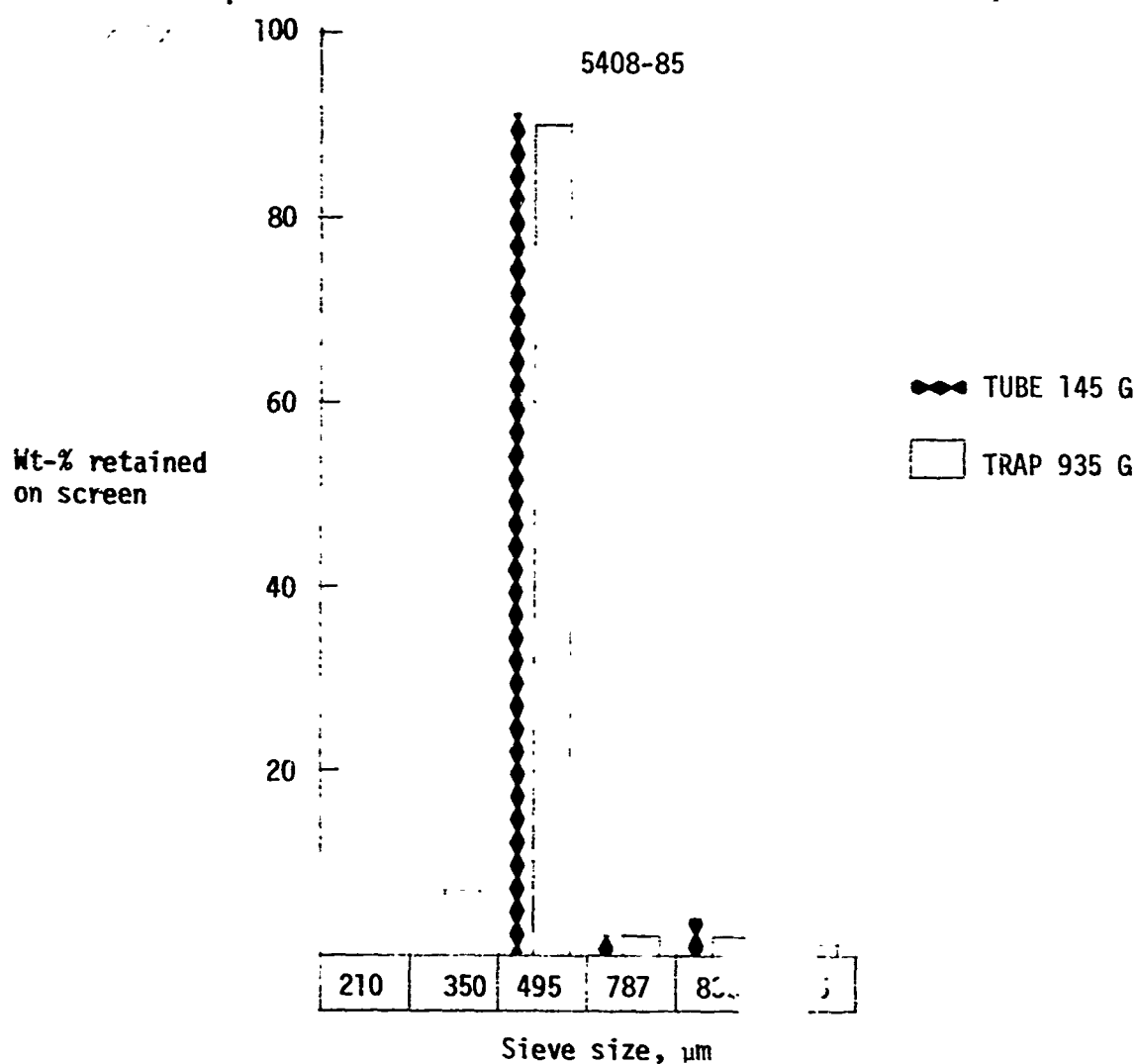


85X

Sample: 5408-83  
 $\text{C}_3\text{H}_8$  concentration: 25%  
 $\text{CH}_3\text{SiCl}_3$  flux: 9.8 g/min.  
 Bed temperature: 1370°C  
 Overall efficiency: 55%  
 Coating rate: 6.8  $\mu\text{m}/\text{min}$ .  
 Microhardness: 279-DPH  
 Si content: 13.5%  
 Density: 2.031 g/cm<sup>3</sup>  
 Carbon density: 1.92 g/cm<sup>3</sup>

Fig. B-23

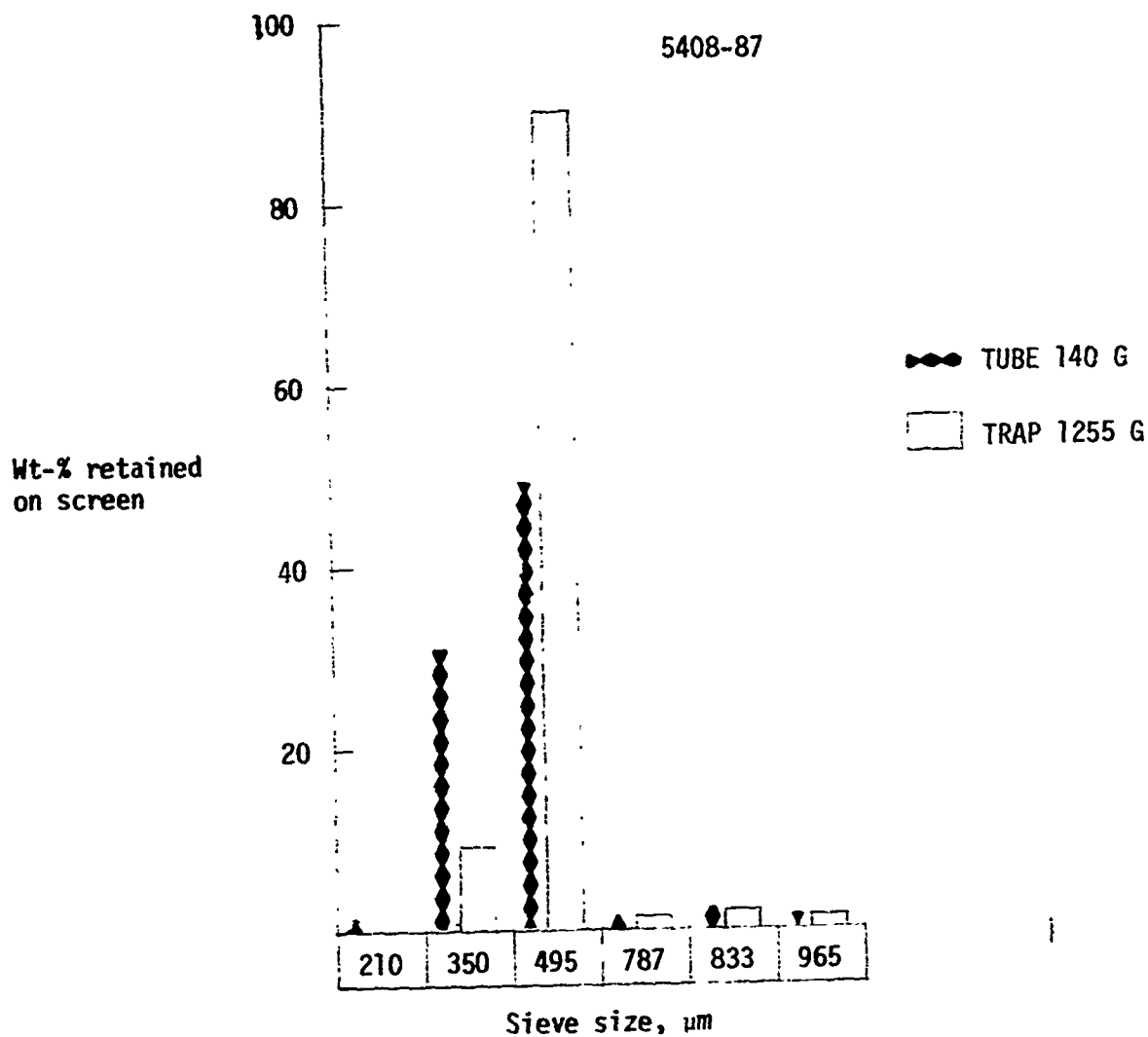




85X

Sample: 5408-85  
 $\text{C}_3\text{H}_8$  concentration: 7%  
 $\text{CH}_3\text{SiCl}_3$  flux: 9.2 g/min.  
 Bed temperature: 1390°C  
 Overall efficiency: 40%  
 Coating rate: 3.0  $\mu\text{m}/\text{min}$ .  
 Microhardness: 378-DPH  
 Si content: 34%  
 Density: 2.149  $\text{g}/\text{cm}^3$   
 Carbon density: 1.64  $\text{g}/\text{cm}^3$

Fig. B-24

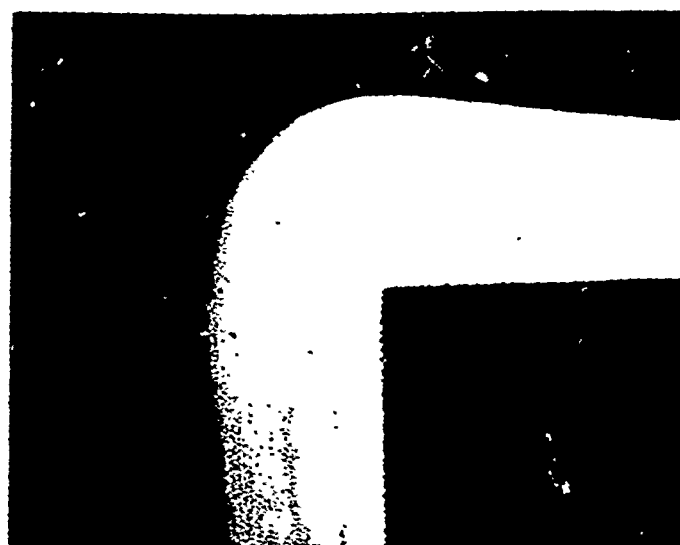
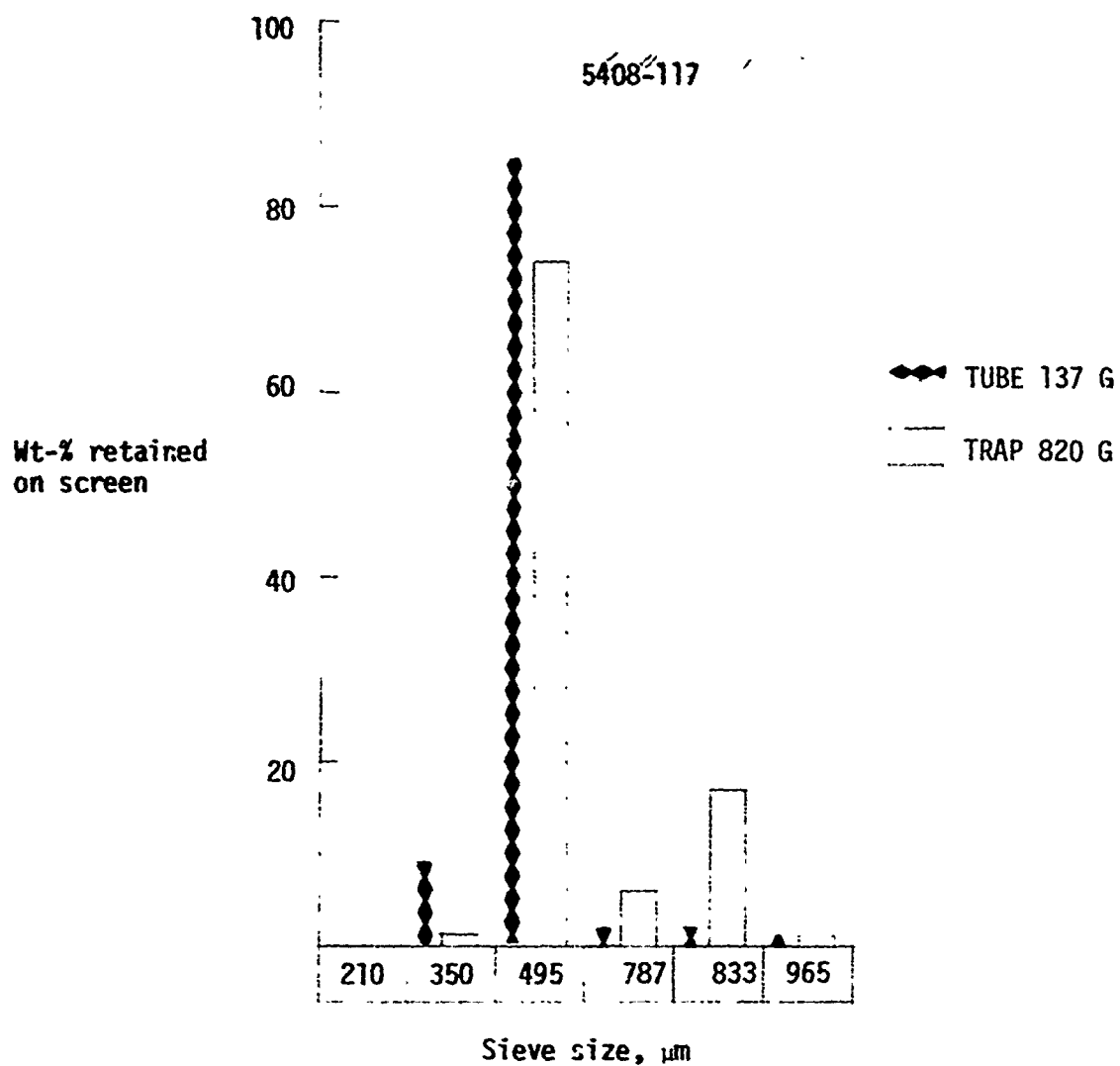


Sample: 5408-87  
 $\text{C}_3\text{H}_8$  concentration: 7%  
 $\text{CH}_3\text{SiCl}_3$  flux: 8.7 g/min.  
 Bed temperature: 1290°C  
 Overall efficiency: 44%  
 Coating rate: 2.1  $\mu\text{m}/\text{min}$ .  
 Microhardness: 430-DPH  
 Si content: 23%  
 Density: 2.178 g/cm<sup>3</sup>  
 Carbon density: 1.88 g/cm<sup>3</sup>

85X

Fig. B-25

B-27



Sample: 5408-117  
 $\text{C}_3\text{H}_8$  concentration: 25%  
 $\text{TiCl}_4$  flux: 1.1 g/min.  
 Bed temperature: 1280°C  
 Overall efficiency: N.D.  
 Coating rate: 2.8  $\mu\text{m}/\text{min}$ .  
 Microhardness: 240-DPH  
 Titanium content: 3.4%  
 Density: 1.980  $\text{g}/\text{cm}^3$

85X

Fig. B-26

B-28

TUBE: 100 G

TRAP: 300 G



85X

Sample: 5408-91

$C_3H_8$  concentration: 60%

$BCl_3$  flux: 2.50 g/min.

Control temperature: 1400°C

Overall efficiency: 74.8%

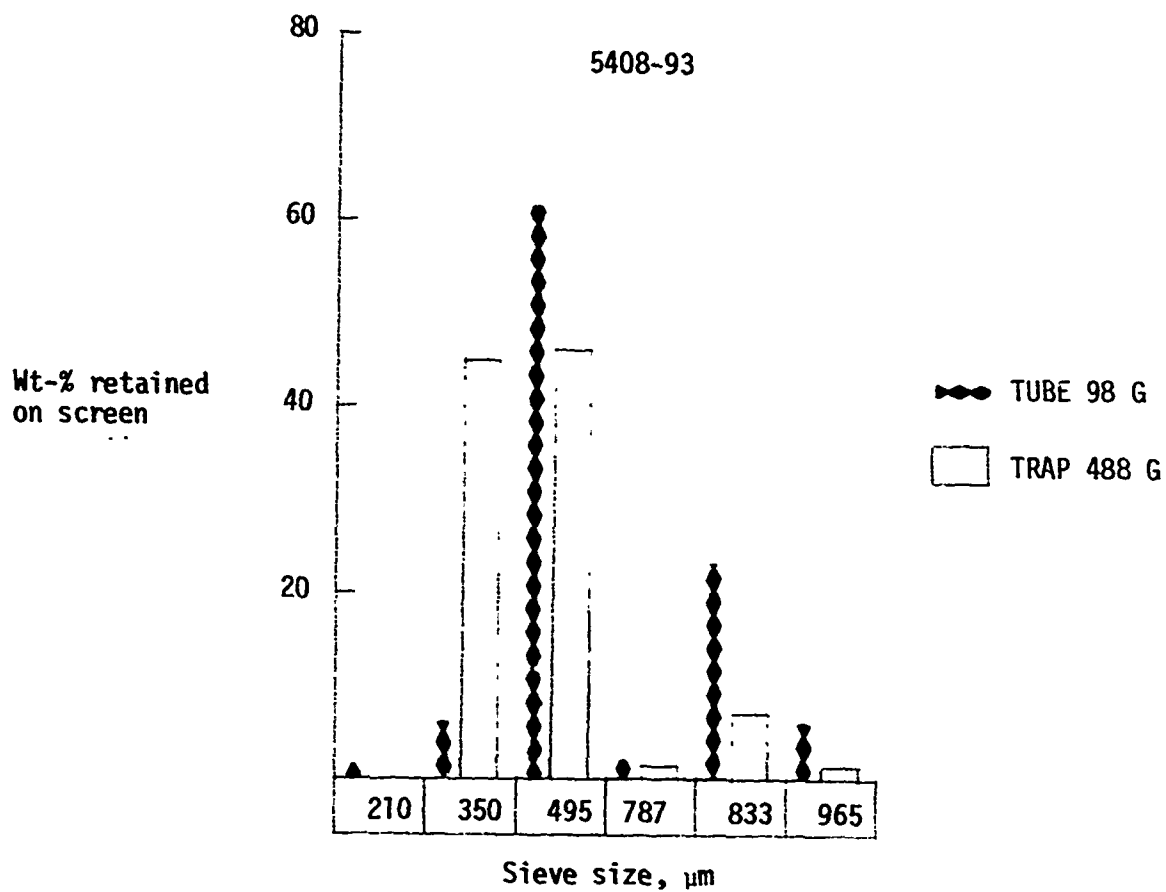
Coating rate: 23.0  $\mu\text{m}/\text{min.}$

Microhardness: 89-DPH

Boron content: 1.8%

Density: 1.964  $\text{g}/\text{cm}^3$

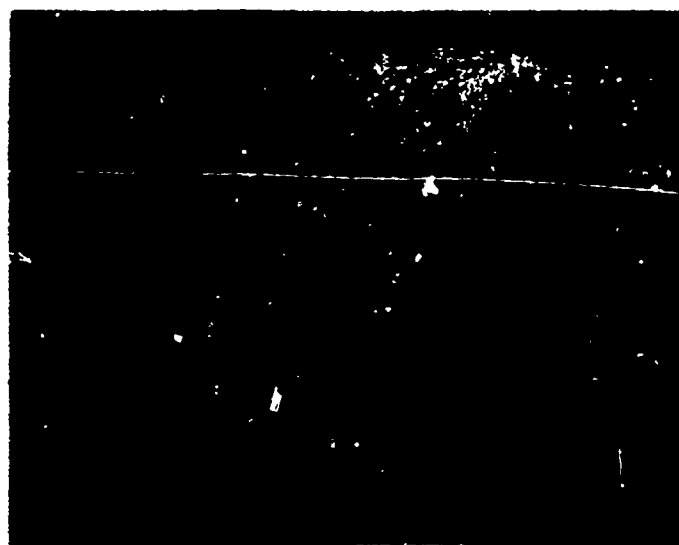
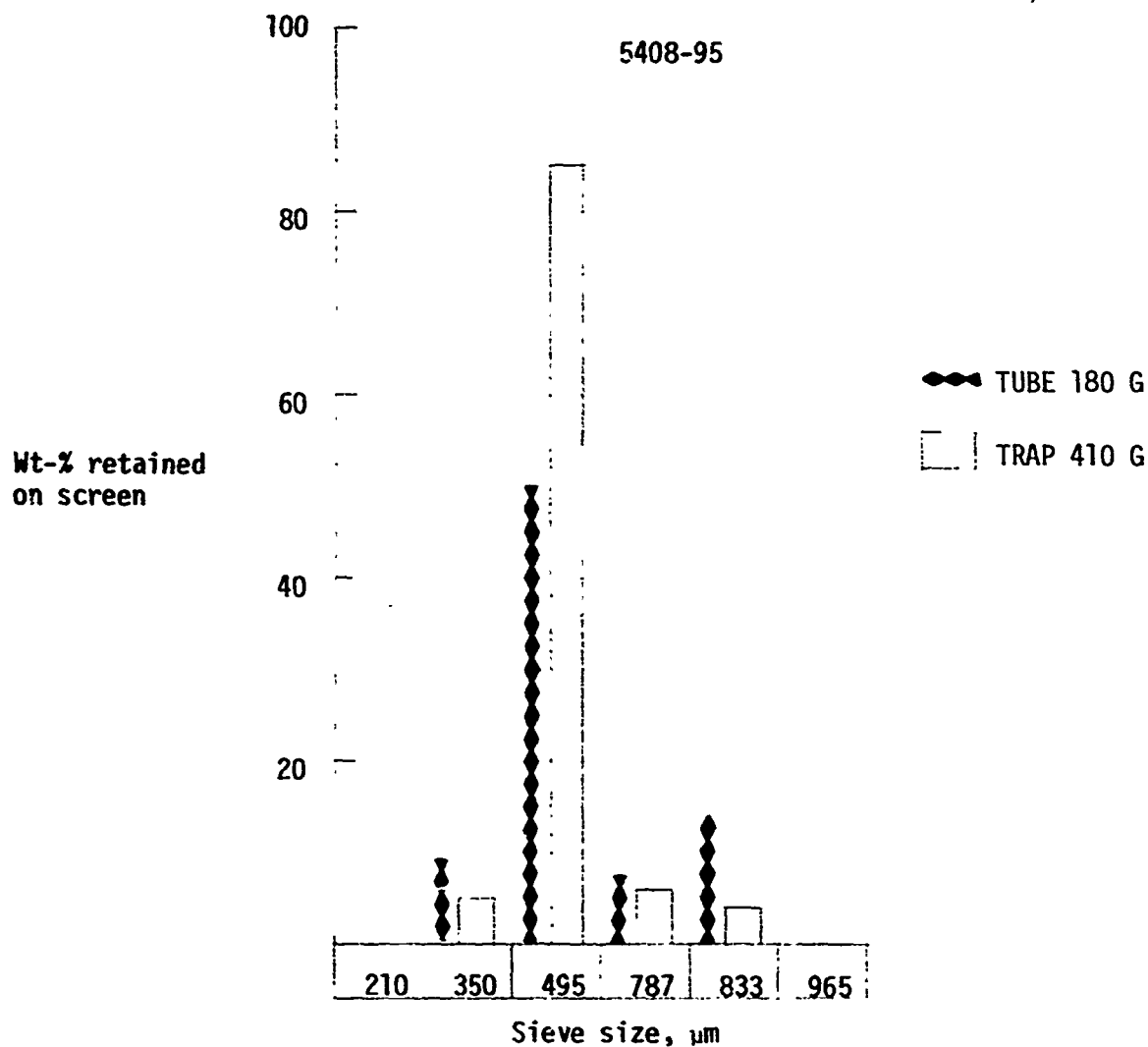
Fig. B-27



85X

Sample: 5408-93  
 $\text{C}_3\text{H}_8$  concentration: 25%  
 $\text{BCl}_3$  flux: 3.75 g/min.  
 Bed temperature: 1300°C  
 Overall efficiency: 68.7%  
 Coating rate: 5.5  $\mu\text{m}/\text{min}$ .  
 Microhardness: 150-DPH  
 Boron content: 4.6%  
 Density: 2.074  $\text{g}/\text{cm}^3$

Fig. B-28

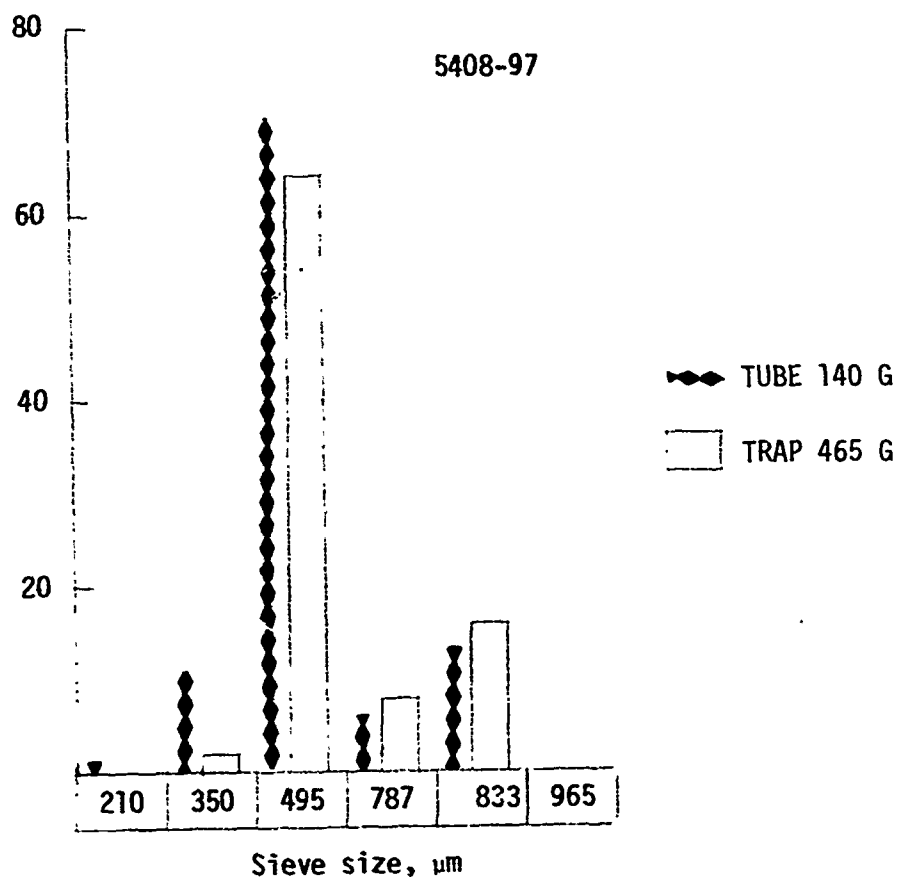


85X

Sample: 5408-95  
 $\text{C}_3\text{H}_8$  concentration: 25%  
 $\text{BCl}_3$  flux: 3.42 g/min.  
 Bed temperature: 1350°C  
 Overall efficiency: 71%  
 Coating rate: 3.4  $\mu\text{m}/\text{min}$ .  
 Microhardness: 136-DPH  
 Boron content: 4.5%  
 Density: 2.114  $\text{g}/\text{cm}^3$

Fig. B-25

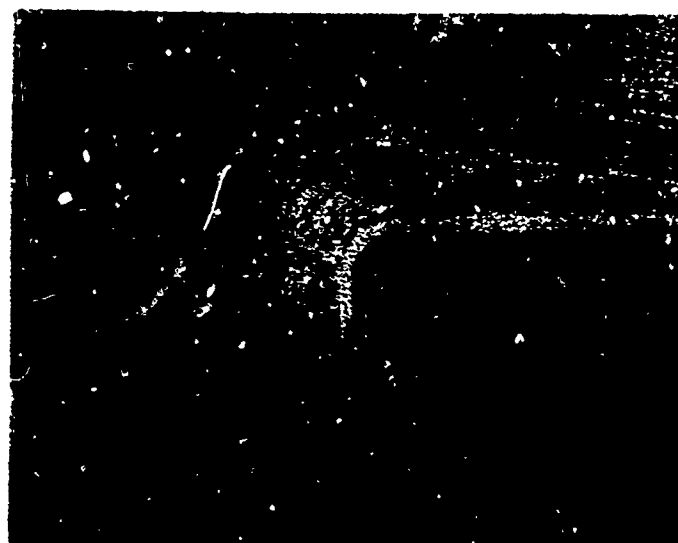
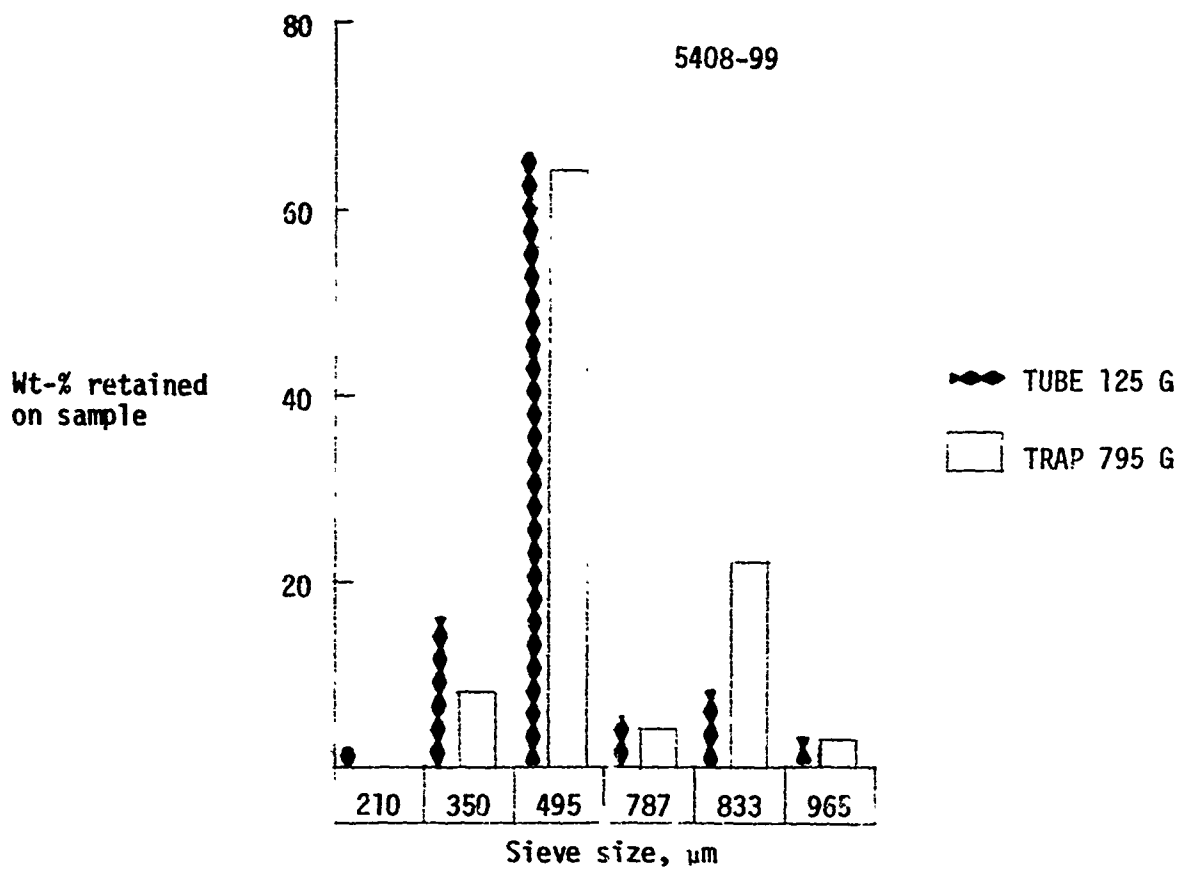
Wt-% retained  
on screen



85X

Sample: 5408-97  
 $\text{C}_2\text{H}_8$  concentration: 25%  
 $\text{BCl}_3$  flux: 3.58 g/min.  
 Bed temperature: 1400°C  
 Overall efficiency: 74%  
 Coating rate: 4.2  $\mu\text{m}/\text{min}$ .  
 Microhardness: 122-DPH  
 Boron content: 3.6%  
 Density: 2.060  $\text{g}/\text{cm}^3$

Fig. B-30



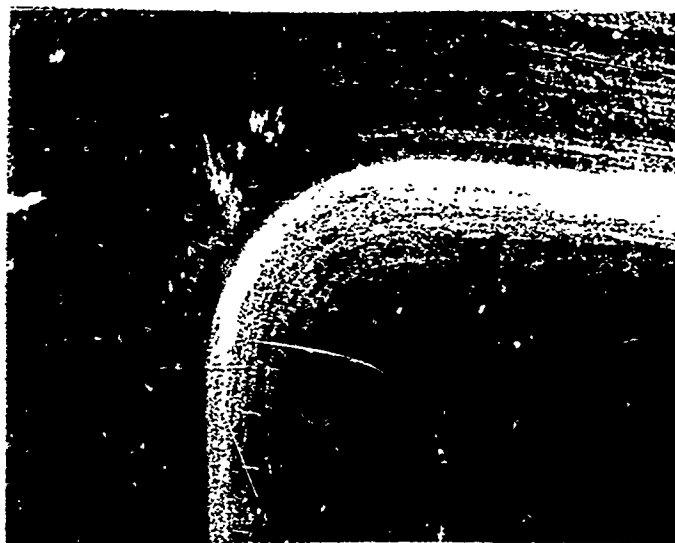
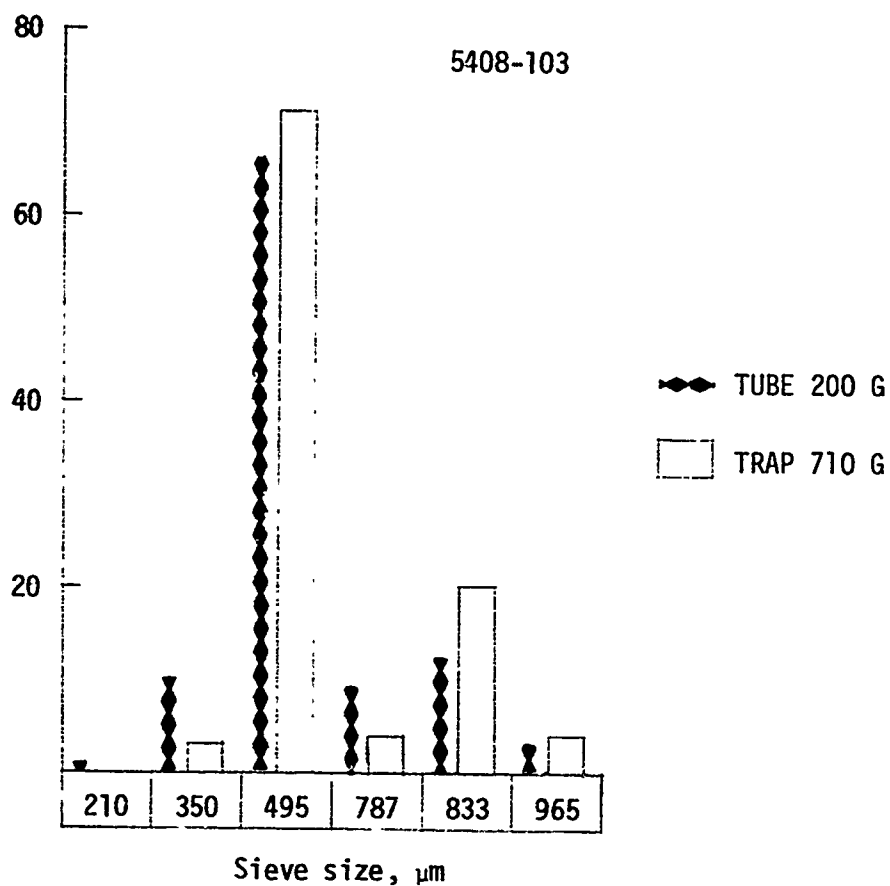
Sample: 5408-99  
 $\text{C}_3\text{H}_8$  concentration: 25%  
 $\text{BCl}_3$  flux: 3.45 g/min.  
 Bed temperature: 1200°C  
 Overall efficiency: 48%  
 Coating rate: 3.2  $\mu\text{m}/\text{min}$ .  
 Microhardness: 186-DPH  
 Boron content: 5.5%  
 Density: 2.128  $\text{g}/\text{cm}^3$

85X

Fig. B-31



Wt-% retained  
on screen

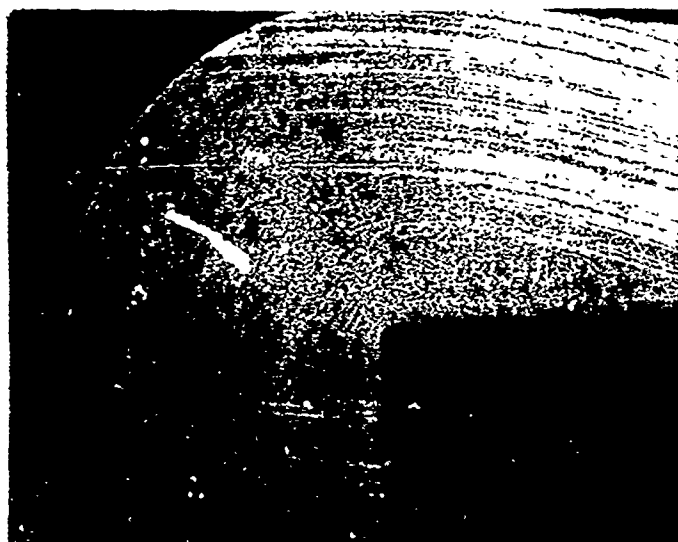
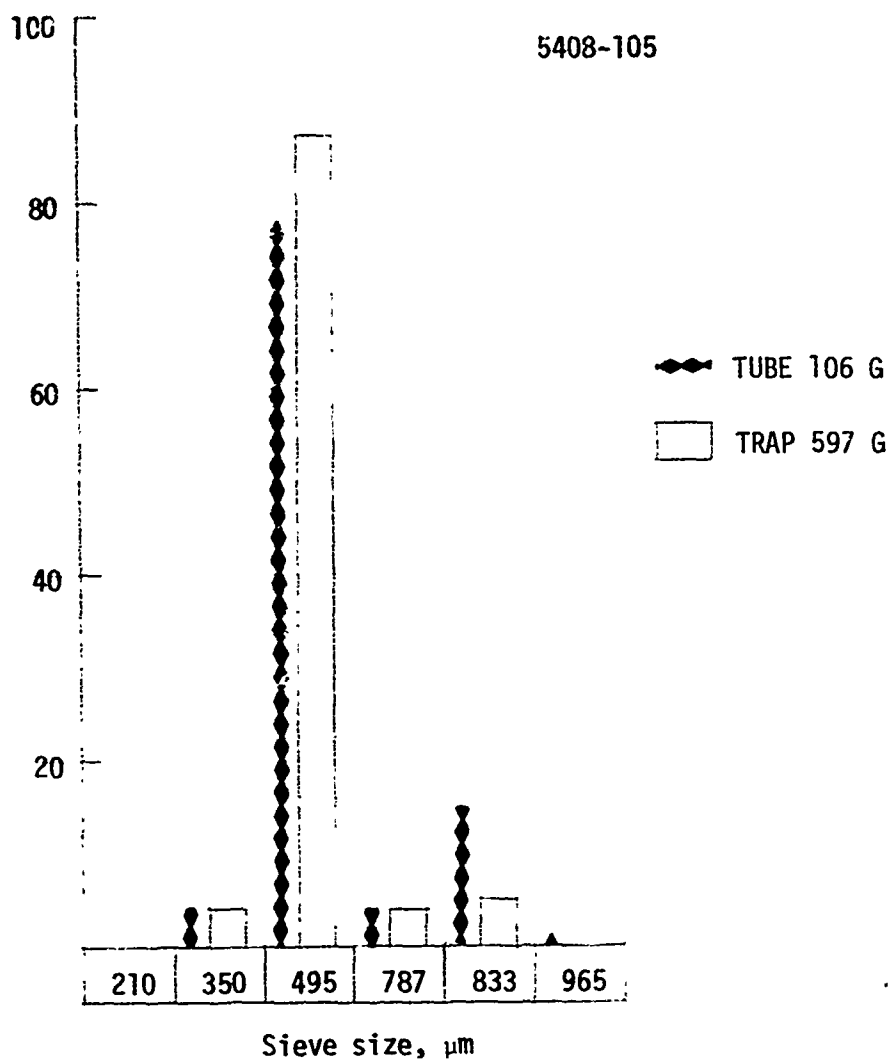


85X

Sample: 5408-103  
 $\text{C}_3\text{H}_8$  concentration: 25%  
 $\text{BCl}_3$  flux: 3.38 g/min.  
 Bed temperature: 1250°C  
 Overall efficiency: 60%  
 Coating rate: 3.4  $\mu\text{m}/\text{min}$ .  
 Microhardness: 161-DPH  
 Boron content: 4.3%  
 Density: 2.053  $\text{g}/\text{cm}^3$

Fig. B-32

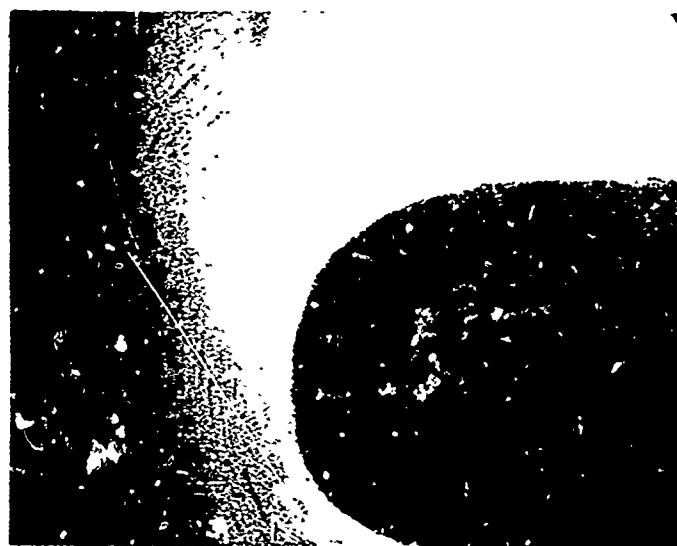
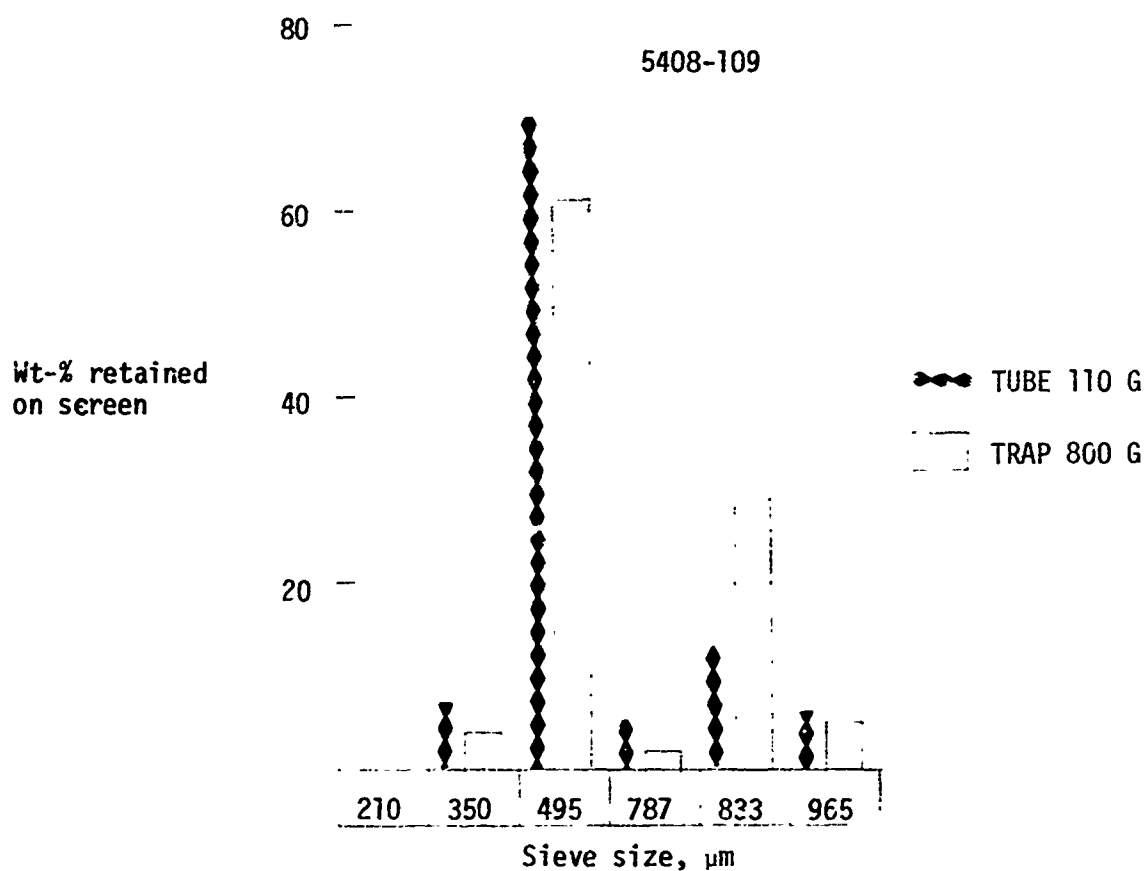
Wt-% retained  
on screen



85X

Sample: 5408-105  
 $\text{C}_3\text{H}_8$  concentration: 25%  
 $\text{BCl}_3$  flux: 5.3 g/min.  
 Bed temperature: 1200°C  
 Overall efficiency: 18.5%  
 Coating rate: 2.8  $\mu\text{m}/\text{min}$ .  
 Microhardness: 216-DPH  
 Boron content: N.D.  
 Density: 2.095  $\text{g}/\text{cm}^3$

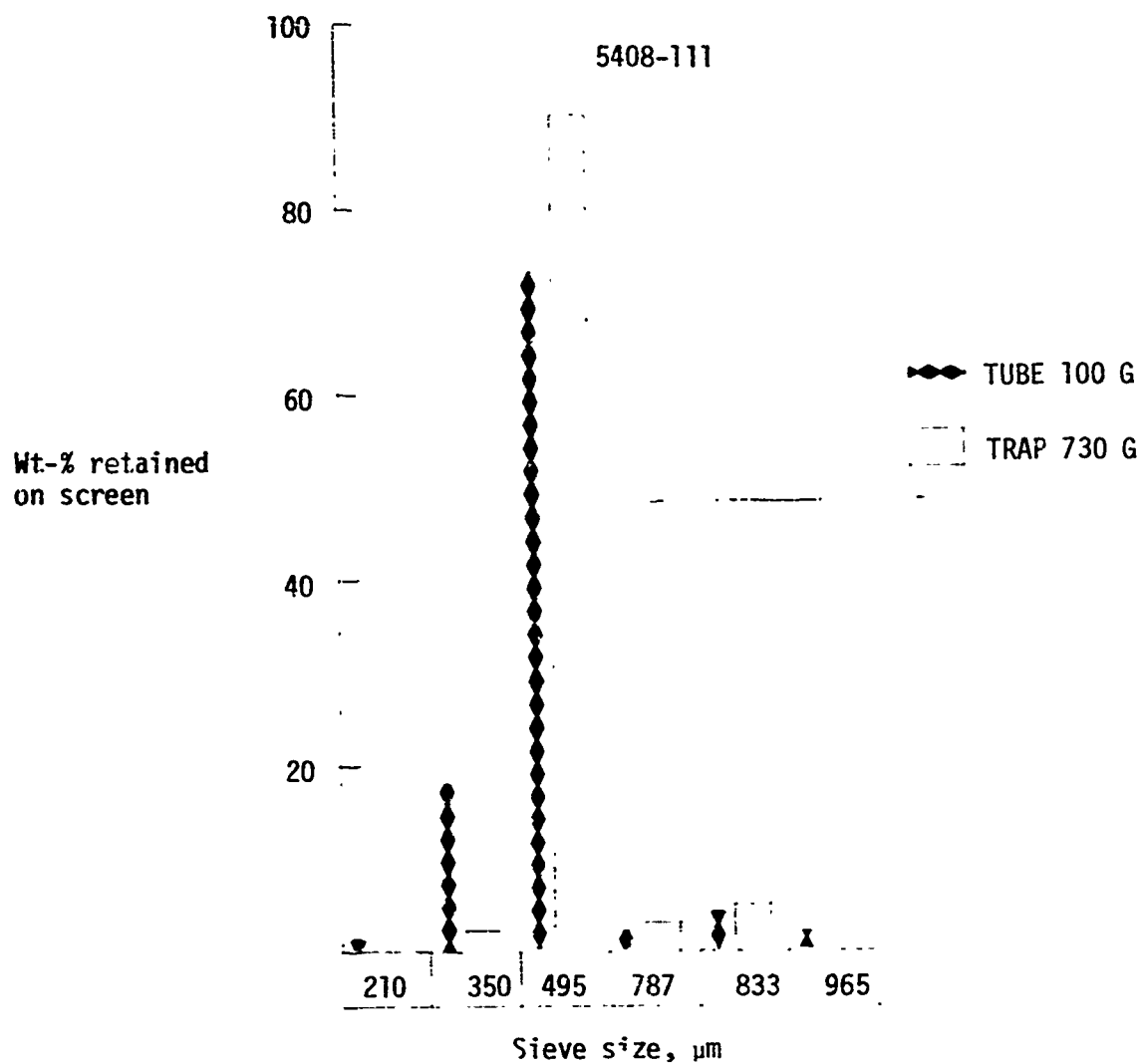
Fig. B-1



85X

Sample: 5408-109  
 $\text{C}_2\text{H}_8$  concentration: 25%  
 $\text{BCl}_3$  flux: 0.28 g/min.  
 Bed temperature: 1350°C  
 Overall efficiency: 48%  
 Coating rate: 5.1  $\mu\text{m}/\text{min}$ .  
 Microhardness: 170-DPH  
 Boron content: In progress  
 Density: 1.628  $\text{g}/\text{cm}^3$

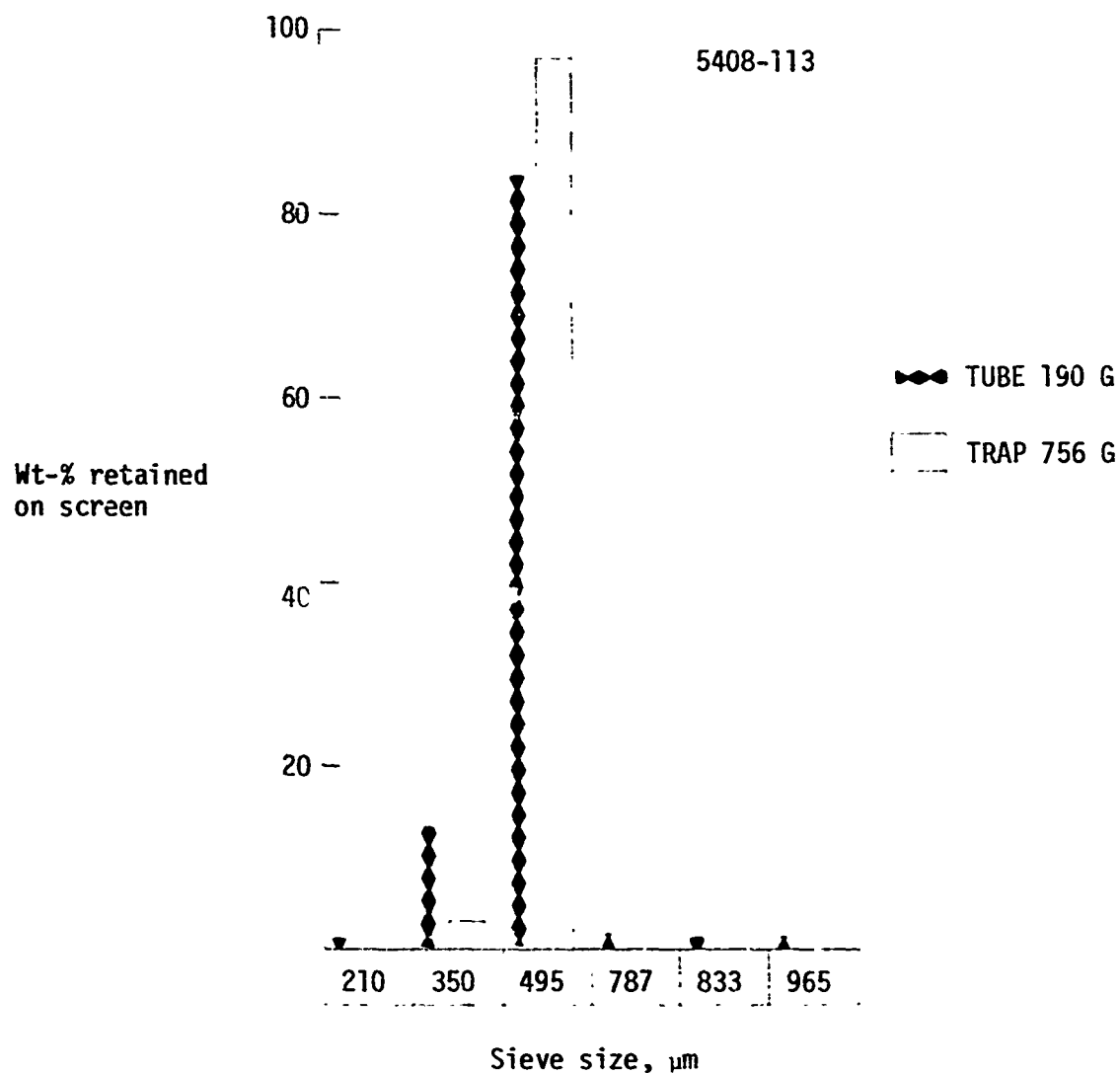
Fig. B-34



Sample: 5408-111  
 $\text{C}_3\text{H}_8$  concentration: 25%  
 $\text{BCl}_3$  flux: 0.33 g/min.  
 Bed temperature: 1250°C  
 Overall efficiency: 37%  
 Coating rate: 3.0  $\mu\text{m}/\text{min}$ .  
 Microhardness: 223-DPH  
 Boron content: In progress  
 Density: 1.928  $\text{g}/\text{cm}^3$

85X

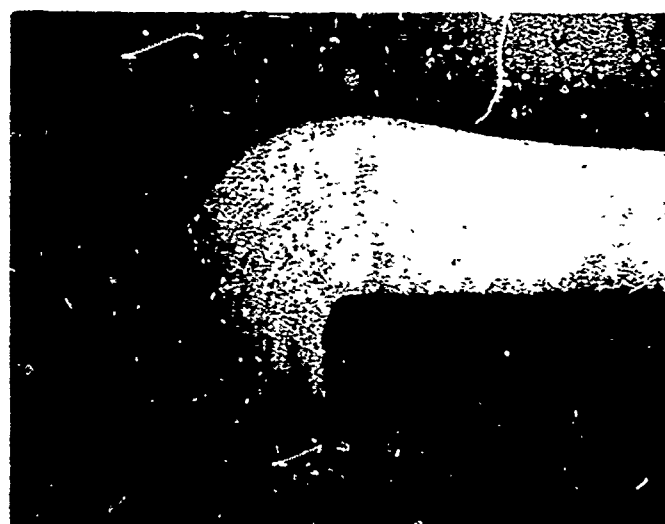
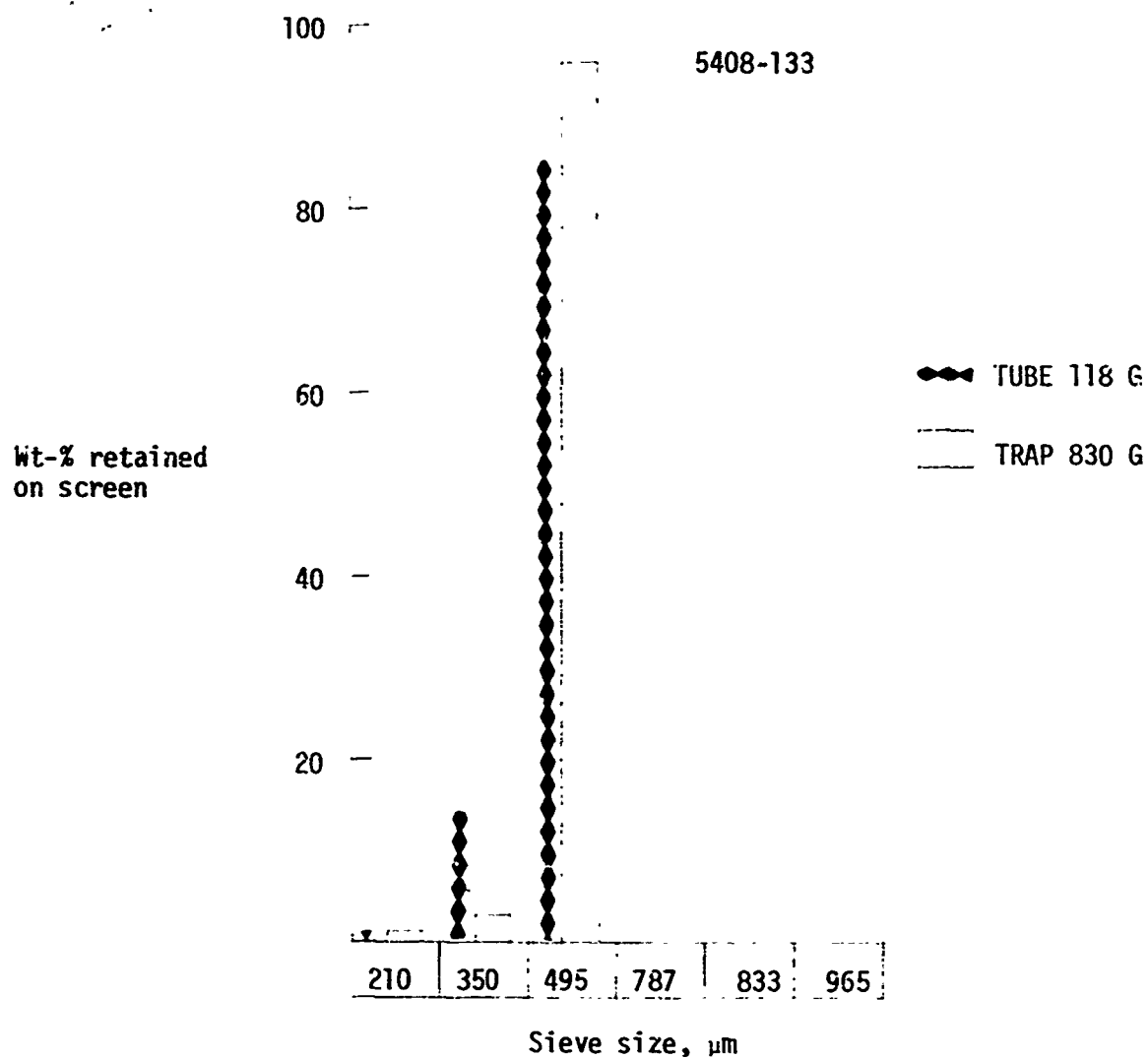
Fig. B-35



Sample: 5408-113  
 $\text{C}_3\text{H}_8$  concentration: 25%  
 $\text{BCl}_3$  flux: 0.30 g/min.  
 Bed temperature: 1150°C  
 Overall efficiency: 12%  
 Coating rate: 1.9  $\mu\text{m}/\text{min}$ .  
 Microhardness: 217-DPH  
 Boron content: In progress  
 Density: 2.204  $\text{g}/\text{cm}^3$

85X

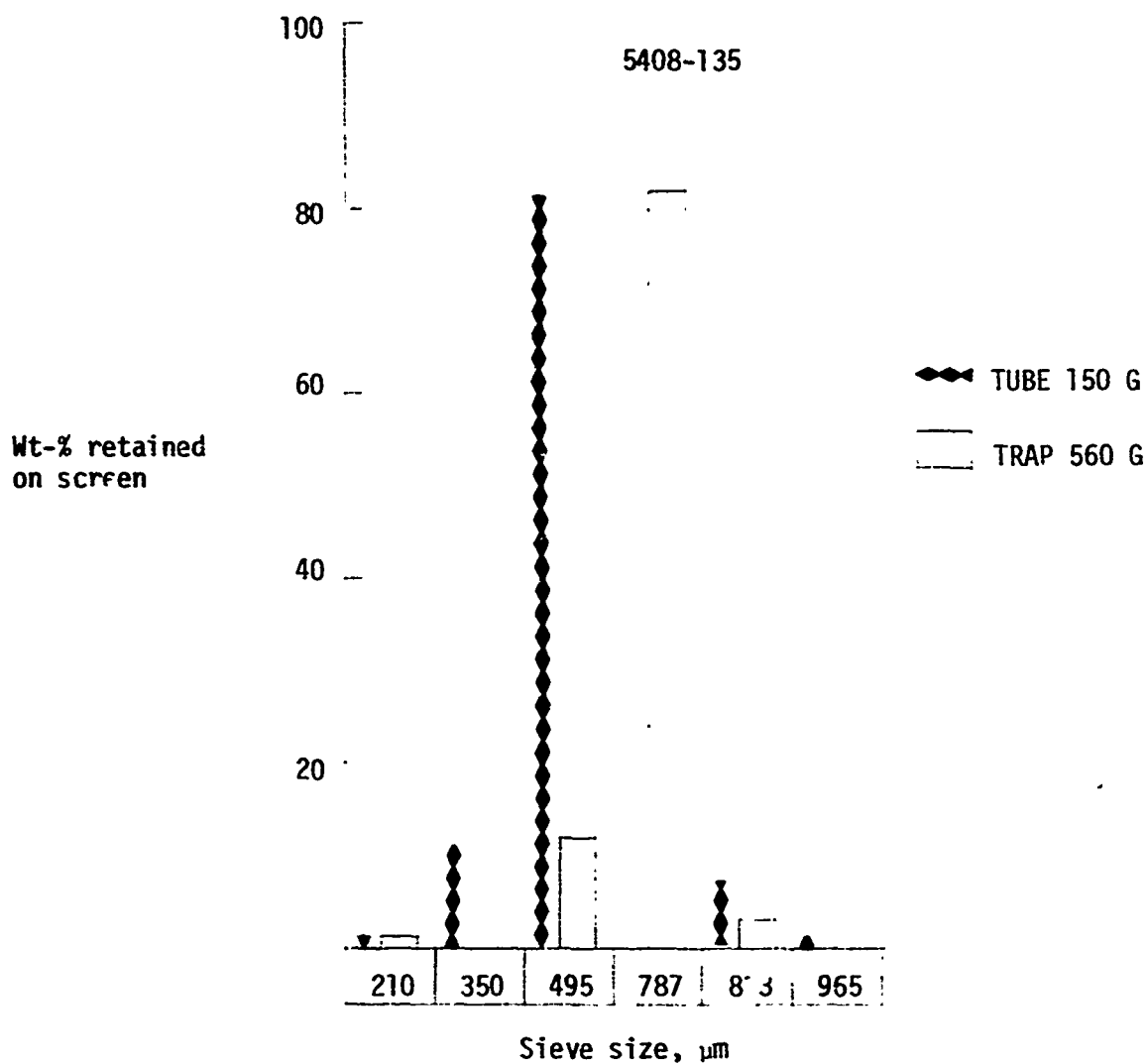
Fig. B-36



Sample: 5408-133  
 $\text{CH}_4$  concentration: 25%  
 $\text{BCl}_3$  flux: 0.35 g/min.  
Control temperature: 1350°C  
Overall efficiency: 38%  
Coating rate: 1.7  $\mu\text{m}/\text{min}$ .  
Microhardness: 150-DPH  
Boron content: In progress  
Density: 1.843  $\text{g}/\text{cm}^3$

42X

Fig. B-37



Sample: 5408-135  
 $\text{CH}_4$  concentration: 60%  
 $\text{BCl}_3$  flux: 0.30 g/min.  
 Bed temperature: 1350°C  
 Overall efficiency: 58%  
 Coating rate: 2.1  $\mu\text{m}/\text{min}$ .  
 Microhardness: 215-200H  
 Boron content: In progress  
 Density: 1.797  $\text{g}/\text{cm}^3$

85X

Fig. B-38

TUBE: 125 G

TRAP: 705 G



85X

Sample: 5408-137

CH<sub>4</sub> concentration: 25%

BCl<sub>3</sub> flux: 0.30 g/min.

Control temperature: 1200°C

Overall efficiency: 27.9%

Coating rate: 0.85 μm/min.

Microhardness: 214-DPH

Density: 2.039 g/cm<sup>3</sup>

Fig. B-39



APPENDIX C  
MECHANICAL PROPERTY DATA

C-1

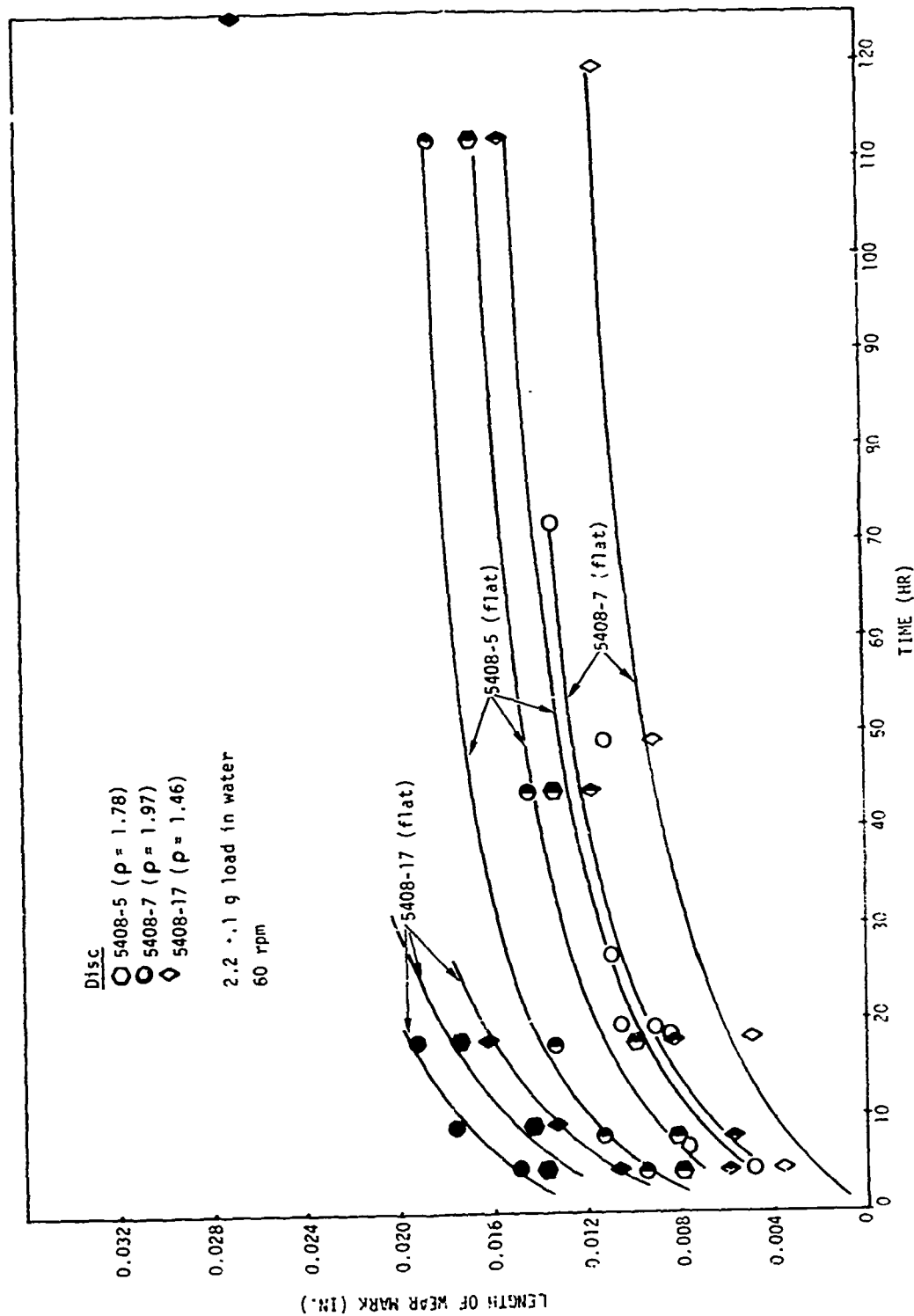


Fig. C-1. Length of wear mark measured on flat as a function of time for pure LTI carbon discs bearing on pure LTI carbon flats. Densities of carbons in g/cm<sup>3</sup> are given in parentheses. DPH values are as follows: 5408-7, 219; 5408-5, 210; and 5408-17, 153.

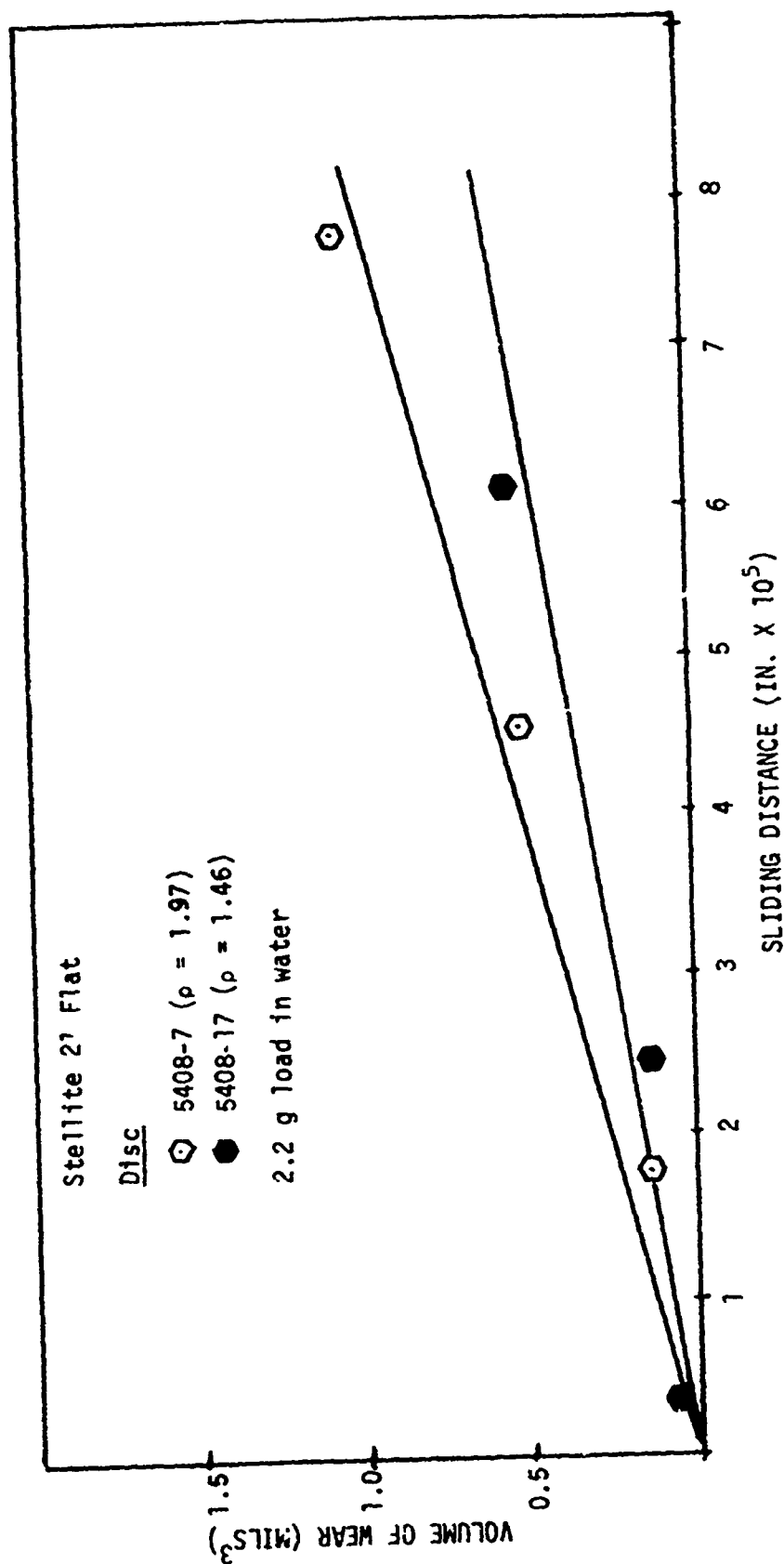


Fig. C-2. Volume of wear measured on flat as a function of sliding distance for pure LTI carbon discs bearing on Stellite 21 flats. Densities of carbons on discs in g/cm<sup>3</sup> are given in parentheses.

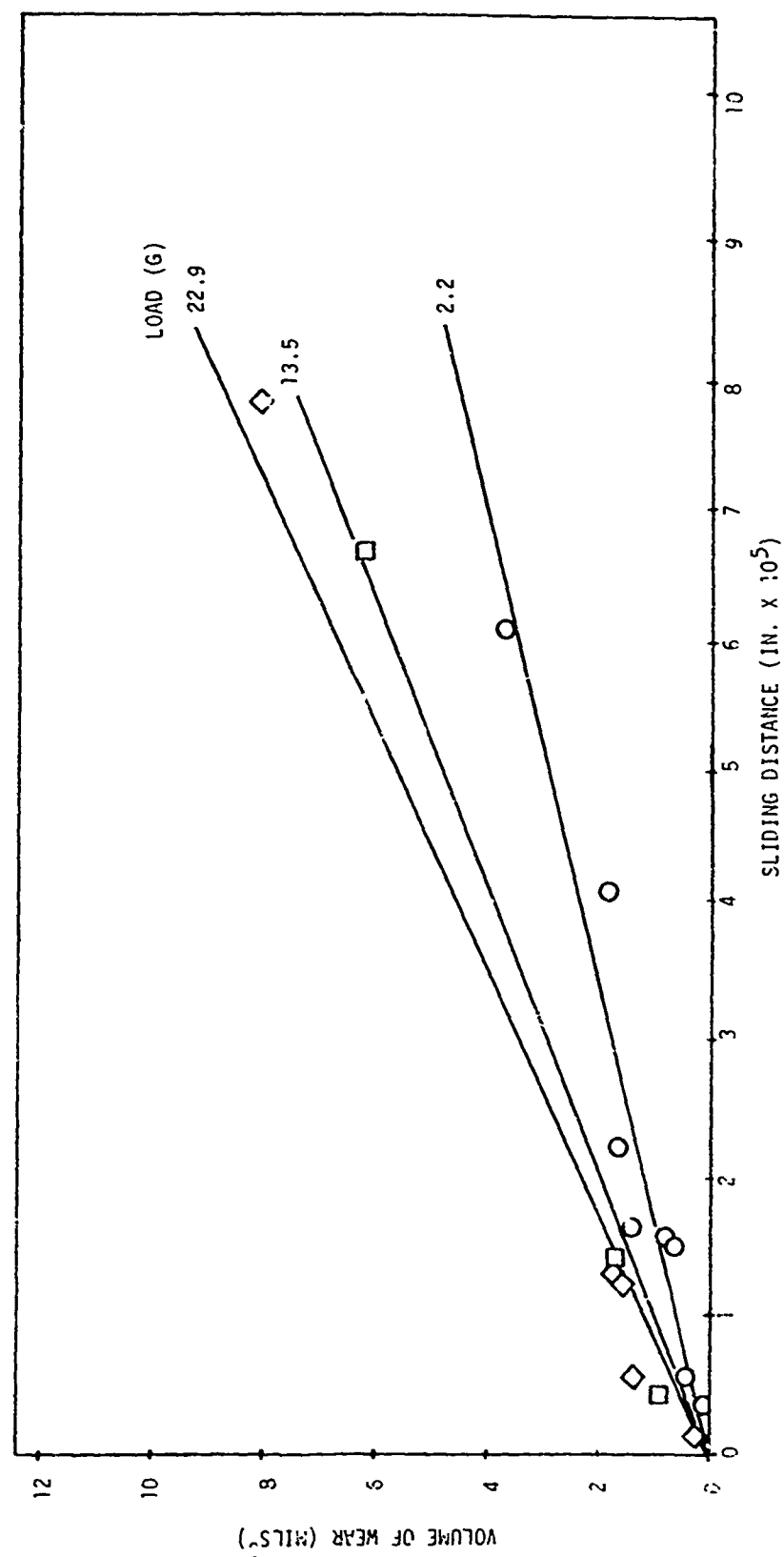
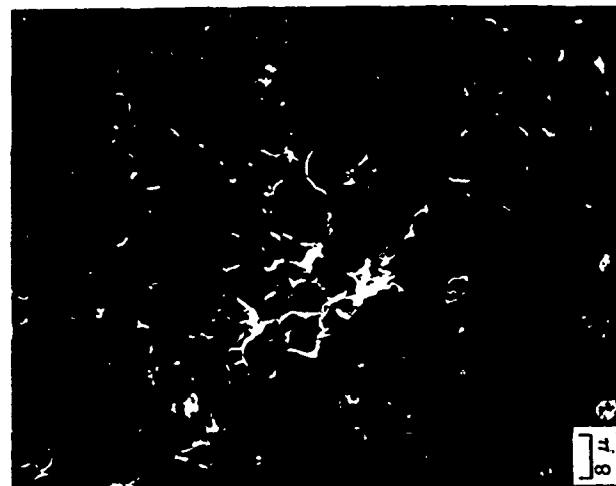
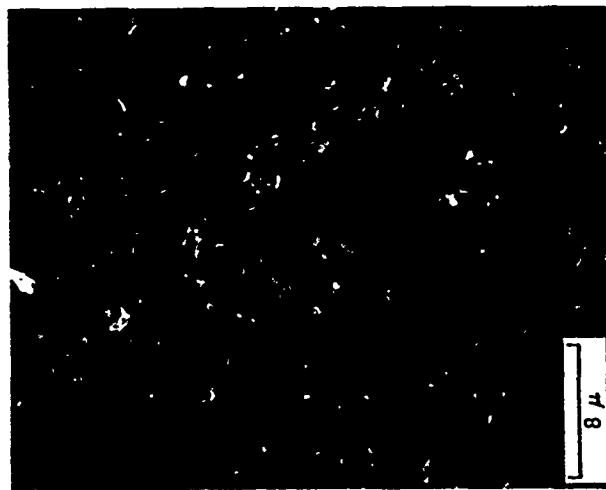


Fig. C-3. Data for pure LTI carbon (5408-7) flats and discs showing effective load



(a)

$\rho=1.97 \text{ g/cm}^3$ ,  $T=1180^\circ\text{C}$ ,  
60%  $\text{C}_3\text{H}_8$



(b)

$\rho=1.97 \text{ g/cm}^3$ ,  $T=1180^\circ\text{C}$ ,  
60%  $\text{C}_3\text{H}_8$



(c)

$\rho=1.78 \text{ g/cm}^3$ ,  $T=1240^\circ\text{C}$ ,  
25%  $\text{C}_3\text{H}_8$  + 2%  $\text{CO}_2$

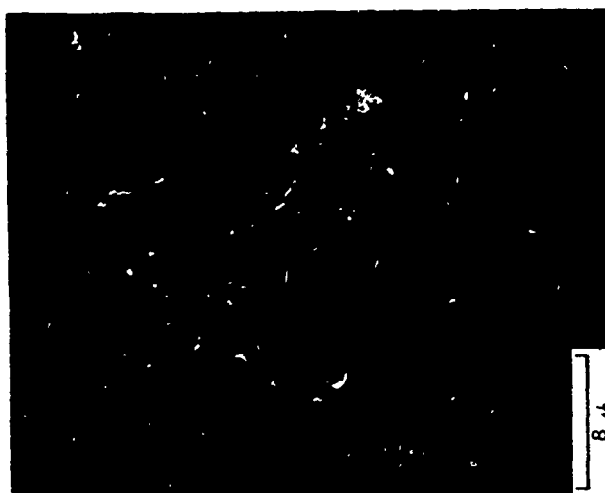
Fig. C-4. Scanning electron micrographs of fracture surfaces of a number of the carbons investigated



(d)  
 $\rho=1.71 \text{ g/cm}^3$ ,  $T=1280^\circ\text{C}$ ,  
 $7\% \text{ C}_3\text{H}_8$



(e)  
 $\rho=1.46 \text{ g/cm}^3$ ,  $T=1330^\circ\text{C}$ ,  
 $3\% \text{ C}_3\text{H}_8$



(f)  
 $\rho=1.45 \text{ g/cm}^3$ ,  $T=1330^\circ\text{C}$ ,  
 $3\% \text{ C}_3\text{H}_8$

Fig. C-4. (Continued)

APPENDIX D  
PHYSICAL PROPERTY DATA

D-1

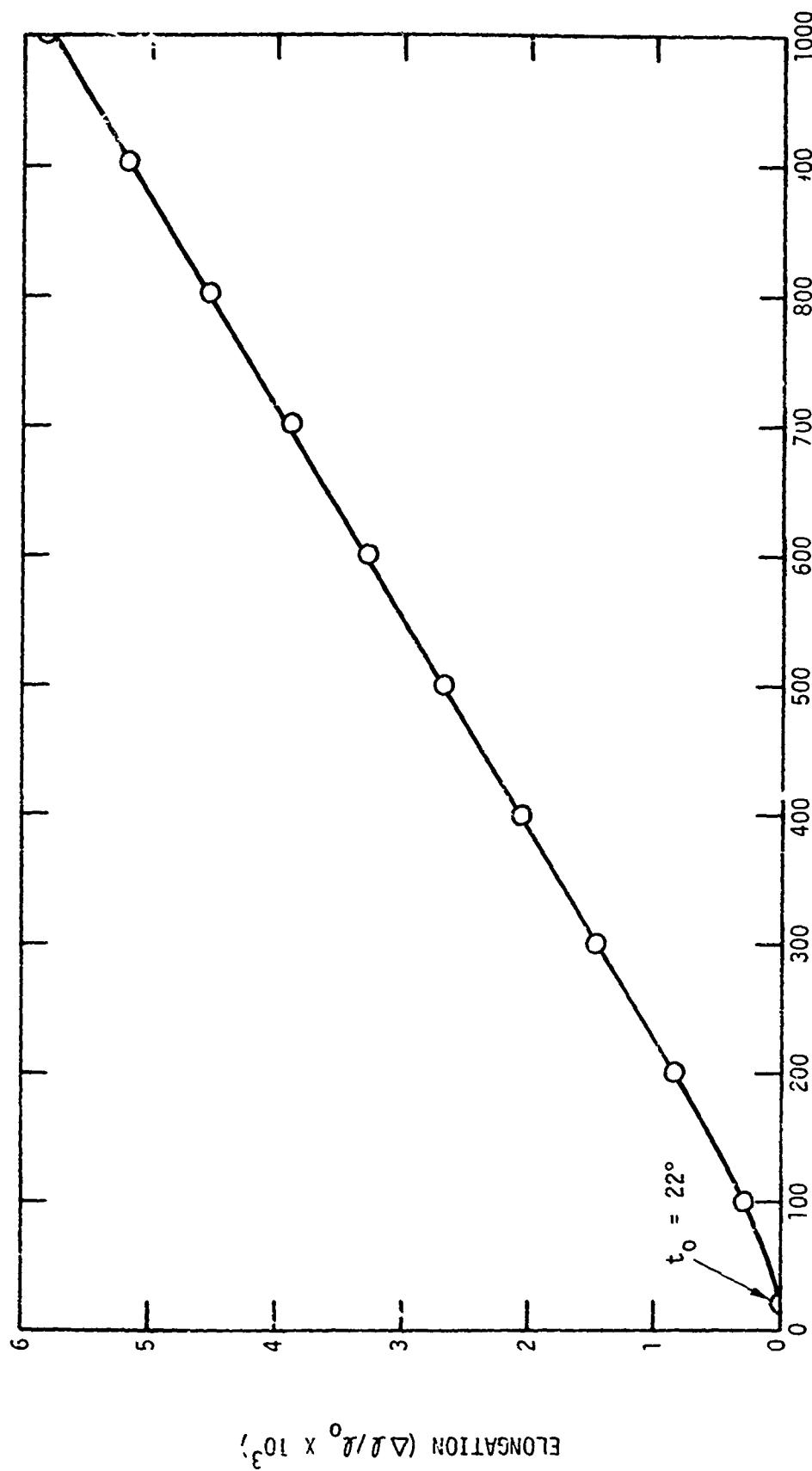


Fig. D-1. Elongation versus temperature for run 5408-7



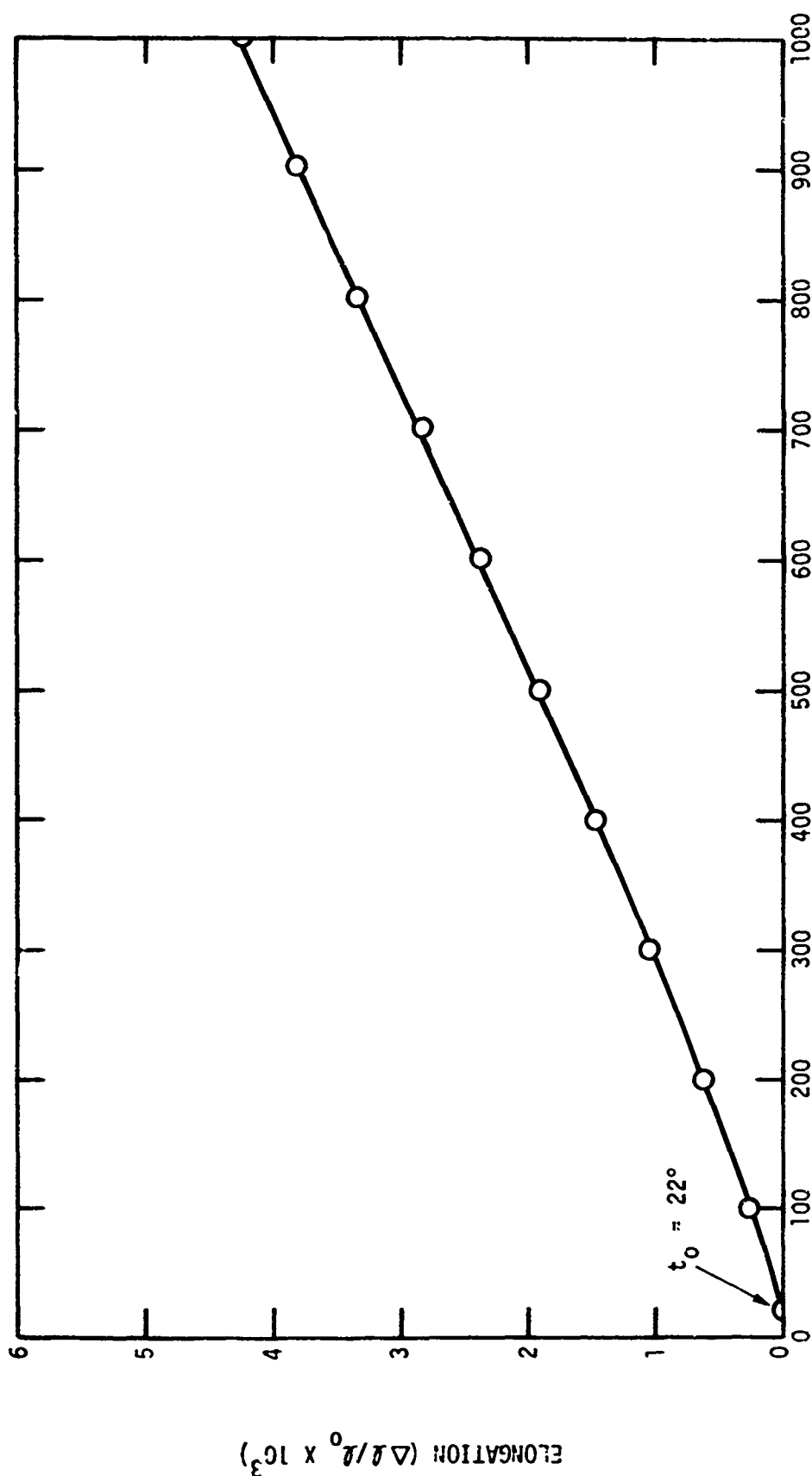


Fig. D-2. Elongation versus temperature for run 5408-11

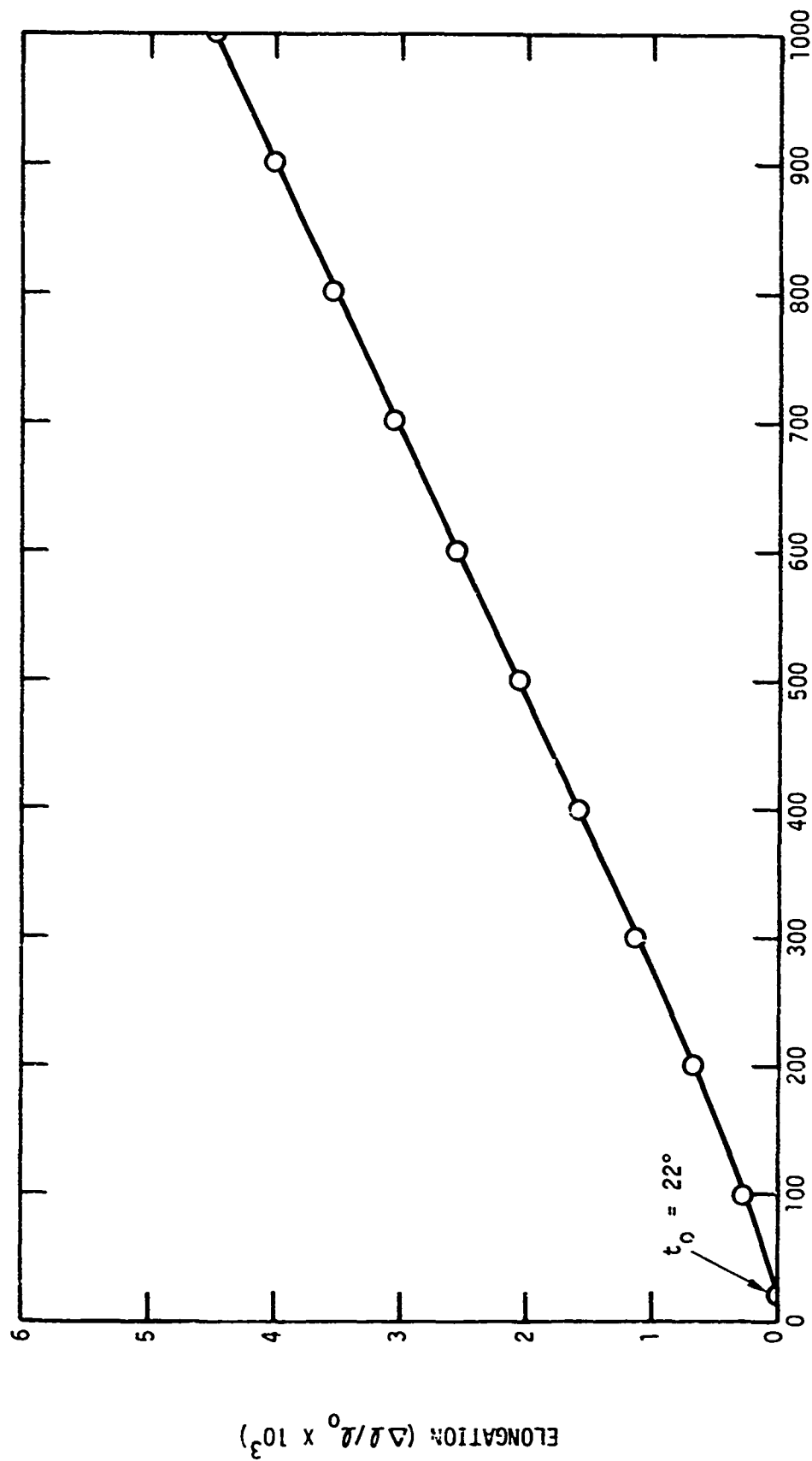


Fig. D-3. Elongation vs. temperature for run 5408-23

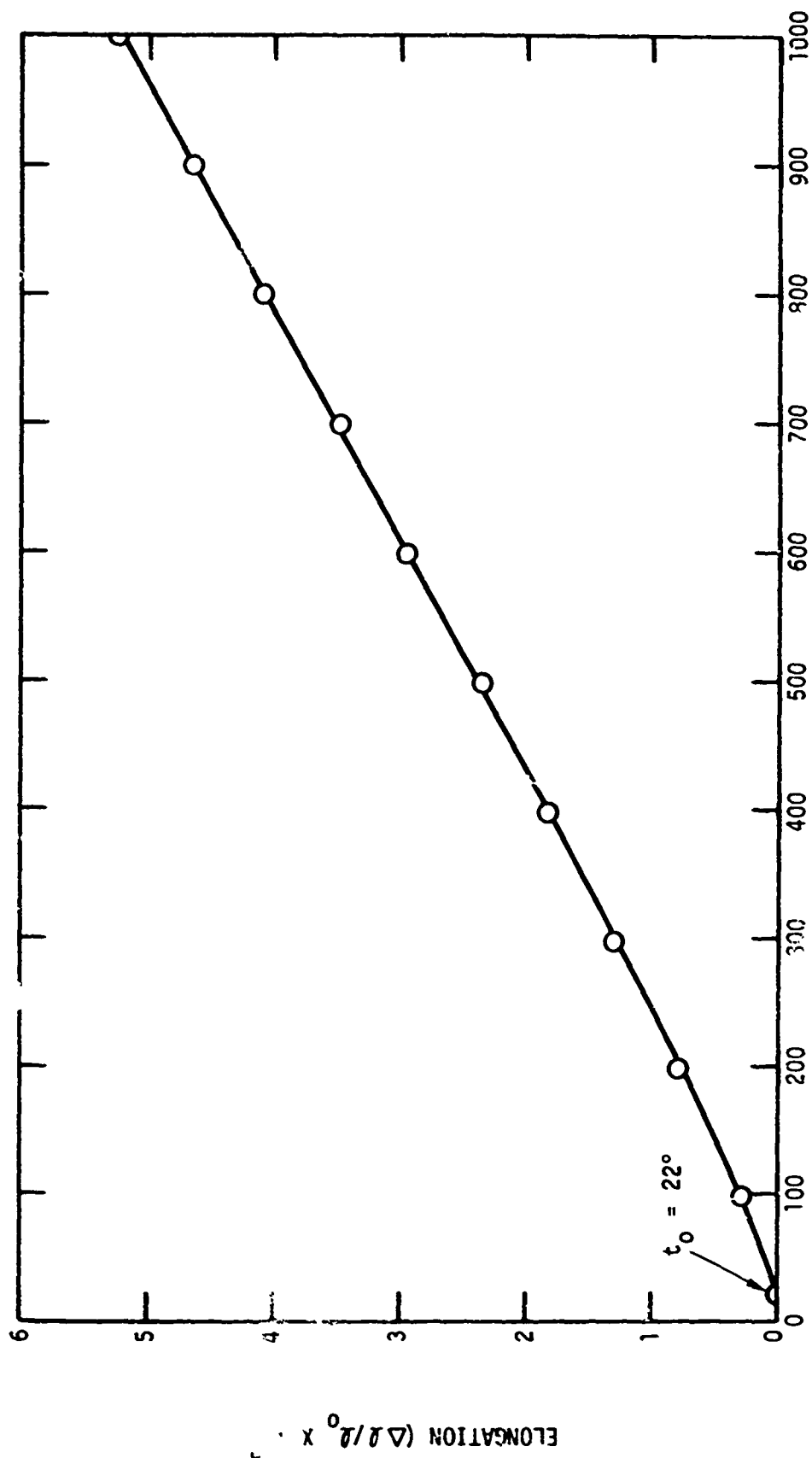


Fig. D-4. Elongation versus temperature for run 5408-25

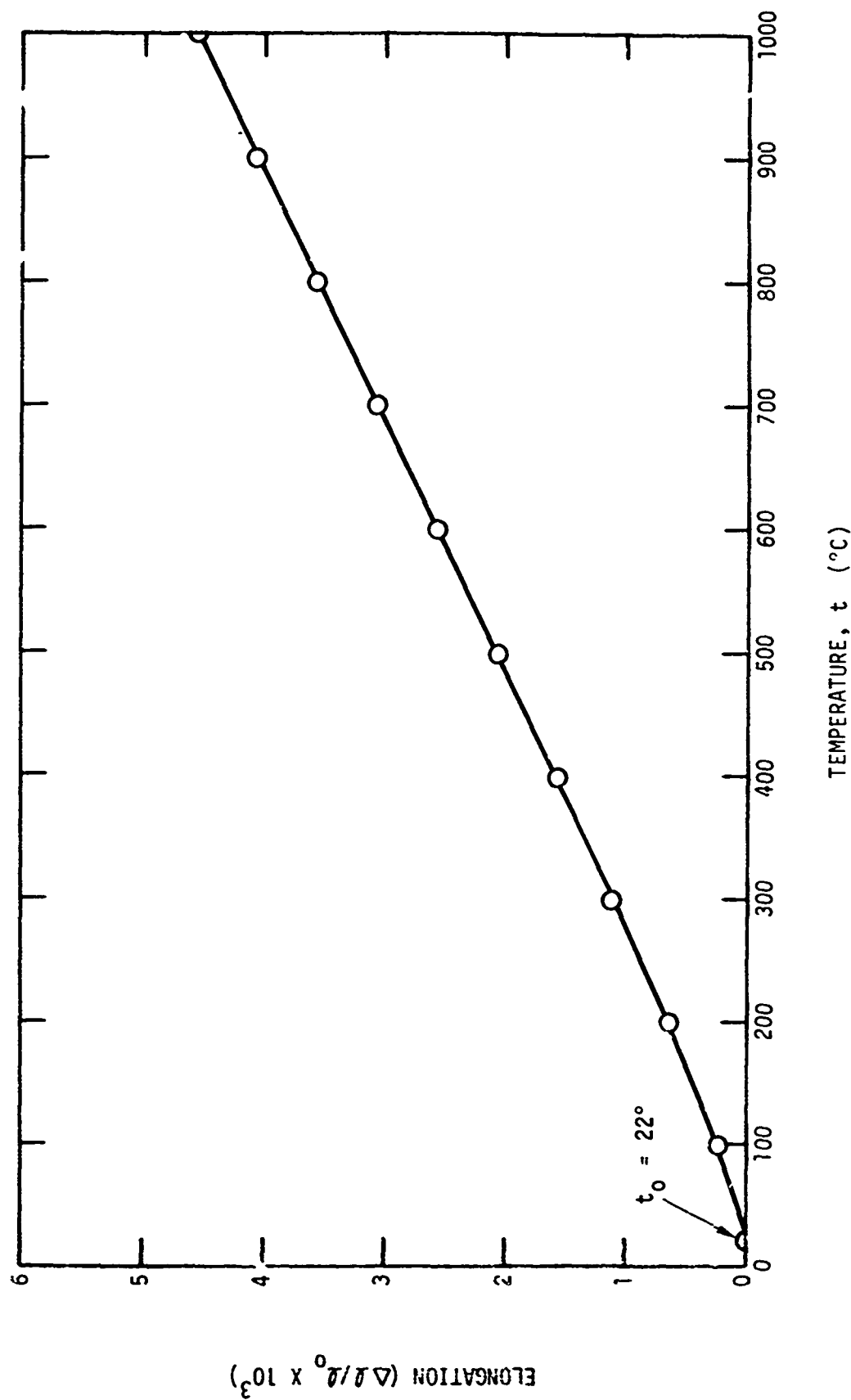


Fig. D-5. Elongation versus temperature for run 5408-27

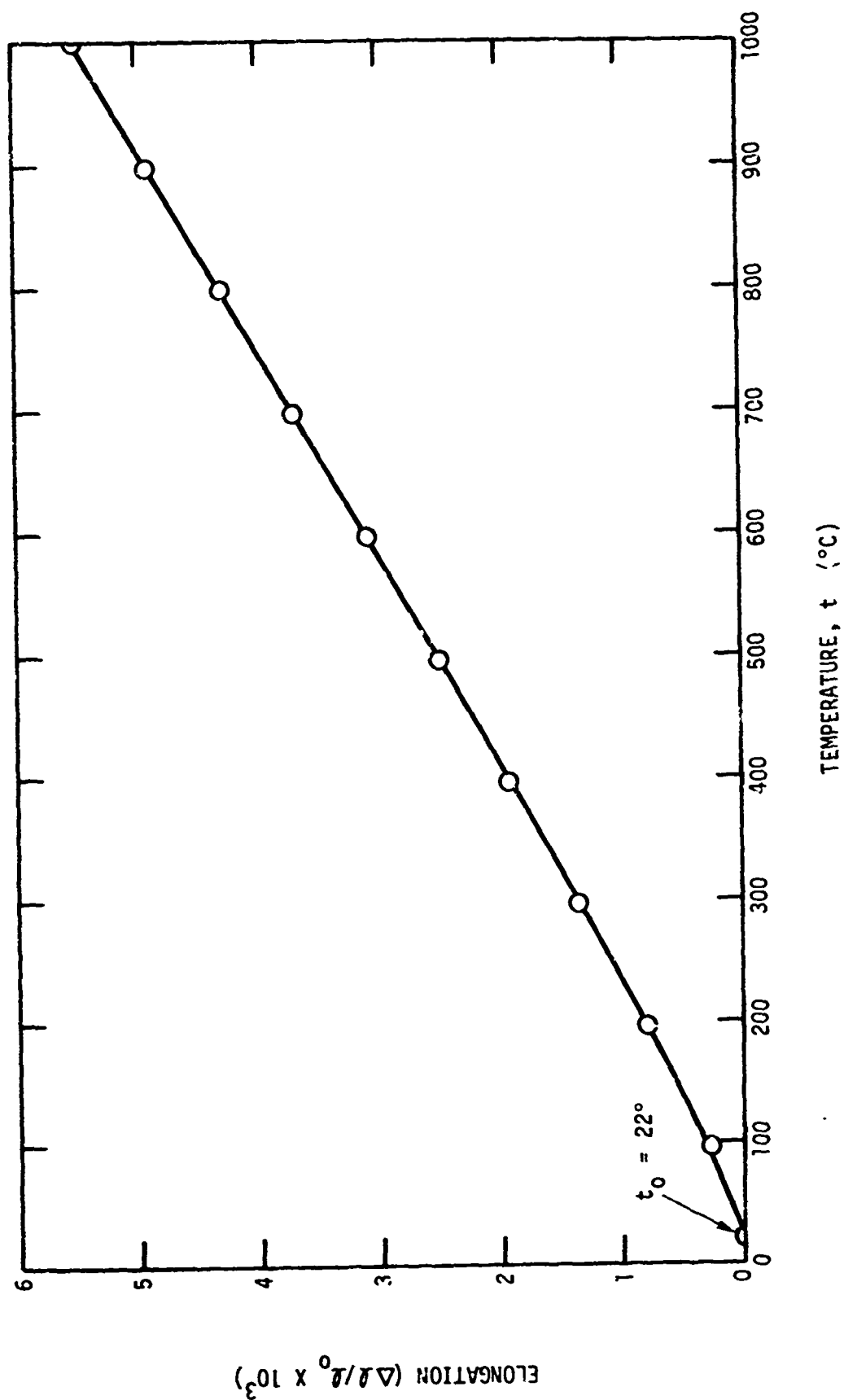


Fig. D-6. Elongation versus temperature for run 5408-31

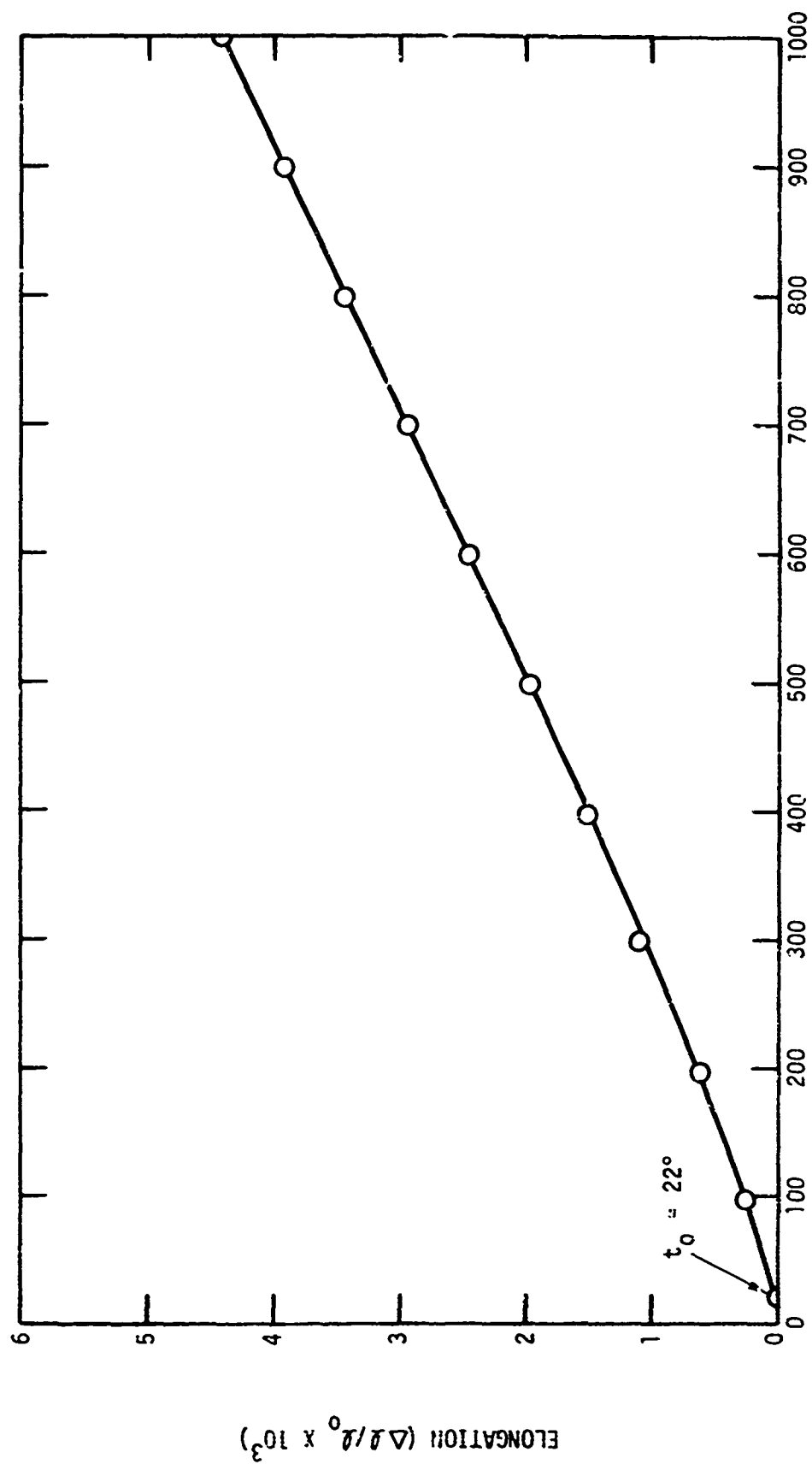


Fig. D-7. Elongation versus temperature for run 5408-33

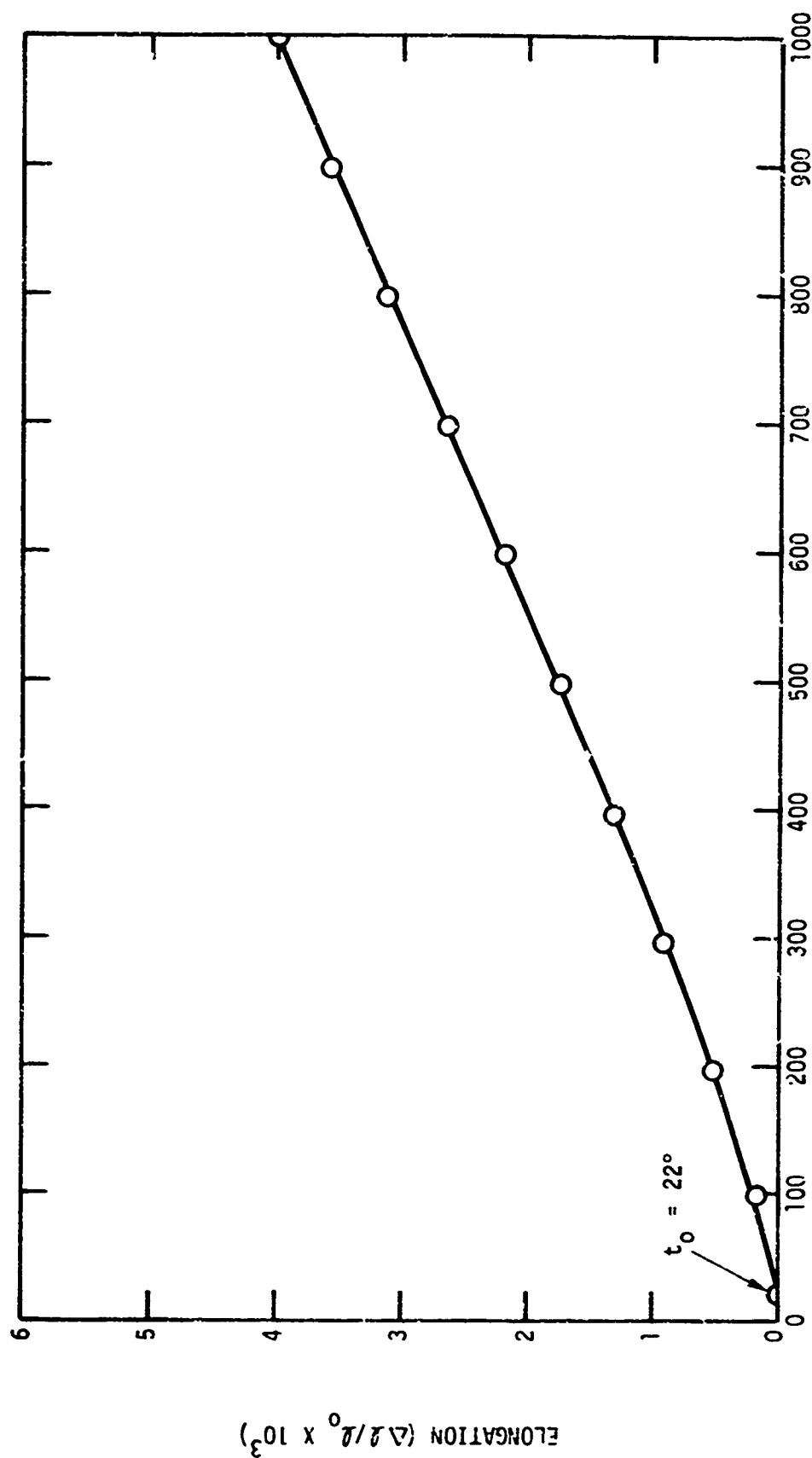


Fig. D-8. Elongation versus temperature for run 5408-35

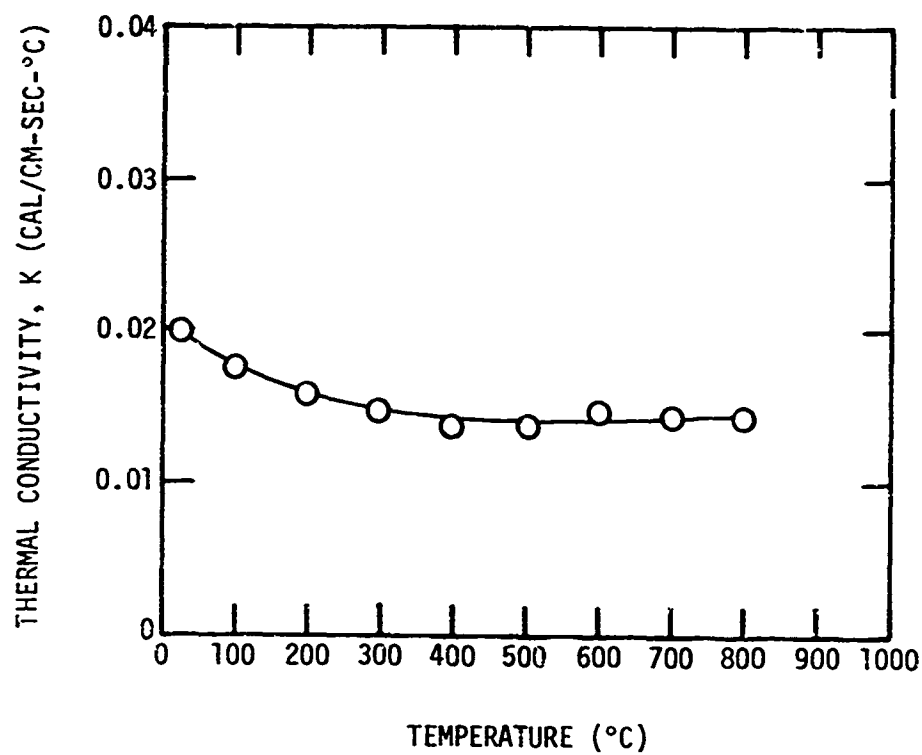


Fig. D-9. Thermal conductivity versus temperature for run 5408-7



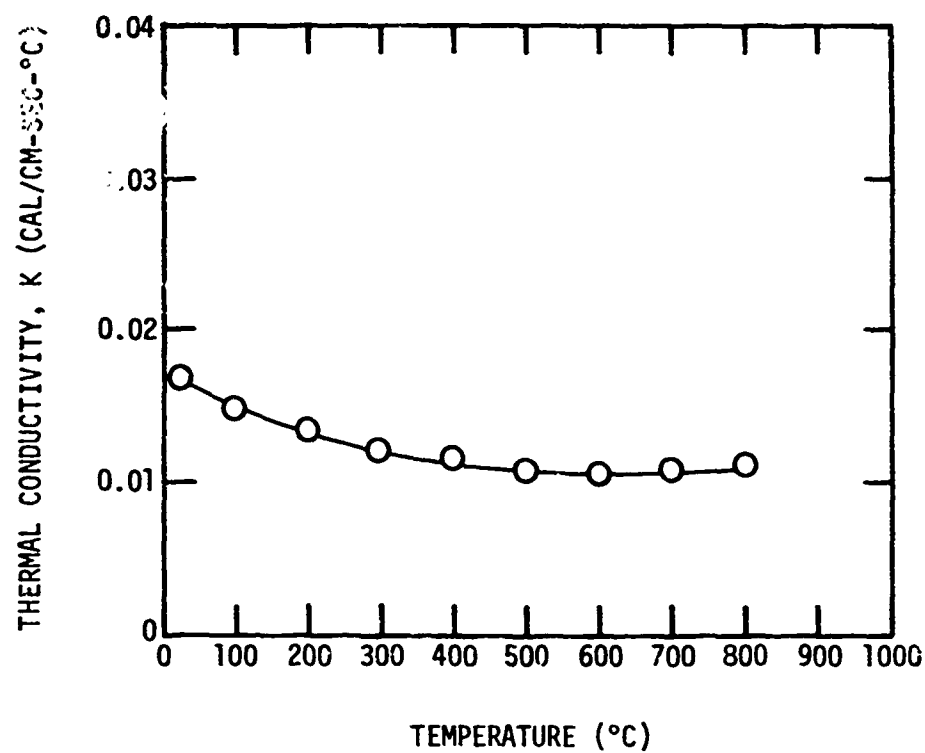


Fig. D-10. Thermal conductivity versus temperature for run 5408-25

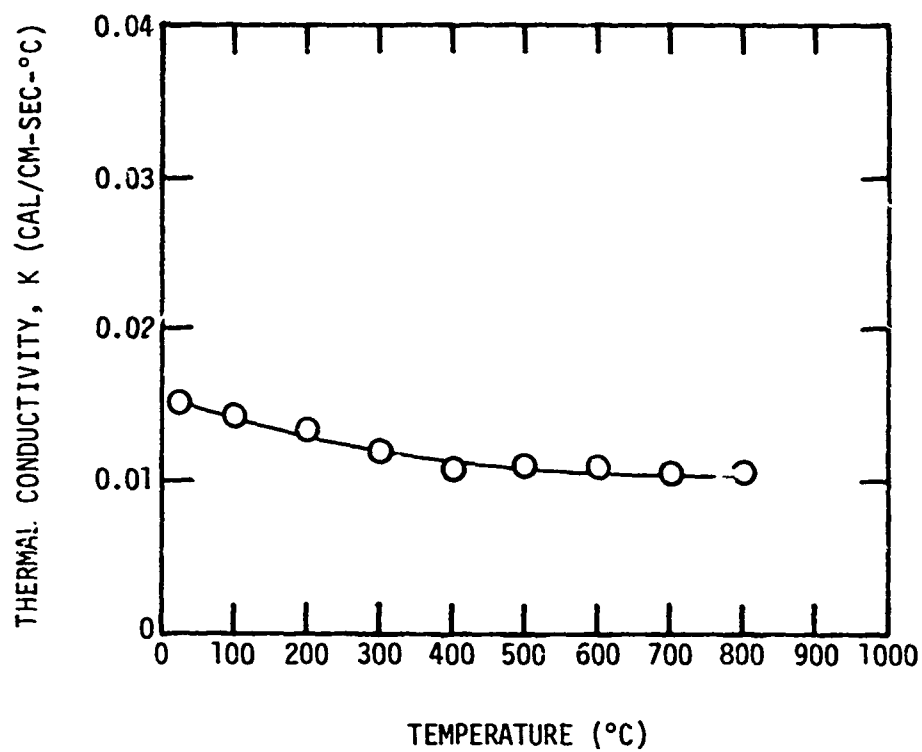


Fig. D-11. Thermal conductivity versus temperature for run 5408-27

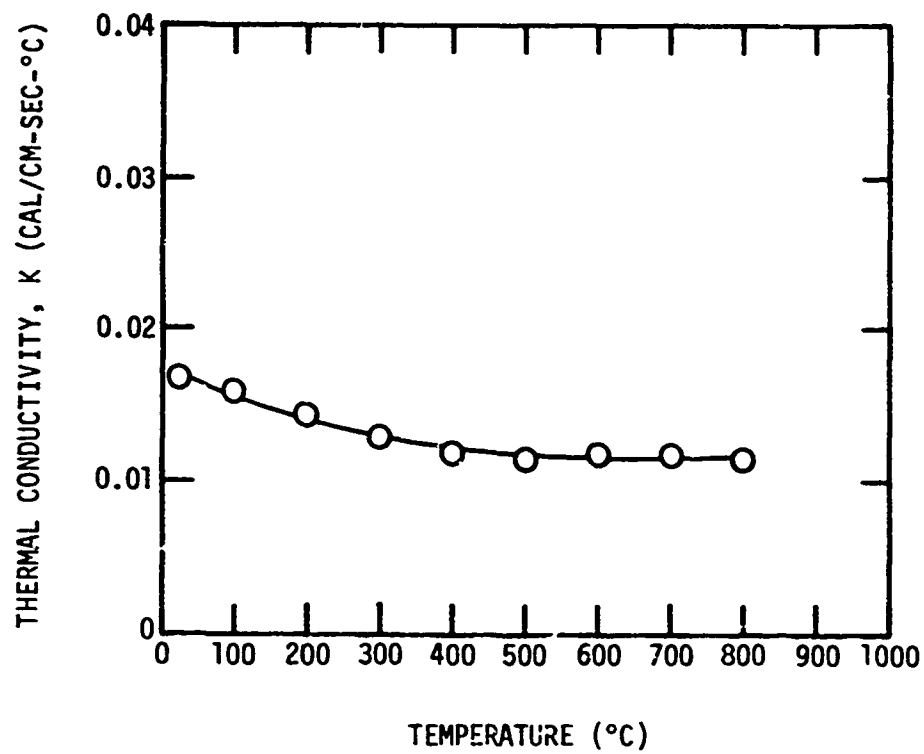


Fig. D-12. Thermal conductivity versus temperature for run 5408-31

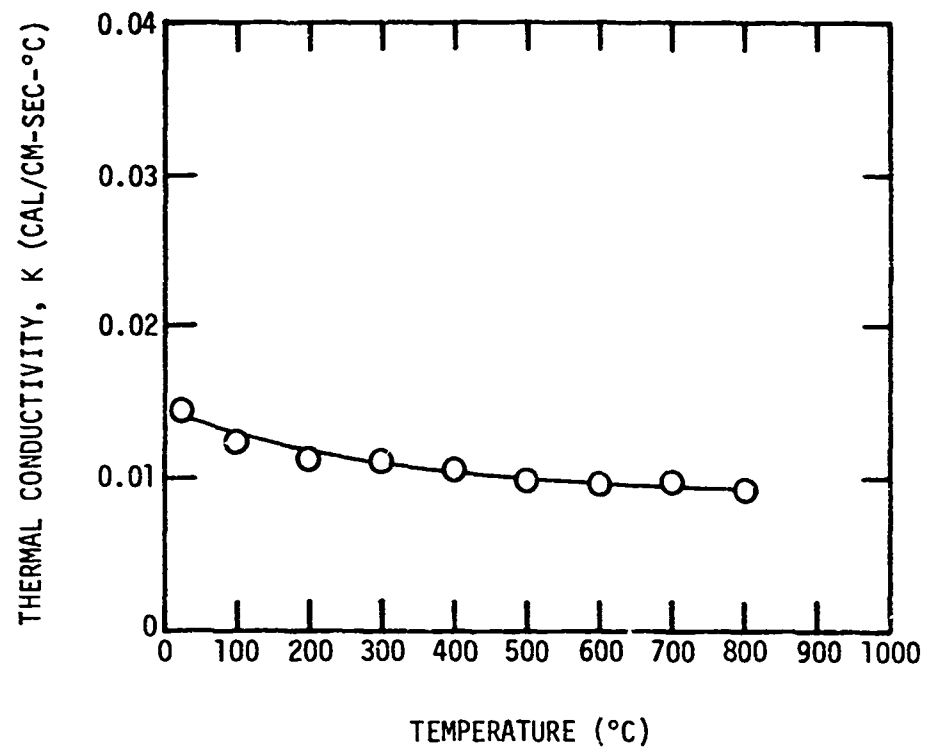


Fig. D-13. Thermal conductivity versus temperature for run 5408-33